Jahn–Teller order in perovskites and Prussian blues: X-ray scattering and Monte Carlo modelling

Elodie A. Harbourne

Hertford College, Oxford



A thesis submitted to the University of Oxford for the degree of Doctor of Philosophy

Supervisors: Prof. Andrew Goodwin and Prof. David Keen

Inorganic Chemistry Laboratory

University of Oxford

Trinity 2026

Declaration

The work presented in this thesis was carried out between October 2022 and June 2026 in the Inorganic Chemistry Laboratory, University of Oxford under the supervision of Professor Andrew L. Goodwin (University of Oxford) and Professor David A. Keen (ISIS). This thesis is the result of my own work, but where parts draw on the work of others, this is acknowledged at the start of every results chapter. This thesis has not been submitted in whole or in part for a degree at this or any other institution. Artificial Intelligence was used for inspiration for the thesis title—my supervisor's ChatGPT account was used.

Elodie Ann Harbourne

30th June 2026

Abstract

Prussian blue analogues (PBAs) have found applications in a variety of different areas, including batteries, gas storage, and cooperative magnetism. The functional versatility of PBAs arguably stems from the rich structural diversity of the PBA family. Hence, designing the next-generation of PBA functional materials requires understanding their many structure–property relationships. This thesis aims to see how well intentionally simple modelling can explain fairly complex phenomena.

This thesis first aims to get a better understanding of the local structure of relatively simple PBAs. The $MPt(CN)_6$ PBAs—of interest due to their negative thermal expansion behaviour—are essentially defect-free and hence their local structures can be characterised in terms of thermal displacements away from their average structure. Exploiting this direct relationship between local structure and dynamics, a new big-box modelling technique of pair distribution function (PDF) measurements is developed based on the optimisation of empirical potentials to obtain atomistic representations of PBAs.

Next, this thesis progresses onto exploring the interplay between cooperative Jahn–Teller (CJT) distortions and vacancies in more complex PBAs. A simple model, based on the competition between strain and crystal-field effects, is developed to understand the nature and emergence of CJT effects in PBAs. The empirical potential PDF refinement approach developed earlier in the thesis is then used to develop atomistic representations of these PBAs for the first time.

Given the relative success of using simple considerations to understand the phenomenology of CJT order in PBAs, this thesis goes on to test whether simple geometric considerations of a similar kind developed for PBAs can be used to understand CJT effects in the manganite perovskites, where a complex interplay between orbital, lattice, charge, and spin degrees of freedom is known to drive the emergence of the useful property of colossal magnetoresistance.

Finally, this thesis finishes by exploring whether PDFs obtained using X-ray free-electron laser (XFEL) technologies can be used to characterise JT/vacancy order in PBAs, with the eventual aim to use XFEL techniques to probe ultra-fast local structure changes in PBAs, *e.g.* during photoinduced charge transfer.

Acknowledgements

I would like to begin by thanking my two supervisors, Andrew Goodwin and Dave Keen. I feel incredibly grateful and privileged to have had the opportunity to learn from two genuinely kind and caring people. Thank you both for your endless patience, guidance, support, and company, and for making my overall experience such a positive and rewarding one. Andrew, your positiveness and excitement for science are infectious and your ability to make everyone feel welcomed and valued with their individuality, have made me feel empowered to explore and (hopefully!) do good science. I have certainly learnt a lot from my time in your group, both academically and personally, and will always be grateful for and look back fondly on the many opportunities and fun times I have had. Dave, thank you for always making time for me when I've been in need of a chat—I hope there will be many more future Keen-raised guide dogs to come(!)—and for showing me how to have some fun with things; both you and Andrew have shown me the importance of surrounding yourself with good and kind people, and I am extremely grateful to have been welcomed into your academic families.

I have been very fortunate to have been introduced to and worked alongside many wonderful people during my DPhil; Goodwin Group members past, present and future, as well as friends (adopted members) of the group. When I first joined the group for my Part II project, I had many people I could look up to and learn the way from: Simon, Harry, Nikolaj, Arianna, Johny, Emily, Tom, John, and Quentin. You all immediately made me feel welcomed and part of the group, and are arguably the biggest reason why I wanted to stay on in the group for a DPhil. Although we are all now alumni of the group, I'm not sure it's actually possible to truly leave the group, and I am continuously grateful for all your continued support. Arianna, thank you for reminding me when it's time to go home. Emily, thank you for being such an inspiring and impressive scientist whom I continue to look up to. Johny, thank

you for always looking out for me and somehow always seeming more excited about my work than me—your genuine interest and love for science is something special! Tom, thank you for somehow always knowing when I'm in need of a chat—your calm guidance and thoughtfulness has been appreciated more than I could thank you for here. John, thank you for believing in me when I doubt myself. Quentin, thank you for keeping me company for many fun years in the L-office, your good humour always brightened my day!

I would also like to thank newer members of the group for always offering an open ear: Nim, Theo, Tristan, Hunter, Yevheniia, Adam, Rob(ert), Guy, Helena, Flo(rence), Sam, Raymond, Kieran, Manisha, and Theo—you are all incredible people with a great diversity of interests, and I am grateful for the many thought-provoking discussions we have shared. Rob, I hope that with whichever path you choose, you approach it with your wholeheartedness. Guy, thank you for your kindness and being a great sounding board. Helena, seeing you grow in confidence over the last few years, giving talks with real conviction and power, has been lovely to watch. Flo, you are an incredible person and scientist, and I hope you can believe this and realise that no apologies are necessary. Sam, I wish that one day I can answer questions with at least half your enthusiasm!

I would also like to thank the many Part IIs and visiting students who have brought so much energy and enthusiasm to the group. Becca, I too will always remember our many interesting conversations, the kind that can only be inspired by waiting for the centrifuge to finish or after a long day!

During my time as a DPhil student, I have been very fortunate to have had the opportunity to interact with many people outside the group at conferences and beamtimes, though I have come to realise that it really is a small world! This is something that I find particularly great about the academic world—with its ability to connect people from all over, I know that if I'm ever visiting somewhere in the future, I likely have a friend there. I would particularly like to thank my Danish friends

for adopting me on beamtimes, and for your thoughtfulness with always making me feel welcome and included. I am also grateful to have had the opportunity to be involved with the XFEL project, which has introduced me to a whole community of great people. I have also very much enjoyed the collaboration with Mark Senn and Ben Tragheim at Warwick, especially seeing how different approaches and ways of thinking can come together and complement one another. I am also grateful to have had the opportunity to teach during my DPhil, something that I have found both enjoyable and incredibly rewarding, and I feel very privileged to have been able to share in many students' journeys that I will follow with eagerness.

I would also like to thank all my fellow D(ance)Phil friends and coaches—particularly Malina, Ei, Jamie, Ben, Stef, Michael, and Kevin—you have helped me in more ways than you might imagine. I am also grateful to my cricket friends, JdB, and Graham for helping me to enjoy cricket again. The breadth of opportunities that have been available to me whilst at Oxford are not lost on me.

Finally, I would like to thank my family for their support and belief in me, and for being good sports when I try to explain what it is that I do.

Publications

- E. A. Harbourne, H. Barker, Q. Guéroult, J. Cattermull, L. A. V. Nagle-Cocco, N. Roth, J. S. O. Evans, D. A. Keen, A. L. Goodwin,
"Local structure and dynamics in $MPt(CN)_6$ Prussian blue analogues",
Chem. Mater. **2024**, *36*, 5796–5804.

- E. A. Harbourne, J. Cattermull, H. L. B. Boström, R. Witte, N. Roth, M. Pasta, D. A. Keen, A. L. Goodwin,
"Rules governing cooperative Jahn–Teller order in Prussian blue analogues",
arXiv:2408.13169, **2024**. (Under revision for *Nat. Commun.*).

- B. R. M. Tragheim, E. A. Harbourne, C. Ritter, A. L. Goodwin, M. S. Senn,
"The interplay between Jahn–Teller distortions and structural degrees of freedom in pseudocubic states in manganite perovskites",
Phys. Rev. B **2025**, *112*, 115119.

- A. F. Sapnik, P. A. Chater, D. S. Keeble, J. S. O. Evans, F. Bertolotti, A. Guagliardi, L. J. Støkler, E. A. Harbourne, A. B. Borup, R. S. Silberg, A. Descamps, C. Prescher, B. D. Klee, A. Phelipeau, I. Ullah, K. G. Medina, T. A. Bird, V. Kaznelson, W. Lynn, A. L. Goodwin, B. B. Iversen, C. Crepisson, E. S. Bozin, K. M. Ø. Jensen, E. E. McBride, R. B. Neder, I. Robinson, J. S. Wark, M. Andrzejewski, U. Boesenberg, E. Brambrink, C. Camarda, V. Cerantola, S. Goede, H. Höppner, O. S. Humphries, Z. Konopkova, N. Kujala, T. Michelat, M. Nakatsutsumi, A. Pelka, T. R. Preston, L. Randolph, M. Roeper, A. Schmidt, C. Strohm, M. Tang, P. Talkovski, U. Zastrau, K. Appel, D. A. Keen,
"High-quality ultra-fast total scattering and pair distribution function data using an X-ray free-electron laser",
IUCrJ. **2025**, *12*, 531–547.

Contents

1 Introduction **1**

1.1 Overview 1

1.2 Degrees of freedom in perovskites and Prussian blue analogues 2

1.3 Characterising disordered systems 20

1.4 Structure–function relationships in key perovskite and PBA systems . 32

1.5 Aims and thesis outline 46

2 Methods **51**

2.1 Crystal structures and symmetry 51

2.2 Scattering theory and reciprocal space 53

2.3 Powder X-ray diffraction measurements 57

2.4 Total scattering 66

2.5 Lattice dynamics 74

2.6 Monte Carlo simulations 84

3 Local structure and dynamics in $MPt(CN)_6$ Prussian blue analogues **86**

3.1 Overview 86

3.2 Acknowledgements 87

3.3 Introduction 88

3.4 Methods 90

3.5 Results and Discussion 93

3.6 Conclusions 115

4 Rules governing Jahn–Teller order in Prussian blue analogues 117

4.1 Overview . . . 117

4.2 Acknowledgements . . . 118

4.3 Introduction . . . 119

4.4 Methods . . . 122

4.5 Results and Discussion . . . 124

4.6 Pair distribution function refinements . . . 143

4.7 Conclusions . . . 152

5 The interplay between Jahn–Teller distortions and structural degrees of freedom in manganite perovskites 154

5.1 Overview . . . 154

5.2 Acknowledgements . . . 155

5.3 Introduction . . . 156

5.4 $LaGa_{1-x}Mn_xO_3$: Monte Carlo simulations . . . 158

5.5 $La_{0.5}Ca_{0.5}MnO_3$: Monte Carlo simulations . . . 168

5.6 Conclusions and future directions . . . 180

6 Measuring pair distribution functions with X-ray free-electron lasers: ultra-fast studies of disorder in Prussian blue analogues 182

6.1 Overview . . . 182

6.2 Acknowledgements . . . 183

6.3 Introduction . . . 184

6.4 Pair distribution function measurements at the EuXFEL . . . 187

6.5 Monte Carlo $G(r)$ . . . 204

6.6 Conclusions and future directions . . . 213

7 Conclusion and Outlook 216

7.1 Conclusions . . . 216

7.2 Outlook . . . 219

Bibliography **223**

Appendix A: Local structure and dynamics in $MPt(CN)_6$ Prussian blue analogues **239**

Appendix B: Rules governing Jahn–Teller order in Prussian blue analogues **247**

B1 Synthesis and characterisation 247

B2 Powder X-ray diffraction 250

B3 Monte Carlo simulations 257

Appendix C: The interplay between Jahn–Teller distortions and structural degrees of freedom in manganite perovskites **259**

C1 $LaGa_{1-x}Mn_xO_3$: Monte Carlo simulations 259

C2 $La_{0.5}Ca_{0.5}MnO_3$: Monte Carlo simulations 263

Appendix D: Measuring pair distribution functions with X-ray free-electron lasers: ultra-fast studies of disorder in Prussian blue analogues **267**

D1 EuXFEL HED IC1: setup 1 267

D2 Monte Carlo $G(r)$ 269

List of Figures

1.1 Perovskite structure 3

1.2 The degrees of freedom of a perovskite 4

1.3 Common compositional ordering patterns of perovskites 5

1.4 Crystal field splitting 7

1.5 The first-order Jahn–Teller E_g distortion space spanned by the Q_2 and Q_3 modes 8

1.6 Orbital ordering patterns in perovskites 9

1.7 Simple tilt patterns in perovskites and their Glazer notation 11

1.8 The degrees of freedom of a Prussian blue analogue 13

1.9 Hexacyanometallate vacancies in PBAs 14

1.10 Hydration geometry of PBAs 15

1.11 Cooperative volume-reducing tilts in PBAs 16

1.12 Conventional tilts, unconventional tilts, and columnar shifts in molecular perovskites 17

1.13 Comparison of exchange interactions and elastic constants in conventional and molecular perovskites 18

1.14 Interplay of cooperative Jahn–Teller order and hexacyanometallate vacancy incorporation in PBAs 19

1.15 The problem of geometric frustration as demonstrated by the Ising triangular antiferromagnet 22

1.16 Correlated disorder in square ice 26

1.17 Vacancy-network variations in PBAs 28

1.18 Small-box 'real-space Rietveld' analysis of $La_{1-x}Ca_xMnO_3$ 30
1.19 Proposed orbital models for $LaMnO_3$ 32
1.20 Different charge and orbital ordering schemes in the phase diagram of $La_{1-x}Ca_xMnO_3$ 33
1.21 $La_{0.5}Ca_{0.5}MnO_3$ structure proposed by Radaelli et al. 35
1.22 Tension effect mechanism 37
1.23 Characterisation of NTE behaviour in PBAs 38
1.24 X-ray PDF measurements of PBAs 39
1.25 Schematic illustration of a PBA battery 40
1.26 Cycling between different phases of $K_{2-x}Mn[Fe(CN)_6]$ during cycling 41
1.27 Schematic representation of spin states in CoFe PBA and optical pump-probe/XANES measurements 45

2.1 Crystal classes 52
2.2 Scattering from a periodic arrangement of atoms 54
2.3 The first Brillouin zone for two cubic lattices 56
2.4 Schematic of a synchrotron 60
2.5 Schematic of an X-ray free-electron laser 61
2.6 Bunch pattern of the EuXFEL 63
2.7 Total scattering experimental considerations 74
2.8 Phonon dispersion curves of one-dimensional monatomic crystals . . . 77
2.9 Phonon dispersion curves of one-dimensional diatomic crystals 78
2.10 Phonon dispersion curves of three-dimensional diatomic crystals . . . 79
2.11 The local tension effect 83

3.1 Prussian blue analogue structure 89
3.2 Pawley fits of $MnPt(CN)_6$ and $CuPt(CN)_6$ 93
3.3 Simultaneous 'real-space Rietveld' PDF and conventional Rietveld refinements of $MnPt(CN)_6$ and $CuPt(CN)_6$ 94
3.4 Iterative process of refining MC parameters 98

3.5 Overview of a MC-driven 'interaction-space' PDF refinement approach 99
3.6 Goodness-of-fit as a function of r_e . . . 104
3.7 Goodness-of-fit as a function of k_r(M–N) . . . 105
3.8 Goodness-of-fit as a function of k_θ) . . . 106
3.9 Experimental X-ray total scattering data and empirical MC fits . . . 107
3.10 Representations of the local and average structures of $MPt(CN)_6$ PBAs determined from PDF refinements . . . 109
3.11 Partial pair-correlation functions for $MnPt(CN)_6$ and $CuPt(CN)_6$ extracted from PDF-driven MC simulations . . . 110
3.12 Lattice dynamics in $MPt(CN)_6$ PBAs . . . 112
3.13 Cross-sections of representative $MnPt(CN)_6$ and $CuPt(CN)_6$ configurations . . . 113
3.14 Phonon dispersion relations for $CuPt(CN)_6$ determined from our PDF-derived lattice dynamical model . . . 115

4.1 Primary mechanisms driving cooperative Jahn–Teller order in dense transition-metal compounds . . . 120
4.2 Strain model for cooperative JT effects in PBAs . . . 125
4.3 Evolution of long-range CJT order in vacancy-free PBAs . . . 127
4.4 Structural behaviour of $Cu_xMn_{1-x}[Pt(CN)_6]$ PBAs . . . 129
4.5 Strain-only model for vacancy incorporation . . . 130
4.6 Evolution of long-range CJT order in partially-vacant JT-active PBAs 131
4.7 Dependence of ground-state CJT order and ground-state residual strain on vacancy concentration determined using MC simulations . . 133
4.8 Updated vacancy model: strain and crystal-field . . . 134
4.9 Summary of the effect of the crystal-field term on the evolution of CJT order in JT-active PBAs . . . 135
4.10 Dependence of ground-state CJT order on vacancy concentration determined using MC simulations . . . 137

4.11 Vacancy-driven CJT melting in $Cs_xCu[Fe(CN)_6]_{(2+x)/3}$: comparison between experiment and MC simulations 138
4.12 Generic ground-state phase map for PBAs 140
4.13 Structural behaviour of $Cu_xMn_{1-x}[Co(CN)_6]_{2/3}$ PBAs 142
4.14 Small-box average structure Bragg and PDF fits of $Cu[Co(CN)_6]_{2/3}$. 144
4.15 A schematic illustrating the process of decorating a coarse-grained JT MC model and then using simple harmonic bond and angle restraints to relax the configuration accordingly 145
4.16 Testing different pictures of local Jahn–Teller order 147
4.17 Sensitivity of the PDF to varying degrees of local CJT order 149
4.18 Variation in single-crystal X-ray diffuse scattering patterns of models of $Cu[Co(CN)_6]_{2/3}$ with different pictures of local JT order 150
4.19 Single-crystal X-ray diffuse scattering patterns from various atomistic models of $Cu[Co(CN)_6]_{2/3}$ 151

5.1 $LaGa_{1-x}Mn_xO_3$ aristotype structure and C-type orbital order 157
5.2 Experimental distortion mode analysis of the $LaGa_{1-x}Mn_xO_3$ series . 158
5.3 Energy penalties used in the Monte Carlo simulation 160
5.4 Representative relaxed Monte Carlo configurations for different compositions 162
5.5 The evolution of the M_3^+, M_2^+ and Γ_5^+ modes extracted from the relaxed MC simulations 163
5.6 LGMO domain formation 164
5.7 Effect of applying shear strain in driving cooperative Jahn–Teller order 166
5.8 Distortion mode analysis of MC simulations under shear strain 167
5.9 Updated energy penalties used in the Monte Carlo simulations of $La_{0.5}Ca_{0.5}MnO_3$ 169
5.10 LCMO unit cell relationships 170

5.11 LCMO configuration and simulated single crystals patterns with next-nearest Jahn–Teller coupling term 173
5.12 Interplay of energy penalties in the LCMO Hamiltonian 174
5.13 LCMO: MC configurations and simulated single crystal patterns with no next-nearest Jahn–Teller coupling term 175
5.14 Investigating which of the charge order, nearest-neighbour JT coupling, and tilt terms needs to be included in the MC Hamiltonian to give the *CE* structure 176
5.15 LCMO interplay of degrees of freedom 177
5.16 The requirement of tilts to achieve the *CE* structure of $La_{0.5}Ca_{0.5}MnO_3$ 178

6.1 XFELs within the context of total scattering measurements 185
6.2 EuXFEL HED IC1 setup no. 1 188
6.3 EuXFEL HED IC1 setup no. 2 189
6.4 Sample mounting at the EuXFEL 190
6.5 Data processing overview 191
6.6 EuXFEL HED IC1 setup 2: crystalline standards 193
6.7 Comparison between XFEL and synchrotron PDF data of $Cu[Co(CN_6]_{2/3}$ PBA 195
6.8 EuXFEL HED IC1 setup 1: NIST Si 640b Rietveld and PDF fits . . 198
6.9 EuXFEL HED IC1 setup 1: data processing 199
6.10 EuXFEL HED IC1 setup 1: $Cu[Co(CN_6]_{2/3}$ PBA PDFs 203
6.11 An overview of the MCGR process using dummy data 207
6.12 Investigating the effect of Q gaps on the resultant PDF 210
6.13 Results from applying the MCGR approach to XFEL setup 1 data . . 212
6.14 Photoinduced charge transfer in $Rb_xMn_xCo_{1-x}[Fe(CN)_6]_{0.98}$ 215

A0.1 Goodness-of-fit as a function of k_r(M–N) 239
A0.2 Goodness-of-fit as a function of r_e(M–N) 240
A0.3 Goodness-of-fit as a function of r_e(C–X) 241

A0.4 Goodness-of-fit as a function of k_θ(M–X–Pt) 242
A0.5 Goodness-of-fit as a function of k_θ(N–M–N) 243
A0.6 Goodness-of-fit as a function of k_θ(C–Pt–C) 243
B2.7 Synchrotron X-ray powder diffraction patterns of $Cu_xMn_{1-x}[Pt(CN)_6]$ 253
B2.8 Synchrotron X-ray powder diffraction patterns of $Cu_xMn_{1-x}[Co(CN)_6]_{2/3}$ and corresponding Rietveld fits 255
B2.9 Synchrotron X-ray powder diffraction patterns of $Cs_xCu[Fe(CN)_6]_{(2+x)/3}$ 256
B3.10 Strain-only model: Effect of box size on the distribution of the ground state order parameter for the composition $x_{\text{vac}} = 1/3$, $x_{\text{JT}} = 1$ 257
B3.11 Effect of varying the weighting of the strain vs crystal-field terms in the composition $x_{\text{vac}} = 1/3$, $x_{\text{JT}} = 1$ 257
C1.12 Fixed box MC simulations 260
C1.13 Jahn–Teller domain formation in a Monte Carlo configuration of $LaMnO_3$ 261
C1.14 Tilt domain formation in a Monte Carlo configuration of $LaMnO_3$ . . 262
C2.15 LCMO configuration and simulated single crystals patterns of sublattices with next-nearest Jahn–Teller coupling term 263
C2.16 $La_{0.5}Ca_{0.5}MnO_3$: Effect of the split-atom term on the MC configurations and simulated single-crystal diffuse scattering patterns 264
C2.17 Effect of preventing rhombuses from tilting in the $La_{0.5}Ca_{0.5}MnO_3$ system 265
C2.18 $La_{0.5}Ca_{0.5}MnO_3$: MC configurations and simulated single-crystal diffuse scattering patterns with no next-nearest Jahn–Teller coupling term but enforced cell γ. 265
D1.19 EuXFEL HED IC1 setup 1: low-Q shadowing 268
D2.20 MCGR dummy data: impact of low-Q gap 269
D2.21 MCGR dummy data: impact of high-Q gap 270

Abbreviations

θ	Scattering angle (diffraction)
λ	Wavelength
1D	One-dimensional
2D	Two-dimensional
3D	Three-dimensional
3D-ΔPDF	Three dimensional difference pair distribution function
CJT	Cooperative Jahn–Teller
CMR	Colossal magnetoresistance
DFT	Density functional theory
EXAFS	Extended X-ray absorption fine structure
FCC	Face-centred cubic
FOJT	First-order Jahn–Teller
GULP	General Utility Lattice Program
HED	High Energy Density
IR	Infrared
irrep	Irreducible representation
JT	Jahn–Teller
LCMO	$La_{1-x}Ca_xMnO_3$
LGMO	$LaGa_{1-x}Mn_xO_3$
NMR	Nuclear magnetic resonance
NTE	Negative thermal expansion

MC	Monte Carlo
MCGR	Monte Carlo $G(r)$
MID	Materials imaging and dynamics
PBA	Prussian blue analogue
PDF	Pair distribution function
PTE	Positive thermal expansion
PXRD	Powder X-ray diffraction
RMC	Reverse Monte Carlo
RUM	Rigid unit mode
TCHZ	Thompson-Cox-Hasting pseudo-Voigt
TS	Total scattering
XFEL	X-ray free-electron laser
XRD	X-ray diffraction

Chapter 1

Introduction

1.1 Overview

Prussian blue analogues (PBAs) are a broad family of materials, long-studied for their many interesting properties. PBAs can harbour a variety of different distortions and defect structures, including Jahn–Teller (JT) distortions, hexacyanometallate vacancies, and octahedral rotations.[1] When seeking to design the next-generation of PBA functional materials, understanding the interplay between different distortions on a fundamental level will be important.

Similarly, the manganite perovskites are known to show a complex interplay between various degrees of freedom—including orbital, spin, charge, and lattice—that is implicated in the emergence of interesting electronic and magnetic properties, including the useful property of colossal magnetoresistance.[2–5] However, how each degree of freedom contributes to the emergence of the various phenomena is not well understood. Hence, there is motivation to understand the various degrees of freedom and how they couple in both the manganite perovskites and PBA families when seeking to tune the functional properties of these materials.

This chapter begins with an overview of the degrees of freedom in perovskites and PBAs, then goes on to discuss tools for characterising the local structure of materials, and finishes by highlighting the importance of understanding structure–function relationships in optimising functional manganite perovskites and PBA materials.

1.2 Degrees of freedom in perovskites and Prussian blue analogues

1.2.1 Conventional perovskites

The perovskite structure, with ABX_3 stoichiometry—where A and B are cations and X is an anionic linker—is deceptively simple; its structure is based on a three-dimensional network of corner-sharing BX_6 octahedra, with the A-site cation occupying the cavity at the centre of each cube [Fig. 1.1(a)]. The perovskite aristotype adopts $Pm\bar{3}m$ space group symmetry with all three ions located on high-symmetry (special) positions. The aristotype structure only contains one degree of freedom, the cubic lattice parameter, hence there exists a simple geometric relationship between the radii of the three component ions that can rationalise the relative stability of the structure. Goldschmidt quantified the geometric relationship between the ratio of the sizes of the three ions in terms of a dimensionless tolerance factor α, given by

$$\alpha = \frac{r_\mathrm{A} + r_\mathrm{X}}{\sqrt{2}(r_\mathrm{B} + r_\mathrm{X})}, \tag{1.1}$$

where r_i is the ionic radius of site i.[6] The tolerance factor gives an indication of how well the A-site cation fills the cavity of the BX_3 framework [Fig. 1.1(b)]; a value of $\alpha = 1$ indicates perfect filling to give a geometrically-stable structure. Empirically, the perovskite structure is found to be stable between $0.8 < \alpha < 1.05$, and it is this tolerance for size-mismatch that gives rise to the compositional diversity of perovskites.[6,7] The ideal case of $\alpha = 1$ is rare,[8] hence many perovskites—including the eponymous mineral perovskite $CaTiO_3$—adopt distorted lower-symmetry structures at room temperature that have more degrees of freedom.[8]

Perovskites can undergo a wide range of different symmetry-lowering structural distortions [Fig. 1.2]. The compositional and structural diversity of perovskites

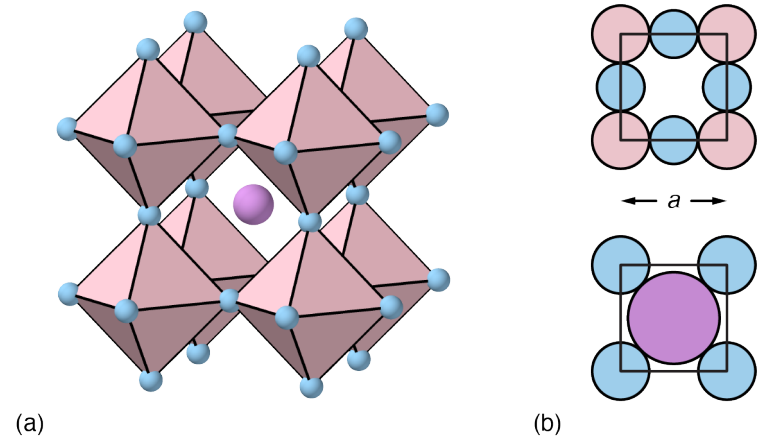


Figure 1.1: (a) A schematic representation of the ABX_3 perovskite structure. A-site cations are shown as purple spheres, B-sites are shown as light pink octahedra, and X-site anions are shown as light blue spheres. (b) The cubic lattice parameter, a, can be given by $a = 2(r_B + r_X)$ (top) or $a = \sqrt{2}(r_A + r_X)$ (bottom).

gives rise to many important properties, including superconductivity,[9,10] ferroelectricity,[11,12] and colossal magnetoresistance (CMR).[13,14] Hence, there is motivation to understand these structural distortions and their interplay on a fundamental level. The work of Chapter 5 is concerned with the interplay of degrees of freedom in two perovskites, $LaGa_{1-x}Mn_xO_3$ and $La_{1-x}Ca_xMnO_3$, hence the following section gives the necessary background to the degrees of freedom pertinent to Chapter 5: namely, compositional and charge order, first-order Jahn–Teller distortions, and octahedral tilts.

Compositional and charge order

Doping with different ions on one or more of the sites of the perovskite structure[15]—*e.g.* doping on the A-site in $La_{1-x}Ca_xMnO_3$[16]—can allow desirable properties to be tuned in functional perovskite materials.[17–20] For example, the coefficient of thermal expansion of $Bi_{1-x}Ln_xNiO_3$ can be tuned by varying the composition,[21] whilst the piezoelectric response of $PbZr_{1-x}Ti_xVO_3$ (PZT) is enhanced at its morphotropic phase boundary—the critical region of its composition phase diagram where there is a phase transition between phases of different crystal symmetries (tetragonal and rhombohedral).[22,23] Hence, the desire to understand the behaviour of solid solutions

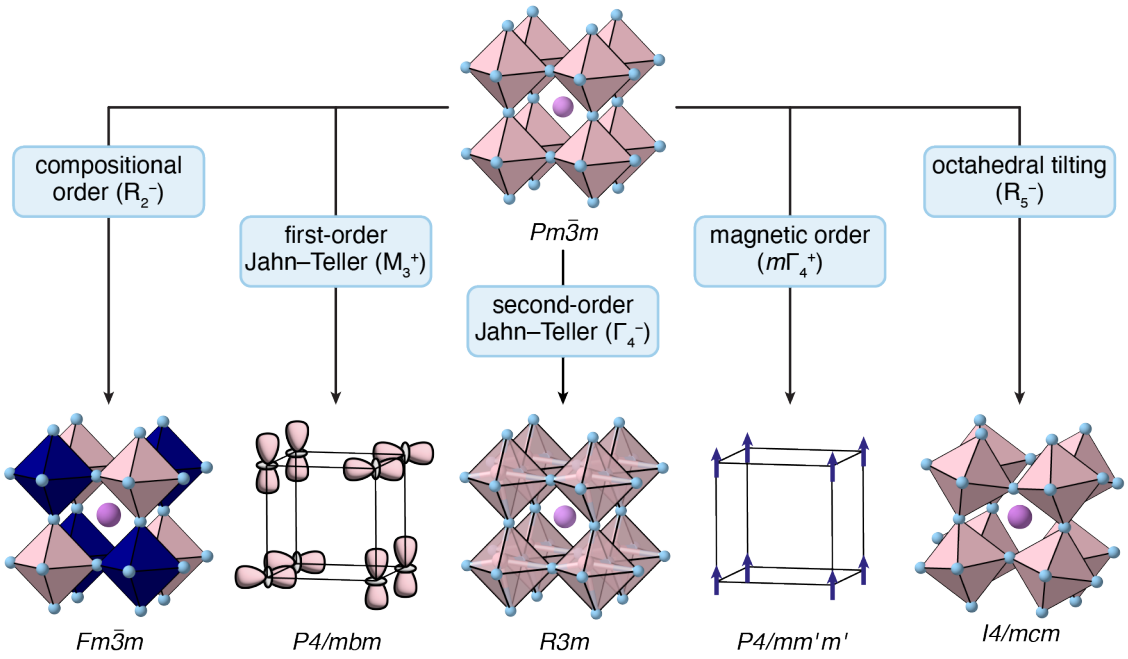


Figure 1.2: An overview of the degrees of freedom in perovskites. The aristotype $Pm\bar{3}m$ perovskite structure is shown as well as possible hettotypes arising from compositional order, first- and second-order Jahn–Teller distortions, magnetic order, and octahedral tilting. The space group and irreducible representation (irrep) for each respective symmetry-lowering distortion is given.

and the degrees of freedom that give rise to their interesting properties has led to much research in the perovskite community.[24–26]

Doping on the three types of ion sites—whether it be the A-, B-, or X-site—gives a range of different cation ordered/disordered arrangements,[24,27–31] which in turn can have a significant effect on the properties of functional perovskites.[32] Double perovskites—$AA'B_2X_6$ or $A_2BB'X_6$—generally favour cation-ordered patterns [Fig. 1.3] when there is a significant difference in the charge and/or size of the two constituent ions, as in the case of Sr_2FeMoO_6 and Sr_2NiWO_6, which show rocksalt ordering of the B-site cations.[13,28,33] However, whether a particular charge order pattern is preferred varies between the three types of ion sites. For example, a random distribution of cations on the A-sites is common, with layered-ordering [Fig. 1.3(a)] occurring occasionally typically in anion-deficient perovskites,[34,35] whereas rocksalt cation-ordered arrangements are generally favoured on the B-sites [Fig. 1.3(b)].[28,29]

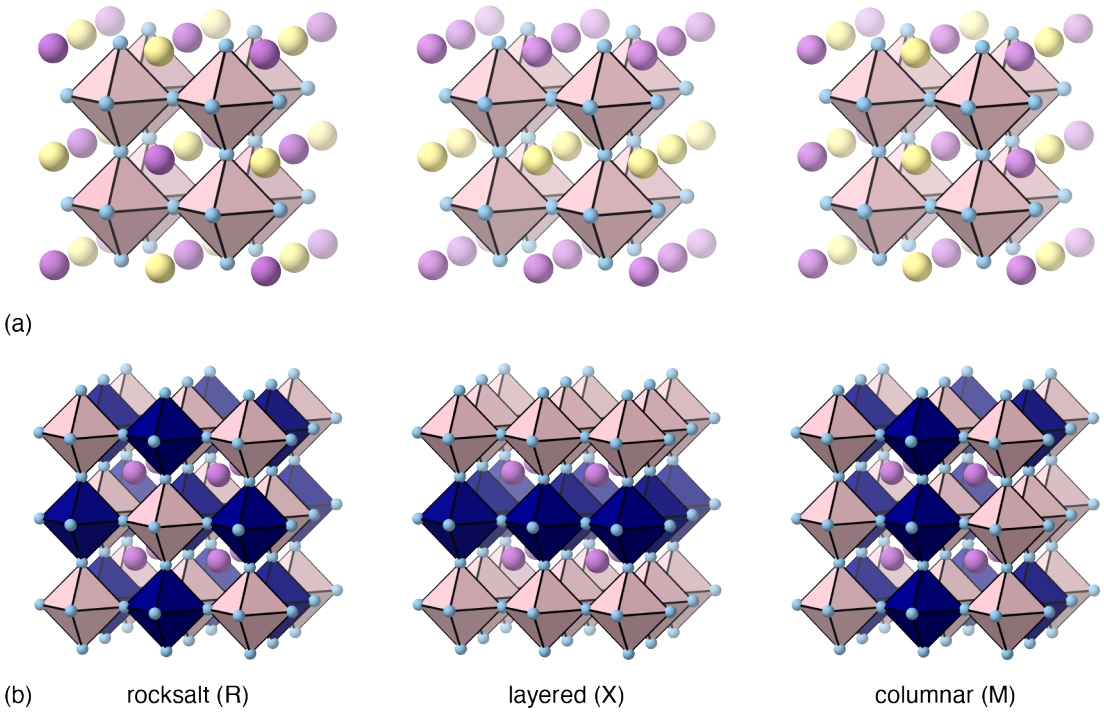


Figure 1.3: An overview of the compositional ordering patterns common to perovskites. The three types of cation order—rocksalt, layered, and columnar—are illustrated for (a) A-site cations and (b) B-site cations. The point in reciprocal space relevant to each ordering pattern is given in brackets.

The preference for a layered arrangement of A-site cations can be understood from the oxide displacements that occur to optimise the bonding of the different A-site cations;[28] these oxide displacements are allowed by the symmetry of the layered cation arrangement. By contrast, the rocksalt cation-ordered pattern is typically favoured on the B-sites to maximise the distance between the typically highly-charged B-site cations. Coexisting cation order on both the A- and B-sites is possible in double-double perovskites, but this is relatively rare.[36] Substitution on the X-site, *e.g.* in ABO_2X systems (where X = N^{3-}, F^-, or H^-), typically results in less straightforward anion (dis)order;[30,31] a *cis* arrangement of X^- anions around the octahedra are generally favoured, which can lead to planes of correlated anion disorder.[37,38]

Charge order is intrinsically related to cation order, and is typically observed in systems containing mixed-valent ions, such as the doped manganite perovskites

(*e.g.* $La_{1-x}Ca_xMnO_3$, where doping on the A-site tunes the mix of Mn^{4+} and Mn^{3+} ions), or in systems with ions prone to charge disproportionation.[39–44] A variety of different charge-ordered patterns are known to exist, ranging from rocksalt and layered to more complicated.[34,45–47] Unambiguously determining the charge order of materials can prove a challenge, and is especially difficult in systems that can adopt different charge-ordered states.[48] Charge order transitions can also occur, where previously delocalised electrons localise on specific ions.[48] Additionally, electrons can delocalise over a few ions to form a polaron, as observed in *e.g.* the polaronic $La_{1-x}Ca_xMnO_3$ and $La_{1-x}Sr_{1+x}MnO_4$ series.[49,50] Understanding and exploiting the complexity of charge order is of fundamental interest due the effect it has on both the electronic and magnetic properties of functional perovskite materials.[51–53]

First-order Jahn–Teller distortions

First-order cooperative Jahn–Teller (JT) instabilities are known to affect the electronic, magnetic, and structural properties of materials.[17–20,54,55] The first-order Jahn–Teller (FOJT) distortion occurs in systems with an unequal occupation of degenerate orbitals; the system undergoes a symmetry-lowering structural distortion to remove this degeneracy.[56] The FOJT can appear in a range of different materials,[57,58] with the most important to this thesis concerning the manganite perovskites, $LaGa_{1-x}Mn_xO_3$ and $La_{1-x}Ca_xMnO_3$, and Prussian blue analogues, $Cu[Pt(CN)_6]$ and $Cu[Co(CN)_6]_{2/3}$. In these systems, the FOJT distortion arises due to the unequal occupation of transition metal *d*-orbitals in an octahedral coordination environment.

Whilst the five *d*-orbitals [Fig. 1.4(a)] of a transition metal ion are all degenerate in a spherical crystal field (the 'free ion') [Fig. 1.4(b)], they become split in an octahedral crystal field such that three orbitals (the t_{2g} set) become lower in energy than the other two (the e_g set) [Fig. 1.4(c)]. Hence, Cu^{2+} (d^9, $t_{2g}^6e_g^3$) and high-spin Mn^{3+} (d^4, $t_{2g}^3e_g^1$) are both susceptible to a FOJT distortion [Fig. 1.4(d)] since they have an unequal occupation of doubly degenerate e_g orbitals. Electronic degeneracy

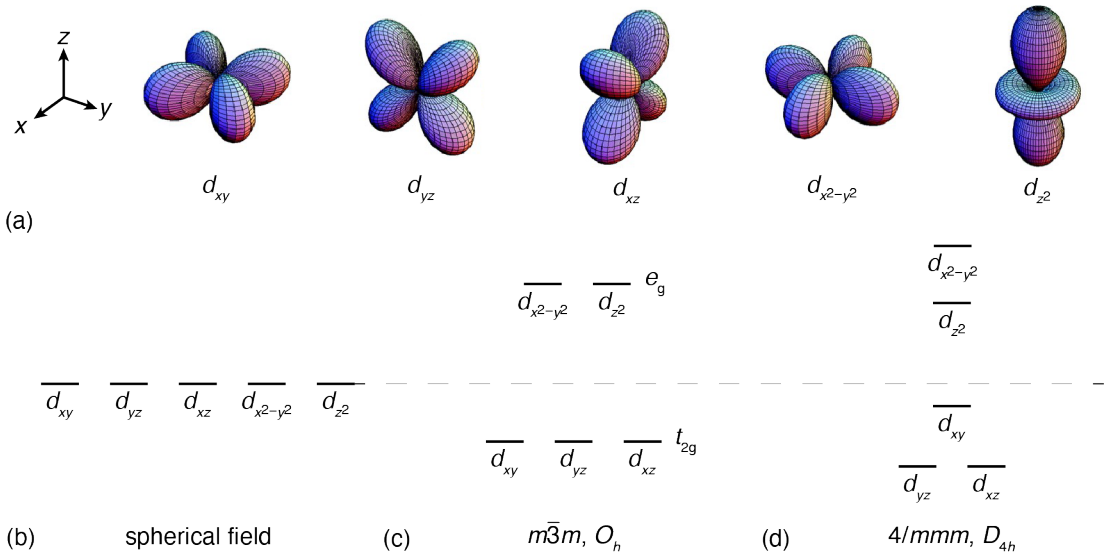


Figure 1.4: (a) The shape of each of the five d-orbitals, which are degenerate in (b) a spherical crystal field, but split into two levels in (c) an octahedral crystal field. In high-spin d^4 (*e.g.* Mn^{3+}) and d^9 (*e.g.* Cu^{2+}) electronic configurations, there is an unequal occupancy of the doubly degenerate e_g orbitals, hence a (d) first-order Jahn–Teller distortion can occur to remove this degeneracy. The splitting arising from a tetragonal Q_3 distortion is depicted in (d). Part (a) adapted from Ref. 59 with permission from AAAS.

within the t_{2g} set is also possible;[60,61] however, the magnitude of its resultant FOJT distortion is often smaller than in the case of e_g degeneracy: the largely non-bonding nature of the t_{2g} orbitals means that variations in orbital occupations have a less significant effect on the M–L σ-bonding character compared to antibonding orbitals such as e_g orbitals.[62]

For FOJT distortions arising from the unequal occupation of degenerate e_g orbitals, the set of possible symmetry-lowering structural distortions can be thought of as spanning a two-dimensional space—the 'E_g distortion plane' [Fig. 1.5]. In the Van Vleck analysis[63] of displacements of octahedrally-coordinated ligands, the FOJT distortion spans the Q_2 and Q_3 distortion modes.[63,64] The Q_2 distortion mode represents an orthorhombic strain, and corresponds to elongation along *e.g.* the x-axis and compression along the y-axis (denoted Q_2^x); note its symmetry-related distortions are also possible (Q_2^y and Q_2^z). The Q_3 distortion mode represents a tetragonal strain, and corresponds to elongation along *e.g.* the z-axis and compression in the

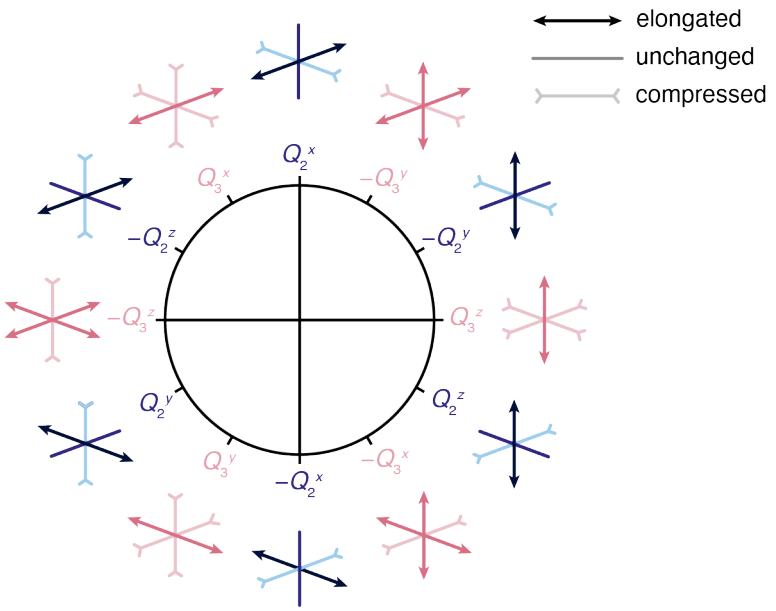


Figure 1.5: The two-dimensional 'E_g' distortion space of a first-order Jahn–Teller distortion arising from degeneracy in the e_g orbitals, spanned by the Q_2 and Q_3 distortions. The orthorhombic Q_2 distortion is depicted using blue arrows showing the possible combinations of one elongated axis, one compressed axis, and one unchanged axis. The tetragonal Q_3 distortion is depicted using pink arrows showing the possible combinations of one elongated axis and compression of the two axes in the perpendicular plane.

perpendicular plane or vice versa (denoted Q_3^z); note its symmetry-related distortions are also possible (Q_3^x and Q_3^y). In the case of Cu^{2+}, the Q_3 distortion (tetragonal elongation) nearly always arises, and is the case for the PBA, $Cu[Pt(CN)_6]$. Whereas in the case of high-spin Mn^{3+}, the structural distortion is usually Q_2-like, and is what is found for the manganite perovskite, $LaMnO_3$.[65,66] The tetragonal elongation tends to be more prevalent as the d_{z^2} orbital in the $4/mmm$ (D_{4h}) point group is symmetry equivalent to that of the $4s$ orbital, allowing an additional stabilisation by mixing of the two orbitals. Yet, the orthorhombic Q_2 distortion is still realised, and may possibly depend on factors such as coupling to tilts and the preference to align in an antiferrodistortive or parallel manner in an extended solid.

When JT-active cations sit on a lattice, cooperative Jahn–Teller (CJT) order can arise, where local JT distortions of individual cations interact to drive a global lowering of the symmetry of the structure.[67] Since the aristotype perovskite structure is topologically cubic, there are multiple symmetry-equivalent crystallographic axes

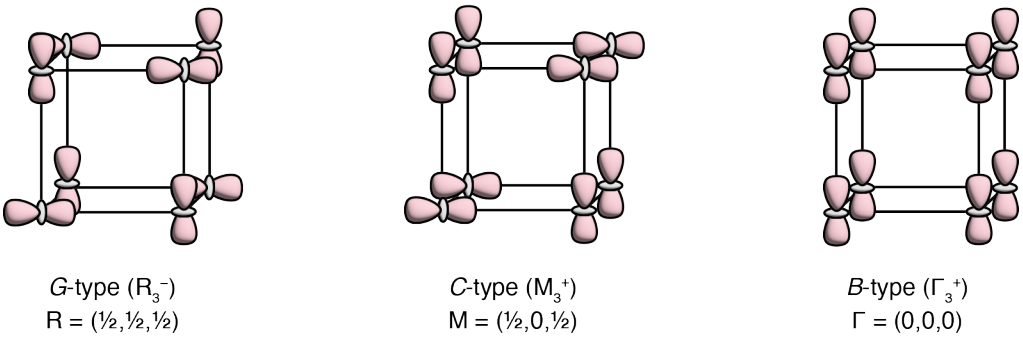


Figure 1.6: A depiction of the G-, C-, and B-type orbital ordering patterns found in perovskites. The corresponding irreducible representations and crystal momentum are given for each of the three orbital ordering patterns.

along which the tetragonal (Q_3^x, Q_3^y, Q_3^z) or orthorhombic (Q_2^x, Q_2^y, Q_2^z) distortion of individual octahedra can occur, hence there is no unique way to arrange all the distorted octahedra within the structure. Generally, the favoured ordering patterns are the ones where neighbouring JT-distortion axes are arranged perpendicular to each other within a plane; when these planes are stacked directly on top of each other, this gives C-type order—as shown by $LaMnO_3$[65]—whereas when the planes are stacked in an offset manner, this gives G-type order—as is observed in $KCuF_3$[54] [Fig. 1.6]. It is also possible to observe a parallel arrangement of neighbouring JT-distortion axes (B-type order), but this occurs much less frequently.[68,69] Hence, CJT (dis)order in perovskites can lead to a variety of different symmetry-distinct states.

CJT/orbital (dis)order is known to play a role in many of the interesting properties of various perovskites. For example, in the manganite perovskites, CMR is believed to arise from the competition between orbital, charge, tilt, and magnetic order,[17–20] whilst in $KCuF_3$, the one-dimensional nature of its magnetism is understood to arise from the arrangement of its orbitals.[16,54,70–72] Hence, understanding the nature of CJT order is not only of fundamental interest, but is also relevant to designing the next generation of functional perovskites.

Octahedral tilts

In perovskites containing an A-site cation that is too small to fill the BX_3 framework cavity sufficiently ($\alpha < 1$), its bonding requirements will not be satisfied, hence rotations (tilting) of the octahedral BX_3 framework occur to remedy this.[73] Since the octahedra are linked at their corners, the rotation of one octahedron necessarily causes rotation of its neighbouring octahedra, and is referred to as cooperative octahedral tilting. Cooperative octahedral tilting in framework materials can be described by the Rigid Unit Mode (RUM) model (more in Section 2.5.2), where phonon modes propagate throughout the structure without distorting the coordination polyhedra.[74] Upon cooling, 'soft' modes, which decrease in frequency with decreasing temperature, can condense at a critical temperature, inducing a phase transition from the untilted aristotype cubic perovskite structure to a lower-symmetry structure. For example, at higher temperatures, $SrTiO_3$ adopts the aristotype cubic perovskite structure with dynamic octahedral rotations, but on cooling below 105 K, $SrTiO_3$ undergoes a phase transition to a tetragonal structure with 'frozen-in' cooperative octahedral rotations.[75]

The simple crystallographic rules and notation developed by Glazer[76] can be used to understand and rationalise octahedral tilting patterns.[8,73,76] The notation takes the form $a^{\#}b^{\#}c^{\#}$, where a, b, and c refer to the equivalence of the tilts about each of the pseudocubic perovskite unit cell axes (the cell around one octahedron), and the superscript denotes the kind of tilting, with '0', '+', or '−' indicating no tilting, in-phase tilting, or out-of-phase tilting, respectively [Fig. 1.7(a)–(c)]. To give an example, the $a^+b^-b^-$ tilt pattern—which is very common in perovskites,[77] *e.g.* $GdFeO_3$[78]—represents an in-phase tilt about the a-axis, and out-of-phase tilts of equal magnitude about both the b- and c-axes [Fig. 1.7(d)]. Since tilts have the ability to affect a material's properties,[79] characterising and exploiting tilt distortions ('tilt engineering') has become an important aspect of targeted materials design.[77]

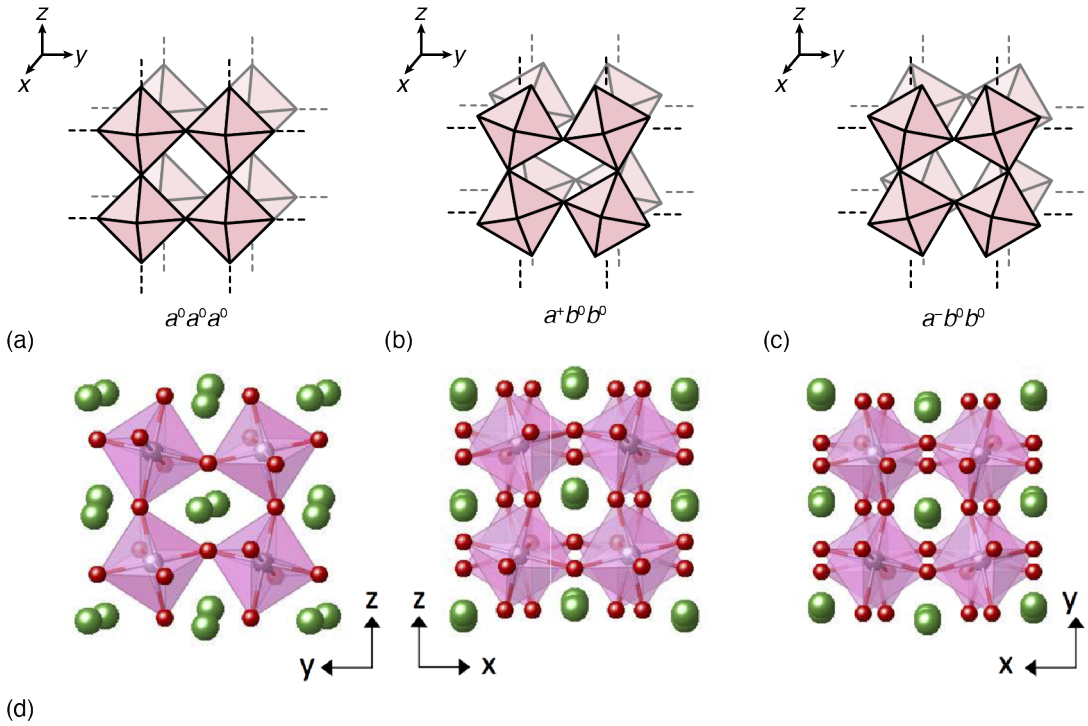


Figure 1.7: Simple tilt patterns in perovskites and their Glazer notation. (a) No tilts, (b) an in-phase tilt, and (c) an out-of-phase tilt. (d) The common tilt pattern $a^+b^-b^-$, as found in *e.g.* $LaInO_3$[80] and $GdFeO_3$[78]. Panel (d) reproduced from Ref. 80, which is an open access article distributed under the terms of the Creative Commons CC BY license.

Coupling

Many perovskites do not contain just one type of distortion; indeed, multiple degrees of freedom can coexist and couple together to give rise to many interesting and functionally useful properties.[59,64,81,82] Coupling is used to describe the mechanism by which the activation of one degree of freedom can induce, inhibit or affect another, or alternatively to describe how independent distortions collectively act to give rise to a particular symmetry or property. The interplay between different degrees of freedom (*e.g.* charge, orbital, tilt, and spin) often gives rise to useful properties—as is the case in the CMR manganites[17–20]—but this coupling can also make it difficult to understand how each degree of freedom contributes to driving a particular phenomenon.[45,68,83,84] This motivates the work of Chapter 5, which seeks to explore whether simple geometric modelling of corner-sharing octahedra can be used to

rationalise the coupling between JT, tilt, and shear strain modes in the manganite perovskite $LaGa_{1-x}MnO_3$, as well as the coupling between charge, JT, tilt, and shift degrees of freedom in $La_{1-x}Ca_xMnO_3$.

A large focus of this thesis (Chapters 3, 4, and 6) is the interplay of competing distortions in one family of molecular perovskites, Prussian blue analogues. Hence, the following section gives an overview of some of the different types of distortions found in Prussian blue analogues [Fig. 1.8].

1.2.2 Prussian blue analogues

Prussian blue analogues (PBAs) are a compositionally-diverse family of molecular perovskites that have found applications in a wide variety of different areas, including cathode materials,[85] magnetism,[86] catalysis,[87] and more.[88,89] Molecular perovskites, such as the organic-halide perovskites (*e.g.* $(CH_3NH_2)PbI_3$)[90] and the metal formates (*e.g.* $NH_2(CH_3)_2[Cu(OOCH)_3]$),[91] adopt the ABX_3 perovskite structure but contain a molecular component. The basic PBA structure can be described as a molecular perovskite or 'hybrid' double perovskite, $A_2MM'X_6$, where transition-metal cations on the M and M′ sites are joined by CN^- linkers on the X-site to give a rocksalt-type cation ordering. The polyatomic linker gives greater flexibility to the framework than a monatomic linker and increases the size of the sub-cubes, allowing interstitial water and a wide range of cations to occupy the A-site within the cavities [Fig. 1.8, centre].[1] The universal composition of PBAs is given by $A_xM^m[M'^n(CN)_6]_y \cdot zH_2O$, with the charge-balance constraint $x+m = y(6-n)$.[1] The intercalation of A-site cations charge balances the variable oxidation states of the M- and M′-site transition metals as well as any hexacyanometallate $[M'^n(CN)_6]^{(6-n)-}$ vacancies in the structure.

Whilst the parent face-centred cubic (FCC) structure is widespread amongst PBAs,[92] PBAs can harbour a wide variety of different types of distortions that can break the cubic symmetry, both globally and locally [Fig. 1.8].[93] Arguably, it is this

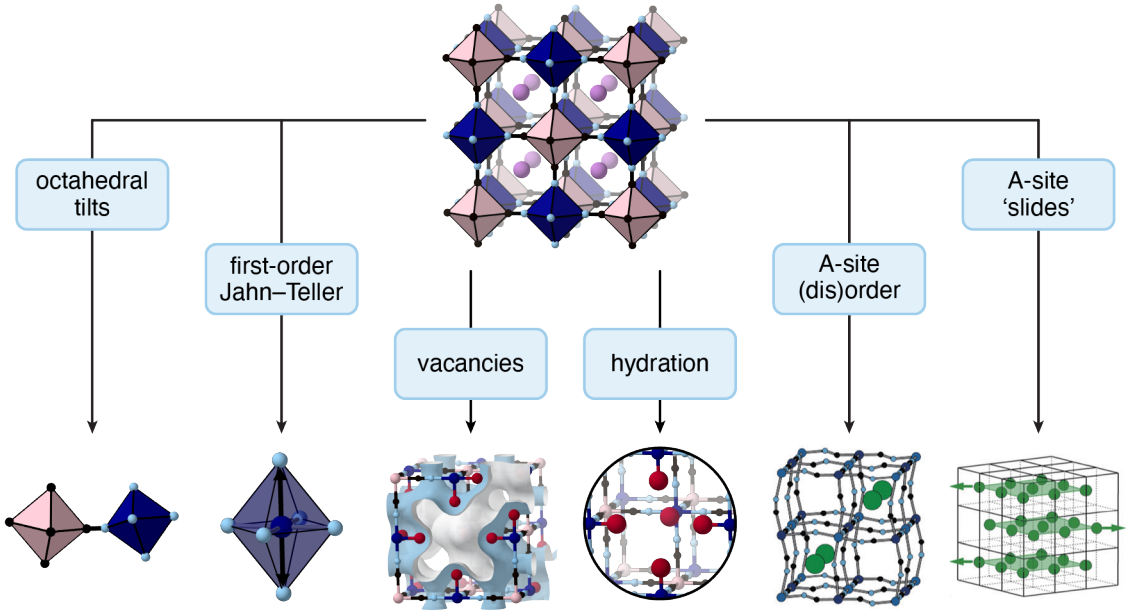


Figure 1.8: An overview of the common degrees of freedom of Prussian blue analogues. The parent PBA structure is shown at the top, with depictions of some commonly found degrees of freedom shown underneath: octahedral tilt, first-order Jahn–Teller distortion, hexacyanometallate vacancies, coordinated (framework) ligand water, A-site occupancy (dis)order, and correlated A-site 'slides'. Figure adapted in part from Ref. 1, which is licensed under a Creative Commons Attribution 3.0 Unported Licence.

compositional and structural diversity[1] that gives the PBA family its wide range of applications [Fig. 1.8].[85–87] Before structure–function relationships are discussed in Section 1.4, the most pertinent PBA distortions to this thesis are highlighted next: namely, hexacyanometallate vacancies, octahedral tilts, and Jahn–Teller activity.

Hexacyanometallate vacancies

The incorporation of hexacyanometallate ($[M'^{n}(CN)_6]^{(6-n)-}$) vacancies into the PBA structure [Fig. 1.9] is at the heart of many of the interesting properties of this family;[94–97] however, despite their widespread relevance amongst functional PBAs, the nature of vacancy distributions has historically not been well understood. A fully-ordered vacancy distribution is possible in PBAs with a vacancy fraction of 25%—as is the case in Prussian blue itself ($Fe^{III}[Fe^{II}(CN)_6]_{0.75}$)—where it has been shown by single-crystal X-ray diffraction that vacancies adopt this vacancy-ordered arrangement by avoiding one another with a complete isolation of vacancies.[98] Such

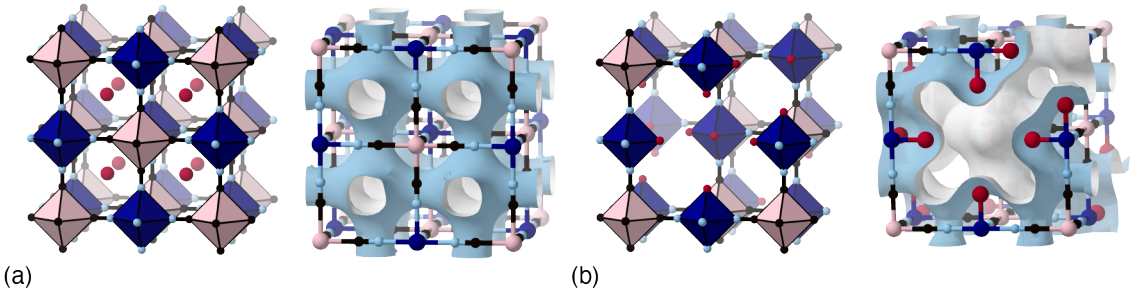


Figure 1.9: The effect of hexacyanometallate vacancy incorporation on the pore-networks of PBAs. (a) A schematic representation of a vacancy-free $AM[M'(CN)_6]$ PBA structure. M-sites are shown as dark blue octahedra; M′-sites are shown as pink octahedra; A-sites (in this case, interstitial water) are shown in red; C and N atoms are shown as black and light blue spheres, respectively. Cavities at the centre of each sub-cube connect to form a pore-network structure with a simple cubic topology. (b) A schematic representation of the $M[M'(CN)_6]_{2/3} \cdot xH_2O$ structure containing 33% vacancies on the M' site. Where an M-site cation is adjacent to a vacancy, it is capped with a coordinated ligand water molecule, which is shown as a red O-atom. The incorporation of hexcyanometallate vacancies creates channels along the diagonals of the cube face. Void volumes are shown as isosurfaces with a white interior and a light-blue exterior. This figure was inspired by Ref. 1, which is licensed under a Creative Commons Attribution 3.0 Unported Licence.

a complete isolation of vacancies is not possible on an FCC lattice with a vacancy fraction greater than 25% as geometry necessarily dictates that in such cases, at least some vacancies must form connected neighbour pairs [Fig. 1.9(b)]. So, in cases with higher vacancy fractions than 25%, such as PBAs with the composition $M^{II}[M'^{III}(CN)_6]_{2/3} \cdot xH_2O$, there must be some vacancy disorder.[99,100] Whilst a random vacancy distribution has often been assumed,[100,101] there is evidence for correlated vacancy distributions, especially in single crystals of PBAs.[102–104]

The form of the correlated vacancy distribution in a given PBA is understood to depend on both the crystal-field preference of the M-site metal as well as the conditions in which the PBA is synthesised.[102] This interplay between vacancies and crystal-field effects arises from the fact that an M–NC (framework) bond is replaced by an $M–OH_2$ (ligand water) bond when an M-site metal is adjacent to an M′ hexacyanometallate vacancy [Fig. 1.9(b)]. Based on Pauling's 'electroneutrality' principle,[105] one might expect a vacancy distribution that has a uniform distribution of M-site coordination numbers. Hence, for an M′-site vacancy fraction of 33%, an

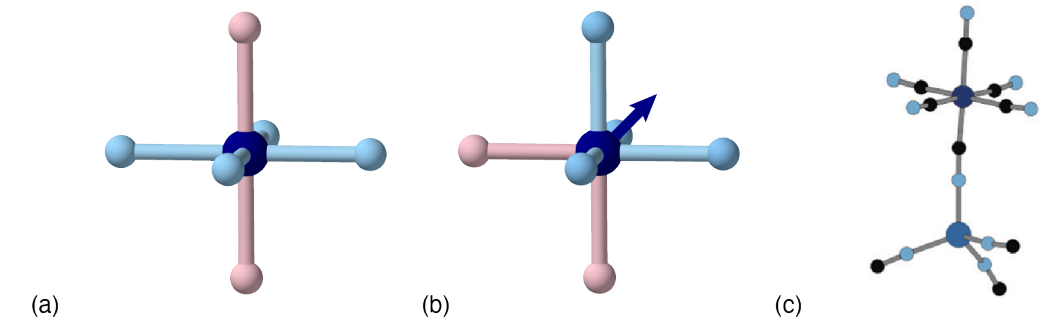


Figure 1.10: Possible hydration geometries of M sites in PBAs. (a) The *trans*-$[MN_4O_2]$ arrangement, favoured by PBAs containing *e.g.* Cu^{2+} ions. (b) The *cis*-$[MN_4O_2]$ arrangement, observed in some PBAs containing *e.g.* Zn and Mn. (c) A portion of the framework of the rhombohedral (non-PBA) polymorph of $Zn[Co(CN)_6]_{2/3}$, where Zn^{2+} ions (lighter blue) are surrounded by four hexacyanocobaltate anions in a tetrahedral geometry.[108] The coordination geometry of the Zn^{2+} ion is similar to what is observed when the *cis*-N_4O_2 coordination environment shown in (b) is dehydrated. This figure is adapted from Ref. 1, which is licensed under a Creative Commons Attribution 3.0 Unported Licence.

arrangement where each M-site metal is surrounded by four occupied M′-sites and two vacancies might be expected. If there are two vacancies surrounding an M-site metal, it is possible to arrange the two ligand waters in either a *trans* [Fig. 1.10(a)] or *cis* [Fig. 1.10(b)] octahedral $[MN_4O_2]$ coordination environment. With an M′-site vacancy fraction of 33%, it is not possible to simultaneously have a uniform vacancy distribution and all M-sites centrosymmetric (*trans* arrangement of ligand waters). Hence, the balance between having centrosymmetric M-site metals and a uniform vacancy distribution will depend on the crystal-field stabilisation energy of the M-site metal; PBAs with crystal-field active cations will tend to have a greater preference for centrosymmetric M-sites[106]—to increase its crystal-field stabilisation energy—than crystal-field inactive cations such as Zn and Cd, which tend to adopt acentric coordination geometries to minimise steric and electronic repulsions between ligands.[107,108] Hence, depending on the nature of the M-site metal and the synthesis conditions used (*e.g.* temperature, crystal growth rate, precursor concentration), a diverse range of vacancy-network polymorphs can be achieved.[102]

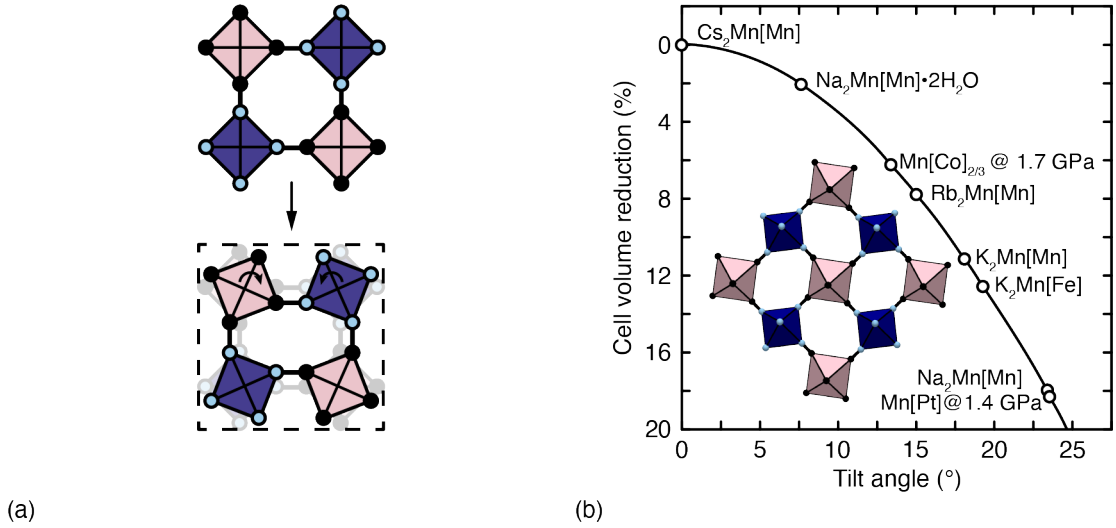


Figure 1.11: (a) An illustration to show how cooperative octahedral tilts in PBAs can reduce the volume of the structure. (b) The relationship between percentage cell volume reduction and tilt angle—the average distortion of M′···M–N and M···M′–C angles—in various PBAs.[93,114–116] An illustration of one representative cooperative PBA tilt distortion is shown as an inset. Part (b) is adapted in part from Ref. 1, which is licensed under a Creative Commons Attribution 3.0 Unported Licence.

Octahedral tilts

Octahedral tilts are perhaps one of the most prevalent distortions in PBAs and perovskites more generally.[8,76,109–112] When one octahedron rotates, it induces rotation of its neighbours [Fig. 1.11(a)]; when these cooperative octahedral tilts become long range at a critical external pressure, they lower the global symmetry of the system [Fig. 1.11(b), inset]. Octahedral tilts reduce the volume of the structure [Fig. 1.11(a)], hence systems with vacancies—and so a greater free pore space—show greater compressibility.[113] For example, $Mn[Co(CN)_6]_{2/3}$, with a vacancy concentration of 33%, shows a greater reduction in cell volume than vacancy-free $Mn[Pt(CN)_6]$ [Fig. 1.11(b)]. Additionally, since cooperative octahedral tilting leads to a decrease in the size of the A-site cavity, the distance between the anionic cyanide linkers and the A-site cation is reduced; hence one might expect smaller, more polarising cations to lead to greater octahedral tilting, which is exactly what is observed in the $A_2Mn[Mn(CN)_6]$ (A = Na, K, Rb, Cs) series [Fig. 1.11(b)].[93,114]

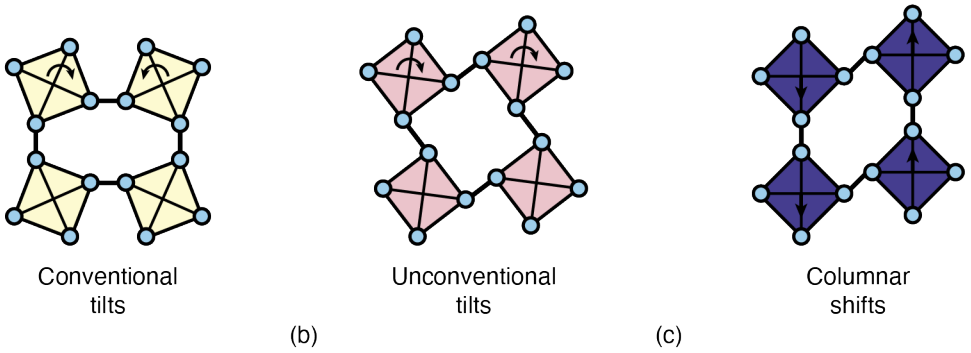


Figure 1.12: An overview of the types of tilts that can be found in molecular perovskites. (a) Conventional octahedral tilts, where neighbouring octahedra rotate in opposite directions. (b) Unconventional tilts, where neighbouring octahedra rotate in the same direction. (c) Translations of columns of octahedra. Figure modified from Ref. 119, which is licensed under a Creative Commons Attribution 4.0 International License.

In theory, PBAs should have access to a larger variety of different tilt distortions than conventional perovskites.[109,110] This variety arises from the fact that in systems with a molecular X-site linker—such as PBAs—neighbouring octahedra are not restricted to tilting in opposite directions.[94] Hence, whilst molecular perovskites do show many of the conventional tilt modes common to conventional perovskites,[117,118] so-called 'unconventional tilts' are also allowed [Fig. 1.12(b)].[109,110] Additionally, so-called 'columnar shifts' are theoretically possible, which involve collective translations of columns of octahedra [Fig. 1.12(c)].[113] Columnar shifts can drive symmetry-lowering processes that octahedral tilt mechanisms cannot, and hence may provide an alternative route to accessing *e.g.* polar space groups—vital for multiferroicity—or phonon modes that drive negative thermal expansion (NTE).[113]

Generally, it is thought that the key phonons responsible for NTE in PBAs involve correlated rotations of MN_6 and $M'C_6$ octahedra,[99,120–124] but this and the magnitude of potential 'columnar shifts' remains to be tested.[109,113] With this in mind, Chapter 3 explores using a combination of X-ray pair distribution function measurements, lattice dynamical calculations, and *ab initio* density functional theory calculations to study the local structure and dynamics in various $MPt(CN)_6$ PBAs to confirm that the key NTE phonons are indeed correlated octahedral tilts

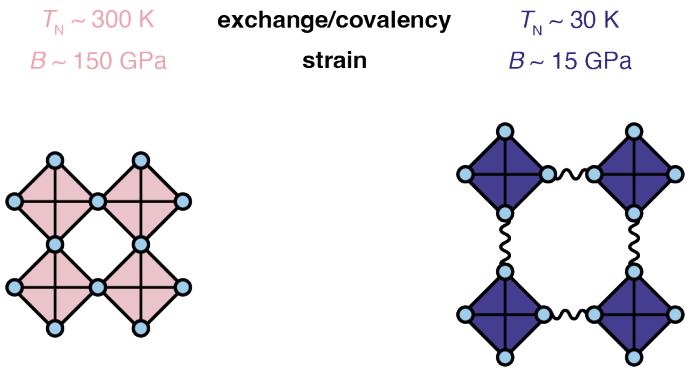


Figure 1.13: Comparison of exchange interactions and elastic constants in conventional (left) and molecular (right) perovskites.

and also to explore the contribution of 'columnar shifts' modes to their NTE.

First-order Jahn–Teller distortions

Cooperative Jahn–Teller (CJT) effects are known to impact the physical behaviour of different classes of solid materials.[64,67,125] Whilst hybrid framework materials can also show CJT order,[1,119,126] their orbital (dis)order phenomena are likely to differ from those of conventional perovskites. For example, due to the flexible, open structures of framework materials, their elastic constants are much lower than those of conventional ceramics,[127] hence, strain effects are generally less important [Fig. 1.13]. Similarly, due to the greater distance between the transition-metal centres, orbital overlap is reduced, hence exchange interactions are also substantially weaker [Fig. 1.13].[128] So, a higher propensity for orbitally-disordered states might be expected in molecular perovskites.

A number of JT-active molecular perovskites are known to exist, including PBAs[121,129] (*e.g.* $Cu[Pt(CN)_6]$) and formates[91,130–132] (*e.g.* $[C(NH_2)_3]Cu(HCOO)_3$). In PBAs, JT-active cations—*e.g.* Cu^{2+} or Mn^{3+}—typically occupy the M-sites of the PBA structure.[121,133] PBAs with a high concentration of JT-active cations may not necessarily show long-range CJT order; whilst stoichiometric $Cu[Pt(CN)_6]$ is tetragonal [Fig. 1.14(b), left],[121] defective $Cu[Co(CN)_6]_{2/3}$ is cubic [Fig. 1.14(b), right].[134] $Cu[Co(CN)_6]_{2/3}$ has been shown to have a strong preference for a *trans* arrangement

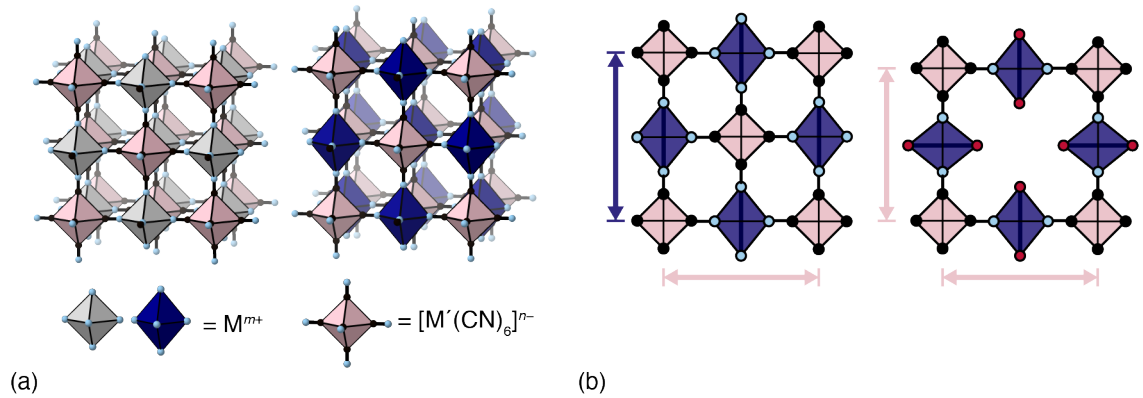


Figure 1.14: The interplay of cooperative Jahn–Teller (JT) order and hexacyanometallate vacancy incorporation in PBAs. (a) The aristotype PBA structure (left), with alternating M^{m+} (grey/blue) and $[M'(CN)_6]^{n-}$ (pink) octahedral ions on a simple cubic lattice. $Cu[Pt(CN)_6]$, with long-range cooperative JT order, has tetragonal symmetry (right). (b) Incorporating hexacyanometallate vacancies, which are often capped by ligands such as water (red circles), can allow the JT-distortion axis of individual JT-active ions to vary such that the structure remains cubic on average, as observed in *e.g.* $Cu[Co(CN)_6]_{2/3}$.

of vacancies around each Cu^{2+} site,[102] with the local JT-distortion axis pointing towards the vacancies[135] [Fig. 1.14(b), right] rather than the cyanide framework. Since the orientation of the local JT-distortion axis can vary throughout the structure [Fig. 1.14(b), right], the structure may remain cubic on average, hence showing how vacancies can prevent long-range CJT order. Finally, it is worth highlighting that due to the preference of the JT axes of Cu^{2+} ions to point towards vacancies,[135] the arrangement of JT-distortion axes within the globally-undistorted cubic structure is unlikely to be random; this final point is explored in Chapter 4, which develops a model based on crystal-field preferences and strain effects to understand the interplay between vacancies and CJT effects in PBAs.

Concluding remarks

It is clear that PBAs can possess a rich compositional and structural diversity[1]—and it is likely this that gives PBAs their functional versatility—hence when seeking to optimise the performance of functional PBA materials, gaining a better understanding of the individual distortions as well as their interplay will likely be cru-

cial.[116,136,137] In this vein, Chapter 4 uses both high-resolution synchrotron X-ray diffraction measurements and Monte Carlo modelling to explore the interplay between vacancies and CJT effects in PBAs.

1.3 Characterising disordered systems

Having explored the degrees of freedom in perovskites and PBAs—including, but not limited to, compositional, charge, vacancy, and orbital order—and how these degrees of freedom can lead to the local structure of a material deviating from its long-range average structure, it now seems pertinent to explore the methods and challenges associated with characterising disordered systems.

1.3.1 Monte Carlo modelling

Monte Carlo (MC) modelling is a versatile tool that can be used to understand the nature of local order within disordered materials (or vice versa). MC modelling is an interaction-driven method, thus it can be used to study the underlying physics or chemical interactions governing a structure. It has proven to be an extremely successful technique for studying ordering phenomena in a range of different types of material including molecular systems,[138] functional oxides, and even proteins.[139] The two-dimensional (2D) Ising model is perhaps the most well-known example of a MC model, and was originally developed to explore the ferromagnetic ordering transition in iron.[140] MC modelling works by simplifying complex phenomena—*e.g.* in the case of the Ising model, the quantum-mechanical interaction between magnetic moments—into a problem that is mathematically straightforward but yet still captures the underlying physics or chemical interactions. The predictions from the MC simulations can then be validated by comparison with experimental data, hence rationalising behaviour that might be difficult to study using conventional structure-determining techniques.

A particular attraction of MC modelling is its versatility, with the ability to

translate MC models to a wide range of systems beyond those for which they were originally developed. For example, the Ising model can be used to explore a wide range of ordering phenomena beyond the field of magnetism.[141,142] Since the Ising model is based on the pairwise interaction between binary variables—sites may be spin 'up' or spin 'down'—it can be applied to understand any phenomena where the degree of freedom can be described by a binary variable. For example, in the case of vacancy ordering, sites can be occupied or vacant. Similarly, in the case of charge ordering, cation sites can be described by two different formal charges. Hence, the Ising model has been translated to understand ordering in many different systems, including short-range ordering in alloys,[141] and charge ordering in spinels.[142]

MC modelling is not restricted to problems of binary (dis)order—higher-order statistical mechanical models can be used to study ordering phenomena in systems where sites can adopt one of n possible states. For example, the n-state Potts model—with the Ising model equivalent to a 2-state Potts model—can be applied to systems with more than two discrete degrees of freedom, and has been used to rationalise multipolar transitions arising from both orbital and molecular quadrupolar ordering.[143–147] For continuous degrees of freedom (*i.e.* $n \to \infty$), a Heisenberg model can be used, *e.g.* to describe a molecular entity free to rotate in a plastic crystal.[148] Whilst such statistical mechanical models might have originally been developed to describe magnetic phase transitions, they can be applied to a wide range of phenomena; the choice of model will depend on the particular degree of freedom and the lattice on which these degrees of freedom sit.[144,149]

The Ising model can be extended to explore more complex problems, *e.g.* the Ising triangular antiferromagnet, which is the classic example of a geometrically frustrated system. In this model, Ising spins sit on a triangular lattice [Fig. 1.15(a)], and when two neighbouring spins are coupled antiferromagnetically (*i.e.* one is spin 'up' and the other is spin 'down'), there is no arrangement where the third neighbour can couple antiferromagnetically to both. Hence, each triangle can adopt either a

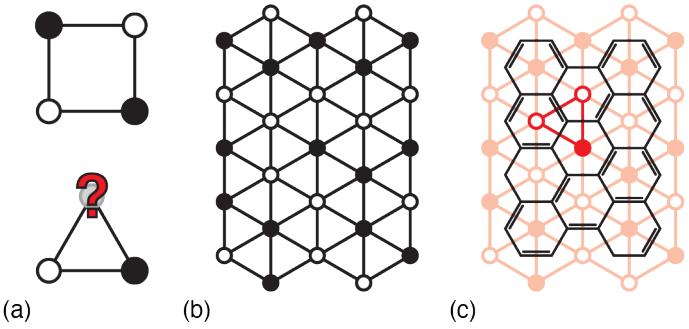


Figure 1.15: The problem of geometric frustration as demonstrated by the Ising triangular antiferromagnet. (a) An antiferromagnetic arrangement of Ising spins can be satisfied on a square lattice (top), but cannot be fully satisfied on a triangular lattice (bottom). (b) One of the many possible arrangements where each triangle has a one-up-two-down or a one-down-two-up arrangement of Ising spins. (c) The problem of geometric frustration can be translated to explain the possible arrangements of π bonds in the resonant valence bond model of graphene.[150] Reproduced from Ref. 151 with permission from Springer Nature.

one-up-two-down or a one-down-two-up arrangement. However, many macroscopic configurations can satisfy this local arrangement [Fig. 1.15(b)], hence the system is described as 'frustrated', lacking a unique ground state.

The problem of geometric frustration is not exclusive to the Ising triangular antiferromagnet, emerging in many different systems with varying types of degrees of freedom and interactions.[150,152–154] For example, in the resonating valence bond model for graphene, the π bonds are associated with the 'ferromagnetic' pairs on each triangle and the σ-only bonds are associated with the 'antiferromagnetic' pairs [Fig. 1.15(c)]. Similarly, in $Ba_3CuSb_2O_9$, the Jahn–Teller-distorted Cu^{2+} ions are geometrically frustrated, hence the problem of orbital order in this system can be mapped onto the same Ising configurations.[154] Whilst much of the interest in geometric frustration has historically been in the context of frustrated magnetism[155]—owing to the many types of spin system (*e.g.* Ising, Potts, and Heisenberg), spin interaction (*e.g.* ferromagnetic, antiferromagnetic, and bilinear–biquadratic), and lattice geometries (*e.g.* triangular, kagome, and pyrochlore), which can hence be expected to give rise to a large number of complex magnetic states—the importance of geometric frustration in governing the behaviour of a range of other types of

ordering phenomena is becoming increasingly clear; for example, orbital order in the CMR manganites,[156] and orientational correlations in plastic crystals.[157] A key takeaway from the mapping of the triangular antiferromagnet onto other systems with similar geometric frustration is that models initially developed to understand (dis)order in one system can often be applied to understand phenomena in other systems.

For example, a range of different MC models have been tested to understand orbital ordering phenomena in perovskites.[144,145,158,159] $LaMnO_3$ undergoes an orbital order/disorder transition at $T_o = 750\,K$,[65,160,161] but understanding the orbitally-disordered phase has proven difficult.[65,162,163] To understand the nature of orbital disorder in the high-temperature phase, Ahmed *et al.* tested an anisotropic three-state Potts model where each site can assume an elongation along either x, y, or z (Q_3 distortion);[144,145,158,164] a recent study found some evidence in favour of this model, but others could not be eliminated.[162] In contrast with the 3-state Potts model proposed for the orbital-disordered phase of $LaMnO_3$,[144,145,158] Tanaka *et al.* employed a compass model[165,166] for $KZn_{1-x}Cu_xF_3$ where the JT distortion of individual sites was treated as a freely variable pseudovector within the distortion space defined by the Q_2 and Q_3 distortions [Fig. 1.5].[159] Since this model was able to reproduce the experimental behaviour of $KZn_{1-x}Cu_xF_3$ well, it has since been extended to model magnetically-active materials.[167]

Validating a model of a disordered system by comparison to experimental data can be a challenge.[162] The structure observed by conventional scattering techniques is a spatially and temporally averaged structure and hence may be significantly different from the local structure.[162,168,169] For example, the absence of long-range order in the spin arrangements in an Ising triangular antiferromagnet will be reflected by the absence of Bragg reflections in the scattering pattern;[151] hence, no structure solution will be possible using conventional Bragg diffraction techniques. Thus, understanding and ultimately exploiting structure–property relationships in

functional materials requires methods that can characterise the local structure and not just the average structure.

1.3.2 Local structure probes

Local structure probes, *e.g.* total scattering/pair distribution function (PDF) measurements, extended X-ray absorption fine structure (EXAFS), and infrared (IR) and nuclear magnetic resonance (NMR) spectroscopies, are sensitive to short-range (dis)ordering.[170–172] Since these techniques are generally most sensitive to correlations between nearest-neighbours, they can be less sensitive at greater distances. This can lead to a situation where the local structure determined by a local structure probe might not appear consistent with the average structure determined by conventional crystallographic techniques. Hence, total scattering/PDF techniques can be especially powerful tools as they can measure both the local and average structure simultaneously.

1.3.3 Total scattering

Materials with long-range translational periodicity produce diffraction patterns with discrete Bragg peaks; consequently, the average structure can usually be determined by considering only the Bragg scattering. Materials with disorder give rise to intensity away from Bragg peaks—known as diffuse scattering[173]—and hence contains information about the local structure—the deviations away from the average structure. Total scattering is a diffraction technique that considers both the Bragg and diffuse scattering, and hence contains information regarding both long- and short-range order. Total scattering can therefore be used to study short-range order in long-range disordered materials,[174,175] as well as to study long-range ordered materials with short-range disorder.[176–178] Some disordered materials produce a mixture of Bragg and diffuse scattering; in many such cases, the diffuse scattering is highly structured despite lacking long-range translational periodicity, and is characteristic

of correlated disorder.[151]

The different signatures of random and correlated disorder in diffuse scattering is perhaps best demonstrated by the simple toy model of square ice [Fig. 1.16]—the 2D analogue of water ice. In this model, water molecules sit on a square lattice, and although the positions of the oxygen atoms translate periodically, there are a number of positions that the protons can adopt. Consequently, there are a number of ways to orient a water molecule relative to another, giving rise to the potential for ordered [Fig. 1.16(a)], correlated disordered [Fig. 1.16(b)], and randomly disordered [Fig. 1.16(c)] configurations. In the ordered configuration [Fig. 1.16(a)], all water molecules are identical, whereas in the randomly disordered configuration [Fig. 1.16(c)], they are all distinct; the correlated disordered configuration [Fig. 1.16(b)] is then somewhere in between.

Importantly, these configurations produce different scattering patterns [Fig. 1.16(d)–(f)] and partial PDFs [Fig. 1.16(g)–(i)],[151] highlighting how total scattering techniques can be sensitive to different local structure models. When (local) interactions are weak or absent, as in the case of the configuration with random disorder [Fig. 1.16(c)], the diffuse scattering is broad and unstructured [Fig. 1.16(f)], whereas when (local) interactions are well-defined, as in the case of the configuration with correlated disorder [Fig. 1.16(b)], the diffuse scattering appears structured [Fig. 1.16(e)]. Similarly, differences in the local structure models are reflected in the low-r region of the partial PDFs [Fig. 1.16(g)–(i)]. Hence, total scattering techniques can be particularly powerful as they are able to probe both the local and average structure simultaneously.

1.3.4 Modelling of total scattering data

Having seen how total scattering techniques can in theory be sensitive to different local structure models, it now seems pertinent to discuss the current methods for interpreting and analysing both single-crystal diffuse and powder total scatter-

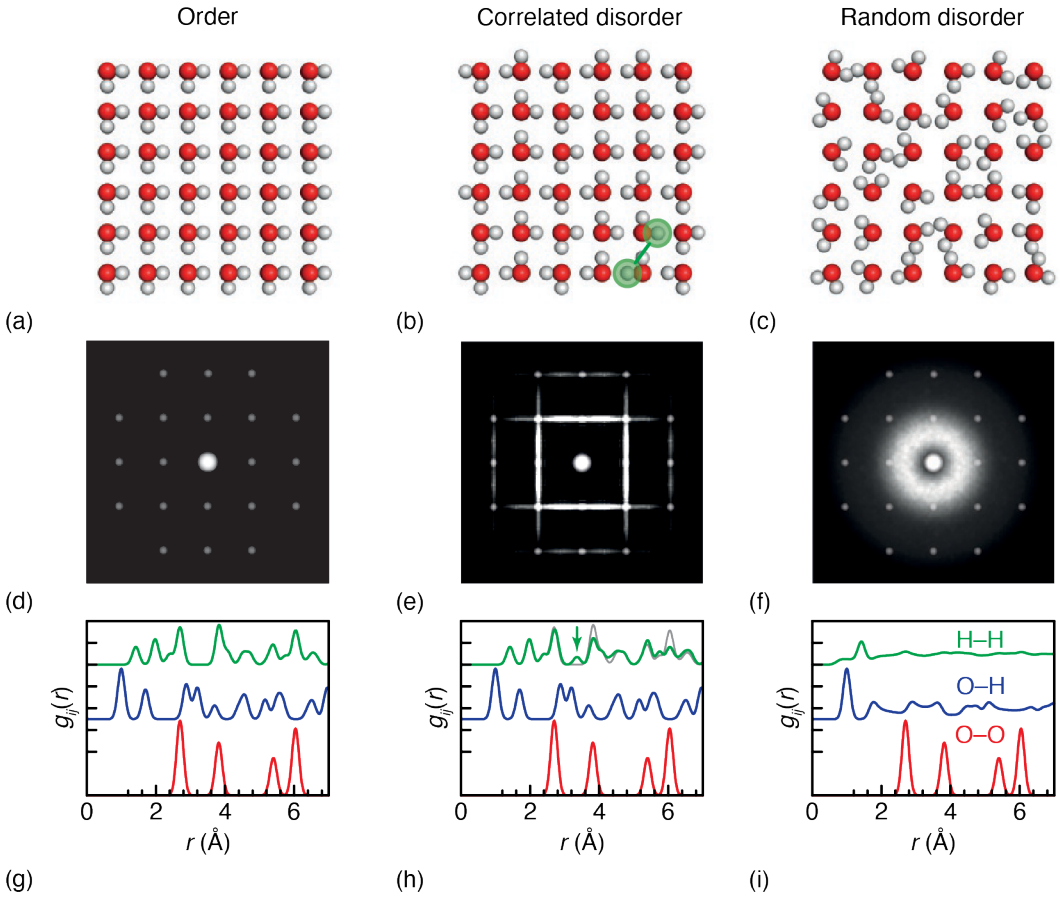


Figure 1.16: The effect of an ordered (a), correlated disordered (b), and randomly disordered (c) arrangement of protons on the observed scattering in square ice. In each configuration (a)–(c), the oxygen position is periodic, which produces well-defined Bragg peaks in the single-crystal diffuse scattering patterns (d)–(f). Whilst a correlated disordered arrangement of protons results in the highly structured diffuse scattering seen in (e), a random arrangement of protons results in the broad and featureless diffuse scattering seen in (f). The equivalent partial PDFs of the configurations (a)–(c) are shown in (g)–(i), respectively; $g_{\mathrm{OO}}(r)$ is shown in red, $g_{\mathrm{HH}}(r)$ is shown in green (the $g_{\mathrm{HH}}(r)$ from (g) is shown in (h) as a thin grey line to aid with comparison), and $g_{\mathrm{OH}}(r)$ is shown in blue. The different local structure pictures of (a)–(c) produce noticeably different partial PDFs (g)–(i). Reproduced from Ref. 151 with permission from Springer Nature.

ing data, and how well in practice these methods can differentiate different local structure models.

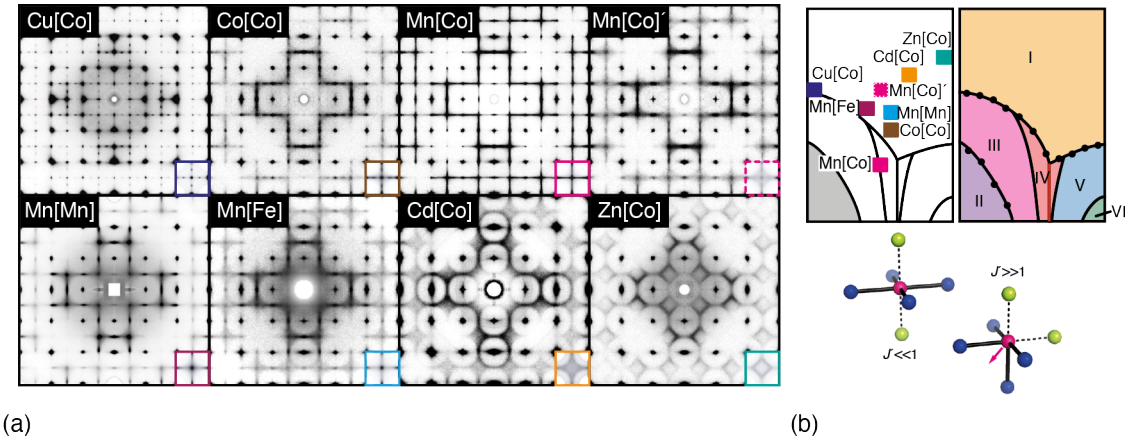
Single-crystal three dimensional pair distribution function analysis

The three dimensional difference pair distribution function (3D-ΔPDF) is an emerging method for refining single-crystal diffuse scattering data.[179] The 3D-ΔPDF ap-

proach involves taking the Fourier transform of just the diffuse scattering, allowing the correlations between deviations from the average structure to be refined. The resulting refined covariances can be used as data points in *e.g.* Reverse Monte Carlo (RMC) modelling,[180] hence this method offers a quantitative approach to local structure analysis. This method does not come without challenges, which can include accurately accounting for background scattering as well as accurately determining Bragg peak width and intensity when removing Bragg peaks.[181] Furthermore, any thermal diffuse scattering underneath the Bragg peaks will be lost.

One example where the 3D-ΔPDF approach has proven invaluable is in the characterisation of vacancy distributions in PBAs. The long-standing obstacle to characterising the vacancy distributions in PBAs has been the difficulty associated with growing their single crystals.[182] Recently, Simonov *et al.*[102] successfully grew single crystals of a range of PBAs and characterised their vacancy correlations through 3D-ΔPDF analysis and MC simulations. The form of the diffuse scattering shown in Fig. 1.17(a) is highly structured, suggesting the presence of correlated disorder. The structure of the diffuse scattering could be described by a convolution of the contribution from an individual hexacyanometallate anion with an occupational correlation function; hence, this highly-structured diffuse scattering was attributed to correlations in hexacyanometallate occupancy.[102] Thus, the 3D-ΔPDF approach was instrumental in showing that the vacancy distribution in single-crystals of a range of PBAs is correlated and not random.

Additionally, a diversity of diffuse scattering patterns was observed for the PBAs studied, even amongst crystals with the same nominal composition but grown in different synthesis conditions.[102] A simple MC model based on local rules of electroneutrality[105] and centrosymmetry [Fig. 1.17(b)] was able to replicate the complex phase behaviour observed experimentally. With the two interaction terms of electroneutrality and centrosymmetry acting in competition, it turns out that they are resolvable when the vacancy fraction is 0.25—giving the ordered vacancy arrangement in



(a) (b)

Figure 1.17: Vacancy-network variations in PBAs. (a) Reconstructed single-crystal $(hk0)$ diffuse scattering planes ($-6 < |h|, |k| < 6$) from a range of PBAs,[102] where intensities from Bragg peaks with even h, k have been removed from the corners of the squares. (b) (Top) Distribution of PBAs (left) and vacancy polymorphs (I–VI) (right) as determined by Monte Carlo simulations.[102] (b) (Bottom) A *trans* and *cis* arrangement of vacancies around an M-site. Reproduced from Ref. 102 with permission from Springer Nature.

Prussian blue itself[98]—but are frustrated at vacancy fractions higher than 0.25 up to 1/3 (the maximum possible vacancy fraction experimentally). This problem of geometric frustration of 1:2 decoration on the FCC lattice is also likely to be relevant to the geometrically frustrated relaxor ferroelectrics (*e.g.* $Pb(Mg_{1/3}Nb_{2/3})O_3$) and relaxor ferromagnets (*e.g.* $La(Sb_{1/3}Ni_{2/3})O_3$).[183,184] Taken together, the 3D-ΔPDF analysis and MC modelling in Ref. 102 allowed the identification and rationalisation of previously unknown phase domains of correlated vacancy distributions that were previously hidden from conventional powder diffraction analysis; this example serves to highlight the power of combined single-crystal, 3D-ΔPDF, and MC techniques.

Powder total scattering: small-box modelling

Materials that cannot be grown as single-crystals can instead be investigated using powder total scattering techniques; the normalised total scattering data are Fourier transformed to give the PDF, which represents a histogram of interatomic distances weighted by the corresponding atomic concentrations and scattering strengths.[175,185–187] This method is widely used to study short-range order in

materials lacking long-range order, as well to study correlated disorder in crystalline materials.[151,188]

One method for modelling powder total scattering data is the 'real-space Rietveld' technique, as implemented in the program PDFgui,[189] which refines a periodic unit cell (the 'small box' of small-box modelling) to the PDF. Different structural models can be fit to different regions of the PDF, making it is possible to obtain information about the lengthscales of any local correlations as well as to determine how the local structure evolves into the long-range average structure.

Small-box, 'real-space Rietveld' modelling, has been used in the effort to understand how the structure of the CMR manganite perovskites $La_{1-x}Ca_xMnO_3$ (LCMO) changes as a function of composition and temperature, in particular how the local JT distortion evolves across the series.[161,190–194] When the Mn JT-distortion axes are only correlated over short lengthscales, the symmetry of the short-range (local) structure will be lower than that of the long-range (average) structure; hence, to be able to characterise the presence, nature or variation in JT order in the LCMO series, a local structure probe such as PDF is needed. An example of where small-box PDF modelling has helped to link the evolution of the local JT distortion to the phase diagram of LCMO is given by the work of Ref. 192; it was shown that whilst the average structure—as determined by conventional Rietveld analysis [Fig. 1.18(a)] and PDF refinement over a 20 Å range [Fig. 1.18(b)]—is largely unaffected by the orbital and electronic transitions observed across the LCMO series, the electronic phase diagram is replicated by local correlations seen from small-box PDF refinements [Fig. 1.18(c)].[192]

Powder total scattering: big-box modelling

Powder PDF data can also be fit using 'big-box' modelling techniques such as Reverse Monte Carlo (RMC).[195,196] In this method, a large box of atoms is generated as a starting configuration—usually a supercell of the underlying unit cell—and

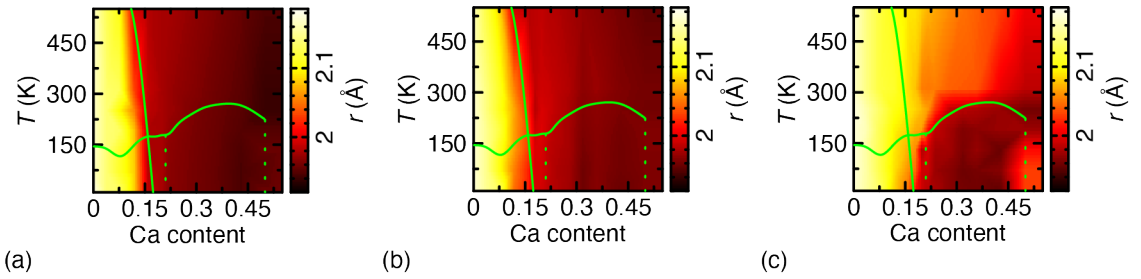


Figure 1.18: Small-box 'real-space Rietveld' analysis of $La_{1-x}Ca_xMnO_3$. (a)–(c) Contour plots of the longest Mn–O bond length (representing the magnitude of the JT distortion) as a function of the temperature and composition. The contour plot shown in (a) is data from Rietveld analysis. The contour plots shown in (b) and (c) are data obtained from PDF analyses over (b) 20 Å and (c) 6 Å ranges. The solid green curves in (a)–(c) indicate the T_{JT} and T_c phase boundaries, whilst the dotted green vertical lines indicate the insulator-metal phase boundaries. Reprinted with permission from Ref. 192. Copyright 2007 by the American Physical Society.

the refinement procedure proceeds by moving atoms by small amounts, accepting or rejecting moves according to the Metropolis algorithm.[197] In this way, the refinement is driven by minimising the difference between the PDF of the calculated big-box model and the experimental data. In contrast to direct MC modelling, RMC does not require prior knowledge of the local interactions in a system.[195,196] Further advantages of RMC modelling include its generality—other than periodic boundary conditions, it is not constrained by symmetry—and the ability to simultaneously fit the model to different types of data (*e.g.* X-ray PDF, neutron PDF, EXAFS). The refined big-box model captures information about both the average and local structure, and represents a snapshot of the structure; hence, all disordering processes—static or dynamic—can be captured within the big-box model, further emphasising the generality of this technique. However, big-box modelling does not come without challenges. For example, complex systems can require a large number of parameters/constraints to produce a model that is physically and chemically sensible that also fits the PDF (and any other data). Additionally, two very different models can fit the data similarly well. Hence, caution must be taken when assessing refined models.

Big-box PDF modelling has been used to investigate the nature of orbital order in the high-temperature disordered state of $LaMnO_3$, with mixed success.[162,198] In one study,[198] the configurations perhaps showed some evidence for short-range C-type orbital ordering [Fig. 1.19(a)], though an alternative interpretation could be a correlated disordered state of the anisotropic three-state Potts (3SP) model [Fig. 1.19(b)] developed by Ahmed *et al.*.[158] A second study,[162] which used a combination of big-box RMCProfile[199] and small-box PDFgui[189] refinements of both X-ray and neutron PDF data, showed some evidence in support of the anisotropic 3SP model [Fig. 1.19(b)]; however, due to the limitations of PDF techniques, a conclusive answer could not be given.[162] The RMC refinements favoured the most disordered proposed model for orbital ordering, the L-type arrangement [Fig. 1.19(c)]. Since RMC modelling is probabilistic, it will produce the most disordered model that is consistent with the data and restraints; hence, the L-type model is statistically more likely to be found by RMC refinement than either the 3SP- [Fig. 1.19(b)] or C-type models [Fig. 1.19(a)], and the small differences between the models' goodness of fit to the data is not large enough to bias against the statistical result. This study[162] also went on to show that similar fits to PDF data can be obtained for different small-box models [Fig. 1.19(e)]. Hence, the issue of uniqueness should be considered when assessing both big- and small-box models.[162,199,200]

What these examples serve to highlight is that whilst total scattering/PDF probes are sensitive to both the short-range (local) and long-range (average) structure, it is not always possible to use these techniques in isolation to differentiate between different structural models. Furthermore, it is also worth bearing in mind when assessing PDF fits that a decent PDF fit cannot always be taken as direct evidence in support of a particular model, as other models may exist that might give a similar fit to data.

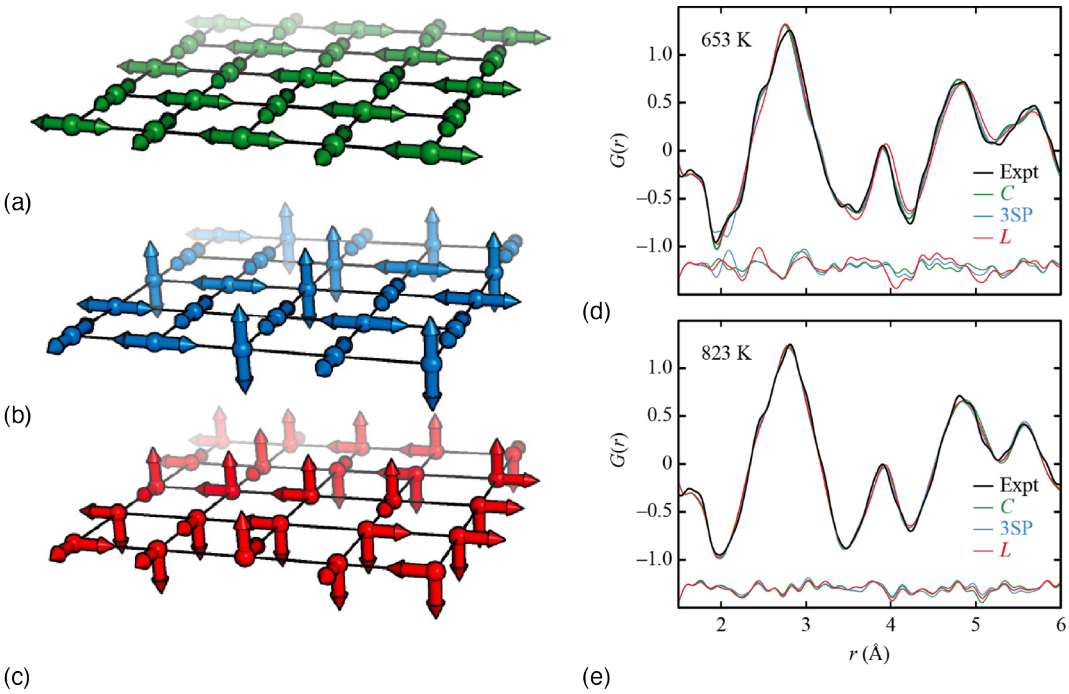


Figure 1.19: Proposed orbital models for $LaMnO_3$. (a) C-type, (b) 3-state Potts-type, and (c) L-type orbital ordering arrangements shown on a single plane of the Mn sublattice. Arrows denote the orientation of the long (JT) Mn–O bonds. Small-box neutron PDF fits of the (d) orthorhombic orbital ordered and (e) orthorhombic orbital disordered regimes of $LaMnO_3$. The experimental data are shown in black, and the fits from the C-type, 3SP-type, L-type orbital models are shown in green, blue, and red, respectively, with their corresponding difference functions (data−fit) shown in the relevant colour, shifted vertically by 1.25 units. Reproduced with permission from Ref. 162. Copyright 2017 by the American Physical Society.

1.4 Structure–function relationships in key perovskite and PBA systems

Having explored the structural complexity of perovskites and PBAs, and how one might go about characterising the local structure of such disordered materials, this final section aims to highlight the importance of understanding how structural complexity can impact the performance of a few functional perovskite and PBA materials, specifically those that are of direct relevance to the results of this thesis.

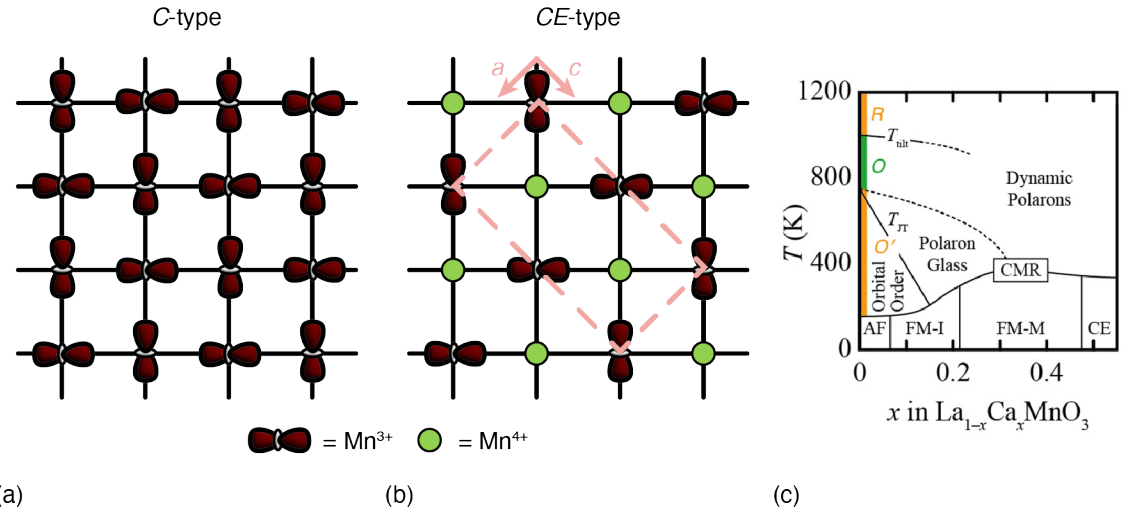


Figure 1.20: An illustration of the (a) *C*-type and (b) *CE*-type charge and orbital ordering schemes observed in manganite perovskites. Each Mn site in both ordering schemes corresponds to the ABO_3 perovskite B site; note that the perovskite A- and O-sites are omitted for clarity. The pink dashed box in (b) indicates the minimum repeating unit required to describe the *CE* ordering. (c) The phase diagram of $La_{1-x}Ca_xMnO_3$, illustrating the interplay of competing JT, tilt, spin, and charge degrees of freedom. (c) Reproduced with permission from Ref. 162. Copyright 2017 by the American Physical Society.

1.4.1 Colossal magnetoresistive manganite perovskites

The importance of understanding and ultimately exploiting structure–function relationships in functional materials design is especially pertinent to the $La_{1-x}Ca_xMnO_3$ (LCMO) series of manganite perovskites, where the interplay of charge, spin, lattice, and orbital degrees of freedom gives rise to the useful property of colossal magnetoresistance (CMR).[17–20] The interplay of these different degrees of freedom are implicated in the emergence of various charge and orbital ordering schemes, including *C*-type ordering in $LaMnO_3$ [Fig. 1.20(a)],[16,201,202] and *CE*-type ordering in $La_{0.5}Ca_{0.5}MnO_3$ [Fig. 1.20(b)].[16,203] Hence, a fundamental understanding of the interplay of the different degrees of freedom and how they couple to drive the various charge and orbital ordering phenomena should give us the knowledge of how to tune the properties of these LCMO materials to suit our functional needs.

Understanding the interplay of different degrees of freedom and how they give rise to the various charge and orbital ordering schemes has proven to be a significant

challenge.[16,162,192] The phase diagram of LCMO is complex [Fig. 1.20(c)],[204,205] with multiple degrees of freedom affected simultaneously when the composition and temperature are varied. Hence, this interdependence of degrees of freedom has made it difficult to obtain an accurate microscopic understanding of how and to what extent each contributes to the various ordering phenomena. Prototype systems are commonly used in such cases to overcome this problem of competing complexity; in theory, only one control parameter is varied systematically, making it possible to isolate how each control parameter contributes to the emergence of the various phenomena. For example, by using the cubic manganite quadruple perovskites $A\mathrm{Mn_3Mn_4O_{12}}$ (A = $\mathrm{Ca_{1-}}_x\mathrm{Na}_x$, $\mathrm{Hg_{1-}}_x\mathrm{Na}_x$) to decouple the *Pbnm* structural degrees of freedom from chemical doping, it has been possible to show that an orbital order:charge disorder striping occurs for compositions of x with the same average Mn B site oxidation as $\mathrm{La_{5/8}Ca_{3/8}MnO_3}$—the composition of LCMO with maximal CMR effects.[25,206] Hence, by using prototype systems, it is possible to determine the role that each degree of freedom plays in driving the various ordering phenomena, something that might otherwise be too difficult using the LCMO solid solution itself.

Using the half-doped $\mathrm{La_{0.5}Ca_{0.5}MnO_3}$, the degrees of freedom that couple to give rise to the *CE* structure can be explored [Figs. 1.20(b) and 1.21].[16,203] In the *CE* structure, checkerboard charge ordering is accompanied by orbital ordering (OO), where the JT-distorted $\mathrm{Mn^{3+}}$ ions form zig-zag chains in the $\boldsymbol{a}$-$\boldsymbol{c}$ plane [Fig. 1.20(b)]. Since the common *Pnma* perovskite superstructure contains only one symmetry-equivalent Mn site, it cannot be used to describe long-range CO; Radaelli *et al.* showed that a quasicommensurate $[\frac{1}{2} - \varepsilon, 0, 0]$ modulation of the common $\sqrt{2a_p} \times 2a_p \times 2a_p$ *Pnma* perovskite ($a_p \approx 3.8\,\text{Å}$) superstructure can be used to describe the *CE* structure of $\mathrm{La_{0.5}Ca_{0.5}MnO_3}$.[203,207] At low temperatures, ε tends to small values, hence for simplicity, the superstructure can be considered to be commensurate and to have $P2_1/m$ space-group symmetry with $a \approx 2 \times \sqrt{2}a_p$, $c \approx \sqrt{2}a_p$, and $b \approx 2a_p$ (exact doubling along the a axis) [Fig. 1.21]. Radaelli *et al.* proposed that OO occurs

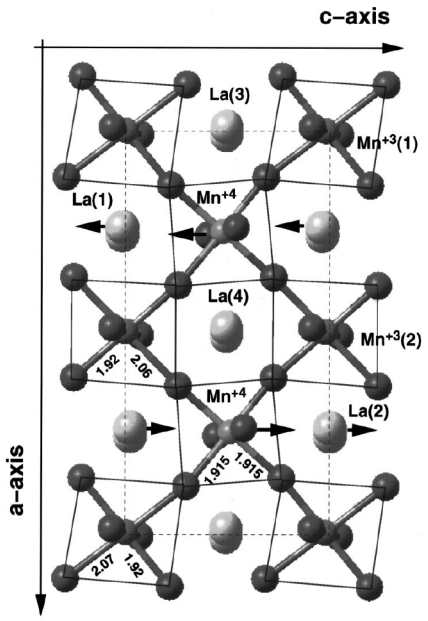


Figure 1.21: The low-temperature $La_{0.5}Ca_{0.5}MnO_3$ superstructure proposed by Radaelli *et al.* in Ref. 203 with $P2_1/m$ space-group symmetry. The projection shown is in the **a**-**c** plane. The direction of displacements of the $Mn^{4+}O_6$ octahedra and the La atom are indicated by arrows. The oxygen atoms are shown in the darkest grey shade and are unlabelled. Reproduced with permission from Ref. 203. Copyright 1997 by the American Physical Society.

with alternate shift displacements of the JT-inactive $Mn^{4+}O_6$ octahedra along the [001] and [00$\bar{1}$] directions (a *transverse* modulation) [Fig. 1.21],[203] and suggested that there might be a coupling between the octahedral tilt pattern and the displacements that give rise to the modulation.[203]

Having noted how prototype systems simplify the task of exploring how different degrees of freedom contribute to various phenomena, Chapter 5 uses the prototype system $LaGa_{1-x}Mn_xO_3$ to explore whether simple geometric rules can explain the coupling between JT, tilt, and shear strain modes that drives the C-type orbital ordering of $LaMnO_3$. The results of MC simulations are compared to experiment using distortion mode analysis. Chapter 5 then goes on to explore whether these same geometric rules can explain the coupling between charge, JT, shift, and tilt degrees of freedom that has been suggested to drive the *CE* structure of $La_{0.5}Ca_{0.5}MnO_3$.

1.4.2 Negative thermal expansion in Prussian blue analogues

Whilst the vast majority of materials expand when heated, some materials contract; this perhaps counterintuitive behaviour is known as negative thermal expansion (NTE).[208,209] NTE has been identified in both oxide-based materials[210–213] and cyanide-based molecular framework materials,[214,215] including the PBA family.[120,121,123,216,217] NTE materials are mostly of interest due to their ability to counteract the positive thermal expansion (PTE) of other materials, and have found applications as cooker hobs,[218] dental fillings,[219,220] and in high-precision optics.[221] When seeking to design next-generation NTE composites, gaining a better understanding of the underlying mechanisms of NTE and how they might be exploited for a specific function is an important step.

Usually, either electronic or phonon mechanisms drive NTE;[209,222–226] amongst network materials, including PBAs, phonon mechanisms generally dominate.[209,222] The mechanism responsible for NTE in the oxide and PBA families is generally understood to arise from the thermal population of low-energy transverse vibrational modes of the bridging atoms; when the metal centres are joined by bonds with minimal PTE, these transverse vibrations have the effect of drawing the strongly bridged metal centres closer together [Fig. 1.22(a),(b)].[210,213,215,224] These transverse vibrations can then couple throughout the lattice such that a combination of cooperative polyhedral rotations [Fig. 1.22(c),(d)], translations, and deformations drive collective NTE.[215,227,228] The additional dynamic flexibility given by polyatomic linkers facilitates other volume-reducing correlated motions—*e.g.* unconventional tilts and polyhedral shifts [Fig. 1.22(e)]—[109,110,113] increasing the number of low-energy phonon modes that can contribute to NTE and hence the capacity for NTE.[120,213,216]

Despite the widespread observation of NTE amongst the PBA family,[120,121,123,216] their lattice dynamics are not particularly well understood. What is known, from a

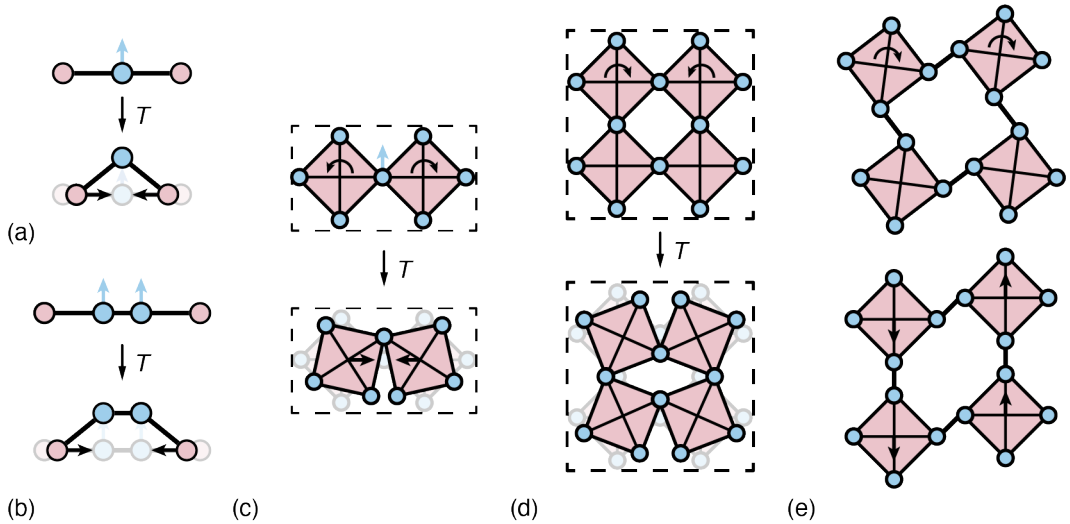


Figure 1.22: The tension effect mechanism. (a), (b) When bonds are stiff, a transverse vibration of the bridging atom(s) draws the metal centres closer together. (c), (d) In framework structures, these transverse vibrations can couple throughout the lattice through cooperative polyhedral rotations. (e) In molecular perovskites, where the bridging moiety is polyatomic, unconventional tilts (top) and translations of columns of polyhedra (bottom) can also facilitate volume-reducing correlated motions.

comparative study of the $M^{II}Pt^{IV}(CN)_6$ series, is that larger M^{II} cations can drive stronger NTE [Fig. 1.23(a),(b)];[121] since larger M^{II} cations typically form weaker M–N interactions, their phonon frequencies will be lower, hence the phonon modes responsible for NTE will be more readily populated. It is also known that PBAs containing a substantial fraction of vacancies show greater NTE, which is understood to arise from an increased density of NTE modes.[94,229] By comparison, incorporating water molecules within the framework cavities dampens NTE modes, which is known to even cause a switch from NTE to PTE in $ZnPt(CN)_6 \cdot xH_2O$.[120] Hence, the phonon modes that drive NTE in PBAs are likely to involve displacements into the open framework cavities. Phonon dispersion curves calculated for $ScCo(CN)_6$ [Fig. 1.23(c)] do indeed suggest that correlated octahedral tilts into the framework cavities are the strongest NTE modes;[124] however, due to choosing an unconventional unit-cell setting, interpretation of their phonon relations is complicated as they were not adjusted for the unconventional unit-cell setting. Hence, the extent to which conventional tilts, unconventional tilts, and shift distortions contribute to

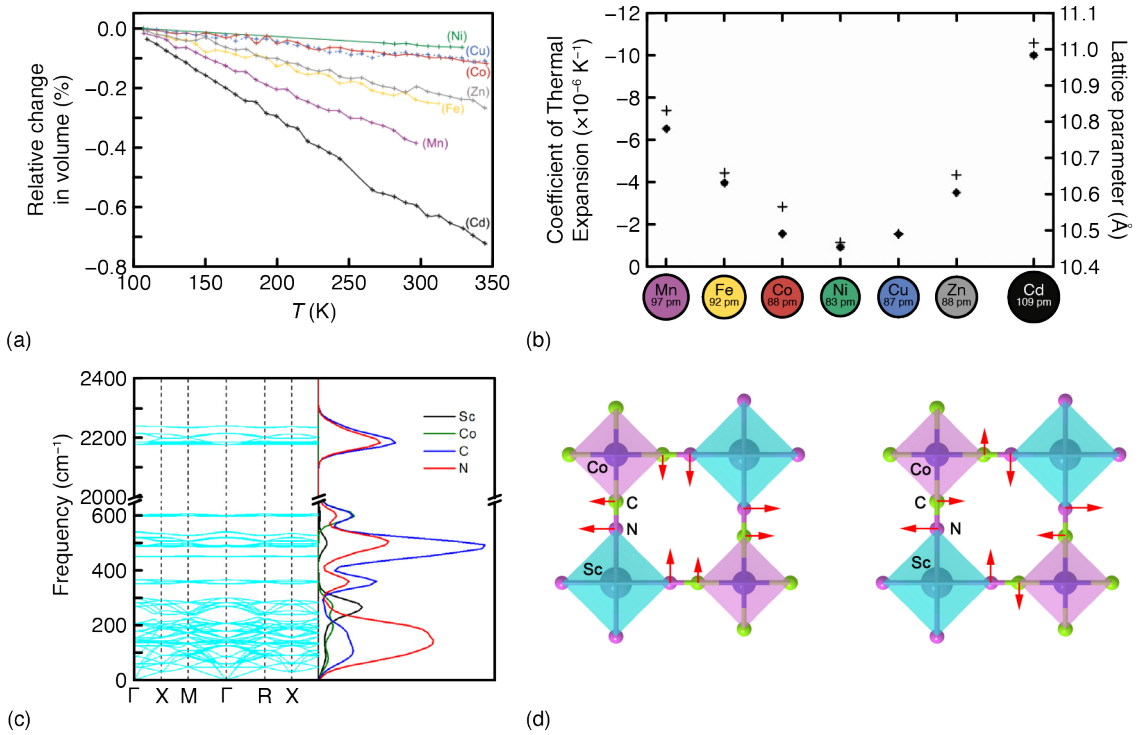


Figure 1.23: Characterisation of NTE behaviour in PBAs. $M^{II}Pt^{IV}(CN)_6$ (M = Mn, Fe, Co, Ni, Cu, Zn, Cd) PBAs: (a) the temperature dependence of the change in unit cell volume relative to the relevant 100 K $M^{II}Pt^{IV}(CN)_6$ structure, and (b) linear coefficients of thermal expansion (♦) and cubic lattice parameters at 100 K (+). Panels (a) and (b) adapted from Ref. 121 with permission. Copyright 2006 American Chemical Society. (c) Phonon dispersion curves and phonon density of states calculated in Ref. 124 for $ScCo(CN)_6$. (d) Representations of the two predominant transverse vibrational modes (conventional tilts and unconventional tilts) as determined in Ref. 124. Panels (c) and (d) adapted from Ref. 124 with permission from Elsevier.

NTE still remains to be determined and validated experimentally.

Due to the dynamic nature of NTE materials, the instantaneous structure differs significantly from the average structure; hence, local structure probes such as total scattering/PDF techniques are more ideally suited to studying dynamically-disordered materials than conventional Bragg diffraction techniques.[230–232] Indeed, X-ray PDF measurements have previously provided insight into the local structure of PBAs [Fig. 1.24].[182,214,231,233,234] However, achieving a quantitative analysis of PBA PDFs is particularly challenging. In PBAs, atom-pairs at similar distances can be correlated to very different extents (*e.g.* inter- *vs* intra-polyhedral combinations), hence there can be a mixture of broad and sharp features at similar distances. This

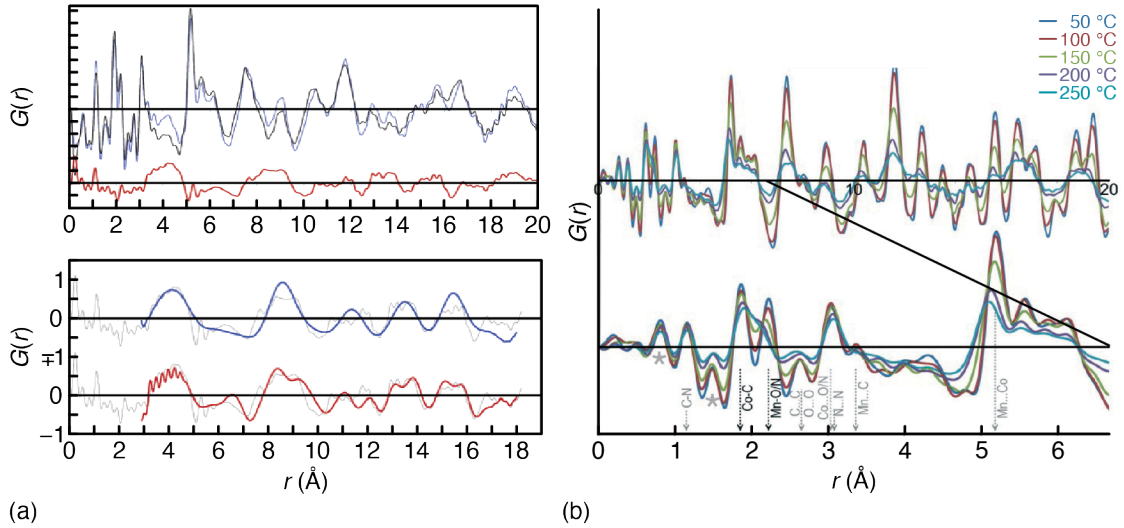


Figure 1.24: X-ray PDF measurements of PBAs. (a) (Top) PDFs extracted for vacant and loaded frameworks are shown in black and blue respectively, with the corresponding differential PDF shown in red. (Bottom) Calculated differential PDFs of a host-guest model[214] and a model accounting for lattice expansion effects[214] are shown in blue and red, respectively. The experimental differential PDF is shown in grey for comparison. Panel (a) reprinted with permission from Ref. 214. Copyright 2005 American Chemical Society. (b) PDF data obtained during desorption of guest water molecules from $Mn^{II}[Co(CN)_6]_{2/3}(H_2O)_6 \cdot \{H_2O\}$. Artefacts in the low-$r$ region of the PDFs are indicated with an asterisk (*). Panel (b) reproduced from Ref. 233 with permission from CrystEngComm; permission conveyed through Copyright Clearance Center, Inc..

will be a problem for standard PDF analysis methods, since they typically assume that as the distance between pairs of atoms increases, the degree of correlation in their pairwise displacements decreases monotonically.

Hence, a key focus of the work presented in Chapter 3 is developing a MC-driven 'interaction-space' approach[235,236] for interpreting the PDFs of $MPt(CN)_6$ PBAs. In this approach, the parameters of an intentionally simplistic empirical potential model are optimised so as to reproduce the experimentally-determined pair correlations. This method ultimately allows the experimental identification of the key modes responsible for NTE in the $MPt(CN)_6$ PBAs.

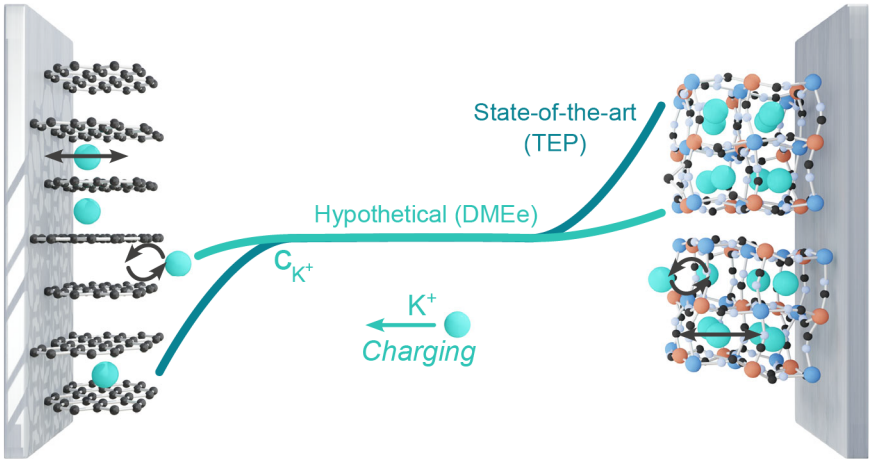


Figure 1.25: Schematic illustration of a PBA battery, including the graphite negative electrode (left) and the potassium manganese hexacyanoferrate $K_2Mn[Fe(CN)_6]$ positive electrode (right). Electrolytes include the current state-of-the-art K-ion electrolyte, potassium bis(fluorosulfonyl)imide (KFSI) in triethyl phosphate (TEP),[239] and a hypothetical electrolyte, KFSI in 1,2-dimethoxyethane (DME);[240] their concentration gradients are shown for comparison. Adapted from Ref. 241, which is distributed under the terms of the Creative Commons CC BY license.

1.4.3 PBA cathode materials

The role of structural complexity in governing the NTE behaviour of PBAs has already been highlighted: whilst the incorporation of vacancies increases the magnitude of NTE,[94,229] the incorporation of water molecules into the framework cavities dampens NTE.[120] The impact that structural complexity can have on functionality is especially important in the case of PBA cathode materials [Fig. 1.25].[1,237,238]

PBAs have emerged as a promising family of Na- and K-ion cathode materials[85,242–244] owing to their open-framework structure that facilitates rapid ionic conduction and hence high rate capability.[85] Na- and K-ion batteries offer attractive alternatives to Li-ion batteries due to the greater abundance of Na- and K-ions. A leading PBA K-ion cathode material is often considered to be potassium manganese hexacyanoferrate $K_xMn[Fe(CN)_6]_y$ because of its low cost and high redox potential;[244] however, this material undergoes two structural phase transitions every charge/discharge cycle [Fig. 1.26],[245] which are thought to affect mechanical stability

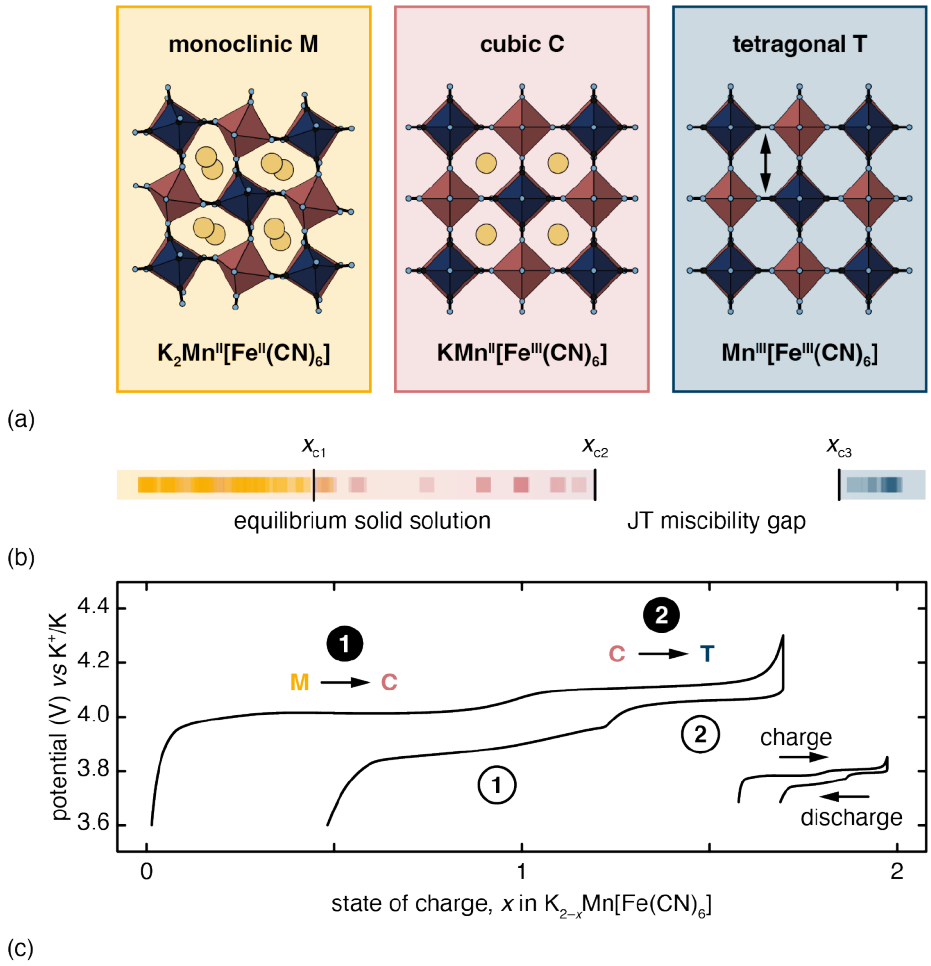


Figure 1.26: Cycling between different phases of $K_{2-x}Mn[Fe(CN)_6]$ during electrochemical cycling. (a) A schematic two-dimensional representation of the three PBA structures that are present during electrochemical cycling. (b) An illustration indicating the structure adopted at each composition. (c) The charge-discharge profile of the $K_2Mn[Fe(CN)_6]$/K half-cell. The monoclinic to cubic transition (1) and cubic to tetragonal transition (2) are indicated. Figure reproduced from Ref. 246, which is licensed under a Creative Commons Attribution License 4.0 (CC BY).

and result in capacity loss.[245] Hence, when seeking to design PBA cathode materials that are capable of rivalling current Li-ion technologies, a better understanding of the structure–property relationships on a fundamental level will be important.

A notable example of the importance of understanding structure–function relationships in PBA cathode materials is given by the significant impact that cooperative Jahn–Teller (CJT) effects can have on the performance of these materials. For example, the promising $K_xMn[Fe(CN)_6]_y$ cathode material is tetrago-

nal in the low vacancy ($y \to 1$), fully oxidised state ($x \to 0$),[247] arising from the long-range CJT order of the JT-active high-spin Mn^{3+} ($t_{2g}^3 e_g^1$) coordination environments. However, during discharge, JT-active Mn^{3+} reduces to JT-inactive Mn^{2+}, hence CJT order dissolves to give a cubic structure (tetragonal $Mn^{III}[Fe^{III}(CN)_6]$ to cubic $KMn^{II}[Fe^{III}(CN)_6]$). This CJT-driven symmetry breaking causes structural damage to the cathode—from the repeated cycling between tetragonal and cubic phases—and is thought to result in capacity loss.[248] By contrast, the non-stoichiometric cathode material $K_{0.71}Cu[Fe(CN)_6]_{0.72}$ (with the redox cycling driven by Fe^{II}/Fe^{III} redox), despite a high content of JT-active Cu^{2+} ions does not show long-range CJT order of the Cu^{2+} ions and possesses vastly superior cycling stability to $KMn[Fe(CN)_6]$.[242] This illustrates how $[M'(CN)_6]^{n-}$ vacancy incorporation can disrupt long-range CJT order [Fig. 1.14(b)], and hence presents as a strategy for mitigating damaging CJT-driven symmetry breaking in $K_xMn[Fe(CN)_6]_y$; understanding the interplay between vacancies and CJT effects will therefore be important in optimising the performance of this cathode material.

When seeking to use vacancies to prevent damaging CJT-driven phase transitions in $K_xMn[Fe(CN)_6]_y$, other effects that vacancy incorporation might have on the performance of this cathode material should be considered. For example, minimising the number of vacancies in the structure should maximise capacity as well as remove water from the framework;[239] the latter should prevent damaging side reactions with electrolyte[249] that are known to cause capacity fade.[116] However, the downsides of reducing the vacancy concentration include sacrificing the framework flexibility that is thought to improve cycle life,[242] as well decreasing the ionic conductivity.[241] In the limit of zero vacancies, ions can only move through the windows of the sub-cubes [Fig. 1.9(a)], whereas in PBAs with higher vacancy concentrations, ions can also move through the vacancy pores themselves [Fig. 1.9(b)]. In the latter case,[250] the pore-network geometry itself is also likely to impact ionic diffusivity.[95,96] Hence, one can imagine that some kind of compromise might be found that balances preventing

CJT-driven symmetry breaking with the other factors considered here.

An alternative strategy to prevent CJT-driven symmetry breaking in low-vacancy $K_xMn[Fe(CN)_6]_y$ might be to substitute the M-site with a JT-inactive ion. For example, long-range CJT order was prevented in $Na_xMn[Fe(CN)_6]_{0.98}$ by doping with as little as 12% Ni.[251] Again, there are pros and cons with this strategy; whilst doping with electrochemically-inactive Ni sacrifices some capacity, it seems to improve cycling stability.[251] Doping with an electrochemically-active ion such as Fe^{2+} in $K_xFe_{0.33}Mn_{0.67}[Fe(CN)_6]_{0.98}$ seems to avoid such a loss in capacity whilst retaining the benefit of an improved cycle-life from the suppression of long-range CJT order.[248] So, it seems doping the M-site with a JT-inactive ion could be an effective strategy to prevent CJT-driven symmetry breaking in low-vacancy $K_xMn[Fe(CN)_6]_y$.

This is the motivation behind the work of Chapter 4, which explores the interplay between CJT order, M-site doping with JT-active/inactive ions, and M′-site hexacyanometallate vacancy incorporation. In Chapter 4, high-resolution synchrotron X-ray diffraction measurements are used to characterise the phase stability and extent of long-range CJT order as a function of JT dilution and hexacyanometallate vacancy concentration in three compositional series: namely, $Mn_{1-x}Cu_x[Pt(CN)_6]$, $Cs_xCu[Fe(CN)_6]_{(2+x)/3}$, and $Mn_{1-x}Cu_x[Co(CN)_6]_{2/3}$. MC simulations are then used to test a simple model governing CJT order. From these MC simulations, a generic phase map is generated, giving an indication of how PBA compositions might be tuned—in terms of their vacancy and JT concentration—to control the emergence of long-range CJT order, which is important when seeking to tune the composition to meet our functional needs.

1.4.4 Photoinduced charge transfer processes in PBAs

The role of structure-function relationships in designing the next-generation of functional PBA materials has been discussed in the context of NTE materials (subsection 1.4.2) and PBA cathode materials (subsection 1.4.3); this idea continues here in

the context of PBA photoinduced charge transfer materials. Photoinduced charge transfer is a process fundamental to *e.g.* solar energy harvesting[252] and photocatalysis.[253] PBA photoinduced charge transfer materials are of particular interest since the reversible charge transfer between the M-site and M′-site transition metal ions gives rise to various physical properties.[254–256]

The already-encountered ability of hexacyanometallate vacancies to impact the function of PBA materials (subsections 1.4.2 and 1.4.3) is also pertinent to PBA charge transfer materials. In the $Cs_xCo[Fe(CN)_6]_y$ family, whilst $Co^{II}[Fe^{III}(CN)_6]_{0.67}$ is a candidate for photoinduced charge transfer, $Co^{III}[Fe^{II}(CN)_6]_{0.97}$ is not; whilst the former has the flexibility—due to the high number of hexacyanometallate vacancies—to accommodate the change in bond lengths associated with charge transfer, $Co^{III}[Fe^{II}(CN)_6]_{0.97}$—with a more rigid framework—does not.[97] Despite the significant interest in PBAs, the underlying ultra-fast photoinduced charge transfer mechanism is still not well understood.[257–261]

Historically, determining charge transfer mechanisms has proven difficult due to the fast timescales involved and the interplay between orbital, spin, and lattice degrees of freedom.[257–259] Recently, an intriguing discovery was made using optical-pump/XANES measurements, which identified an initial photoinduced spin-state transition that pre-empts charge transfer in $Cs_{0.7}Co[Fe(CN)_6]_{0.9}$ [Fig. 1.27].[262] Since spin- and charge-transfer processes involve a change in the population of the e_g orbitals [Fig. 1.27(a)], atomic positions are strongly coupled to orbital occupations, and so bond-length variations are relatively large. Hence, local structure probes such as total scattering techniques can be expected to possess the sensitivity required to probe such local structure variations. In principle, determination of the mechanism by which excitation at a Co^{3+} site leads to the oxidation of a specific neighbouring Fe^{2+} ion should be possible using total scattering techniques. However, whilst synchrotrons offer excellent real-space resolution, they do not possess the required temporal resolution to capture ultra-fast changes; whilst it is possible to

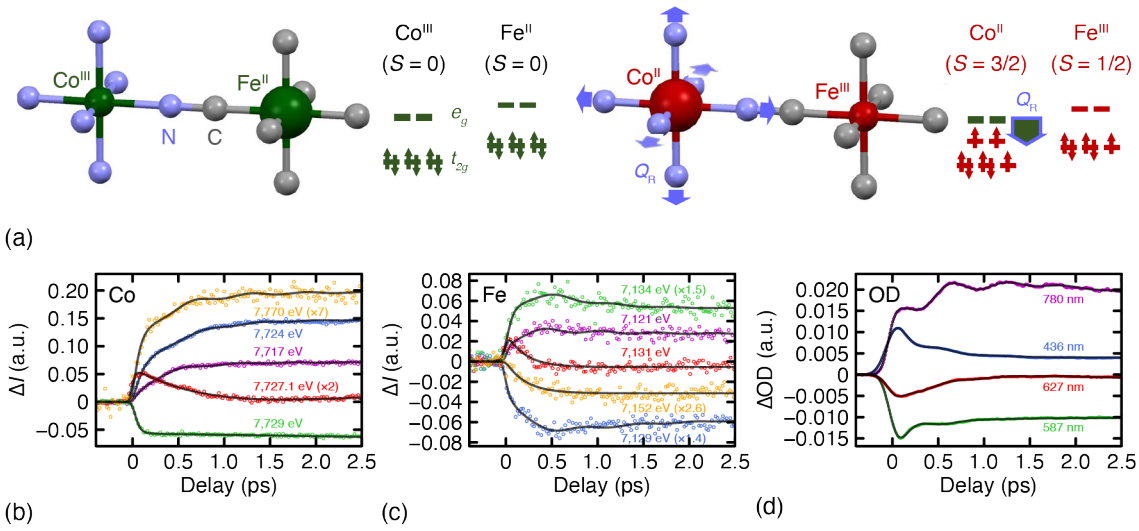


Figure 1.27: (a) Schematic representation of spin states in $Co[Fe(CN)_6]$, and (b)–(d) optical pump-probe/XANES measurements of photoinduced charge transfer in $Co[Fe(CN)_6$. Figure adapted from Ref. 262 with permission from Springer Nature.

perform some time-resolved PDF studies using X-ray synchrotron sources,[263] most measurements typically take ∼seconds–minutes. This is insufficient to measure the photoinduced changes in the $Cs_{0.7}Co[Fe(CN)_6]_{0.9}$ system, since the spin-state transition occurs over 50 fs with the charge-transfer transition occurring over 200 fs.[262] Hence, technologies capable of measuring ultra-fast changes occuring on a femtosecond timescale will be required.

An emerging technology capable of producing femtosecond-pulsed X-ray beams is the X-ray free-electron laser (XFEL).[264] Whilst XFEL technologies might have the potential to measure total scattering on femtosecond timescales, the real-space resolution they provide is currently insufficient for many advanced studies.[265] Hence, to make full use of the femtosecond temporal resolution offered by XFELs for ultra-fast total scattering studies, the real-space resolution of XFEL technologies will need to be improved. This motivated the work of Chapter 6, which primarily details the efforts made to establish high-quality ultra-fast total scattering techniques at the European XFEL. Chapter 6 assesses the quality of XFEL PDF data obtained at the European XFEL by comparison to synchrotron data and goes on to explore whether

XFEL technologies can be used to characterise the local structure of complex PBA materials containing *e.g.* JT-active ions and vacancies. It is hoped that eventually XFEL technologies might be capable of providing insight into ultra-fast processes such as photoinduced charge transfer in PBAs.

1.5 Aims and thesis outline

The aim of this thesis is to improve our fundamental understanding of the interplay between various degrees of freedom in perovskites and Prussian blue analogues (PBAs) with a view to control them to suit our functional needs. It has already been flagged how a complex interplay between orbital order, spin, charge, tilt and lattice degrees of freedom is implicated in the emergence of the useful property of colossal magnetoresistance (CMR) in the manganite perovskites. Hence, in order to optimise the CMR effect, and to appreciate how the different charge and orbital phenomena control this property in these materials, there is motivation to obtain an accurate microscopic understanding of these states in order to successfully tune the properties in a targeted way. Clearly, cooperative Jahn–Teller (CJT) order can affect the electronic, magnetic, and structural properties of the materials in which it occurs, and whilst conventionally studied in dense ceramics, can also occur in hybrid materials such as PBAs. Whilst CJT effects can play a useful role in the physical behaviour of materials—*e.g.* CMR in the manganite perovskites—they can also be undesirable if they *e.g.* lead to symmetry-breaking in (PBA) cathode materials. Hence, there is a clear motivation to establish rules governing CJT order in solids—both theoretical and empirical—when seeking to tune the practical applications of these functional materials. PBAs can harbour a wide variety of different distortion and defect structures, including vacancies and tilts, so it is necessary to understand the nature and interplay of these different distortions when *e.g.* trying to avoid damaging CJT-driven symmetry breaking in PBA cathode materials.

Having highlighted the impact that local structure can have on material properties and set out the desire to understand and exploit these structure–property relationships in functional materials design raises the non-trivial problem of characterising the local structure of materials. A strong understanding typically requires a coupled approach involving multiple techniques, both experimental and computational. Total scattering (TS)/pair distribution function (PDF) techniques can be especially powerful as it is possible to model both the short-range (local) and long-range (average) structure simultaneously. Monte Carlo (MC) modelling can be employed in conjunction with total scattering analysis and is useful in testing the underlying physics or chemical interactions governing a structure. Hence, this thesis makes use of both X-ray total scattering and MC modelling to understand CJT order in PBAs and perovskites. The methods used in this thesis are discussed in more detail in Chapter 2, with the remaining chapters of this thesis laid out as follows:

In Chapter 3, a combination of atomistic MC modelling, X-ray PDF measurements, lattice dynamical calculations, and *ab initio* density functional theory (DFT) calculations are used to study the local structure and dynamics in various negative thermal expansion (NTE) $MPt(CN)_6$ PBAs. A new 'interaction-space' PDF refinement approach is developed in order to link directly the local distortions captured by the PDF with the lattice dynamics of this family. $MnPt(CN)_6$ is effectively defect free, with no JT-active cations nor vacancies, and so presented an ideal starting system on which to develop this relatively simple big-box modelling technique. Having obtained an atomistic representation of a relatively simple PBA using this new big-box modelling technique, the technique is then extended to develop models of the local structure of more complex PBAs, *e.g.* $CuPt(CN)_6$ with JT-active cations. A benefit of this interaction-space' PDF refinement approach is that it yields effective harmonic force constants from which the (experiment-derived) low-energy phonon dispersion relations can be approximated. Comparison to phonon disper-

sion relations determined using DFT calculations then correctly identifies correlated octahedral tilts of coordination octahedra as the key modes responsible for NTE.

Having obtained a local structure picture for relatively simple PBAs that are effectively defect free and having established the role of correlated octahedral tilts in driving NTE, another layer of structural complexity is added in Chapter 4 with the aim to understand the effect of vacancy incorporation on CJT-driven symmetry breaking. To determine links between vacancy incorporation and CJT order in PBAs, three compositional series are studied, using synchrotron powder X-ray diffraction measurements to characterise their phase stability and extent of long-range CJT order as a function of JT and vacancy concentration. Coarse-grained MC modelling using a simple geometric model governing CJT order is developed based on the competition between strain and crystal-field stabilisation that can account for the extent of CJT order, crystallite strain, and stability measured experimentally. This model gives an indication of how PBA compositions might be tuned to control the emergence of long-range CJT order. Notably, the model suggests that PBAs may contain a complex interplay between compositional, structural, orbital, and magnetic degrees of freedom related to that of strongly-correlated functional materials such as the manganite perovskites. Access to coarse-grained representations of JT orientations in JT-dilute and/or partially-vacant PBAs then allowed, for the first time, the construction of atomistic models of the local structure in these materials by using the MC-driven 'interaction-space' big-box PDF refinement approach developed in Chapter 3.

Chapter 5 aims to obtain an accurate microscopic understanding of different charge and orbital ordering phenomena in the $LaGa_{1-x}Mn_xO_3$ (LGMO) and $La_{1-x}Ca_xMnO_3$ (LCMO) manganite perovskites. The LMGO solid solution is an ideal system to trace how JT distortions tune the orthorhombic–pseudocubic phase transition in *Pbnm* manganite perovskites. To understand the local ordering that gives rise to the crystallographically observed average structural distortions, a series

of MC simulations are performed. A simple geometric approach—of a similar kind to the one employed in Chapter 4 for the JT PBAs—is developed to explore the coupling between JT, tilt, and shear modes that drives the C-type orbital ordering observed in the $LaGa_{1-x}Mn_xO_3$ systems. A symmetry-motivated analysis is used to map the evolution of the JT, tilt, and shear strain modes as a function of composition onto experimentally-determined values. It is shown that a trilinear coupling term between shear strain, octahedral rotation, and the C-type orbital ordering mode is responsible for driving the pseudocubic to orthorhombic phase transition occurring in the composition range $0.4 < x < 0.5$. The Hamiltonian developed for LGMO is then extended to incorporate the additional complexity of charge ordering in LCMO, where it is shown that charge order, JT order, shifts, and tilts couple to drive the *CE* structure observed in $La_{0.5}Ca_{0.5}MnO_3$.

Chapter 6 primarily details the efforts made by a large group of people to develop high-quality ultra-fast TS/PDF data at the High Energy Density (HED) scientific instrument at the European XFEL. There is a particular focus on improving the real-space resolution needed to fully leverage the temporal capabilities of XFELs for TS applications. The experimental setup is described in detail, including the use of a tilted detector geometry designed to maximise counting statistics in the high-Q region. Additionally, the data processing and reduction pipeline is outlined, with a focus on ensuring precision and efficiency. The quality of data obtained from a single $\sim 30\,\text{fs}$ XFEL pulse for different sample types is discussed. Chapter 6 goes on to explore whether XFEL technologies can be used to characterise local JT/vacancy order in PBAs. The project forms an important proof of concept of using XFEL TS measurements to study local structure in functional materials, for example, characterising local JT/vacancy order in PBAs. Finally, an inverse MC transformation method for generating a numerical form of the PDF from reciprocal space TS data is used to discuss whether sacrificing a continuous Q range to push Q_{max} to higher values will be more beneficial for materials requiring greater real-

space resolution than a setup that provides a continuous Q range but does not achieve as high $Q_{\max}$ values. Having developed the methodology for achieving high-quality ultra-fast TS/PDF data, Chapter 6 concludes with an outlook, identifying where the temporal capabilities of XFELs may be crucial for studying time-resolved processes, *e.g.* photoinduced charge transfer in PBAs.

Lastly, the final chapter, Chapter 7, begins with a discussion of the key results of this thesis in the context of the aims set out at the beginning of this section, and concludes with an outlook, offering suggestions for future research and discussing whether the approaches taken in this thesis may be used to study other similarly complex materials.

Chapter 2

Methods

This chapter aims to provide the necessary background for the methods used in this thesis. This chapter begins with an outline of symmetry, scattering theory, and measurement of X-ray diffraction patterns, and is followed by total scattering, lattice dynamics, and Monte Carlo simulations. Parts of this chapter follow standard textbook treatment.[266–268]

2.1 Crystal structures and symmetry

When seeking to gain an understanding of crystallography, the definition of a crystal seems a good place to start. A solid can be defined as a crystal if it possesses, on average, a long-range periodic arrangement of atoms, ions and/or molecules related by translational symmetry.* This can be expressed mathematically as the convolution of a motif with a lattice; *i.e.*

$$\rho(\mathbf{r}) = \text{motif} \otimes \text{lattice}, \tag{2.1}$$

where the electron density of a crystal is given by $\rho(\mathbf{r})$ and $\mathbf{r}$ is a vector. The periodic array of points in space gives the crystal its lattice, and in three-dimensional space, is given by the lengths and orientations of the three linearly independent basis vectors, $\mathbf{a}$, $\mathbf{b}$, and $\mathbf{c}$. Thus, the electron density within a motif is located at coordinates x, y, z, where

$$\mathbf{r} = x\mathbf{a} + y\mathbf{b} + z\mathbf{c}. \tag{2.2}$$

As a consequence of translational symmetry, a crystal structure can also be described by a repeating set of unit cells. In addition to the inherent translational

*This thesis is not concerned with aperiodic crystals, which are therefore ignored.

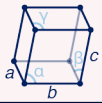
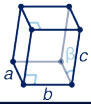
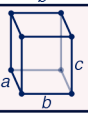
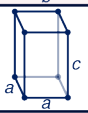
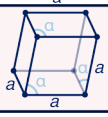
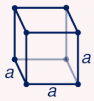
Unit cell	Crystal system	Symmetry	Lattice parameters	Centring	Classes
	Triclinic	None	$a \neq b \neq c$ $\alpha \neq \beta \neq \gamma$	*P*	$1(C_1)$, $\bar{1}(C_i, S_2)$
	Monoclinic	One twofold axis	$a \neq b \neq c$ $\alpha = \gamma = 90°$ $\beta \neq 90°$	*P*, *C*	$2(C_2)$, $m[=\bar{2}](C_3)$, $2/m$
	Orthorhombic	Three perpendicular twofold axes	$a \neq b \neq c$ $\alpha = \beta = \gamma = 90°$	*P*, *C*, *I*, *F*	$222(D_2)$, $mm2(C_{2v})$, $mmm(D_{2h})$
	Tetragonal	One fourfold axis	$a = b \neq c$ $\alpha = \beta = \gamma = 90°$	*P*, *I*	$4(C_4)$, $\bar{4}(S_4)$, $4/m(C_{4h})$, $422(D_4)$, $4mm(C_{4v})$, $\bar{4}2m(D_{2d})$, $4/mmm(D_{4h})$
	Trigonal	One threefold axis	$a = b \neq c$ $\alpha = \beta = 90°$ $\gamma = 120°$	*P*, *R*	$3(C_3)$, $3(S_6, C_{3i})$, $32(D_3)$, $3m(C_{3v})$, $3m(D_{3d})$
	Hexagonal	One sixfold axis	$a = b \neq c$ $\alpha = \beta = 90°$ $\gamma = 120°$	*P*	$6(C_6)$, $\bar{6}(C_{3h})$, $6/m(C_{6h})$, $622(D_6)$, $6mm(C_{6v})$, $\bar{6}m2(D_{3h})$, $6/mmm(D_{6h})$
	Cubic	Four threefold axes	$a = b = c$ $\alpha = \beta = \gamma = 90°$	*P*, *I*, *F*	$23(T)$, $m3(T_h)$, $432(O)$, $43m(T_d)$, $m3m(O_h)$

Figure 2.1: The seven crystal systems along with an illustration of their respective unit cell. The symmetry, lattice parameter constraints, possible centrings, and symmetry classes are given for each crystal system.

symmetry, the majority of crystal structures contain additional symmetry elements within the unit cell, *e.g.* rotation axes, mirror planes, etc. The presence of rotation axes imposes restrictions on the geometry of the unit cell, which is described by its cell parameters (lengths a, b, c) and angles (α, β, γ). As a result, there are only seven crystal systems that can arise from the various combinations of cell lengths and angles, with cubic systems ($a = b = c$, $\alpha = \beta = \gamma = 90°$) having the highest symmetry and triclinic systems having the lowest ($a \neq b \neq c$, $\alpha \neq \beta \neq \gamma$) [Fig. 2.1]. Combining the seven crystal systems with the possible centrings gives the 14 Bravais lattices. Additionally, the seven crystal systems may contain further symmetry elements, giving the 32 crystallographic point groups. The combination of the Bravais lattices with the relevant point groups (crystal classes) gives rise to the 230 crystallographic space groups. Detailed information for each space group is available from the International Tables of Crystallography.[269]

2.2 Scattering theory and reciprocal space

Many of the results in this thesis have been obtained through the analysis of X-ray diffraction (XRD) patterns. XRD has become a routine tool for structure determination, and is underpinned by crystallography.

XRD is based on the elastic scattering of X-rays, *i.e.* there is no change in energy between the incident and scattered waves. If atoms are arranged periodically on a lattice such that it has long-range translational periodicity (*i.e.* is a crystal), incident waves will be scattered by the atoms and they will interact to form an interference pattern of discrete spots known as a diffraction pattern; a diffraction pattern therefore contains information about the underlying arrangement of the atoms (the lattice). W. L. Bragg and his father W. H. Bragg determined that planes of atoms would only scatter X-rays in phase—and hence lead to the constructive interference of scattered X-rays to give sharp diffraction peaks—if the path difference between the scattered waves is equal to an integer multiple of the wavelength of the X-rays. This relationship is given by Bragg's law:[270,271]

$$n\lambda = 2d_{hkl}\sin\theta, \tag{2.3}$$

where λ is the wavelength of the X-rays, d_{hkl} is the spacing between successive lattice planes labelled by a given set of Miller indices h, k, l, and θ is the angle between the incident wavevector $\mathbf{k}_\mathrm{i}$ and the plane of the lattice (*i.e.* the angle of incidence, which is equal to the angle of reflection). Using Bragg's law, it is possible to determine the long-range, average structure of a crystal through the interpretation of its diffraction pattern, which is generated by precisely rotating the crystal through many values of θ and measuring the scattered X-rays; by measuring the scattered X-rays at many values of θ, it is possible to determine the d-spacing (using Eq. 2.3) between many sets of planes, which allows the construction of a crystal structure with a unit cell.

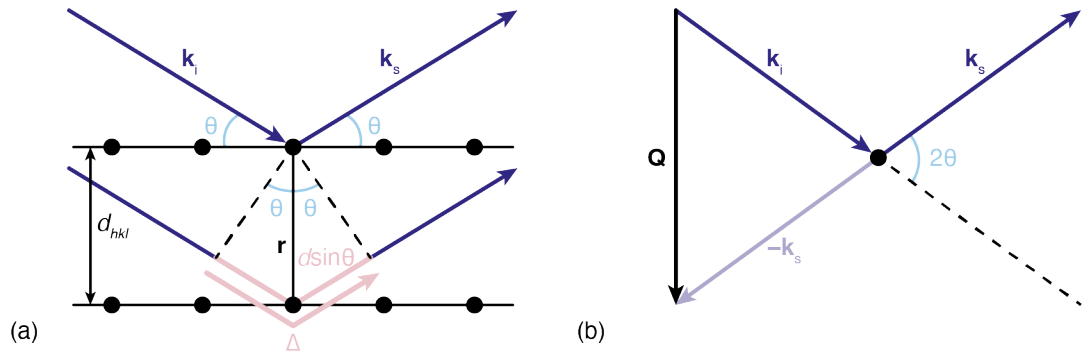


Figure 2.2: (a) The coherent scattering of X-rays by a periodic arrangement of atoms. d_{hkl} is the distance between successive planes labelled by Miller indices h, k, l, $\mathbf{k}_i$ is the propagation vector of the incident radiation, $\mathbf{k}_s$ is the propagation vector of the scattered radiation, θ is the angle of incidence/reflection, and Δ is the phase shift between the incident and scattered beams. (b) The geometric relationship between $\mathbf{k}_i$, $\mathbf{k}_s$, $\mathbf{Q}$ and 2θ.

When an incident wave [Fig. 2.2(a)] is scattered elastically by an atom, the scattering vector, $\mathbf{Q}$, will be given by the difference between the incident $\mathbf{k}_\mathrm{i}$ and scattered $\mathbf{k}_\mathrm{s}$ wavevectors [Fig. 2.2(b)],

$$\mathbf{Q} = \mathbf{k}_\mathrm{i} - \mathbf{k}_\mathrm{s}, \tag{2.4}$$

with magnitude

$$|\mathbf{Q}| = Q = \frac{4\pi}{\lambda} \sin\theta, \tag{2.5}$$

where 2θ is the angle between $\mathbf{k}_\mathrm{i}$ and $\mathbf{k}_\mathrm{s}$ [Fig. 2.2(b)]. Combining Eq. 2.5 with Bragg's law (Eq. 2.3), it can be seen that

$$Q = \frac{4\pi}{\lambda} \sin\theta = \frac{4\pi}{\lambda} \left(\frac{\lambda}{2d_{hkl}} \right) = \frac{2\pi}{d_{hkl}}. \tag{2.6}$$

The waves scattered by atoms in a crystal will only give constructive interference and give rise to Bragg reflections in the diffraction pattern for a periodic set of $\mathbf{Q}$. The unit cell dimensions can be found by indexing these reflections, whilst the centring can be found by determining the systematic absences, hence constraining the possibilities for the space group.

In XRD, waves are scattered by the electron density, $\rho(\mathbf{r})$, of a crystal:

$$F(\mathbf{Q}) = \int \rho(\mathbf{r}) \exp(\mathrm{i}\mathbf{Q} \cdot \mathbf{r}) \, \mathrm{d}\mathbf{r}. \tag{2.7}$$

Hence, the structure factor is the Fourier transform of the electron density, meaning that it will also be the Fourier transform of the crystal structure. The crystal structure is a convolution of a motif and a lattice; hence, using the convolution theorem, the structure factor is a product of the Fourier transform of the lattice and Fourier transform of the motif. The Fourier transform of the real-space lattice yields the reciprocal lattice, which is described by the reciprocal basis vectors, $\mathbf{a}^*, \mathbf{b}^*, \mathbf{c}^*$. The reciprocal basis vectors are related to the real-space lattice vectors by

$$\mathbf{a}^* = \frac{2\pi}{V_{\text{cell}}} \mathbf{b} \times \mathbf{c}, \tag{2.8}$$

$$\mathbf{b}^* = \frac{2\pi}{V_{\text{cell}}} \mathbf{c} \times \mathbf{a}, \tag{2.9}$$

$$\mathbf{c}^* = \frac{2\pi}{V_{\text{cell}}} \mathbf{a} \times \mathbf{b}, \tag{2.10}$$

where V_{cell} is the volume of the unit cell. The positions of the reciprocal lattice points are given by the reciprocal lattice vector, defined as

$$\mathbf{Q} = h\mathbf{a}^* + k\mathbf{b}^* + l\mathbf{c}^*, \tag{2.11}$$

where h, k, and l are integer values of Miller indices. A particularly useful construction in reciprocal space is the first Brillouin zone [Fig. 2.3]: the Wigner–Seitz cell—or Voronoi cell of a lattice point—located at the origin of reciprocal space.

Substituting the explicit definitions of $\mathbf{Q}$ (Eq. 2.11) and $\mathbf{r}$ (Eq. 2.2) into $\mathbf{Q} \cdot \mathbf{r}$ gives

$$\mathbf{Q} \cdot \mathbf{r} = (h\mathbf{a}^* + k\mathbf{b}^* + l\mathbf{c}^*) \cdot (x_j\mathbf{a} + y_j\mathbf{b} + z_j\mathbf{c}) = 2\pi(hx_j + ky_j + lz_j), \tag{2.12}$$

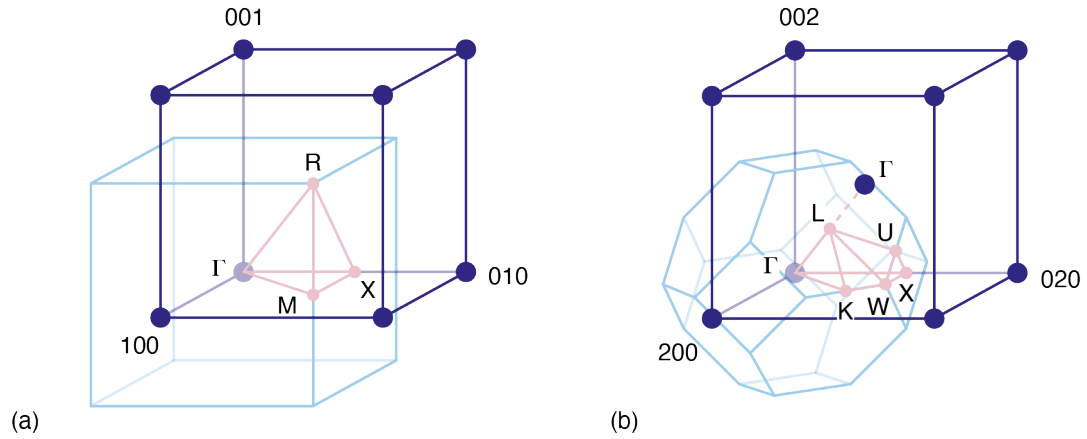


Figure 2.3: The first Brillouin zone for two cubic lattices. (a) The first Brillouin zone (light blue) for a primitive cubic unit cell showing the $\Gamma = (0,0,0)$, $\mathrm{X} = (0,\frac{1}{2},0)$, $\mathrm{M} = (\frac{1}{2},\frac{1}{2},0)$, and $\mathrm{R} = (\frac{1}{2},\frac{1}{2},\frac{1}{2})$ high-symmetry points, in the units of $2\pi/a$, where a is the lattice constant of the conventional lattice. The reciprocal lattice of the primitive cubic unit cell is shown in dark blue. (b) The first Brillouin zone (light blue) for a face-centred cubic (FCC) unit cell (dark blue), showing the $\Gamma = (0,0,0)$, $\mathrm{X} = (0,1,0)$, $\mathrm{L} = (\frac{1}{2},\frac{1}{2},\frac{1}{2})$, $\mathrm{K} = (\frac{3}{4},\frac{3}{4},0)$, $\mathrm{W} = (\frac{1}{2},1,0)$, $\mathrm{U} = (\frac{1}{4},1,\frac{1}{4})$, in the units of $2\pi/a$. Note that the reciprocal lattice of an FCC lattice is body-centred, and is shown in dark blue. The high-symmetry points are labelled by the Bradley–Cracknell notation.[272]

and substituting Eq. 2.12 into Eq. 2.7 gives

$$F_{hkl} = \int_{\text{cell}} \rho(x,y,z) \cdot \exp[2\pi i(hx + hk + lz)]\mathrm{d}V, \tag{2.13}$$

where, x, y, z are the coordinates of the atoms, h, k, l are the Miller indices, and $\rho(x,y,z)$ is the electron density function. However, $\rho(x,y,z)$, is not easily calculated, so Eq. 2.13 is not particularly useful for crystal structure determination. Hence, a more useable form involves using atoms to describe the electron density and summing over the unit cell:

$$F_{hkl} = \sum_j f_j(\theta) \cdot \exp[2\pi i(hx_j + ky_j + lz_j)]. \tag{2.14}$$

Here, $f_j(Q)$ is the Fourier transform of the electron density at atom type j, and is often approximated by an empirical sum of exponential terms; hence, in general, the scattering intensity falls off with increasing θ.

To account for the thermal motion of atoms in a crystal, a term is often added to Eq. 2.14:

$$F_{hkl} = \sum_j f_j(\theta) \cdot \exp(-8\pi^2 U_j \sin^2\theta/\lambda^2) \cdot \exp[2\pi i(hx_j + ky_j + lz_j)], \qquad (2.15)$$

where U_j is an isotropic displacement parameter; thermal displacements are usually given as a mean square displacement (Å^2) either by U or by $B = 8\pi^2 U$.

To obtain a structural model (structure solution), the unit cell and space group must first be found. The unit cell dimensions can be found by determining the positions of the diffracted reflections—where $F(Q)$ is non-zero—and is known as indexing. The possible centring and symmetry elements can be found by identifying systematic absences, which occur for structures possessing centred cells and/or translational symmetry elements; hence, identifying systematic absences can help to limit the choice of possible space groups. Once a suitable space group has been determined, a starting model can be found. The spatial electron density distribution can be found by performing the inverse Fourier transform of $F(Q)$; however, since the structure factor is a complex number and detectors can only measure the intensity $I(Q)$ ($\propto F(Q) \cdot F^*(Q)$, hence $I(Q) \propto |F(Q)^2|$) of the diffracted beam, only the amplitudes of the structure factor can be determined and information on the phases are lost. A number of methods have been developed to overcome this "phase problem", including direct methods,[273] the Patterson synthesis,[274] Sayre's equation,[275] and charge flipping;[276] these methods allow a starting structural model to be determined, which can then be refined (see subsection 2.3.4).

2.3 Powder X-ray diffraction measurements

Powder X-ray diffraction (PXRD) can be a powerful analytical tool for samples that cannot easily be grown as single crystals. Powdered samples contain small crystallites and so the resulting powder diffraction pattern consists of a large number

of superimposed single crystal patterns. Powder diffraction therefore relies on the crystallites being randomly orientated and present in sufficient numbers such as to give a statistical averaging of intensities. Sometimes, there might be a preferred orientation of the crystallites, which mainly occurs in systems with crystallites that have plate- or needle-like morphology, and can be exacerbated by small sample volumes. Careful grinding to create a fine powder, diluting the powder, and rotating the sample when measuring the powder to improve sampling statistics can partially overcome this problem.

2.3.1 In-house powder diffraction

In-house X-ray diffractometers produce X-rays by firing a high-energy beam of electrons at a metal target (Cu in the case of this thesis). The bombarding electrons are of sufficient energy to ionise a core electron, which results in the relaxation of a higher-energy electron to fill the hole. This process results in the emission of a photon with a discrete energy that is characteristic of the electronic transition and metal in question. The transition used to generate X-rays from Cu is between the L and K shell as it has the highest energy and intensity, and three discrete wavelengths of X-ray are generated—Kα_1, Kα_2, and Kβ. Whilst the Cu Kβ is typically filtered out, both Kα_1 and Kα_2 can be used since they are of similar energy; the wavelength of Kα_1, the more intense of the two, is typically quoted for analysis ($\lambda = 1.542\,\text{Å}$), with K$\alpha_2$ removed in the analysis. Cu ($\lambda = 1.542\,\text{Å}$) is predominantly chosen as the metal target, but Mo ($\lambda = 0.709\,\text{Å}$) and Ag ($\lambda = 0.559\,\text{Å}$) sources can also be used,[269] with the choice depending on the characteristics of the sample. For weakly scattering and/or small crystals, longer wavelengths can give higher diffraction intensities, whilst shorter wavelengths are less prone to absorption, and hence particularly relevant for samples containing metals.

For in-house PXRD, the sample is typically prepared by evenly distributing the finely-ground powder on a sample holder that has a thin layer of grease, which

acts to hold the crystallites in an unbiased orientation. Diffraction is performed in reflection geometry with both the detector and sample rotated in θ during data collection.

The main use of in-house PXRD in this thesis was to check sample composition and purity.

2.3.2 Synchrotron powder diffraction

Sometimes, advanced structural studies require a higher flux (intensity) of hard(er) (high(er) energy) X-rays and higher resolution detection than that offered by in-house diffractometers. In such cases, synchrotron radiation is often sufficient.

Synchrotron radiation is the electromagnetic radiation emitted when charged particles, such as electrons, travelling at relativistic speeds, are subject to an acceleration perpendicular to their velocity. In a synchrotron, electrons are first accelerated to relativistic speeds in a linear accelerator and then a booster ring [Fig. 2.4]. Next, the electrons enter a large storage ring, which, despite its name, is not circular, but rather polygonal, with alternating straight sections connected by bending magnets at the corners. The bending magnets serve to curve the electrons around the corners of the storage ring, generating continuous synchrotron radiation of a broad spectrum that can be monochromated and collimated in an optics hutch before passing to a bending magnet beamline. The alternating straight sections of the storage ring contain either undulator or wiggler insertion devices, which are made up from a periodic array of magnets that induce an oscillation of the electrons, giving very brilliant and intense radiation. Undulators are used to provide a highly collimated, very narrow beam of very bright radiation, of which the energy can be controlled by varying the spacing between the magnets. A wiggler insertion device produces radiation in a wider cone than undulators, spanning a broader spectrum of intense X-rays; wigglers are typically used by beamlines that require very high-energy X-rays.

Diamond Light Source is the UK national synchrotron, which is located south

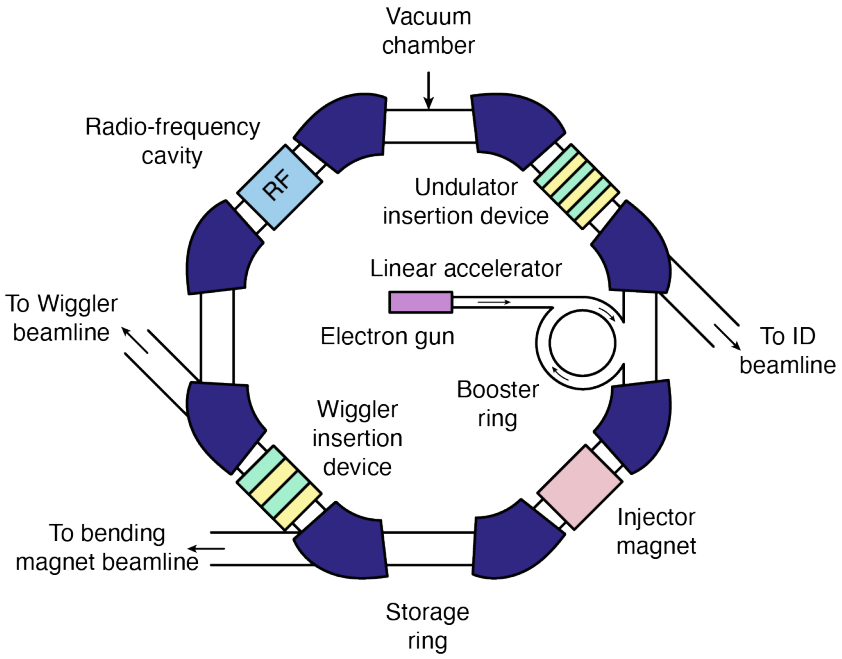


Figure 2.4: A schematic of the main features of a synchrotron.

of Oxford at the Harwell Science and Innovation Campus. The I11 beamline at Diamond Light Source specialises in providing high-resolution powder diffraction with a better signal-to-noise than can be provided by in-house diffractometers; this can be crucial for enabling the detailed refinement of complex structures. The synchrotron PXRD measurements presented in Chapter 4 were collected at the I11 beamline, with the powders measured in capillaries in transmission mode.

2.3.3 X-ray free-electron laser diffraction

Whilst synchrotrons offer an excellent balance between high resolution and good temporal resolution, they do not possess the ultra-fast capabilities required to study *e.g.* crystallisation, nanoparticle formation, or responses to ultra-fast external stimuli. X-ray free-electron laser (XFEL) technologies are unparalleled in terms of the brilliance and temporal resolution they offer. XFELs generate an exceptionally brilliant and coherent X-ray laser beam of high-energy electrons using the process of self-amplified spontaneous emission (SASE).[264] The major components of an XFEL are [Fig. 2.5]: (i) the electron gun and injector, which generate an electron beam and

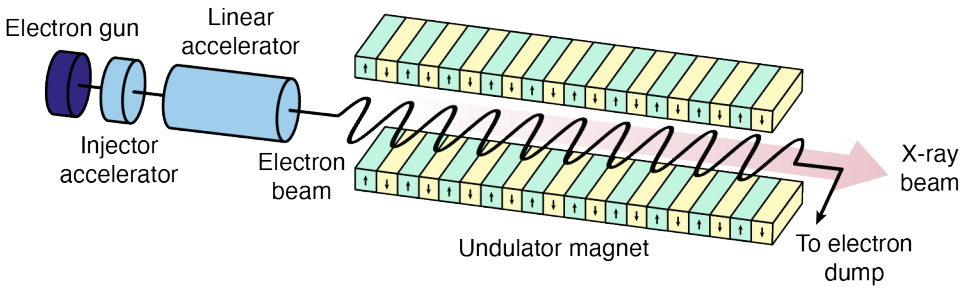


Figure 2.5: A schematic of the main features of an X-ray free-electron laser.

then accelerate the electrons close to relativistic speeds; (ii) the linear accelerator (linac), where the electrons are accelerated further, bringing the electron beam to higher energy; and (iii) the undulator, a periodic array of magnets that cause the electrons to oscillate and emit X-ray radiation.

Chapter 6 details the progress made with developing high-quality ultra-fast total scattering and pair distribution function data at the European X-ray Free-Electron Laser Facility GmbH (EuXFEL) in Hamburg, Germany, and so the following description of the major components of an XFEL are based on the setup and specifications at the EuXFEL. The EuXFEL facility currently delivers soft and hard XFEL radiation to six scientific instruments,[277] providing (up to) 25 keV femtosecond-pulsed X-rays with a high degree of coherence.[278]

The electron gun and injector

The electron beam is generated by using a conventional laser to knock electrons out of a piece of metal ('electron gun'), which are then accelerated to relativistic speeds by cavities ('injector'). The electron gun is designed to produce as narrow beam as possible such that the electrons do not fly apart during the acceleration process. A low emittance—the product of beam width and divergence—is critical for obtaining a tightly focused and intense X-ray beam; this is the purpose of accelerating the electrons to relativistic speeds—bringing the electrons into the relativistic regime overcomes the mutual repulsion between them, thereby preventing the electrons in

the beam from flying apart.

The linear accelerator

After exiting the injector, the electron beam enters a 1.7 km-long linear accelerator ('linac'), which brings the electrons to high energies (11.5, 14, or 16.5 GeV at the EuXFEL[278]). The electrons are accelerated in 768 cavities, called resonators, in which the energy of an oscillating microwave is transferred to the electrons. The linac at the European XFEL makes use of superconducting niobium resonators to make the acceleration process as efficient as possible: any amount of electromagnetic signal that enters the cavity will be transferred directly to the electrons. Additionally, the superconducting resonators deliver a highly focused and uniform electron beam, a prerequisite for a high-quality X-ray laser.

The undulator

After exiting the linear accelerator, the electrons proceed through SASE undulators[279] with horizontal polarisation. The undulators, a periodic array of magnets, force the electrons onto a tight wiggly path—it is this curved path that induces each electron to emit X-ray radiation, which is increasingly amplified. This amplification process results from the interaction of the electric field of the X-ray radiation with the electrons: since the radiation travels faster than the electrons, depending on the relative phase between the electrons and photons, some electrons will be accelerated and others slowed down. As a result, the electrons are gradually organised into bunches (micro bunching). The key property of this process is that all the electrons in a given bunch will emit their radiation together, producing ultra-fast (femtosecond) pulses of intense, hard X-rays that are coherent (waves emitted from different electron bunches interfere constructively). This is the principle of self-amplified spontaneous emission. Since the micro bunching process takes some time, very long undulators are needed; at the EuXFEL, they are more than 100 m long.

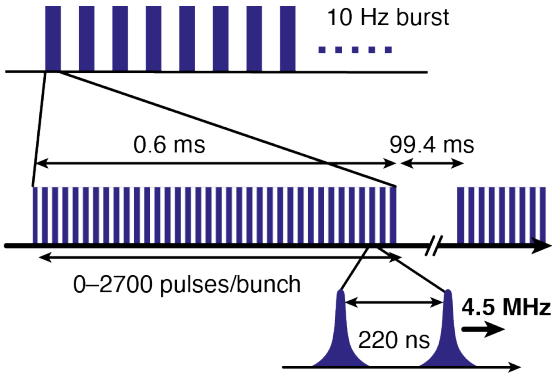


Figure 2.6: An illustration of the bunch pattern produced by the European XFEL.[278] Within an up to 0.6 ms-long train, up to 2700 intense (10^{10-11} photons/pulse) X-ray pulses can be created. The European XFEL can deliver pulses at repetition rates of 4.51, 2.26, or 1.13 MHz, with a pulse spacing of 222, 443 or 886 ns, respectively. Figure adapted from Ref. 278, which is an open-access article distributed under the terms of the Creative Commons Attribution (CC-BY) Licence.

The High Energy Density (HED) beamline

One electron accelerator can supply more than one undulator, so it is possible to tailor the properties of the radiation for different experiment stations. Additionally, the X-ray pulses can be focused, widened, weakened, or filtered using optical elements such as gratings, mirrors, crystals, or slits. The photon energy can be tuned in each beamline by varying the undulator gaps.

The High Energy Density (HED) science instrument at the EuXFEL,[277,280] the beamline at which the data presented in Chapter 6 was collected, is located after the SASE2 undulator, which provides X-ray pulses of ∼25 fs duration with photon energies of 5–25 keV.[278,281] The HED beamline is typically used for experiments that require hard X-rays and a large coverage of reciprocal space. The instrument offers a 10 Hz burst containing an up to 0.6 ms-long train made up from X-ray pulses that are separated by 222 ns, which is equivalent to a rate of $(222\,\text{ns})^{-1} = 4.514\,\text{MHz}$ [Fig. 2.6];[278] thus, the instrument delivers a bright X-ray burst every 100 ms. Given the MHz capability, the evolution of sub-millisecond dynamics can be measured with a single X-ray burst.

2.3.4 Refinement of diffraction data

A crystal structure solution from diffraction data is typically obtained using computer software; throughout this thesis, the TOPAS-Academic software[282] has been used. Refinement of XRD data involves refining the parameters of a starting model gradually and iteratively by minimising the weighted sum of the squared differences between the observed and calculated intensities. A useful metric for the goodness-of-fit can be the weighted R-factor

$$R_{\mathrm{wp}} = \sqrt{\frac{\sum_i w_i (y_i^{\mathrm{obs}} - y_i^{\mathrm{calc}})^2}{\sum_i w_i (y_i^{\mathrm{obs}})^2}}, \tag{2.16}$$

where w_i is a weighting factor, and y_i^{obs} and y_i^{calc} are the experimentally-observed and calculated intensities at position i, respectively. Whilst a lower R_{wp} indicates a better fit to the data, a low R_{wp} does not necessarily indicate a physically sensible solution, so the result from a refinement requires careful evaluation.[283]

Pawley refinement

A Pawley refinement[284] can be useful for determining the crystallographic unit cell and space group of a structure based purely on its XRD pattern, *i.e.* it does not require an explicit structural model. The peak shapes in the diffraction pattern are typically modelled using a modified Thompson-Cox-Hasting pseudo-Voigt (TCHZ) peak shape function,[285] and the peak intensities are treated as freely adjustable fitting parameters, enabling the accurate refinement of the unit cell parameters. A first guess of the unit cell parameters and a possible space group is given, which generates the allowed hkl reflections and their positions in 2θ using the instrumental parameters provided (*e.g.* X-ray wavelength, axial divergence of the incident/diffracted beams). A background function is usually modelled with a Chebyshev polynomial, which will absorb any diffuse scattering arising from *e.g.* the air, sample holder, etc.

Pawley refinement can be valuable for validating the space group of an unknown structure, tracking the change in the unit cell parameters as function of an external stimulus, or when seeking to do further analysis, such as a Rietveld refinement, where it might be useful to fix the unit cell and peak shape parameters to the values determined in the Pawley refinement.

Rietveld refinement

A Rietveld refinement can be used in cases where a starting structural model is available to determine the structure from powder diffraction data.[286] A Rietveld refinement uses quantitative information about the contents of the unit cell—including atom coordinates, relative occupancy, and the atomic displacement parameters—to determine reflection intensities.[286] An issue to be aware of when fitting the intensities using multiple refinable parameters is that they can be correlated, so it is important to keep an eye on the correlation in uncertainties between the different parameters. When achieving a reliable fit is difficult due to variable peak widths, this can be indicative of effects intrinsic to the sample, *e.g.* anisotropic strain or a pattern of defects. Whilst implementing *e.g.* Stephens' model for anisotropic peak broadening[287] can improve the fit, careful consideration should always be given when adding extra refinable parameters; obtaining a physically sensible model—in terms of *e.g.* atomic occupancy, bond lengths, thermal displacements, etc.—is just as, if not more, important than achieving a better fit to data.

2.3.5 Distortion-mode analysis

There can be a number of challenges associated with refining models against XRD data using lattice parameters and atomic positions, such as capturing phase changes in the correct space group. An effective way to navigate these challenges can be to use group theoretical analysis, such as through the software package ISODISTORT,[288,289] which generates symmetry-adapted strain and atomic displacement

patterns in terms of the irreducible representations (irreps) of the parent (aristotype) structure. ISODISTORT can be implemented in TOPAS to perform a distortion-mode refinement where the magnitude of the strain and displacement irreps are refined rather than the lattice parameters and atomic positions. Whilst a distortion-mode refinement does not reduce the number of refinable parameters, it orthogonalises them, and allows orthogonal structural distortions to be encapsulated as one parameter that can then be used to track changes with temperature, pressure, or chemical composition.

Briefly, irreps take the form $\mathrm{K}_n^{+/-}$, where K denotes the k point in the aristotype Brillouin zone, the $+/-$ describes whether inversion symmetry is retained/broken at the cell origin, and n is a tabulation/enumeration number. As such, any distortion to the parent structure can be described by an irrep, which can facilitate the comparison to other materials with the same space group and aristotype, or aid in tracking changes during a phase transition.

Distortion-mode analysis will be used in Chapter 5 to investigate the coupling between different degrees of freedom in the perovskites, $\mathrm{LaGa}_{1-x}\mathrm{Mn}_x\mathrm{O}_3$ and $\mathrm{La}_{0.5}\mathrm{Ca}_{0.5}\mathrm{MnO}_3$.

2.4 Total scattering

Traditional crystallographic techniques that rely on Bragg scattering analysis alone are often inadequate for local structure analysis of systems that are disordered on average but contain short-range order or *vice versa*. As discussed in the introduction (Section 1.3.3), diffraction patterns can consist of two parts: sharp Bragg peaks, arising when there is long-range translational periodicity in the structure, and diffuse scattering, arising when there is disorder in the structure. Diffuse scattering is often treated as part of the background as its intensity can be orders of magnitude weaker than that of Bragg scattering. However, diffuse scattering can contain vital information as to a material's local structure, which can be critical when seeking

to understand the properties of a material. In such cases, total scattering analysis methods are often employed, which consider both Bragg and diffuse scattering; this thesis uses both conventional Bragg PXRD refinements and total scattering (Chapters 3, 4, and 6) to probe the local structure of Prussian blue analogues.

2.4.1 Theory of powder total scattering

Analysis of total scattering data is typically done in real space: the Fourier transform of the normalised total scattering data yields the pair distribution function (PDF),[175,186,187] a histogram of interatomic distances weighted by the corresponding atomic concentrations and their scattering strengths. Many different definitions and functions are often employed amongst the different communities using total scattering analysis, which often leads to confusion.[185] Much of this confusion arises from different subject areas using different formalisms to emphasise particular physical features of the PDF whilst using the same or similar symbols for different definitions. The formulations will also be slightly different for X-ray and neutron total scattering due to the Q-dependence of the X-ray atomic form factor that gives more complex correlation functions in the case of X-rays.[290–292] The following discussion aims to clarify the nomenclature and definitions used in this thesis and follows that of Ref. 185, beginning with functions for neutron scattering and ending with the modification of these expressions to take into account the X-ray weighted scattering functions.

Neutron total scattering nomenclature

The total scattering structure factor, $F(Q)$, differs from that used for Bragg scattering (F_{hkl} defined in Eq. 2.13 in Section 2.2); it represents an intensity, is radially averaged across reciprocal space, is real-valued, and is no longer dependent on hkl values. The total scattering structure factor can be derived from Eq. 2.7 via *e.g.* the Debye equation.[293,294] Because $I(Q) \propto |F(Q)|^2$, the scattering intensity carries

information about the relative distances between atoms; if diffuse scattering is ignored, then the (Bragg) scattering is sensitive only to the distances between average positions, but including the diffuse scattering allows sensitivity to the average distance between instantaneous positions. The *total scattering* structure factor is given by

$$F(Q) = \rho_0 \int_0^\infty 4\pi r^2 G(r) \frac{\sin Qr}{Qr} \, \mathrm{d}r, \tag{2.17}$$

where ρ_0 is the average number density of the material, and $G(r)$ is the total radial distribution function, defined as

$$G(r) = \sum_{i,j=1}^{n} c_i c_j \bar{b}_i \bar{b}_j [g_{ij}(r) - 1]. \tag{2.18}$$

Here, $\bar{b}_i$ is the coherent bound neutron scattering length of species i, averaged over the different isotopes and nuclear spin states in the material, c_i is the corresponding fraction of species i in the material, and $g_{ij}(r)$ is the partial radial distribution function between all pairs of atoms i and j, defined as

$$g_{ij}(r) = \frac{n_{ij}(r)}{4\pi r^2 \, \mathrm{d}r \, \rho_j}. \tag{2.19}$$

Here, $n_{ij}(r)$ is the number of particles of type j within a radius between r and $r + \mathrm{d}r$ from a particle of type i, and $\rho_j = c_j \rho_0$. $G(r)$ is the Fourier transform of the total scattering function $F(Q)$ [Eq. 2.17]:

$$G(r) = \frac{1}{(2\pi)^3 \rho_0} \int_0^\infty 4\pi Q^2 F(Q) \frac{\sin Qr}{Qr} \, \mathrm{d}Q. \tag{2.20}$$

Equation 2.20 is one amongst a number of normalisations of $G(r)$, each implemented slightly differently in various software. Each formulation has different limiting values, so it is important to be aware of the different definitions when performing normalisations. One additional definition, often used in this thesis, is particularly

useful for highlighting structural features at high values of r:

$$D(r) = 4\pi r \rho_0 G(r). \tag{2.21}$$

X-ray total scattering nomenclature

The PDF data given in this thesis (Chapters 3, 4, and 6) are from X-ray total scattering experiments. Obtaining X-ray total-scattering correlation functions is not as straightforward as for neutron scattering, since the Q-dependent X-ray scattering factors modify some of the function definitions non-trivially.[185] For this reason, a simple set of equations is developed here, following Ref. 185 very closely. The superscript X is used to denote functions for X-rays, whilst the functions that do not have this superscript are the same as those already defined.

Starting from Eq. 2.17, *i.e.*

$$F(Q) = \rho_0 \int_0^\infty 4\pi r^2 G(r) \frac{\sin Qr}{Qr} \, \mathrm{d}r,$$

and replacing $G(r)$ with the definition given in Eq. 2.18,

$$G(r) = \sum_{i,j=1}^{n} c_i c_j \bar{b}_i \bar{b}_j [g_{ij}(r) - 1],$$

gives the following expression for $F(Q)$:

$$F(Q) = \rho_0 \sum_{i,j=1}^{n} c_i c_j \bar{b}_i \bar{b}_j \int_0^\infty 4\pi r^2 [g_{ij}(r) - 1] \frac{\sin Qr}{Qr} \, \mathrm{d}r. \tag{2.22}$$

The extension to X-ray total scattering then begins by exchanging the coherent bound neutron scattering lengths, $\bar{b}_i$ and $\bar{b}_j$, for the Q-dependent X-ray scattering factors, $f_i(Q)$ and $f_j(Q)$. $F^X(Q)$, the X-ray weighted total-scattering structure

factor, may then be written as:

$$F^X(Q) = \rho_0 \sum_{i=1}^{n} c_i c_j f_{ij}(Q) \int_0^\infty 4\pi r^2 [g_{ij}(r) - 1] \frac{\sin Qr}{Qr} \, \mathrm{d}r, \tag{2.23}$$

where

$$f_{ij}(Q) = f_i(Q) f_j(Q) \Bigg/ \left[\sum_{i=1}^{n} c_i f_i(Q) \right]^2 . \tag{2.24}$$

Noting that

$$G^X(r) = \sum_{i,j=1}^{n} c_i c_j f_{ij}(Q) [g_{ij}(r) - 1] \tag{2.25}$$

gives the following expression for $F^X(Q)$:

$$F^X(Q) = \rho_0 \int_0^\infty 4\pi r^2 G^X(r) \frac{\sin Qr}{Qr} \, \mathrm{d}r. \tag{2.26}$$

The Fourier transform of $F^X(Q)$—$G^X(r)$—may be defined as [following Eq. 2.20]

$$G^X(r) = \frac{1}{(2\pi)^3 \rho_0} \int_0^\infty 4\pi Q^2 F^X(Q) \frac{\sin Qr}{Qr} \, \mathrm{d}Q. \tag{2.27}$$

So, $F^X(Q)$ and $G^X(r)$ for X-rays are related in an identical manner as $F(Q)$ and $G(r)$ are related for neutrons, *i.e.* $F^X(Q)$ and $G^X(r)$ are related by

$$\begin{aligned} F^X(Q) &= \rho_0 \int_0^\infty 4\pi r^2 G^X(r) \frac{\sin Qr}{Qr} \, \mathrm{d}r \\ G^X(r) &= \frac{1}{(2\pi)^3 \rho_0} \int_0^\infty 4\pi Q^2 F^X(Q) \frac{\sin Qr}{Qr} \, \mathrm{d}Q, \end{aligned} \tag{2.28}$$

whilst $F(Q)$ and $G(r)$ are related by

$$\begin{aligned} F(Q) &= \rho_0 \int_0^\infty 4\pi r^2 G(r) \frac{\sin Qr}{Qr} \, \mathrm{d}r \\ G(r) &= \frac{1}{(2\pi)^3 \rho_0} \int_0^\infty 4\pi Q^2 F(Q) \frac{\sin Qr}{Qr} \, \mathrm{d}Q. \end{aligned} \tag{2.29}$$

The presence of $f_{ij}(Q)$ in $F^X(Q)$ [Eq. 2.23] has the effect that $G^X(r)$ will have a very different behaviour from that of neutron weighted $G(r)$; hence, it is not always helpful to consider Eq. 2.23. To understand $G^X(r)$, $g_{ij}^X(r)$ can be defined such that

$$G^X(r) = \sum_{i,j=1}^{n} c_i c_j g_{ij}^X(r), \tag{2.30}$$

where $rg_{ij}^X(r)$ is the convolution of $r[g_{ij}(r) - 1]$ and $j_{ij}(r)$,

$$g_{ij}^X = \frac{1}{r} \int_{-\infty}^{\infty} y[g_{ij}(y) - 1] j_{ij}(r - y)\, \mathrm{d}y, \tag{2.31}$$

and $j_{ij}(r)$ is the Fourier transform of $f_{ij}(Q)$,

$$j_{ij}(r) = \frac{1}{\pi} \int_0^{\infty} f_{ij}(Q) \cos Qr\, \mathrm{d}Q. \tag{2.32}$$

To simplify the convolution of Eq. 2.32, the scattering factors, $f_i(Q)$ are often approximated as $f_i(Q) = K_i f_e(Q)$. Here, K_i is the effective number of electrons of species i, which is approximately equal to the atomic number Z_i, and $f_e(Q)$ is an average scattering factor per electron of the material, given by

$$f_e(Q) = \sum_{i=1}^{n} c_i f_i(Q) \Bigg/ \sum_{i=1}^{n} c_i Z_i \tag{2.33}$$

Then, with

$$f_{ij}(Q) = K_i K_j \Bigg/ \left(\sum_{i=1}^{n} c_i K_i \right)^2, \tag{2.34}$$

$G^X(r)$ is now proportional to $[g_{ij}(r) - 1]$,

$$G^X(r) = \sum_{i,j=1}^{n} c_i c_j \frac{K_i K_j}{\left(\sum_{i=1}^{n} c_i K_i\right)^2} [g_{ij}(r) - 1]. \tag{2.35}$$

Finally, noting Eq. 2.34, this then gives Eq. 2.25 given earlier:

$$G^X(r) = \sum_{i,j=1}^{n} c_i c_j f_{ij}(Q)[g_{ij}(r) - 1].$$

2.4.2 Experimental considerations

Total scattering and conventional powder diffraction measurements are typically made using similar experimental setups. However, there are a number of additional considerations that need to be made when collecting total scattering data, which stem from the fact that the PDF is the Fourier transform of the reciprocal-space diffraction data. Eq. 2.20 (for neutrons) and Eq. 2.27 (for X-rays) contain an integral over infinite Q; however, in practice, data is only collected over a finite region of reciprocal space (or Q space). The relationship between the value of Q, the scattering angle, θ, and the wavelength of the incident radiation, λ, is given by

$$Q = \frac{4\pi}{\lambda} \sin\theta. \tag{2.36}$$

Returning back to Bragg's law ($\lambda = 2d\sin\theta$), it can be seen then that the real-space resolution is given by $\Delta r = \frac{2\pi}{Q_{\max}}$, and hence measuring over a wider region in reciprocal space will give a PDF with greater real-space resolution.[175,177,186] From Eq. 2.36, it is clear that (i) short wavelength radiation and (ii) detectors capable of collecting data over a wide range of angles are needed to collect data to high values of Q. When collecting total scattering data, it is also important to try to minimise background scattering in order to aid with more accurate normalisation and measurement of high-quality data at higher Q values.

Standard in-house diffractometers that use Cu ($\lambda = 1.542\,\text{Å}$) X-ray sources can measure to a $Q_{\max} = \frac{4\pi}{\lambda} = 8.15\,\text{Å}^{-1}$, which gives a real-space resolution ($\Delta r = \frac{2\pi}{Q_{\max}} \sim 0.75\,\text{Å}$) that is usually insufficient to resolve most structural features of interest. Hence, shorter-wavelength radiation is required; usually synchrotrons (*e.g.*

the high-energy X-ray PDF (I15-1) beamline at Diamond Light Source, which can measure up to $Q_{\max} \sim 40\,\text{Å}^{-1}$) and some modern in-house Mo ($\lambda = 0.709\,\text{Å}$, $Q_{\max} = 17.72\,\text{Å}^{-1}$) and Ag ($\lambda = 0.559\,\text{Å}$, $Q_{\max} = 22.48\,\text{Å}^{-1}$) X-ray sources are capable of achieving $Q_{\max}$ values that give sufficient real-space resolution. However, as noted previously (Eq. 2.14), X-ray intensity decreases with increasing θ/Q; for X-rays, this intensity fall off becomes significant at $Q \sim 25\,\text{Å}^{-1}$, meaning data above this value are not generally used, irrespective of $Q_{\max}$. Neutron total scattering instruments have the advantage that they are not affected by any fall off in scattering power with increasing Q, whilst also providing the widest coverage of reciprocal space ($Q_{\max} \geq 50\,\text{Å}^{-1}$).[177]

Another important factor to consider can be the time it takes to collect the measurements, especially when seeking to perform time-resolved studies. Synchrotron beamlines, with higher flux and specially-designed sample environments, generally have much faster collection times (∼seconds–minutes) than in-house instruments (∼days). Whilst some time-resolved studies can be performed using dedicated synchrotron beamlines,[263] synchrotrons do not possess the ultra-fast capabilities required to capture structural changes that occur on the much faster timescales of atomic motion. Neutron total scattering measurements typically require even longer collection times (∼hours). Current XFEL setups, in comparison, provide femtosecond-pulsed X-ray beams, enabling *e.g.* pump–probe experiments and femtosecond serial crystallography to be performed.[295–297] However, current XFEL setups suffer from a low coverage of reciprocal space and hence low-resolution PDFs; the highest $Q_{\max}$ recorded for the difference structure factor, $\Delta S(Q)$, is $12.6\,\text{Å}^{-1}$, which corresponds to a real-space resolution of $\sim 0.50\,\text{Å}$.[265] Whilst perhaps adequate for more simple structural transitions, such real-space resolutions are insufficient for many advanced structural studies. To make full use of the high temporal resolution of XFELs for total scattering studies, their real-space resolution must be improved;

Source	Q_{max} (Å^{-1}) (r-resolution~2π/Q_{max})	Timescale for measurement	Year method started
Cu/Mo X-ray	~ 16	~ days	1930s
Neutron	~ 40	~ hours	1990s
Synchrotron X-ray	~ 26	~ seconds	2000s
XFELs	~ 8	~ 100fs	2010s

Figure 2.7: An overview of the $Q_{\max}$ values achievable and acquisition times associated with current total scattering setups: standard laboratory, neutron spallation, synchrotron X-ray, and X-ray free-electron laser (XFEL) setups.

this is the focus of Chapter 6. A comparison of $Q_{\max}$ and the timescale for measurements for the currently established total scattering setups is given in [Fig. 2.7].

2.5 Lattice dynamics

2.5.1 Theory

Vibrational motion in crystals

Lattice dynamics is the study of atomic vibrations in a crystal.[298] Due to thermal excitations and zero-point motion, atoms in solids are constantly vibrating about their equilibrium position[268,299]—the time-averaged position as found by traditional crystallographic methods. Whilst conventional crystallography accounts for thermal motion in terms of the Debye–Waller factors,[300,301] which carry information about the magnitude of vibrational motion for individual atoms, they do not contain information about the relative (correlated) displacements of atoms. Lattice dynamics is implicated in various material properties, such as thermodynamics, superconductivity, phase transitions, thermal conductivity, and thermal expansion (the last of which is particularly relevant to Chapter 3). Thus, it is necessary to have an understanding of the lattice dynamics of a system in order to gain a more complete picture.

The atoms in a crystal can be thought of as three-dimensional (3D) oscillators, with their atomic motion described by harmonic travelling waves. As for molecular vibrations, these waves have a discrete energy, with the fundamental quantum of a wave known as a phonon. Each wave can be characterised by its wavelength, λ, angular frequency, ω, amplitude, and direction of travel. Since wavelengths can range from infinity to that of interatomic spacings, it is easier to use wave vector, $\mathbf{k}$, the spatial periodicity of the vibration. The wave vector, $\mathbf{k}$, is defined as the vector parallel to the direction of propagation of the wave, and normalised such that $|\mathbf{k}| = \frac{2\pi}{\lambda}$. In the general case, a wave travelling through a crystal will displace an atom κ by

$$\mathbf{u}_\kappa(\mathbf{r}_\kappa, t) = \sum_{j\mathbf{k}} \tilde{\mathbf{u}}_\kappa \exp[\mathrm{i}(\mathbf{k}\cdot\mathbf{r}_\kappa - \omega_j(\mathbf{k})t)], \tag{2.37}$$

where $\tilde{\mathbf{u}}_\kappa$ is the amplitude of a given mode and its specific effect on atom κ, $\omega_j(\mathbf{k})$, is the angular frequency of mode j, and $\mathbf{r}_\kappa$ is the position of atom κ. The summation is over all modes, j, over all wave vectors, $\mathbf{k}$. Due to the periodic nature of $\mathbf{k}$, waves that differ by a reciprocal lattice vector will give identical atomic displacements. Hence, all unique waves can be contained within a single unit cell in reciprocal space—the first Brillouin zone—with the Γ-point ($\mathbf{k} = (0,0,0)$) at the origin. Eq. 2.37 shows that the atomic displacements in a crystal are the superposition of all the thermally accessible phonon modes weighted by their population factor, hence, the displacements of atoms in a crystal are collective and complex. With a few simplifying approximations, an exact, quantitative framework of phonon modes can be derived, and is explored next.

Phonon dispersion curves

The theory of lattice dynamics aims to characterise the collective and complex atomic motions in a crystal and hence how the phonon frequencies, ω, vary as a function of the wave vector, $\mathbf{k}$. For simplicity, it is instructive to begin with a one-dimensional (1D) model of a crystal containing one type of atom in its unit

cell [Fig. 2.8(a)]. Within the harmonic approximation, the energy of species n in a monatomic chain of N atoms of mass m connected by simple harmonic springs of stiffness J is given by

$$E_n = \frac{1}{2}J(u_{n+1} - u_n)^2 + \frac{1}{2}J(u_n - u_{n-1})^2, \tag{2.38}$$

where u_n is the instantaneous displacement of atom n from its equilibrium position. This representation treats bonds as simple harmonic springs, with each term in Eq. 2.38 giving the energy required to stretch/compress one spring. The force is given by the positional derivative of Eq. 2.38 and by assuming simple harmonic motion, the dependency of ω on k, the *dispersion relation*, can be derived as

$$\omega(k) = \sqrt{\frac{4J}{m}}\left|\sin\frac{ka}{2}\right|, \tag{2.39}$$

where a is the unit cell length. A phonon dispersion *curve* is a plot of ω as a function of k (a scalar quantity in 1D) [Fig. 2.8(b)]. Due to the periodicity of the underlying lattice, the phonon dispersion curve is a periodic function, with all the unique information contained within $-\frac{\pi}{a} < k < \frac{\pi}{a}$: the first Brillouin zone. Since a monatomic 1D chain only contains one type of atom with one degree of freedom, its phonon dispersion curve only contains a single vibrational mode. As can be seen from Eq. 2.39, $\omega \to 0$ as $k \to 0$, which is reflective of the vanishing vibrational energy cost of a simple translation of a chain of atoms in a crystal [Fig. 2.8(c)]. By contrast, at the boundary of the Brillouin zone, the vibrational energy is highest as the wavelength reaches its maximum. These simple considerations are applicable to the phonon dispersion curves of more complicated systems with more dimensions and/or more atoms per unit cell, but this will add complexity to the appearance of their phonon dispersion curves.

In multiatomic crystals [Fig. 2.9(a)], distinct neighbouring atoms within a unit cell may displace in phase or out of phase [Fig. 2.9(c)]; if atoms move in phase,

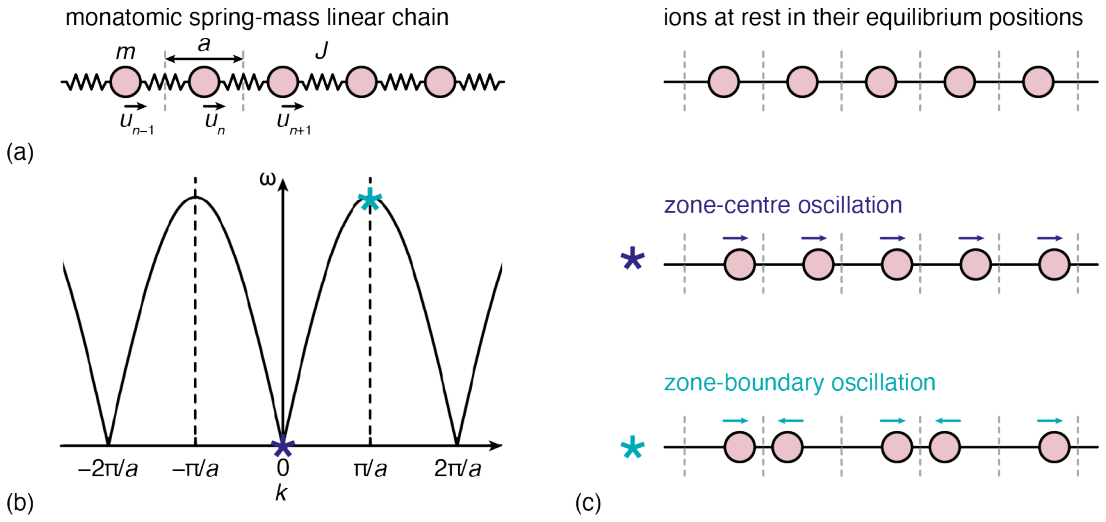


Figure 2.8: (a) A one-dimensional monatomic chain model of a crystal, with atoms of mass m connected by springs of force constant J. The unit cell length is given by a, and the displacement of an atom from its equilibrium position in unit cell n is given by u_n. (b) A schematic phonon dispersion curve of a monatomic one-dimensional chain of atoms with one degree of freedom. (c) Illustrations of the atomic motion of a one-dimensional monatomic chain of atoms in the limit of $k \to 0$ (zone-centre oscillation) and at $k = \pi/a$ (zone-boundary oscillation).

they are referred to as acoustic modes, and if atoms move out of phase, they are referred to as optic modes. The frequencies of acoustic modes tend to zero as $\mathbf{k} \to 0$ [Fig. 2.9(b)], whereas optic modes have non-zero frequencies, even at the Γ-point. At the zone boundary, the terms optic and acoustic modes are no longer meaningful as the distinction between them is only valid in the limit of small values of $\mathbf{k}$.

Extending this simple model to 3D increases the number of degrees of freedom for the atoms and consequently the number of branches in the phonon dispersion curve. A 3D crystal with N distinct atoms in the primitive unit cell will always have $3N$ branches in its phonon dispersion curve—3 acoustic and $3N - 3$ optic—though certain modes may be degenerate along some high-symmetry directions in reciprocal space. Of the three acoustic modes, two are *transverse* acoustic modes (TA) and one is the *longitudinal* acoustic mode (LA). For a given $\mathbf{k}$-vector, the atoms can displace either parallel or perpendicular to the direction of the wave vector; these two cases are referred to as longitudinal and transverse modes, respectively. Whilst for a given

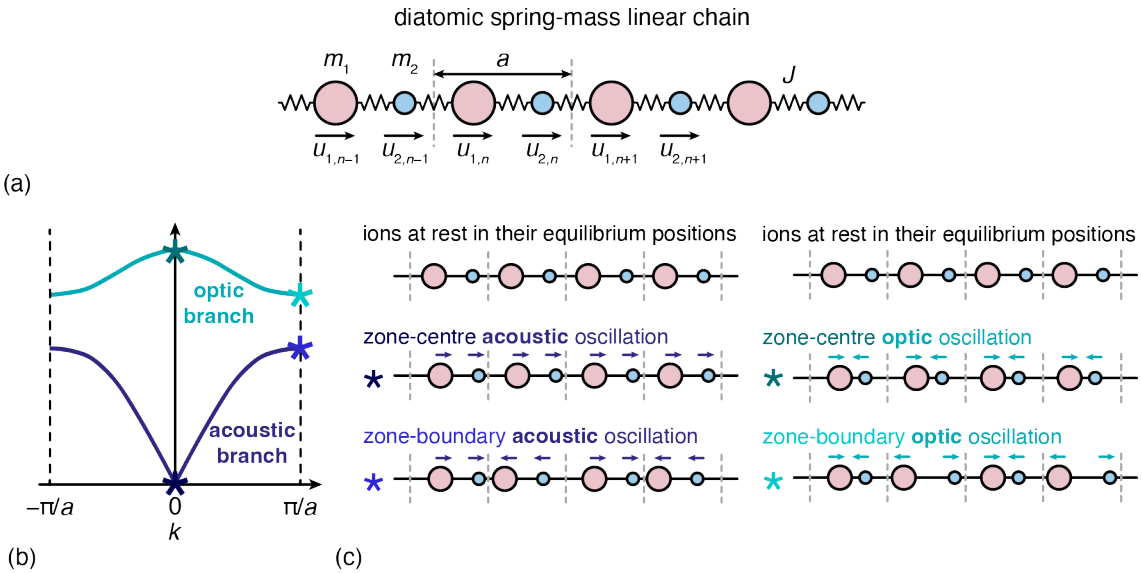


Figure 2.9: (a) A one-dimensional diatomic chain model of a crystal, with atoms of different mass m_i connected by springs of force constant J. The unit cell length is given by a, and the displacement of atom i in unit cell n is given by $u_{i,n}$. (b) A schematic phonon dispersion curve of a diatomic linear chain, with the acoustic mode shown in blue and optic mode shown in green. (c) Illustrations of the atomic motions of the acoustic and optic modes in the limit of $k \to 0$ (zone-centre oscillation) and at $k = \pi/a$ (zone-boundary oscillation).

direction of **k** there are two transverse modes, they can be degenerate along certain paths as a result of the symmetry of the crystal. The TA modes are often lower in energy than the LA modes as there is less bond-stretching associated with their atomic displacements. Optic modes can also be separated into longitudinal optic (LO) and transverse optic (TO) modes. In crystals with polar bonds (*e.g.* NaCl), LO and TO modes are split near the Γ-point and cannot be modelled with short-range force-constant parameters; to adequately model the LO–TO splitting in these systems, non-analytical corrections are often required.

As an illustration of the concepts introduced above, the phonon dispersion curve for NaCl as measured by inelastic neutron scattering (INS) is shown in Fig. 2.10(c).[302] NaCl adopts the rocksalt structure with $Fm\bar{3}m$ symmetry. As there are two different types of atoms in the primitive unit cell setting of NaCl, the phonon dispersion curve features six branches, three acoustic and three optic. The acoustic and optic branches are easily identified at the Γ-point, since for acoustic modes,

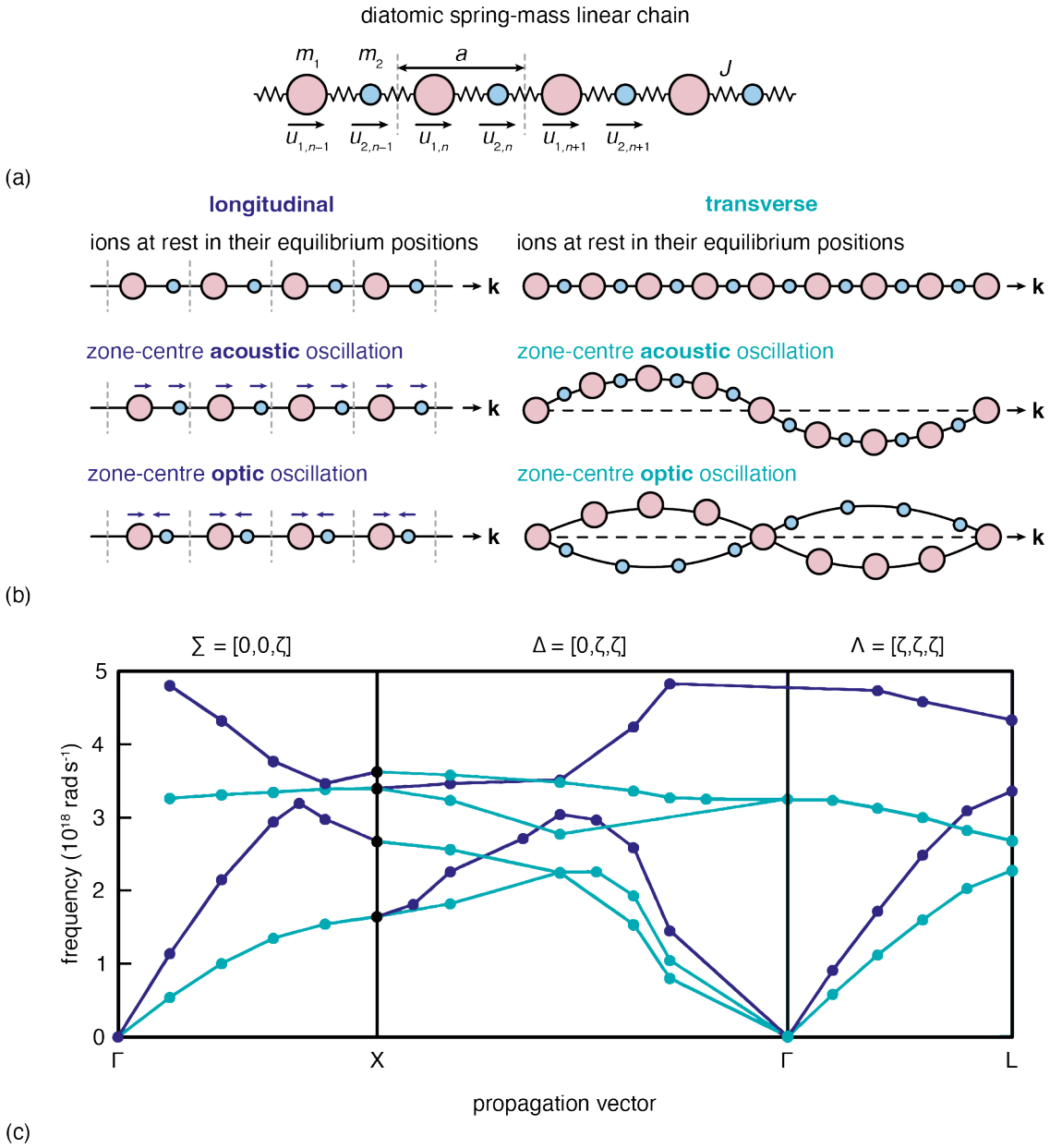


Figure 2.10: (a) A three-dimensional diatomic chain model of a crystal, with atoms of different mass m_i connected by springs of force constant J. The unit cell length is given by a, and the displacement of atom i in unit cell n is given by $u_{i,n}$. (b) Illustrations of the longitudinal acoustic and optic modes as well as transverse acoustic and optic modes for a diatomic linear chain in the limit $k \to 0$ (zone-centre oscillation). (c) The phonon dispersion curves of NaCl, as measured by inelastic neutron scattering (INS). The transverse modes are highlighted in green and the longitudinal modes are highlighted in blue. Data reproduced from Ref. 302.

$\omega \to 0$ as $\mathbf{k} \to 0$, whilst for optic modes, $\omega \neq 0$. The possibility for modes to be degenerate can also be seen; both the TA and TO branches are doubly degenerate along Γ–L, but split along the less symmetric Δ path. This NaCl example illustrates

how even relatively simple systems can show relatively complex phonon dispersion behaviour.

2.5.2 Anharmonicity and (negative) thermal expansion

Anharmonic effects

The discussion so far has been presented within the harmonic approximation, where the Taylor expansion of the lattice energy is terminated at the second-order terms (Eq. 2.38), neglecting anharmonic higher-order terms. The harmonic approximation can be invoked to explain many features of lattice dynamics and can be solved exactly. However, since harmonic phonon mode frequencies are neither temperature- nor pressure-dependent, there are phonon-mediated phenomena that cannot be captured by the harmonic model, *e.g.* thermal expansion, thermal conductivity, and phase transitions. To allow properties such as thermal expansion to be captured within the harmonic model framework, anharmonic terms can be added as perturbations to the harmonic model, provided atomic displacements are not too large. As phonon-mediated (negative) thermal expansion is relevant to Chapter 3, an outline is given here.

Thermal expansion

Thermal expansion usually refers to the expansion of a crystal caused by thermally-induced strain. The isobaric coefficient of volume thermal expansion, α_V, is defined as

$$\alpha_V = \frac{1}{V}\left(\frac{\partial V}{\partial T}\right)_p, \tag{2.40}$$

where V is the volume of the crystal, T is the temperature, and p is the pressure.[303] α_V is the sum of the linear coefficients of thermal expansion of the three principal

axes, α_{11}, α_{22}, and α_{33}, each defined as

$$\alpha_{ii} = \frac{1}{l_{ii}} \left(\frac{\partial l_{ii}}{\partial T} \right)_p , \tag{2.41}$$

where the length of the principal axis ii is given by l_{ii}. For cubic materials, $\alpha_{11} = \alpha_{22} = \alpha_{33}$, hence $\alpha_V = 3 \cdot \alpha_{11}$.

The volume dependence of the phonon frequencies is the driving force for thermal expansion, and is commonly described by the quasi-harmonic approximation; within the quasi-harmonic approximation, it assumed that interatomic force constants are volume-dependent such that phonon frequencies will be affected by changes in the volume of the crystal.[268,299,304] The driving force can be characterised by the mode Grüneisen parameter,[304] defined for a given mode j at wave-vector $\mathbf{k}$ as

$$\gamma(\mathbf{k}, j) = -\frac{\partial \ln \omega(\mathbf{k}, j)}{\partial \ln V}. \tag{2.42}$$

This definition captures the dependence of the phonon frequency ω on changes in the volume of the crystal V, such that at a given temperature, the energy required to expand or contract the lattice is balanced by the vibrational entropy change accompanying the change in phonon frequencies. Modes with $\gamma > 0$ drive positive thermal expansion (PTE), whilst modes with $\gamma < 0$ drive negative thermal expansion (NTE). In the case of NTE, the phonon frequencies decrease as the volume decreases, and this is why the vibrational entropy of the material can increase with a reduction in its volume.

The Grüneisen formalism is invaluable for its ability to directly link microscopic lattice dynamics—specifically the phonon modes of the system—with the macroscopic property of thermal expansion. As a crystal contains a collective ensemble of phonons, the individual mode Grüneisen parameters can be combined to give a

temperature-dependent bulk Grüneisen parameter:

$$\bar{\gamma}(T) = \frac{\sum_j \gamma_j c_{V,j}(T)}{\sum_j c_{V,j}(T)}, \tag{2.43}$$

where $c_{V,j}(T)$ is the mode-specific heat capacity at constant volume. From this, the volume coefficient of thermal expansion α_V can be rewritten as

$$\alpha_V(T) = \frac{1}{V}\left(\frac{\partial V}{\partial T}\right)_p = \frac{1}{K_T V}\sum_j \gamma_j c_{V,j}(T), \tag{2.44}$$

where K_T is the bulk isothermal modulus, and the summation is over all modes j.[305] The magnitude of thermal expansion of a material depends on the type of interatomic or intermolecular forces of the material. Whilst dense inorganic materials with strong covalent and metallic bonds typically show relatively modest coefficients of thermal expansion,[303,306] molecular crystals with weaker intermolecular forces may exhibit much larger coefficients of thermal expansion.[307]

Negative thermal expansion and the RUM model

For phonon-mediated NTE to occur, the population of NTE modes must outweigh the population of PTE modes over the whole of reciprocal space for a given T. The local picture commonly used to explain the occurrence of phonon-mediated NTE is the tension effect [Fig. 2.11(a)];[209,224,308,309] for materials with linear linkages of atoms and stiff bonds, the transverse vibrations of bridged atoms lead to a contraction between the metal centres that outweighs the PTE of bonds. In framework materials, the Rigid Unit Mode (RUM) model is used to describe how the low-energy transverse vibrational modes are correlated throughout the structure, and has proven successful for a number of different systems.[94,310,311]

RUMs are phonon modes that propagate without deformation of the coordination polyhedra of a structure, *i.e.* the metal coordination geometries and bond lengths are preserved. RUMs use collective and cooperative rotations and translations of

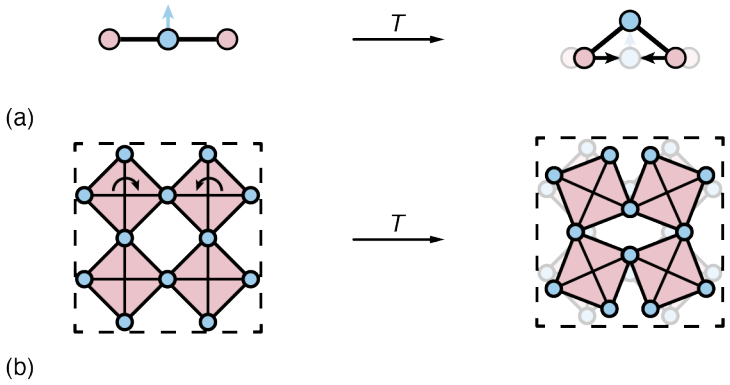


Figure 2.11: The local tension effect mechanism. (a) The thermal population of transverse vibrational modes can lead to a contraction between the metal centres and hence negative thermal expansion when the joining bonds are stiff.[209] (b) In framework materials, *e.g.* perovskites and PBAs, the Rigid Unit Mode (RUM) model is used to describe how these transverse vibrations propagate throughout the structure; the local tension effect mechanism can be propagated through *e.g.* cooperative rotations of rigid structural polyhedra.

the structural polyhedra to propagate the transverse vibrations of the local tension effect mechanism [Fig. 2.11(b)]. The RUM model relies on the fact that the energy associated with distorting structural polyhedra is usually much larger than flexing the linkage of two neighbouring polyhedra. Thus, RUMs are generally low in energy and often have very large and negative Grüneisen parameters.[312,313]

In some cases, RUMs are unable to drive NTE on their own.[314,315] In such cases, quasi-RUMs (qRUMs), which lie close to RUMs in reciprocal space, can provide the volume of phonons required to drive macroscopic NTE.[316,317] qRUMs are cooperative translations and/or rotations of *minimally distorted* coordination polyhedra; it is this minimal distortion that allows qRUMs to maintain a low frequency whilst existing over a broader range of wave-vectors.[317,318] If the polyhedra were too stiff, the frequency of the qRUM phonons would be too high to be (sufficiently) populated, and there would be no NTE. The importance of polyhedral flexibility for NTE, especially in systems with a restricted range of RUMs (*e.g.* the perovskites, which only have lines of RUMs), is illustrated by ScF_3 and $SrTiO_3$: the F–Sc–F octahedral bond angle is flexible enough to allow a large number of low-frequency qRUMs, whilst the linkages in $SrTiO_3$ are much stiffer, which increases the qRUM

frequencies, leading to an overall PTE.[317–319]

2.6 Monte Carlo simulations

Monte Carlo (MC) simulations are often used to study local order and ordering phenomena within materials, especially in cases where it can be difficult using conventional structure-determining techniques.[320] This thesis employs the Metropolis algorithm,[197,321] which is briefly described here.

MC simulations begin by generating a starting model where the relevant parameter is assigned a random value at each site; *e.g.* spin up or down, or Jahn–Teller axis orientation along x, y, or z. In the case of an atomistic MC simulations, the initial structure may be assigned the high-symmetry parent structure. A site is then chosen at random and changed by a random amount; *e.g.* the JT-distortion axis of a random site might be changed from x to z, or the position of a random atom within a structure might be changed by a random amount. Each time a MC move is proposed, the energy change associated with the change in configuration, $\Delta E = E_f - E_i$, is computed. Moves are accepted or rejected based on Boltzmann statistics such that

$$r = \exp\left[-\frac{\Delta E}{k_\mathrm{B}T}\right], \tag{2.45}$$

where r is a random number between $0 \leq r < 1$, T is the temperature, and k_B is the Boltzmann constant. A move is accepted if $r < \exp\left[-\frac{\Delta E}{k_\mathrm{B}T}\right]$. Hence, when $\Delta E \leq 0$ (when $\exp\left[-\frac{\Delta E}{k_\mathrm{B}T}\right] \geq 1$), the move is always accepted, and when $\Delta E > 0$, the move is accepted based on a probability determined by how energetically unfavourable the move is. The result is that some energetically unfavourable moves will be accepted, which is important when seeking to reduce the risk of the simulation getting stuck in a local minima when trying to find the global minimum. The simulation continues at a chosen temperature until it has reached equilibrium/convergence, which can be for either a predetermined number of accepted moves or until a predefined energy

has been reached. In the MC simulations in Chapters 3, 4, 5, and 6, equilibration was determined during initial testing stages by plotting MC energy against number of accepted moves and seeing after how many accepted moves does the energy stop decreasing significantly but rather fluctuates around a final energy. So-called simulated annealing[322] can be performed by decreasing the value of T; during simulated annealing, the probability of accepting an unfavourable move decreases as the energy of the system decreases. Since T is a freely variable parameter, MC simulations provide a way of studying thermally induced changes of systems, *e.g.* phase transitions.[323] MC simulations proceed by lowering the energy of the system according to a predetermined Hamiltonian, which is determined by knowledge of the local interactions in the material; thus, MC simulations can be used to test the underlying interactions governing a system.

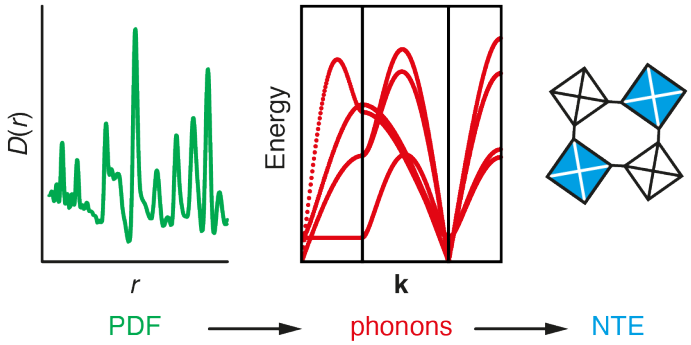
Important computational factors to consider when performing MC simulations are the time for equilibration and the size of configurations ("box size"). Whilst an infinitely large box would give the most accurate representation of a real system, the computational cost of the calculation is greater for bigger boxes. Additionally, the tendency for domain formation increases with increasing box size.[324] Hence, some compromise must be found, which is often determined by testing different box sizes and checking what effect this has on observable properties ("box-size effects"). However, the box size chosen must be larger than the length scale of any short-range correlations in the system. Additionally, periodic boundary conditions are usually applied to eliminate edge-effects, so that the MC configuration is representative of the internal bulk of a sample.

The MC simulations in all results chapters were coded using Fortran 90.

Chapter 3

Local structure and dynamics in $MPt(CN)_6$ Prussian blue analogues

3.1 Overview



An important challenge when seeking to understand the local structure of structurally-complex Prussian blue analogues (PBAs), especially those with an interplay of competing distortions, is developing a robust understanding of the local structure of more simple, higher-symmetry PBAs. The open-framework structure of PBAs and the presence of often multiple different distortions/defects within their structures makes obtaining atomistic local structure representations of PBAs a significant computational challenge. Hence, the work of this chapter is concerned with developing atomistic representations of the local structure of relatively simple PBAs, the $MPt(CN)_6$ hexacyanoplatinates, through the development of an intentionally simplistic Monte Carlo (MC)-driven pair distribution function (PDF) refinement approach. In order to link directly the local distortions captured by the PDF with the lattice dynamics of this family, a big-box modelling method based

on the iterative refinement of empirical potentials is developed. A combination of these X-ray PDF measurements, as well as lattice dynamical calculations and *ab initio* density functional theory (DFT) calculations are then used to study the local structure and dynamics in these $MPt(CN)_6$ PBAs. The 'interaction-space' PDF refinement approach yields effective harmonic force constants from which the (experiment-derived) low-energy phonon dispersion relations can be approximated. Calculation of the corresponding Grüneisen parameters allows the identification of the key modes responsible for negative thermal expansion (NTE) as arising from correlated tilts of coordination octahedra. The results of the empirically-derived phonon dispersion relations are compared against those determined using DFT calculations, which identify the same NTE mechanism.

3.2 Acknowledgements

The syntheses of the hexacyanoplatinates, $MnPt(CN)_6$ and $CuPt(CN)_6$, using the method described in Section 3.4.1, were performed by John Cattermull. Quentin Guéroult performed the harmonic lattice-dynamical calculations using GULP [Section 3.4.3], which were driven by the empirical potentials provided by myself from the Bragg/PDF refinements. Helena Barker performed the DFT calculations on the closed-shell analogue $ZnPt(CN)_6$ [Section 3.4.4]. I thank John Evans for providing an initial joint Bragg/PDF TOPAS input file and for useful discussions; I also thank Liam Nagle-Cocco in this regard. I am grateful to Nikolaj Roth for useful discussions about methods of iteratively refining parameters to data. I acknowledge Diamond Light Source for the provision of beamtime on I15-1 (Experiment CY26330), and I would like to thank Arianna Minelli for assistance with the I15-1 beamtime. The work in this chapter was published in *Chemistry of Materials*:

E. A. Harbourne, H. Barker, Q. Guéroult, J. Cattermull, L. A. V. Nagle-Cocco, N. Roth, J. S. O. Evans, D. A. Keen, A. L. Goodwin,
"Local structure and dynamics in $MPt(CN)_6$ Prussian blue analogues",

Chem. Mater. **2024**, *36*, 5796–5804.

3.3 Introduction

As introduced in Section 1.2.2, Prussian blue analogues (PBAs), $A_xM[M'(CN)_6]_y \cdot zH_2O$,[106,325,326] are a compositionally-diverse family of materials that have found applications as battery materials,[85] molecular magnets,[86] in catalysis,[87] and more.[88,89] PBAs can contain a wide variety of different kinds of structural complexity,[1] including hexacyanometallate vacancies,[102] tilts,[327] and cooperative Jahn–Teller (JT) (dis)order.[328] Arguably, the functional diversity of the PBA family stems from this compositional and structural versatility. Hence, there is motivation to understand better the vast parameter space accessible to PBAs[136,137] and the interplay between different distortions and defect structures at the local structure level. However, in order to obtain pictures of the local structure in complex PBAs, *e.g.* those with cooperative JT (dis)order and/or hexacyanometallate vacancies, the local structure of the most simple PBAs first needs to be understood.

The transition-metal hexacyanoplatinates, $M^{II}Pt^{IV}(CN)_6$, are a compositionally-simple subfamily of PBAs that are of particular interest due to their negative thermal expansion (NTE) behaviour.[120,121] Their structures are assembled from a simple cubic network of octahedrally-coordinated M^{2+} and Pt^{4+} ions bridged by linear Pt–CN–M linkages [Fig. 3.1(a)]. Whereas many PBAs harbour a variety of different kinds of structural complexity,[1] the hexacyanoplatinates are structurally much simpler and effectively defect-free.[121] Consequently, their local structures can be characterised by thermal (phonon-driven) displacements away from the average structure [Fig. 3.1(b),(c)], and it is these phonon modes that are responsible for the NTE of this family. Hence, a direct relationship between local structure and dynamics can be expected in the hexacyanoplatinates; it is this relationship that can be exploited to simultaneously gain a better understanding of both the local structure in relatively simple PBAs as well as the key phonon modes responsible for NTE in these

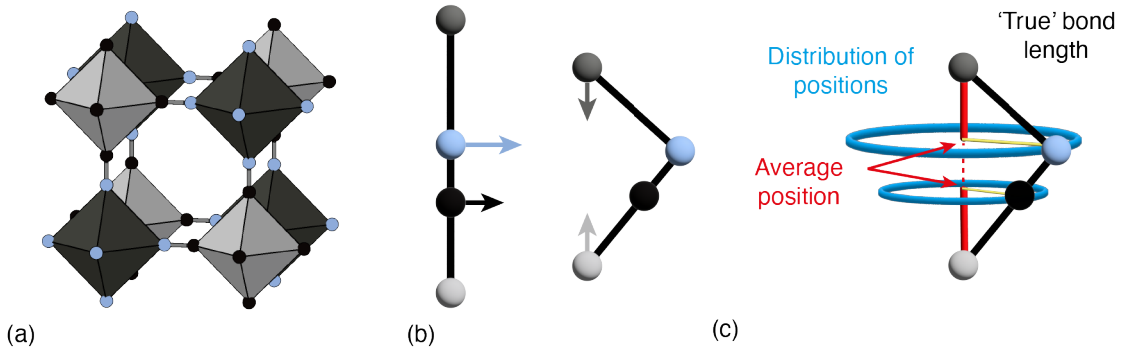


Figure 3.1: (a) Representation of the basic structure of transition-metal hexacyanoplatinate PBAs.[326] M^{2+} and Pt^{4+} coordination environments are shown as dark and light octahedra, respectively; C and N atoms are shown as black and blue spheres. (b) Representation of a transverse vibration of the bridging C and N atoms, which leads to a contraction between the M^{2+} and Pt^{4+} metal centres when bonds are stiff. (c) The 'true' bond length—the average distance between instantaneous atom positions as determined from PDF analysis—and the average position of the C and N atoms—as determined by Bragg analysis—are indicated.

materials.

Total scattering/pair distribution function (PDF) analysis can be a powerful tool for studying the local structure of materials.[176,186] However, quantitative interpretation of X-ray PDFs of PBAs can be particularly difficult;[182,214,231,234] standard PDF analysis methods assume that the degree of correlation in pairwise displacements decreases monotonically with increasing distance, but in PBAs, atom-pairs at similar distances can be correlated to very different extents (*e.g.* inter- *vs* intra-polyhedral combinations). Hence, there is motivation to develop a new PDF refinement approach that can reproduce the experimentally-determined pair correlations that better captures the variation in peak widths observed for PBAs.

Seeking to exploit the relationship between local structure and dynamics in the hexacyanoplatinates, a modified 'interaction-space' approach[235,236] for interpreting the PDFs of PBAs was developed;[329] this approach is based on the optimisation of the parameters of an intentionally simplistic empirical potential model so as to reproduce the experimentally-determined pair correlations. In spirit, this approach shares much in common with the empirical potential structure refinement (EPSR) methodology used to interpret the PDFs of heavily disordered materials such as liq-

uids and glasses;[330] hence the new 'interaction-space' approach seems ideally suited to the eventual interpretation of the PDFs of structurally-complex PBAs beyond the hexacyanoplatinates. In the context of understanding NTE in the hexacyanoplatinates, a particular advantage of determining effective potentials that govern their lattice dynamics is that it is possible to identify directly the likely phonon modes most important in driving NTE. An interesting corollary is that this insight can be gained even by fitting data collected at a single (ambient) temperature, avoiding the need to decode the thermal evolution of specific distortion patterns as is customary in the field.[331,332]

The results of this chapter will come to show that the experimental PDFs of $MnPt(CN)_6$ and $CuPt(CN)_6$ can be described well using a very simple potential with strong intra-polyhedral force constants and weak inter-polyhedral angular force constants. The specific parameterisations obtained by fitting to the PDFs allow the determination of simplified phonon dispersion relations, which identify the correlated rotations of MN_6 and PtC_6 octahedra that are often assumed to be the the key microscopic driving forces for NTE in PBAs.[99,120–124] Density functional theory (DFT) calculations carried out for the closely-related closed-shell analogue $ZnPt(CN)_6$ reflect the same key NTE phonon branches, suggesting a universal NTE mechanism in this family.

3.4 Methods

3.4.1 Synthesis

We prepared polycrystalline samples of $MnPt(CN)_6$ and $CuPt(CN)_6$ following the procedure of Ref. 134. An aqueous solution of $M(SO_4)_2 \cdot xH_2O$ (0.5 mmol in 0.5 mL H_2O) was added dropwise with stirring to an aqueous solution of $K_2Pt(CN)_6$ (0.5 mmol in 0.5 mL H_2O). Pale crystalline powders of $MPt(CN)_6 \cdot xH_2O$ appeared in solution over a matter of minutes, and the solids were isolated by filtration. The

solids were dehydrated by heating under vacuum for 24 h to afford ∼100 mg each of white polycrystalline $MnPt(CN)_6$ and pale-green polycrystalline $CuPt(CN)_6$.

3.4.2 X-ray PDF Measurements

X-ray total scattering measurements were performed using the I15-1 (XPDF) beamline at the Diamond Light Source. Samples were loaded in thin-walled borosilicate capillaries (1 mm diameter) and data measured under ambient conditions with an exposure time of 600 s. The X-ray energy used was 76.69 keV ($\lambda = 0.161669$ Å), which gave a useable scattering range $0.35 \leq Q \leq 19\,\text{Å}^{-1}$. The data were corrected for background, multiple scattering, container scattering, Compton scattering, absorption, and Bremsstrahlung effects and placed on an absolute scale using GudrunX.[333] The normalised data were Fourier transformed to yield the corresponding PDFs, following the procedure outlined in Refs. 185,333.

3.4.3 Harmonic Lattice Dynamical Calculations

The GULP lattice dynamical code,[334,335] driven using the empirical potential determined from our PDF measurements, was used to obtain phonon dispersion relations for $MnPt(CN)_6$. These calculations were carried out following structure optimisation and were evaluated at intervals of 0.05 reciprocal lattice units along high-symmetry directions of the Brillouin zone. When transferring the refined force constants from the MC simulations to the GULP parameterisation, the force constants were adapted to take into account the masses of atoms, which are not considered in the MC simulations that are driven by Eq. 3.1. Grüneisen parameters were determined in the quasiharmonic regime by repeating phonon calculations at fixed volumes respectively 1% greater and 1% lower than the equilibrium cell volume. Eigenvector matching was used to track phonon frequency variations and the corresponding values of γ were calculated according to Eq. 2.42.

3.4.4 DFT Calculations

Ab initio density functional theory calculations were carried out using the CASTEP program, version 16.11.[336] To avoid open-shell configurations, we focussed our calculations on the closed-shell analogue $ZnPt(CN)_6$. Ultra-soft pseudo-potentials as supplied as part of the CASTEP package were used together with the standard PBEsol generalised-gradient approximation. The integration of electronic states was performed using a Monkhorst-Pack grid of $3 \times 3 \times 3$ wave vectors and a plane wave cut-off energy of 700 eV.

All the structure geometries were initially optimised using BFGS method with convergence of energies to 10^{-10} eV per atom and convergence of force to 10^{-6} eV $Å^{-1}$.

For the calculation of phonon modes, CASTEP single point calculations were used in conjunction with Phonopy.[337,338] Phonopy's finite displacement method was used with a $2 \times 2 \times 2$ supercell. Single point calculations were performed on multiple supercells with different displacements to then calculate a force constant matrix. Phonon dispersions were then plotted using intervals of 0.05 reciprocal lattice units along high-symmetry directions of the Brillouin zone. Grüneisen parameters were determined in the quasiharmonic regime by repeating phonon calculations at fixed volumes respectively 1% greater and 1% lower than the equilibrium cell volume. Eigenvector matching was used to track phonon frequency variations and the corresponding values of γ were calculated according to Eq. 2.42. The neutron-weighted phonon density of states was determined from our force constant matrix outputted from CASTEP using the QpointPhononModes module in Euphonic.[339] A Monkhorst-Pack grid of $21 \times 21 \times 21$ was used to sample reciprocal space, with an energy broadening of 0.6 meV, matching that of the experimental data of Ref. 340.

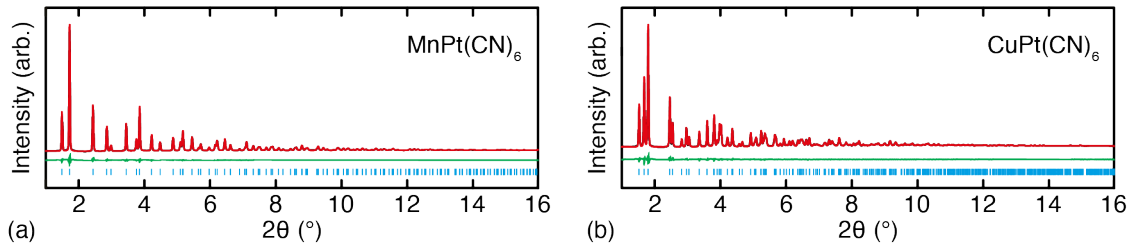


Figure 3.2: I15-1 experimental X-ray total scattering reciprocal-space data and Pawley fits of (a) $MnPt(CN)_6$ and (b) $CuPt(CN)_6$. Data are shown in black, the fit shown in red, the difference function (data−fit) shown as a green line, with calculated reflection positions shown as blue tick marks.

3.5 Results and Discussion

3.5.1 Initial Pawley refinements and small-box PDF refinements

As a preliminary step in our analysis, conventional Pawley refinements of both the $MnPt(CN)_6$ and $CuPt(CN)_6$ X-ray powder diffraction patterns over the angular range $1 \leq 2\theta \leq 16°$ were performed [Fig. 3.2]. These fits allowed us to determine a zero error, an axial divergence parameter, and unit-cell dimensions [Table 3.1]; the unit-cell dimensions are consistent with those previously reported.[134] The zero error and axial parameter were fixed for subsequent TOPAS refinements. The presence of sharp Bragg reflections for both samples is characteristic of highly crystalline samples.

Table 3.1: Refined parameters from Pawley refinements of $MnPt(CN)_6$ and $CuPt(CN)_6$ at ambient temperature and pressure. The experimental data were collected at the I15-1 beamline, Diamond Light Source, using a wavelength of $\lambda = 0.1617$ Å.

	$MnPt(CN)_6$	$CuPt(CN)_6$
Space group	$Fm\bar{3}m$	$I4/mmm$
a/Å	10.7444(5)	7.2764(3)
c/Å	10.7444(5)	11.0237(6)
zero erro	0.0042(3)	0.00479(10)
axial	0	0
R_{wp}/%	6.46	6.76

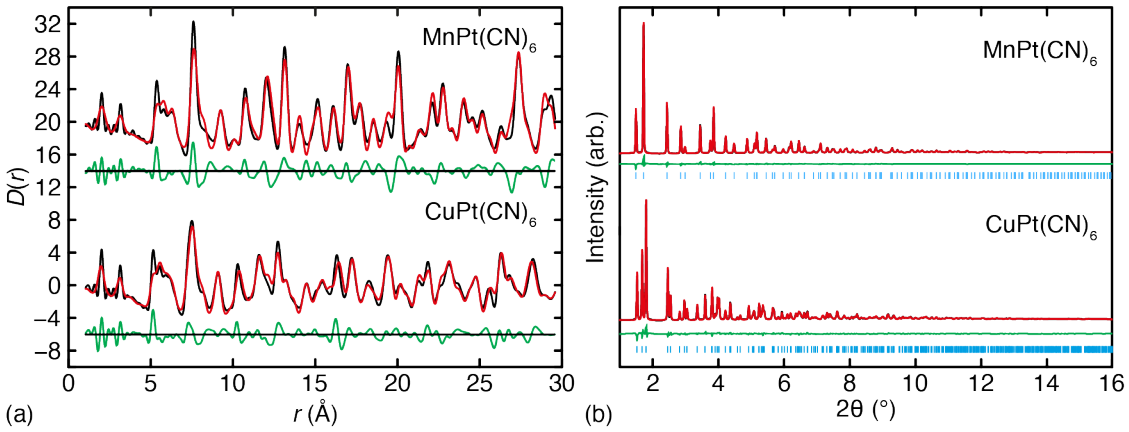


Figure 3.3: Simultaneous 'real-space Rietveld' PDF and conventional Rietveld refinements of $MnPt(CN)_6$ and $CuPt(CN)_6$. Panel (a) shows the 'real-space Rietveld' refinement of the X-ray PDFs of $MnPt(CN)_6$ and $CuPt(CN)_6$. Experimental data are shown in black, the 'real-space Rietveld' fits are shown in red, and the difference functions (data−fit) are shown in green, shifted vertically beneath the data by 6 units. Panel (b) shows the corresponding conventional Rietveld fits obtained from the same average structures as in (a). Colours are as in (a), with calculated reflection positions shown as blue tick marks.

The experimental X-ray pair distribution functions, measured under ambient conditions for our samples of $MnPt(CN)_6$ and $CuPt(CN)_6$ are shown in Fig. 3.3(a). In both cases, the strongest features in the PDFs tend to involve contributions from pairwise interactions involving Pt. For example, we cannot clearly resolve the cyanide C–N pair correlation at 1.15 Å, but the PDFs place strong constraints on this distance nonetheless via the Pt–C/M–N and Pt(–C)–N/M(–N)–C peaks at ∼2.0 and 3.1 Å, respectively. The amplitude of the PDF oscillations is reduced in the case of $CuPt(CN)_6$. This is because long-range cooperative JT order reduces the crystal symmetry from $Fm\bar{3}m$ to $I4/mmm$ and hence splits the positions of otherwise-equivalent pair correlations, giving broader peaks in the PDF.

We initially attempted to fit these data using the 'real-space Rietveld' approach implemented in TOPAS, which uses similar PDF refinement strategies to those performed by *e.g.* PDFgui.[189,341] The fits from this joint PDF + Bragg conventional small-box refinement are shown in Fig. 3.3, and gave R_{wp} values of 32.40% (PDF) and 5.96% (Bragg) for $MnPt(CN)_6$ and 33.98% (PDF) and 7.96% (Bragg) for $CuPt(CN)_6$. When doing these conventional small-box fits, we encountered the

difficulty that PDF peak widths could not be accounted for satisfactorily. The key obstacle was that, in the experimental PDF, peak widths do not increase monotonically with increasing separation r. This effect is characteristic of varying interaction strengths operating over common lengthscales (*e.g.* inter- *vs* intra-polyhedral atom-pairs). In such cases, one commonly-used solution is to employ 'big-box' modelling techniques, such as reverse Monte Carlo (RMC),[196,342,343] which allow atomic co-ordinates in supercell configurations to refine in order to best fit the PDF. Such configurations can then capture the mixture of different pair correlation widths that may be present. One important limitation of such approaches is the very large number of parameters involved. Because our scientific focus is on understanding the underlying dynamical behaviour of hexacyanometallates, we devised a different approach based on empirical potentials.

3.5.2 Interaction-Space PDF Refinements

Overview of interaction-space PDF refinement approach

Our starting point was to assume that the key degrees of freedom accessible to hexacyanometallates involve stretching of Pt–C/M–N bonds (the C–N bond itself being essentially rigid at ambient temperature), and also variation in the intra- and inter-polyhedral angles. In this way, we write the lattice energy for $MnPt(CN)_6$ as the sum

$$E = \frac{1}{2}\sum_{\text{bonds}} k_r(r - r_\text{e})^2 + \frac{1}{2}\sum_{\text{angles}} k_\theta(\theta - \theta_\text{e})^2. \tag{3.1}$$

The first term involves a sum over the two types of deformable bonds, each of which carries its own bond strength k_r and equilibrium distance r_e. Similarly, the second term represents a sum over contributions from three types of angles: we consider the (right-angled) C–Pt–C, N–Mn–N, and (linear) Mn–N–C triplets to be deformable, but in order to limit the number of variables treat the Pt–C–N linkage as stiff. This approximation is justified by the relatively high bending force-constants

observed amongst hexacyanoplatinates.[106] The equilibrium angles θ_e are taken as either $\frac{\pi}{2}$ or π as appropriate. This model has seven independent parameters, to which we add an eighth—namely, the length of the (rigid) C–N bond. The case of $CuPt(CN)_6$ is more complicated as a consequence of the JT distortion of the Cu^{2+} coordination environment. In our model for this system, we now distinguish the stretching force constants and equilibrium distances for axial and equatorial Cu–N links, as we do the various different angular terms involving Cu–N bonds. These additional considerations increase the number of free variables to 12 for $CuPt(CN)_6$.

For a given set of force-constant and equilibrium-distance parameters, we used Monte Carlo (MC) simulations, carried out at ambient temperature, to obtain atomistic representations of the structures of $MnPt(CN)_6$ and $CuPt(CN)_6$. In these atomistic configurations, the displacements of atoms away from their high-symmetry positions are entirely characteristic of the energetics of the bond and angle deformations governed by Eq. 3.1. The PDFs and powder diffraction peak intensities associated with each model can be calculated directly from the atom coordinates within the corresponding supercell. These calculated scattering functions can be compared against our experimental data and a goodness-of-fit determined. By tracking the fit quality as a function of each individual parameter, we can iteratively refine the values of these parameters and hence converge on an experiment-driven parameterisation of Eq. 3.1. It is also possible to calculate a PDF directly from harmonic potentials using GULP without needing to go via a MC refinement to produce an atomistic representation.[344] However, this method falls within the pure harmonic regime. Hence, as we were interested in exploring the local structure of the $MPt(CN)_6$ PBAs, we chose to develop a method that would allow us to obtain atomistic representations where anharmonicity in the structure is allowed.

The MC configuration was then used as input for a constrained PDF + Bragg scattering refinement carried out using the TOPAS software.[282] In this refinement, the positions of atoms were fixed and the corresponding PDF calculated as described

in Ref. 341. The configurational average of this structural description was determined and used to calculate a corresponding fit to the scattering function (Bragg intensities) in reciprocal space. Atomic displacement parameters were fixed at a constant value very much smaller than that associated either with the real-space resolution at $Q_{\max} = 19\,\text{Å}^{-1}$ or with the distribution of atomic sites in the collapsed (average) structure. Unit-cell dimensions, peak-shape parameters, and background functions were collectively refined against the $1 \leq 2\theta \leq 16^{\circ}$ angular range of our experimental Bragg data. The resulting goodness-of-fit represented the simultaneous quality of fits to both real- and reciprocal-space data, weighted as a simple linear sum of the corresponding R_{wp} values.

The iterative nature of our approach then involved, for a given iteration, testing various values of an individual empirical parameter, repeating the MC simulations using these adjusted values, and subsequently fitting to the PDF and Bragg data, noting the resulting fit qualities [Fig. 3.4]. Next, the starting value (at the beginning of the given iteration) of the chosen empirical parameter is once again adopted—*i.e.* the value of this parameter does not accept one of the tested values at this stage—whilst various values of an another empirical parameter are tested. At the end of a given iteration, after different values have been tested for all parameters, only the specific parameter that gave the best global fit-to-data is identified and its value changed, with all other parameters adopting their starting value at the beginning of the iteration. The process is then repeated for subsequent iterations; as such, which parameter ultimately has its value changed at the end of an iteration will vary from iteration to iteration. Enough iterations are performed to give each parameter a chance to change, with the process terminated when the values of the parameters no longer change significantly. The aim of this process is to minimise the effect of optimising the parameters in a specific order—given the interdependence of the parameters—but there is still no guarantee that ending up in a local/false minimum is avoided. Using the method described here, it will tend to optimise first

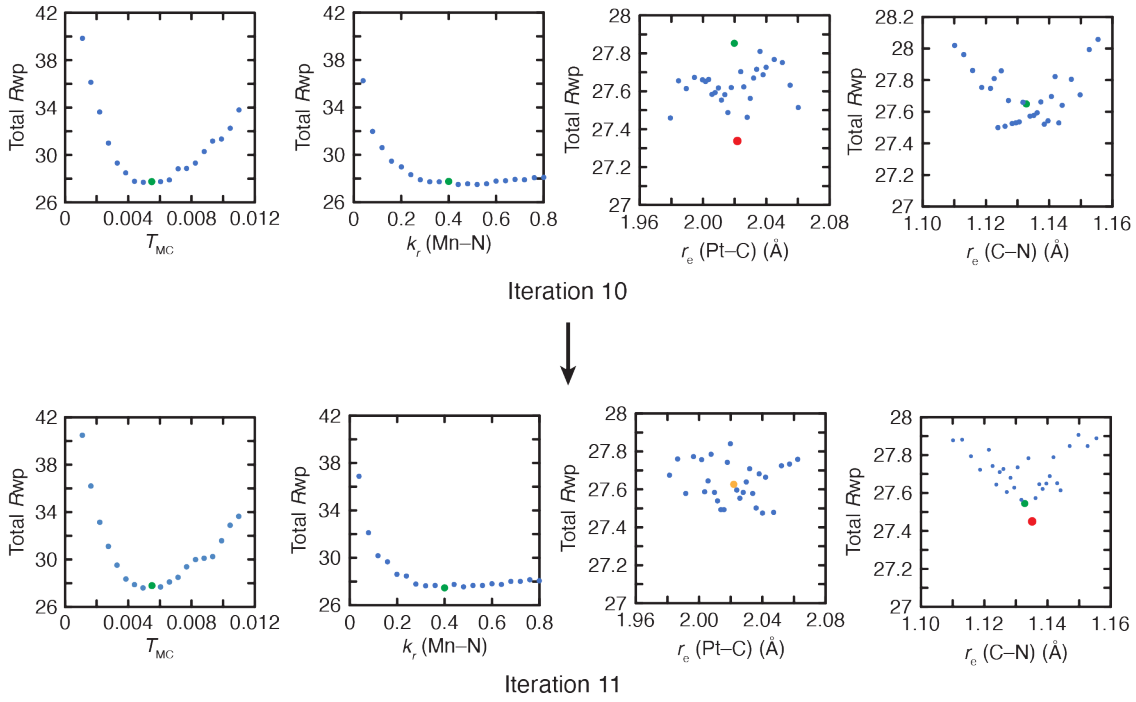


Figure 3.4: The iterative process of refining MC parameters, with a selection of parameters chosen to highlight this process. In a given iteration, various values of each parameter are tested (blue). The value of the parameter that gave the lowest total R_{wp} across the parameter set is identified (red), and this becomes the starting value for this parameter in the next iteration (orange); the starting value of every other parameter remains the same as the previous iteration (green).

the parameters to which the data have greatest sensitivity.

We provide in Fig. 3.5 a schematic illustrating our MC-driven constrained big-box modelling approach for producing atomistic representations of PBAs by refining against both X-ray PDF and conventional powder XRD patterns. The steps taken in a given iteration are as follows. (1) Our starting point is a knowledge of the basic average structure of $MPt(CN)_6$. (2) This structure is then decorated with effective harmonic potentials, as described by Eq. 3.1. In the first instance, the values of the various empirical parameters are initialised using sensible guesses. A supercell configuration of the known average structure is then allowed to reach equilibrium under the action of these empirical potentials, using a MC simulation running at an internal temperature that is eventually rescaled to 300 K (*i.e.* placing all empirical parameters on an absolute scale). (3) The resulting configuration captures both

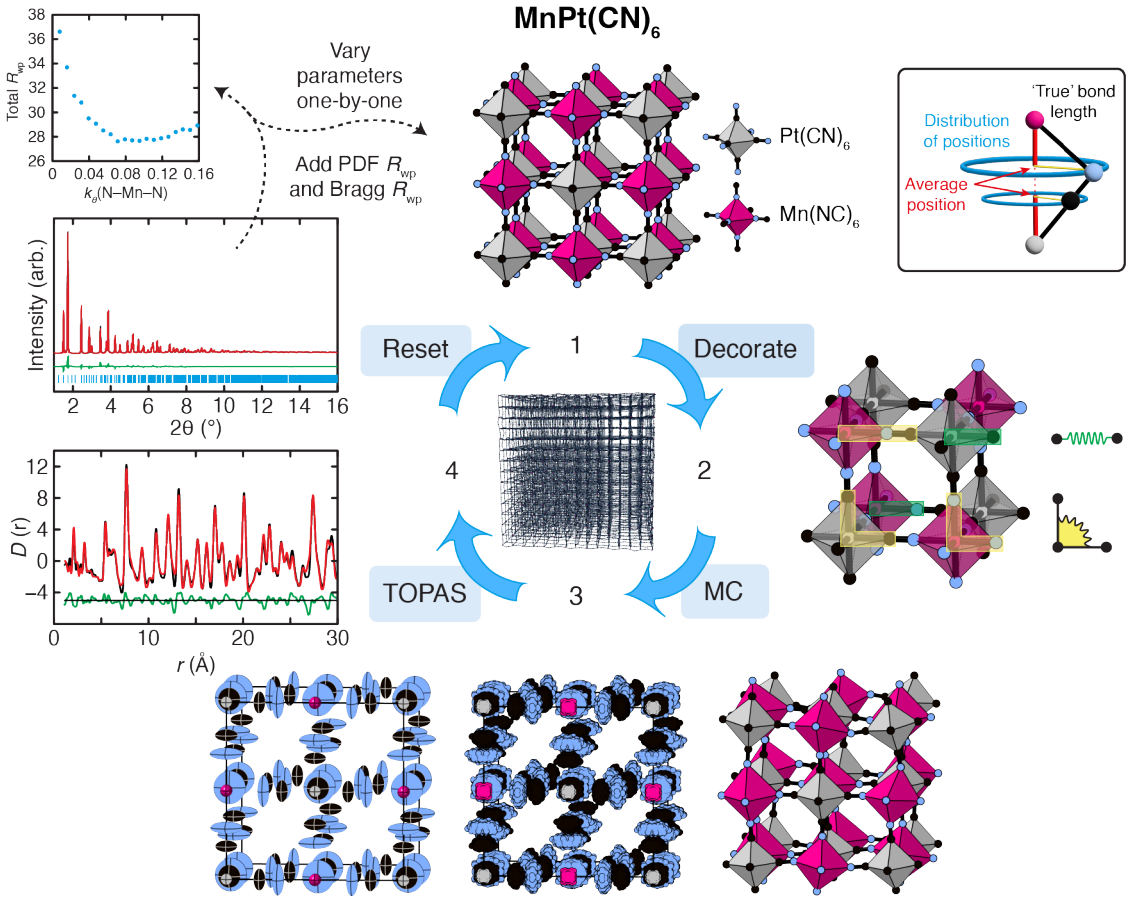


Figure 3.5: Overview of the MC-driven 'interaction-space' PDF refinement strategy employed. The inset in the top-right corner shows a representation of a transverse vibrational mode of cyanide bridging atoms;[232] the 'apparent' polyhedral bond lengths are shown in red, which are inferred from the distance between the average positions of two atoms, as determined from Bragg analysis; the 'true' bond lengths are shown in black, which are the average distance between two atoms.

local structure information—in the form of individual atomic displacements—and average structure information—in the form of the atom distributions obtained by projection onto the parent cell. (4) Using TOPAS, the Bragg diffraction pattern and PDF are calculated from the MC model and additional fitting parameters are allowed to refine. The goodness-of-fit R_{wp} is then recorded. Different values of each empirical parameter are then tested by repeating the cycle. Once all parameters have been assessed, only then is the change in the parameter that gave the lowest total R_{wp} accepted. Further iterations of this process are then performed.

Direct Monte Carlo simulations

MC simulations were carried out using a custom code written in Fortran90. We employed $6 \times 6 \times 6$ supercells of the parent $Fm\bar{3}m$ (or $F4/mmm$,* M = Cu) $MPt(CN)_6$ unit cell, such that each configuration contained 12 096 atoms in total. We fixed the MC supercell dimensions according to the unit-cell parameters determined during our preliminary Pawley refinement of the powder X-ray diffraction data. The coordinates of M, Pt, and N atoms were treated as free variables; the C atom positions were determined by decorating the corresponding Pt–N vectors. In this way, neither the C–N bond length nor the Pt–C–N angle were allowed to deviate from their ideal values. The MC energy was determined according to Eq. 3.1. An atom was selected at random, moved by a small amount, and the move accepted or rejected according to the usual Metropolis algorithm. This process was repeated until convergence (roughly 150 accepted moves / atom), which took approximately 3 mins when running on a standard laptop computer. The simulations were carried out using a MC temperature of 300 K and were allowed to proceed until convergence was achieved. The resulting configuration was then used to output a TOPAS file for subsequent comparison against experimental X-ray scattering data. This file includes two representations of the MC configuration: the explicit atom coordinates are used for calculation of the PDF, and a projection of the coordinates onto the parent cell is used for calculation of the Bragg intensities.

Atomistic TOPAS refinements

Our TOPAS refinements consisted of two main blocks: the first corresponding to the calculation of X-ray Bragg intensities from the MC structure collapsed onto a single unit-cell (hence equivalent to the average structure), and the second corresponding to the calculation of the X-ray PDF from the individual atom coordinates within

*We use the unconventional $F4/mmm$ setting for $CuPt(CN)_6$ in our study so as to simplify comparison to $MnPt(CN)_6$.

the MC configurations.

For the Bragg scattering component, we allowed free refinement of unit-cell parameters (starting from the values of the unit-cell parameters refined in the initial Pawley refinements), scale, a background function, and the parameters of a Thompson-Cox-Hastings pseudo-Voigt (TCHZ) peak shape function. Fits were performed over the angular range $1 \leq 2\theta \leq 16°$. The refinements were carried out using $P1$ crystal symmetry with the cell metric constrained appropriately (cubic for M = Mn and tetragonal for M = Cu). The approach of calculating the X-ray Bragg intensities from the collapsed MC structure in $P1$ crystal symmetry is equivalent to applying the appropriate space-group symmetry ($Fm\bar{3}m$ for $MnPt(CN)_6$ and $F4/mmm$ for $CuPt(CN)_6$) operations to the collapsed coordinates, calculating the average position of each type of atom and its ADP from the distribution, before then performing a Rietveld refinement on this average structure in the corresponding space group setting. In these refinements of the Bragg component, relative atom coordinates were fixed, and each atom site was assigned a (fixed) isotropic displacement parameter $B_{\mathrm{eq}} = 0.1\,\text{Å}^2$, which was chosen to be very much smaller than the width of the atom distributions and also the real-space resolution of the X-ray diffraction pattern.

For the PDF component, we used a fixed Q-damping term of $\mathrm{d}Q = 0.08\,\text{Å}^{-1}$, a fixed Q_{max} convolution term of $19\,\text{Å}^{-1}$, and convolved our calculations with an r-dependent broadening term (α) which was allowed to refine freely. Unit-cell parameters were coupled to those refined in the Bragg scattering component, taking into account the additional factor associated with the supercell size. Fits were performed over the range $1 < r < 30\,\text{Å}$, with data binned at intervals of $0.02\,\text{Å}$. Atom positions were again fixed (now within the larger MC supercell) and each atom was assigned the same small (fixed) isotropic displacement parameter $B_{\mathrm{eq}} = 0.1\,\text{Å}^2$.

The only parameters shared between Bragg and PDF components were the unit-cell parameters, to which the Bragg component has a much greater sensitivity. Ac-

cordingly, the PDF fits were included in the least-squares cycles using a relative weighting of 0.001, which ensured that the cell parameter fitting was dominated by the Bragg component. This weighting does not affect the refined values of any remaining parameters. In practice, the unit-cell parameters did not vary much from those refined in the initial Pawley refinements, so fixing the unit-cell parameters to these initial values could also have been an option. The quality of fit was monitored independently for both Bragg and PDF components through the corresponding R_{wp} values, with final refinements converging to values of about 8% and 20%, respectively.

Parameter Search

Our starting point is a set of parameters $\mathcal{P}_0 = \{k_r, k_\theta, r_\mathrm{e}\}$, whose initial values are guessed from reasonable assumptions (*e.g.* average-structure bond lengths). We use the subscript '0' to denote initial values. Our parameter search then proceeds in cycles. For the i^{th} iteration, the goodness-of-fit is determined—using the cycle shown in Fig. 3.5—by taking the set $\mathcal{P}_{i-1}$ and then varying in turn each parameter within this set by small increments. These variations are carried out independently of one another in the sense that, as one parameter is varied, the others are kept constant at the values in $\mathcal{P}_{i-1}$. In this way, we are effectively mapping the fit-quality landscape in section along each of the variables. Having carried out this search, the instance that corresponds to the highest quality fit-to-data is identified, and the subsequent parameter set $\mathcal{P}_i$ formed by updating the single relevant variable to its new value. Hence parameter sets in subsequent iterations differ only by a single parameter. We continue from iteration to iteration until no further improvement in quality of fit can be obtained.

We found that the experimental data showed differing levels of sensitivity to different parameters. We show in Figs. 3.6–3.8 representative traces of the goodness-of-fit for variations in the equilibrium bond lengths, bond-stretching, and angle-bending

parameters obtained in the final parameter search cycle for both $MnPt(CN)_6$ and $CuPt(CN)_6$ (the full set can be found in Figs. A0.1–A0.6. An important consideration to keep in mind is that varying r_e(M–N) does not correspond to varying the position of the maximum in $g_{M–N}(r)$, but instead affects in a complex manner the interplay of different bond-lengths in the evaluation of the MC energy via Eq. 3.1. Hence uncertainties in these parameters must be interpreted differently to uncertainties in the final partial pair distribution functions. A point made obvious by these figures is that the PDF and Bragg components often drive the model in opposite directions; this tension is well-known in the RMC field, for example.[343] In the absence of a strict rule for weighting the PDF and Bragg components, we have used the simple combined fit to discriminate models.

While other parameter search mechanisms can easily be envisaged, we note that the approach we take here operates by optimising first those parameters to which the data have greatest sensitivity. The search process is itself deterministic and so can easily be automated, albeit that small fluctuations in the values of R_{wp} arise from the stochastic nature of the MC simulations from which the corresponding fits are derived. There is also no guarantee that the methodology arrives at the global minimum and a goal for future work would be to automate the parameter search algorithm using more sophisticated approaches better suited to multi-dimensional landscapes (*e.g.* genetic algorithms). It would also be desirable to extract quantitative measures of the uncertainty in each variable and the corresponding covariances. For the purposes of this study, however, we are content that the final parameter sets obtained provide fit qualities that are comparable to those of conventional PDF (and Rietveld) refinements. Indeed the fit qualities are comparable to those obtained using fully-atomistic refinements (*e.g.* RMC), despite the vast reduction in number of free parameters ($\mathcal{O}(10^1)$ *vs* $\mathcal{O}(10^5)$). Nevertheless, we make no claim that the final parameter sets represent a unique description of the X-ray scattering data.

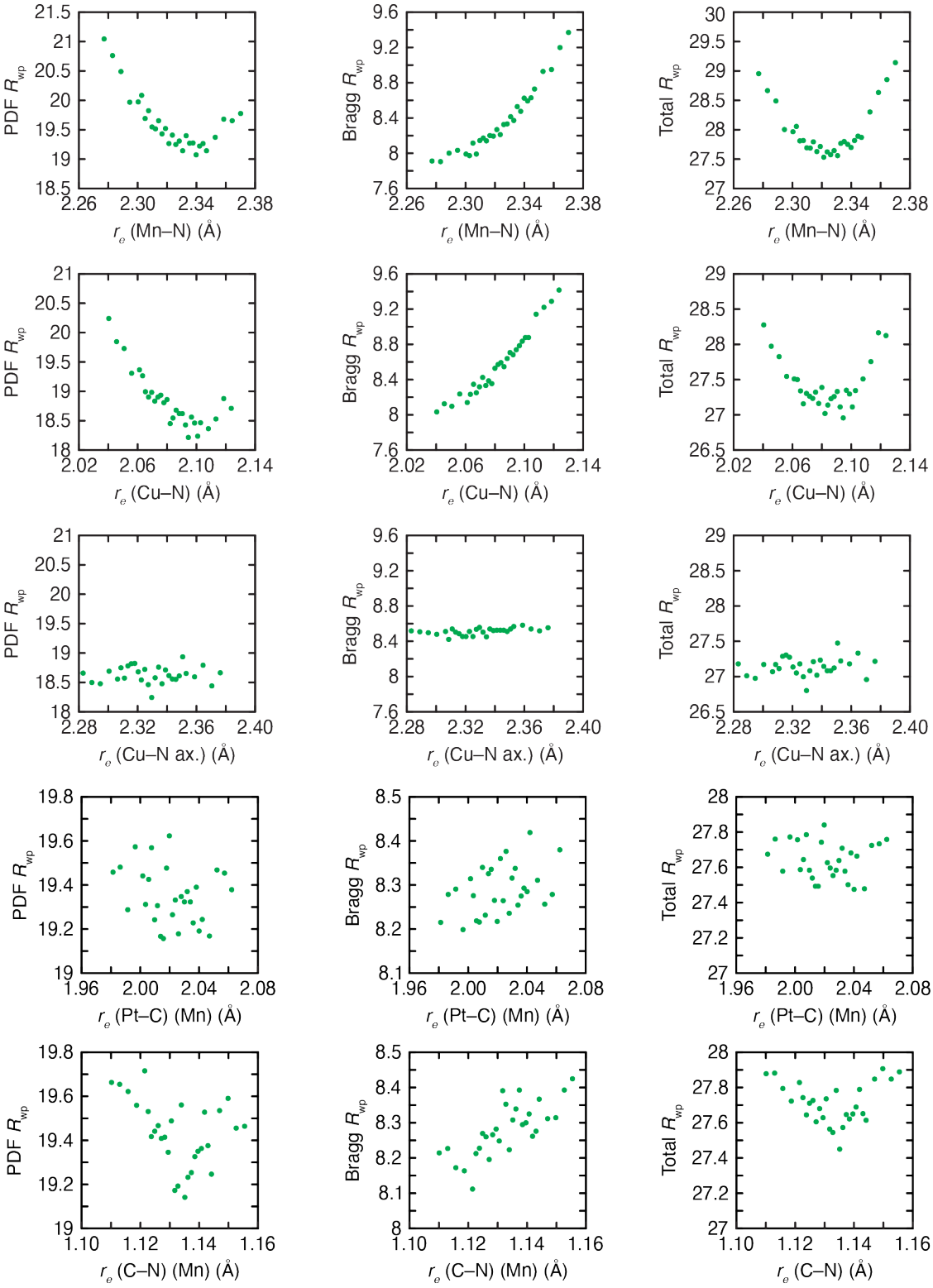


Figure 3.6: Goodness-of-fit as a function of r_e.

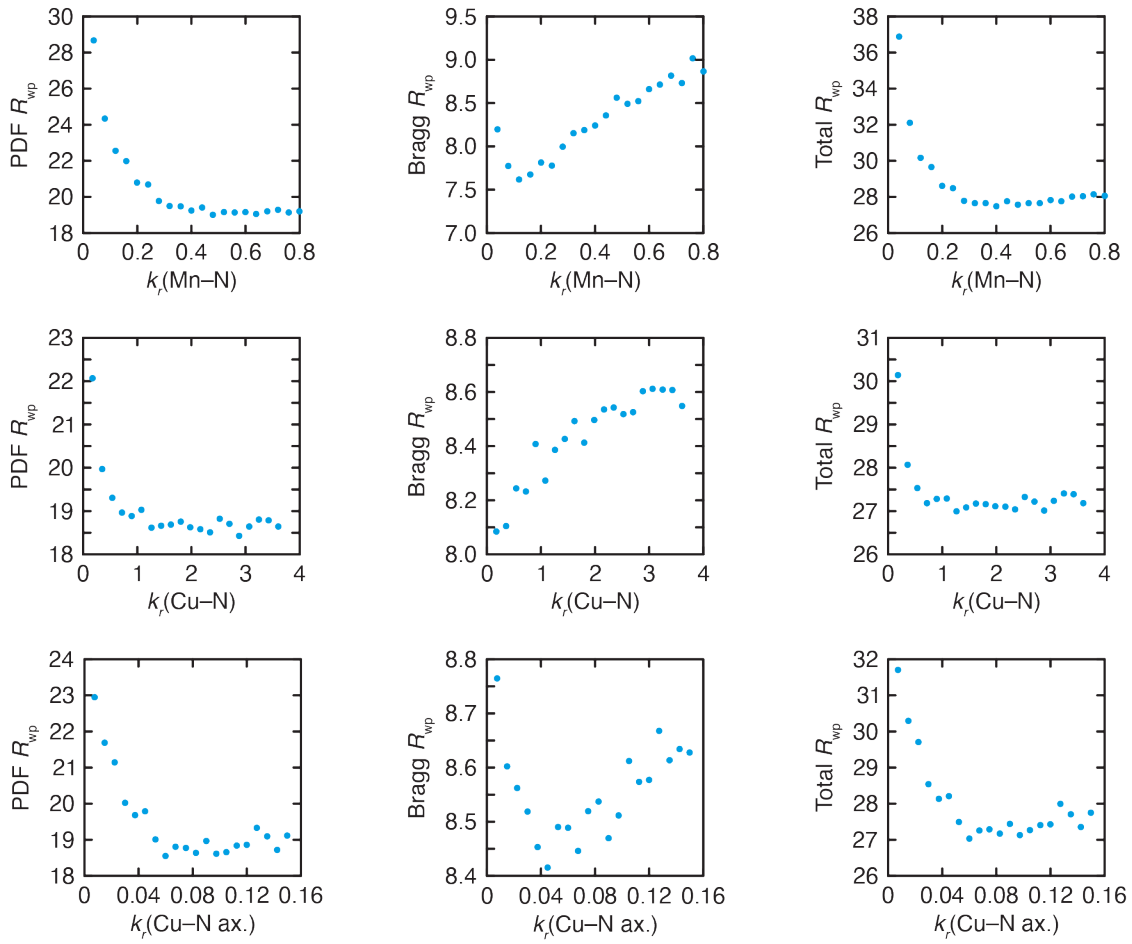


Figure 3.7: Goodness-of-fit as a function of k_r(M–N).

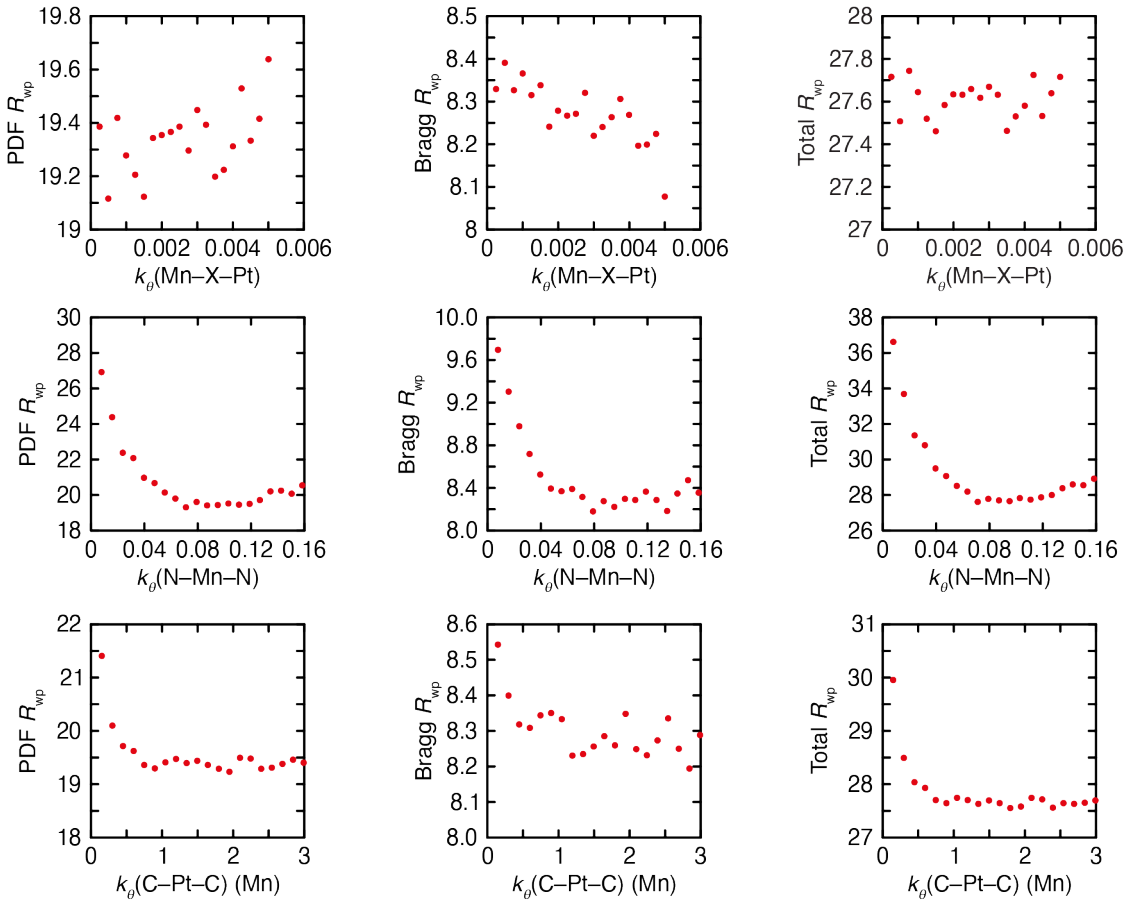


Figure 3.8: Goodness-of-fit as a function of k_θ.

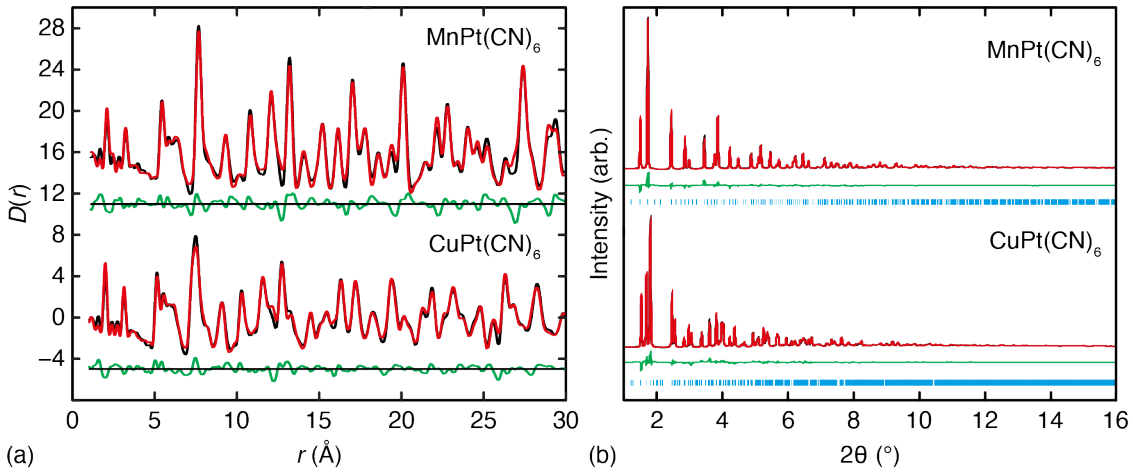


Figure 3.9: Experimental X-ray total scattering data and empirical MC fits. Panel (a) shows the X-ray PDFs for $MnPt(CN)_6$ and $CuPt(CN)_6$. Data are shown in black, the fit shown in red, and the difference function (data−fit) shown as a green line, shifted vertically beneath the data by 5 units. Panel (b) shows the corresponding reciprocal space Bragg diffraction pattern fits obtained from the same MC configurations. Colours are as in (a), with calculated reflection positions shown as blue tick marks.

Results

The fits-to-data obtained using this 'interaction-space' refinement approach are shown in Fig. 3.9 and the corresponding parameters are given in Table 3.2. The variation in parameters for common interactions in both hexacyanoplatinates gives a sense for the corresponding degree of uncertainty (which can be large). The empirical parameters themselves show reasonable trends: deformations of PtC_6 octahedra are more energetically expensive than those of MN_6 octahedra, and the axial Cu–N linkage is associated with weaker interactions, as expected.[134]

An important distinction from conventional PDF refinements is that, in our case, the PDF and Bragg diffraction intensities for a given system are calculated from one and the same model. Representative fragments of such models are shown in Fig. 3.10(a,b). Because X-ray PDF measurements are energy-integrated, these configurations can be interpreted as instantaneous snapshots of the corresponding systems undergoing vibrational motion.[186] The corresponding average structures, obtained by collapsing the supercell onto a single unit-cell and subsequently ap-

Table 3.2: Empirical parameters used to model the X-ray PDFs of $MPt(CN)_6$ (M=Mn,Cu), together with their refined values. For $CuPt(CN)_6$, terms involving axial (ax.) and/or equatorial (eq.) Cu–N linkages are distinguished accordingly.

Parameter	$MnPt(CN)_6$	$CuPt(CN)_6$
k_r(Pt–C) (eV/Å^2)	9.4	8.5
k_r(M–N) (eV/Å^2)	3.5	15.5 (eq.)
		0.6 (ax.)
r_e(Pt–C) (Å)	2.02	2.01
r_e(M–N) (Å)	2.32	2.08 (eq.)
		2.33 (ax.)
k_θ(C–Pt–C) (eV/rad^2)	14.1	4.3
k_θ(N–M–N) (eV/rad^2)	0.74	0.85 (eq./eq.)
		0.68 (eq./ax.)
k_θ(M–N–C) (eV/rad^2)	0.02	0.08 (eq.)
		0.01 (ax.)
r(C–N) (Å)	1.14	1.15

plying the appropriate space-group symmetry ($Fm\bar{3}m$ or $F4/mmm$), are shown in Fig. 3.10(c–f). From these models it is clear that the Mn-containing system is more dynamic than the Cu-containing system. This observation is consistent with the stronger NTE behaviour of $MnPt(CN)_6$ relative to $CuPt(CN)_6$.[121] What is also clear is why conventional PDF refinements using monotonic r-dependent peak widths fail: the distributions around M and Pt positions are very tightly bunched (and hence the corresponding PDF peaks very narrow) while the C/N distributions are very diffuse (and hence any C/N–C/N PDF peaks will be broader). Note also the anisotropy of the Cu^{2+} distributions: displacements along the JT axis are clearly much larger than those in a perpendicular direction. Through cooperative displacements, this anisotropy leaves a small imprint also on the Pt^{4+} distribution, despite the six Pt–C bonds being governed by the same effective interaction.

3.5.3 Local structure analysis

In order to interrogate further the local structural features captured by our PDF-derived MC configurations, we extracted key pair and triplet correlation functions. These are shown in Fig. 3.11 and, by virtue of our fitting process, should be interpreted as the correlation functions deconvolved of instrumental and experimental

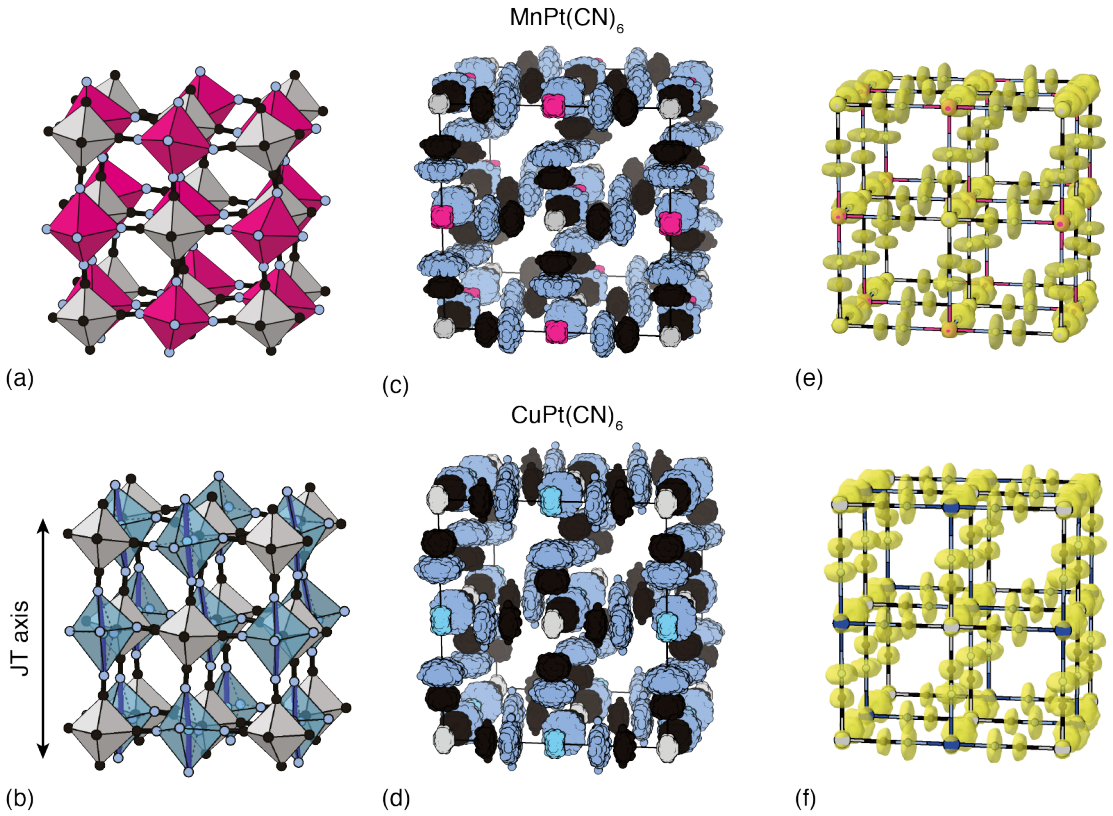


Figure 3.10: Representations of the local and average structures of $MPt(CN)_6$ PBAs determined in our PDF refinements. Panels (a),(b) show small fragments from $MnPt(CN)_6$ and $CuPt(CN)_6$ configurations. Various bond-length and bond-angle distortions are evident and these should be interpreted as snapshots of thermal fluctuations through vibrational motion. Atom colours as in Fig. 3.1(a), with M = Mn and Cu shown in pink and blue, respectively. Panels (c)–(f) show the collapsed configurations from which the Bragg intensities were calculated. The yellow surfaces in panels (e),(f) represent the volume occupied by 98% of sites around each atom position. In both cases, the corresponding crystal symmetry has been applied, and we use the unconventional face-centred tetragonal cell for $CuPt(CN)_6$ to aid comparison between the two structures. The direction of the JT axis is indicated by an arrow.

broadening. Our expectations based on the magnitude of the various empirical interaction parameters are borne out in practice in terms of the corresponding correlations. We see a mixture of broad and sharp features for different pair correlations at similar separations. The presence of a JT distortion in the Cu^{2+} coordination environment is clear in the difference in nearest-neighbour Cu–N pair correlation for axial and equatorial pairs. In Fig. 3.11(c) we show the distribution of intra-polyhedral angles for the PtC_6, MnN_6, and CuN_6 octahedra. In the latter case, we can decompose the distribution into those components from axial–axial, axial–equatorial, and

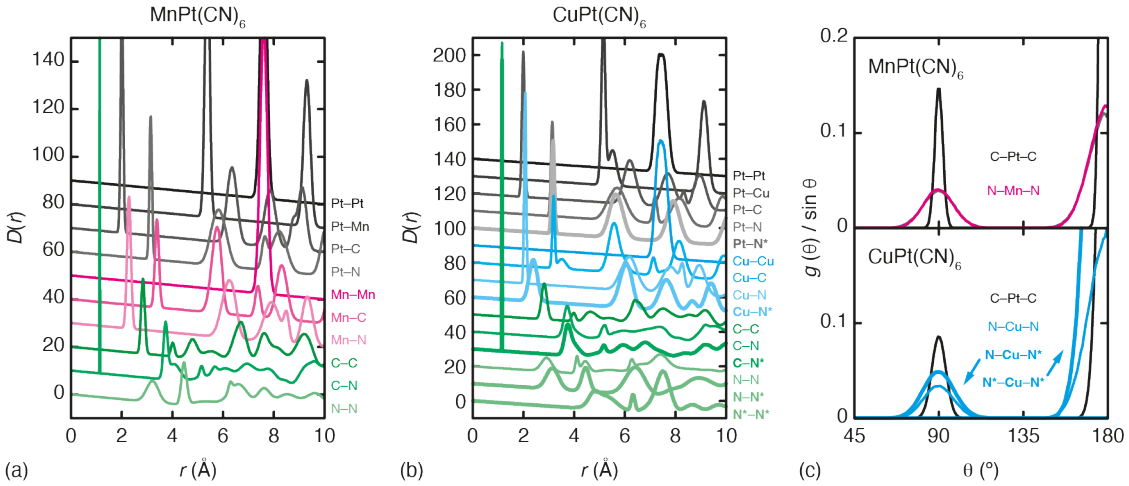


Figure 3.11: Partial pair-correlation functions for (a) $MnPt(CN)_6$ and (b) $CuPt(CN)_6$ extracted from our PDF-driven MC simulations. Successive curves are shifted vertically by ten units. Correlations involving N atoms along local JT axes of Cu^{2+} coordination environments are highlighted by an asterisk and displayed using bolder lines. (c) The intra-polyhedral angle distributions within PtC_6 and MN_6 octahedra, highlighting the additional angular flexibility along the JT axis in (Cu^{2+}) configurations.

equatorial–equatorial N–Cu–N triplets. What emerges is that the in-plane CuN_4 geometry is relatively tightly constrained, but that there is much greater flexibility along the JT axis. Cooperative JT distortion also broadens the Cu–Cu, Cu–Pt, and Pt–Pt pair correlations, which is why the PDF oscillation amplitudes are smaller in magnitude for $CuPt(CN)_6$ than $MnPt(CN)_6$ at high r.

From a methodological perspective, we note that by using a harmonic parameterisation to fit the X-ray PDFs, the various pair correlations necessarily adopt smooth forms that are approximately Gaussian in shape. This contrasts with the situation in other big-box (*e.g.* RMC) refinements, where small fluctuations in the data—especially at low distances—can translate to unphysical features in the partial pair correlation functions, such as spikes and truncation peaks.[343]

3.5.4 Lattice dynamical calculations

A key advantage of interpreting our experimental PDF measurements in this way is that we are able to calculate directly from Eq. 3.1 the corresponding phonon disper-

sion curves and hence quantify the extent to which particular vibrational modes are dominating atomic displacements at ambient temperature. The low-energy phonon dispersion calculated in this way for $MnPt(CN)_6$ is shown in Fig. 3.12(a); the equivalent result for $CuPt(CN)_6$, which is more complicated as a consequence of the lower crystal symmetry, is given and discussed in section 3.5.4. A key feature of the low-energy phonon spectrum is a dispersionless branch that runs along the $\mathbf{k} = [00\xi]$ direction from Γ to X. Inspection of the corresponding mode eigenvectors identifies this branch as the conventional octahedral tilt distortion, with the tilt axis parallel to $\mathbf{k}$. This is the same low-energy branch that would ordinarily extend along the Brillouin zone boundary from M (in-phase tilts) to R (out-of-phase tilts) in the conventional (primitive cubic) perovskite aristotype.[33]

Our DFT calculations for $ZnPt(CN)_6$—the closed-shell analogue of $MnPt(CN)_6$—give the low-energy dispersion relations shown in Fig. 3.12(b). At face value, these dispersion curves appear very different from those of our PDF-derived lattice dynamical model. One difference that is easily explained is that the treatment of C–N bonds and Pt–C–N angles as rigid in the empirical model reduces the number of phonon branches by nearly a factor of two: this is why the DFT result looks more complicated. Indeed, at very low energy, there is an additional set of branches in the DFT dispersion relation that corresponds to the 'shift' degree of freedom identified in Ref. 113 (these become the transverse acoustic modes as $\mathbf{k} \to \Gamma$). These distortions require flexing of the Pt–C–N angle which is why they aren't present in the empirical dispersion curves. Nevertheless, an important similarity between the two sets of phonon dispersion curves is that the octahedral tilt branch is again dispersionless in the DFT calculations and occurs at a very similar energy to that given by the empirical model.

In order to make the link to NTE mechanisms, we calculated the Grüneisen parameters for each branch in the phonon spectra. In Fig. 3.12(c,d) we show the phonon dispersion curves with intensities and colours weighted by the corresponding

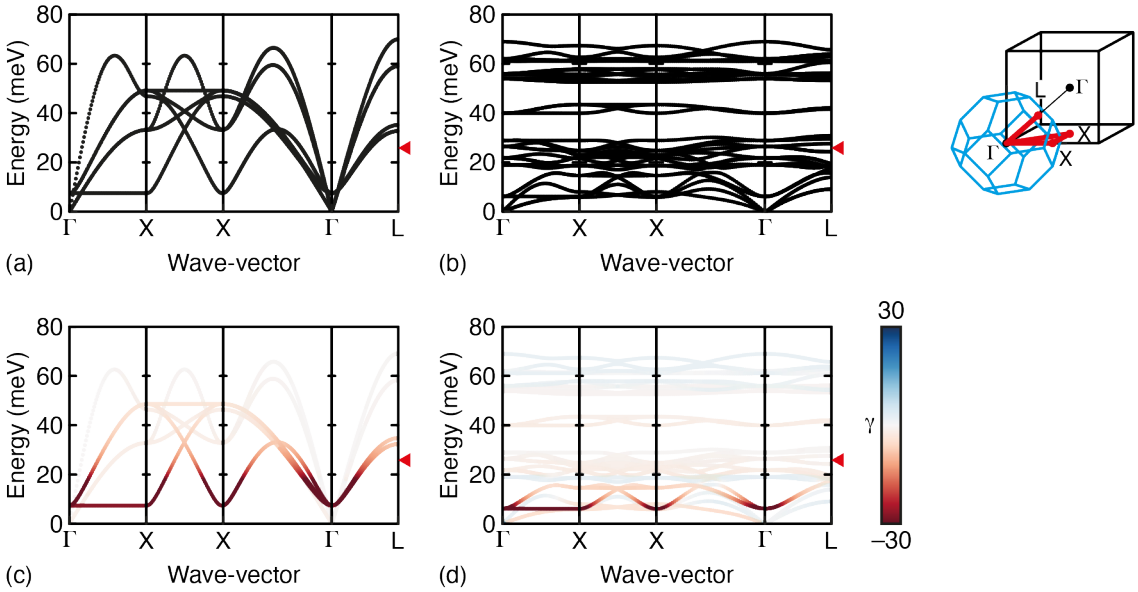


Figure 3.12: Lattice dynamics in $MPt(CN)_6$ PBAs. (a) Simplified low-energy phonon dispersion relation for $MnPt(CN)_6$ obtained from the empirical lattice-dynamical model used in our PDF fits. Note the presence of a dispersionless branch at ∼8 meV along the Γ–X direction, which corresponds to correlated octahedral tilts as shown in Fig. 1.11(a). Thermal energy at 300 K is indicated by a small triangular mark on the right-hand side of the dispersion curves. (b) The all-atom low-energy phonon dispersion of $ZnPt(CN)_6$ determined using DFT. The same dispersionless branch along Γ–X is present, but amongst the many differences from the curves in (a) is a dramatic softening of the transverse acoustic branches, associated with cooperative shift displacements.[110,113] Panels (c) and (d) show the same phonon dispersion curves given in (a) and (b), but with branches coloured according to the corresponding mode Grüneisen parameters. The key NTE modes ($\gamma \ll 0$; deep red) are identified in both cases as the cooperative octahedral tilts. The reciprocal-space path used in our phonon representations is shown schematically on the right-hand side as the bold red trace within and beyond the first Brillouin zone (blue cuboctahedron).

values of $\gamma(\mathbf{k}, \nu)$. We expect the DFT result to capture the true NTE mechanism, and what is immediately obvious is that the octahedral tilts along Γ–X are associated with Grüneisen parameters that are particularly large and negative. The columnar shifts also have negative Grüneisen parameters but their magnitudes are sufficiently smaller that the corresponding contribution to NTE is also reduced. Importantly, the empirical parameterisation also captures precisely this same mechanism—indeed, even the magnitudes of the Grüneisen parameters are remarkably similar to the DFT result. So, despite the differences in much of the phonon spectra between DFT and empirical calculations, the key distortions at low energies from which NTE arise are

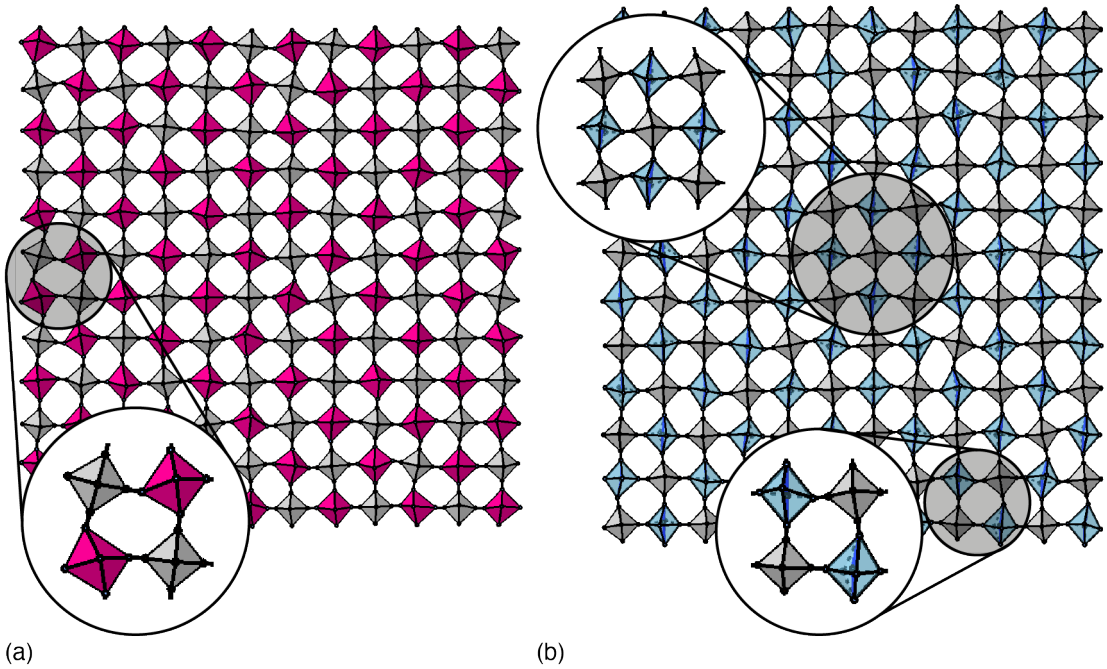


Figure 3.13: (a) Cross-section of a representative $MnPt(CN)_6$ configuration. (b) Cross-section of a representative $CuPt(CN)_6$ configuration.

actually well matched.

The correlated tilt displacement pattern is an example of a rigid-unit mode (RUM), because it preserves the coordination geometries of both M^{2+} and Pt^{4+} centres.[94,310,319] Such tilts are pure RUMs only along Γ–X and only for the transverse-polarised branch (*i.e.* tilts around an axis parallel to **k**). But common to both PDF- and DFT-derived phonon dispersion relations is the observation that correlated tilts contribute to the NTE even away from this branch—albeit with decreasingly extreme negative Grüneisen parameters. Hence the slightly-distortive quasi-RUMs (qRUMs) play an important role, because they extend the reciprocal-space density of NTE modes from one-dimensional lines along specific axes to a volume of space surrounding those lines.[317,319]

An important consideration when interpreting these phonon dispersion relations is the extent to which different branches are populated at ambient temperature. We include in Figure 3.12 a marker at 26 meV—the available thermal energy at 300 K.

Modes at higher energy than this value are relatively unpopulated at the temperature at which our PDF measurements were carried out. Hence we expect reduced sensitivity to the true energies of this part of the phonon spectrum through PDF analysis. By contrast, the PDF will be dominated by displacement driven by the very lowest-energy branches, which is why the force constants governing octahedral tilts appear to be well constrained in our empirical model. Similar conclusions regarding varying sensitivity of the PDF to contributions from different phonons were reached in the earlier studies of Refs. 345–347.

$CuPt(CN)_6$ Phonon dispersion relations

The phonon dispersion relations for $CuPt(CN)_6$, calculated from our empirical model, are shown in Fig. 3.14. While the phonon spectrum spans similar energies to that of $MnPt(CN)_6$ shown in Fig. 3.12, there are a number of key differences that deserve comment. The primary difference arises because the reduced crystal symmetry of $CuPt(CN)_6$ associated with cooperative Jahn–Teller distortion increases the number of symmetry-distinct phonon branches, and also breaks the degeneracy between the two X points (we retain the face-centred cubic nomenclature for high-symmetry points in the Brillouin zone). The tilt modes are nonetheless retained at approximately 10 meV, and again these are associated with large and negative Grüneisen parameters. Interestingly, a non-rotational branch of the phonon dispersion has fallen to a similar energy scale in this case. These non-rotational phonons appear to involve deformations within the CuN_6 octahedra and arise from the weaker potentials involving axial Cu–N linkages. Because the bending of Cu–NC–Pt linkages behaves like the transverse modes of the 'tension mechanism' for NTE, this branch in the phonon spectrum is also associated with strongly negative Grüneisen parameters.

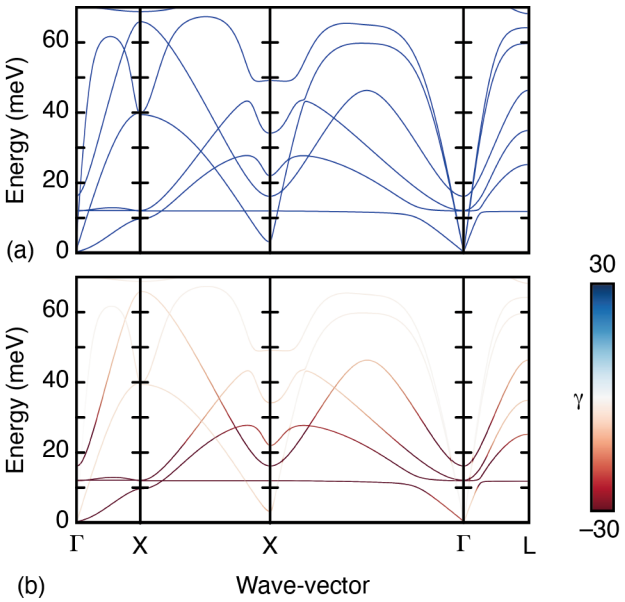


Figure 3.14: Phonon dispersion relations for $CuPt(CN)_6$ determined from our PDF-derived lattice dynamical model. Panel (a) shows the phonon dispersion itself, and panel (b) shows the same set of curves, coloured according to the corresponding mode Grüneisen parameters.

3.6 Conclusions

So what has our analysis achieved? We have shown how a simple model, with remarkably few parameters, is able to describe the key thermal fluctuations in transition-metal hexacyanometallates, accounting for both the experimental PDF and the intensities of Bragg reflections in the X-ray diffraction pattern. The incorporation of the information within PDF data imparts sensitivity to pairwise correlations in these fluctuations, which is what allows us to interrogate the phonon dispersion relations implicit in our empirical model. We find that the low-energy modes—which dominate thermal motion and hence the variation in peak widths in the PDF—are surprisingly well captured in this analysis. In particular, we are able to identify the correct NTE mechanism by inspection of the phonon mode eigenvectors and their corresponding pressure dependence.

The NTE mechanism itself is relatively straightforward: as anticipated elsewhere, the dominant contribution comes from correlated octahedral tilts. The shift

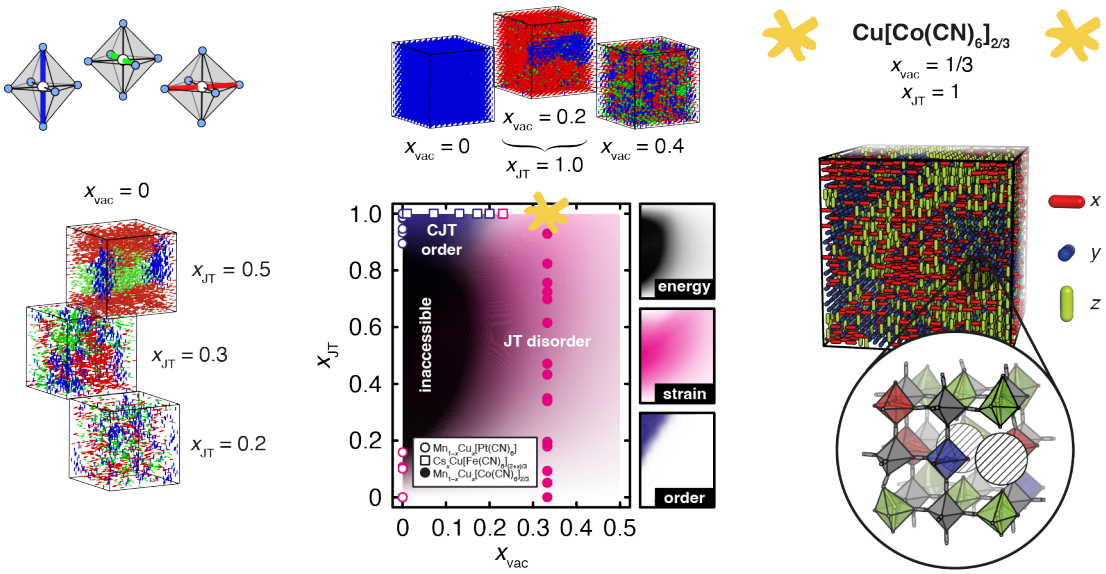
displacements proposed in Ref. 113 also contribute, but to a much lower extent. An important subtlety that emerges from our analysis is that cooperative tilts—which are associated with specific lines in reciprocal space—are only able to drive bulk NTE in hexacyanoplatinates because of the contribution of nearby distortive (qRUM) tilts. Hence the relative deformability of transition-metal coordination environments is an important contributing factor, precisely as implicated in the NTE behaviour of other NTE framework materials such as oxides and fluorides.[317,348] This NTE mechanism may prove to be relatively universal amongst PBAs,[99] given the similar conclusions drawn in the DFT study of $ScCo(CN)_6$.[124]

Thinking beyond these specific hexacyanoplatinate PBAs, our work also introduces a parameter-efficient methodology for fitting PDF data in systems with competing energy scales. Here, we have intentionally focussed on fitting data collected at a single temperature, but our methodology is straightforwardly extended to variable-temperature data sets. In principle, a single set of empirical parameters should account for PDF peak widths across the entire set of data sets, with fits-to-data evaluated using MC simulations performed across a corresponding series of temperatures. This redundancy should improve confidence in the parameter values obtained. In our own work, we have a strong interest in understanding the microscopic behaviour of more complex PBAs, including those applied as cathode materials,[85,242,349] for which the inclusion of hexacyanometallate vacancies and extra-framework cations significantly complicates interpretation of the corresponding PDFs.[1] Our intuition is that sensibly-constrained parameter-efficient methodologies to fitting the PDF will be required for robust characterisation of local structure in these more complex cases.

Chapter 4

Rules governing Jahn–Teller order in Prussian blue analogues

4.1 Overview



Having developed a method for producing atomistic representations of the local structure of relatively simple Prussian blue analogues (PBAs), we are now in a position to explore more complex PBAs, *e.g.* those containing Jahn–Teller (JT) distortions and hexacyanometallate vacancies. JT distortions of transition-metal coordination environments link orbital occupancies to structure. In the solid state, such distortions can be strongly correlated through the propagation of strain and/or through orbital interactions. Cooperative Jahn–Teller (CJT) order of this kind affects the electronic, magnetic, and structural properties of the materials in which it occurs. Conventionally studied in dense ceramics, CJT order also occurs in hybrid materials such as PBAs, but the underlying phenomenology is not well established. In this chapter, synchrotron powder X-ray diffraction measurements are used to de-

termine links between composition and CJT effects in a series of PBA families. A simple model is developed based on the dual considerations of strain and crystal-field stabilisation, and it is shown that this simple model can account for the stability, extent of CJT order, and crystallite strain measured experimentally. This model shows how PBA compositions might be tuned to control the emergence and nature of CJT effects. A key implication of the model is that PBAs harbour their own complex interplay between compositional, structural, orbital, and magnetic degrees of freedom related to that of strongly-correlated functional materials such as the manganite perovskites. Finally, having obtained coarse-grained representations of the directions of JT-distortion axes in PBAs with varying JT and vacancy concentration, the MC-driven 'interaction-space' big-box modelling method for refining pair distribution function (PDF) data (developed in Chapter 3) is used to produce atomistic representations of the local structure of these complex PBA materials for the first time. The hope of measuring PDF data and obtaining a definitive local structure model is discussed in the context of the sensitivity of PDF data to different models of CJT order.

4.2 Acknowledgements

The syntheses of the $Mn_{1-x}Cu_x[Pt(CN)_6]$ and $Mn_{1-x}Cu_x[Co(CN)_6]_{2/3}$ compositional series and initial characterisation were performed by Hanna Boström. John Cattermull carried out the the synthesis of the compositional series $Cs_xCu[Fe(CN)_6]_{(2+x/3)}$ as well as the characterisation of $Cs_xCu[Fe(CN)_6]_{(2+x)/3}$, $Mn_{1-x}Cu_x[Pt(CN)_6]$, and $Mn_{1-x}Cu_x[Co(CN)_6]_{2/3}$ presented in this thesis. The synthesis of the $Cu[Co(CN)_6]_{2/3}$ sample used in the joint Bragg/PDF refinement was carried out by myself, as well as the strain/crystal-field Monte Carlo simulations. I thank Rebecca Witte for providing the correlated vacancy configurations using the model described in Ref. 102. I thank Nikolaj Roth for useful discussions regarding the strain and crystal-field model. I also gratefully acknowledge the provision of beamtime at the Di-

amond Light Source: on beamlines I15-1 (experiment CY26330) and I11 (experiments II16997, EE13284, and CY25166-9). I would like to thank Chloe Coates, Emily Reynolds, Arianna Minelli, Simon Cassidy and the beamline staff for assistance with the collection of diffraction data. Note that the Monte Carlo strain-only model was first developed during my Part II Master's project work. The full work is currently in review and is available on arXiv:

E. A. Harbourne, J. Cattermull, H. L. B. Boström, R. Witte, N. Roth, M. Pasta, D. A. Keen, A. L. Goodwin,
"Rules governing cooperative Jahn–Teller order in Prussian blue analogues",
arXiv:2408.13169, **2024**. Under revision for *Nat. Commun.*

4.3 Introduction

Cooperative Jahn–Teller (CJT) effects are known to impact the physical behaviour of different classes of solid materials.[64,67,125] In the manganite perovskites, the useful property of colossal magnetoresistance is driven by the competition between CJT instabilities, charge, magnetic, and tilt order.[2–5] By contrast, the strain induced when a JT distortion is triggered on extraction of K^+ from the initially-undistorted Prussian blue analogue (PBA) cathode material $KMn[Fe(CN)_6]$ is considered key in limiting the reversible electrochemistry of the system.[245,248] Varying $[M'(CN)_6]^{n-}$ vacancy fraction must also switch on and off CJT order, because the nonstoichiometric cathode material $K_{0.71}Cu[Fe(CN)_6]_{0.72}{\cdot}3.7H_2O$—which exhibits vastly superior cycling behaviour to $KMn[Fe(CN)_6]$—has no cooperative distortion despite its high Cu^{2+} content.[242] Additionally, stoichiometric $Cu[Pt(CN)_6]$ has tetragonal symmetry arising from the cooperative elongation of Cu^{2+} coordination environments along a single common axis [Fig. 1.14(a)], whereas $Cu[Co(CN)_6]_{2/3}$, with a large fraction of vacancies, is cubic despite containing the maximum concentration of JT-active Cu^{2+} ions. A question of the nature of JT disorder in systems lacking long-range CJT order then arises—is there a random arrangement of Cu^{2+} JT distortion axes,

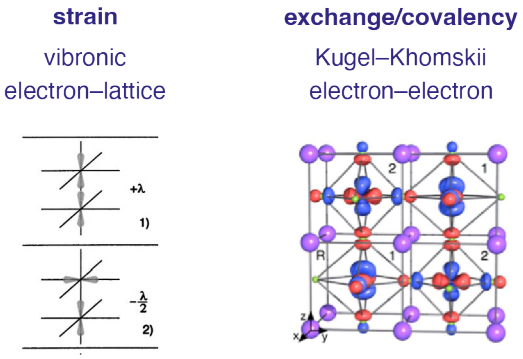


Figure 4.1: Vibronic coupling[125] and electronic exchange mechanisms[351,352] are generally thought to be the primary mechanisms responsible for driving cooperative Jahn–Teller order in dense transition-metal compounds.

or is there some kind of short-range JT order within a globally undistorted cubic structure? In these systems, an interplay between cooperative JT order and vacancy incorporation could be anticipated. Hence, there is motivation for the establishment of rules, both empirical and theoretical, that govern cooperative Jahn–Teller (CJT) order in PBAs.[350]

Whilst the microscopic mechanisms responsible for CJT (dis)order have been extensively studied in the manganite perovskites,[65,160–162] there is currently no clear understanding of these in the case of PBAs. In the context of dense transition-metal compounds, such as perovskites, spinels, and rocksalts, two primary mechanisms dominate [Fig. 4.1]. The first is vibronic coupling, in which the orbital occupation of one JT-active site couples with that of others through lattice strain,[125] and the second is the Kugel–Khomskii mechanism, whereby electronic exchange drives CJT order directly through orbital interactions alone.[351,352] Since strain effects are generally less important in framework materials[127] and exchange interactions are also substantially weaker [Fig. 1.13],[128] it could be argued that the vibronic coupling and Kugel–Khomskii mechanisms might be less likely to drive CJT order in these materials at room temperature. Hence, the work of this chapter explores whether simple geometric ideas might help rationalise the emergence and phenomenology of CJT order in PBAs.

To explore the interplay between cooperative JT effects and vacancy incorporation, three compositional series are studied—*viz.* $Mn_{1-x}Cu_x[Pt(CN)_6]$, $Cs_xCu[Fe(CN)_6]_{(2+x)/3}$, and $Mn_{1-x}Cu_x[Co(CN)_6]_{2/3}$—using high-resolution synchrotron X-ray diffraction measurements to characterise their phase stability and extent of long-range CJT order as a function of JT dilution and hexacyanometallate vacancy concentration. These three particular series have been chosen since they allow us to isolate and hence identify the separate effects of (i) increasing JT concentration in a vacancy-free system, (ii) increasing vacancy concentration in a fully JT-active system, and (iii) introducing JT activity within a partially-vacant PBA. We infer from our experimental measurements of the first two families a simple microscopic model governing CJT order based on the competition between strain and crystal-field effects. This model allows a generic phase diagram for PBAs with different JT/vacancy compositions to be developed, identifying compositions for which CJT-driven symmetry breaking is expected. The veracity of the model is demonstrated by comparing prediction against observation for the third family. An important result that emerges is that local CJT order in vacancy-rich PBAs adopts different patterns to the long-range order observed at low vacancy concentrations, suggesting that the family harbours its own complex interplay between compositional, structural, orbital, and magnetic degrees of freedom not unlike that found in the manganite perovskites.[2,16,59,353] Finally, access to coarse-grained representations of JT orientations in JT-dilute and/or partially-vacant PBAs then allowed, for the first time, the construction of atomistic models of the local structure in these systems using the simple 'interaction-space' PDF refinement approach developed in the previous chapter.

4.4 Methods

4.4.1 Synthesis and characterisation

A powder sample of $Cu[Co(CN)_6]_{2/3}$ for pair distribution function analysis was prepared following a co-precipitation method similar to the one described in Ref. 242. 0.110 g of $K_3[Co(CN)_6]$ (0.333 mmol) was dissolved in 50 mL H_2O, stirring at 50 °C in an oil bath. An aqueous solution of $CuSO_4 \cdot nH_2O$ (0.5 mmol in 40 mL H_2O) was added dropwise with stirring to the $K_3Co(CN)_6$ solution over 20 min, to give a white precipitate. The solution was left to stir for another 30 min at 50 °C before being removed and left to stand at room temperature for 45 min. The precipitate was then separated and washed three times with H_2O by centrifugation. The solid was dried in air at 70 °C overnight.

The syntheses of the $Mn_{1-x}Cu_x[Pt(CN)_6]$ and $Mn_{1-x}Cu_x[Co(CN)_6]_{2/3}$ compositional series were performed by Hanna Boström. The synthesis of the compositional series $Cs_xCu[Fe(CN)_6]_{(2+x/3)}$ was carried out by John Cattermull. The $Cu[Co(CN)_6]_{2/3}$ sample used for the pair distribution function analysis was carried out by myself. Full details of each of these syntheses are given in Appendix B1.

4.4.2 Powder X-ray diffraction measurements

Our powder X-ray diffraction data made use of the synchrotron X-ray source on the I11 beamline at Diamond Light Source, UK. The diffraction patterns of the sample were collected in capillary transmission geometry. A room temperature X-ray diffraction pattern was collected using the Mythen2 Position Sensitive Detector (PSD), two data collections of 20 seconds each were taken at angles 0.25 degrees apart, then summed to account for gaps in the detector coverage. The X-ray wavelengths used were 0.825070 Å($Cu_xMn_{1-x}[Pt(CN)_6]$ and $Cu_xMn_{1-x}[Co(CN)_6]_{2/3}$ series) and 0.826060 Å($Cs_xCu[Fe(CN)_6]_{(2+x)/3}$ series).

Refinement details of $Cu_xMn_{1-x}[Pt(CN)_6]$, $Cu_xMn_{1-x}[Co(CN)_6]_{2/3}$, and powder diffraction patterns of $Cs_xCu[Fe(CN)_6]_{(2+x)/3}$ are given in Appendix B2.

4.4.3 PDF measurements

X-ray total scattering measurements were performed using the I15-1 (XPDF) beamline at the Diamond Light Source. Samples were loaded in thin-walled borosilicate capillaries (1mm diameter) and data measured under ambient conditions with an exposure time of 600 s. The X-ray energy used was 76.69 keV ($\lambda = 0.161669$ Å), which gave a useable scattering range $0.35 \leq Q \leq 19$ Å^{-1}. The data were corrected for background, multiple scattering, container scattering, Compton scattering, absorption, and Bremsstrahlung effects and placed on an absolute scale (normalisation) using GudrunX; details of the core data reduction process and the corrections listed here can be found in Ref. 333. The normalised data were Fourier transformed to yield the corresponding PDFs, following the procedure outlined in Refs. 185,333.

4.4.4 Monte Carlo simulations: simulation implementation

Three-dimensional (3D) supercell configurations of the (face-centred cubic) PBA architecture were generated, assigning a specified fraction of M-site ions as JT-active (x_{JT}). The corresponding number of JT-active M-site ions are distributed randomly across the M-sites. The JT-axis orientation of JT-active M-site ions is treated as a 3-state Potts variable[145] where an individual JT-distortion can point along one of the x-, y-, or z-axes. The JT-distortion orientation of each M-site is assigned randomly. Similarly, given a pre-determined vacancy fraction, x_{vac}, vacancies are distributed randomly across the M′-sites. The distribution of both M-site ions and M′-site vacancies is considered fixed and is not allowed to vary during MC simulations.

A simulated annealing approach was employed, starting with a Monte Carlo temperature $T = 10\,J$. Simulations proceeded by choosing JT-active ions at random and switching the corresponding Potts variable. Moves were accepted or rejected

according to the usual Metropolis algorithm.[197,321] Simulations were continued at each temperature until equilibrium was achieved, which we determined by allowing 150 accepted moves for each JT-active site. We found this to be a suitable balance between safe convergence and computational expense. Following equilibration, the system temperature was reduced by a factor of 0.1, with the same process repeated at each temperature.

We determined the degree of cooperative JT order in a single MC simulation using the order parameter

$$\phi = \frac{1}{2}(|m_x - m_y|^2 + |m_y - m_z|^2 + |m_z - m_x|^2), \tag{4.1}$$

where (*e.g.*) $m_x = N_x/N_{\mathrm{JT}}$ is the fraction of JT-active M-sites oriented along the x-axis, *etc.* Values of ϕ are the averages over 100 independent simulations, and error bars denote the standard uncertainty in the error of each measurement.

4.5 Results and Discussion

4.5.1 $Cu_xMn_{1-x}[Pt(CN)_6]$: varying JT content

Anisotropic strain models are often used to rationalise CJT effects in many conventional oxide perovskites,[67,354] and so we sought to establish the simplest such model that could explain this miscibility gap in PBAs. The starting point to our model was to consider the implications of JT activity on the local strain within the corners of the PBA network. The model we developed was based on deformations of rectangular windows of the PBA framework as a function of the number and (relative) orientation of long JT-active bonds. Here we are following a similar approach to that developed for capturing JT-driven strains in perovskites in Refs. 354 and 355. A Taylor expansion of the energy for each corner-angle, θ_i, around its equilibrium

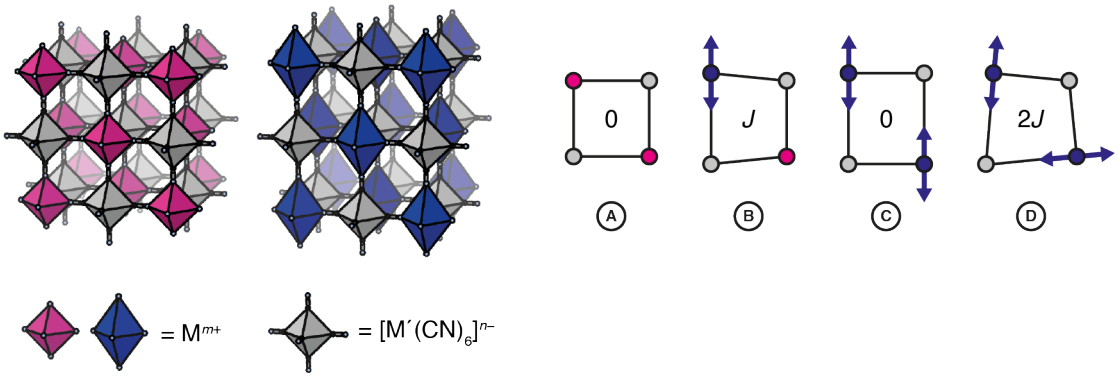


Figure 4.2: Strain model for cooperative JT effects in PBAs. Squares represent windows of the PBA structure, and coloured circles represent M/M′ sites: magenta = JT-inactive M-site or JT-active M-site with out-of-plane axial elongation, blue = JT-active M-site with in-plane elongation, grey = M′-site. Blue arrows denote the local axis of JT-driven elongation. The four possible scenarios give rise to strain energies that are approximate multiples of a common factor J.

value, $\frac{\pi}{2}$, is given by

$$E(\theta_i) = E_0 + E_2(\theta_i - \frac{\pi}{2})^2 + ... \tag{4.2}$$

We express the lattice energy as a sum over the angular strain within PBA network "windows"

$$E_{\text{latt}} = \sum_{\square} \sum_{i \in \square} E(\theta_i), \tag{4.3}$$

where we neglect the anharmonic (higher order) terms in Eq. 4.2. Here the symbol $\square$ denotes a window of the PBA structure. In the absence of vacancies, there are four distinct cases to be considered for each window (Fig. 4.2) and simple geometric considerations allow assignment of strain energies as integral multiples of a common energy scale J. The MC energies are calculated by determining the $(E_{\square} - 4E_0)/\delta^2 E_2 \in \{0, 1, 2\}$ values for each window of the MC configuration and taking the total sum. The equilibrium MC energy is therefore a coarse-grained representation of the internal strain of a configuration with the energy scale given by J.

The incorporation of JT-active ions within the lattice windows leads to a variation in the equilibrium edge-lengths. Since bond-stretching energies are higher than

bond-bending energies, the strain so generated is taken to be accommodated within the window angles. Simple geometry then gives the following first-order strain energies for each window decoration:

Case	θ_1	θ_2	θ_3	θ_4	$(E_\square - 4E_0)/E_2$
A	$\frac{\pi}{2}$	$\frac{\pi}{2}$	$\frac{\pi}{2}$	$\frac{\pi}{2}$	0
B	$\frac{\pi}{2}+\frac{\delta}{2}$	$\frac{\pi}{2}+\frac{\delta}{2}$	$\frac{\pi}{2}-\frac{\delta}{2}$	$\frac{\pi}{2}-\frac{\delta}{2}$	δ^2
C	$\frac{\pi}{2}$	$\frac{\pi}{2}$	$\frac{\pi}{2}$	$\frac{\pi}{2}$	0
D	$\frac{\pi}{2}+\delta$	$\frac{\pi}{2}$	$\frac{\pi}{2}-\delta$	$\frac{\pi}{2}$	$2\delta^2$

where δ is a measure of the relative difference between JT-active and JT-inactive bond lengths and $J \stackrel{\text{def}}{=} \delta^2 E_2$.

The numerical value of J for a given PBA will be related to its elastic moduli, which typically range $9 < E, G < 50\,\text{GPa}$.[356] It is straightforward to show that

$$J \simeq \frac{G(d_{\text{JT}})^2 a}{4}, \tag{4.4}$$

where d_{JT} is the additional cell-length elongation associated with Jahn–Teller distortions ($\sim 0.4\,\text{Å}$), and a the underlying cubic unit cell constant (~ 5) Å. In this way, one expects $1 < J < 6\,\text{kJ mol}^{-1}$.

We used this simplified strain model as the basis of a series of Monte Carlo (MC) simulations in which Cu/Mn sites were allocated randomly and JT-orientations were treated as free variables.

4.5.2 $\text{Cu}_x\text{Mn}_{1-x}[\text{Pt(CN)}_6]$: varying JT content

Our first set of MC simulations involved vacancy-free configurations with varying concentrations of JT-active M-site ions. The key results of these simulations are summarised in Fig. 4.3. At high temperatures, there is a disordered arrangement of JT axes, and for compositions above a critical JT fraction, a phase transition is observed on cooling that is characterised by the evolution of long-range CJT order

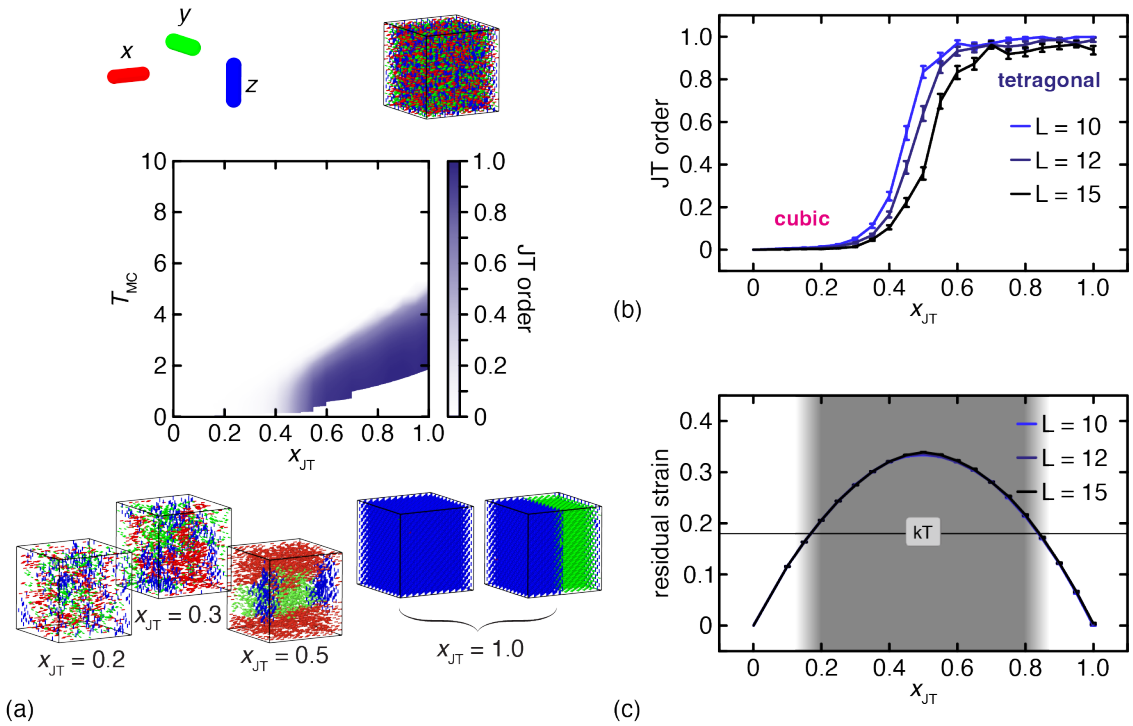


Figure 4.3: Evolution of long-range CJT order in vacancy-free PBAs. (a) Simulated annealing for $12 \times 12 \times 12$ supercells. JT order as function of $T_{\mathrm{MC}} = \frac{T}{J}$ and x_{JT}. (b) Compositional-dependent ground-state order parameter ϕ_{GS} as a function of system size L. (c) The ground-state average strain per window as a function of x_{JT} (also shown for different supercell dimensions).

(Fig. 4.3(a)). Subtle differences in ordering temperature and critical composition are observed for different MC box sizes. As box-size increases, and at low effective temperatures, the composition at which a phase transition to a long-range CJT state is predicted to emerge shifts to higher JT fractions—$x_{\mathrm{JT}} \approx 0.36$, $x_{\mathrm{JT}} \approx 0.37$, and $x_{\mathrm{JT}} \approx 0.45$ for $10 \times 10 \times 10$, $12 \times 12 \times 12$, and $15 \times 15 \times 15$ supercells, respectively (Fig. 4.3(b)). The higher JT fraction for the emergence of long-range CJT order as box-size increases is likely to reflect the greater propensity for domain formation, which reduces the order parameter. An example of a $12 \times 12 \times 12$ $x_{\mathrm{JT}} = 1$ MC configuration that formed domains is shown in Fig. 4.3(a).

The ground-state MC energies capture the degree of residual strain within the configurations, and the corresponding values as a function of JT-active composition are shown in Fig. 4.4(c) and Fig. 4.3(c). Of the four window types shown in Fig. 4.2,

only distortion case "B" contributes to the ground-state strain, and so the binomial distribution gives the analytical form

$$E = \frac{4J}{3} x_{\mathrm{JT}}(1 - x_{\mathrm{JT}}), \tag{4.5}$$

for ground-state strain, which is followed closely by our simulations (Fig. 4.3(c)).

In order to validate our model against experiment, the solid-solution $Cu_xMn_{1-x}[Pt(CN)_6]$ was prepared and characterised experimentally. The Mn^{2+} and Cu^{2+} endmembers gave X-ray diffraction patterns characteristic of the cubic and tetragonal PBA phases anticipated for JT-free and CJT-ordered states, respectively.[121] For a number of intermediate compositions, we observed a mixture of both cubic and tetragonal phases, with lattice parameters slightly different to those of the corresponding endmembers (Fig. 4.4(a)). We estimated the composition of each phase assuming a Vegard's law relation with respect to cell volume, and determined phase fractions using constrained Rietveld refinement (see Appendix B2.2). There was good agreement between overall compositions determined crystallographically and from atomic absorption spectroscopy (AAS) measurements (see Appendix Table B1.3). Our data indicated a miscibility gap for $0.15 \lesssim x \lesssim 0.85$ characteristic of limited solubility of JT-active ions in an undistorted crystal lattice and vice versa (Fig. 4.4(b)). Any samples made with nominal compositions in this range formed as a mixture of two phases, one cubic and one tetragonal, with the compositions of the cubic and tetragonal phases varying between $0 \lesssim x \lesssim 0.15$ and $0.85 \lesssim x \lesssim 1$, respectively (Fig. 4.4(b)). Incorporation of some JT-active Cu within a Mn-rich phase (or vice versa) led to increased strain, as evidenced in the widths of Bragg reflections. Our Rietveld refinements allowed us to quantify this strain, which we found to vary symmetrically with composition (Fig. 4.4(c)).

The composition–strain relationship observed experimentally is captured qualitatively by the MC model (Fig. 4.4(c)). Hence, we interpreted these ground state

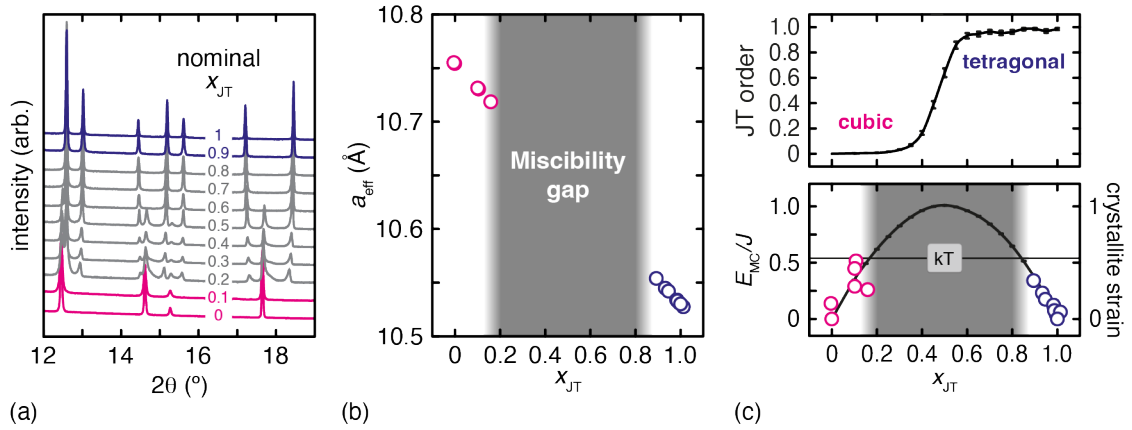


Figure 4.4: Structural behaviour of $Cu_xMn_{1-x}[Pt(CN)_6]$ PBAs. (a) Representative region of the X-ray diffraction patterns ($\lambda = 0.825070$ Å) measured as a function of nominal composition. On substitution of Mn^{2+} by Cu^{2+} (increasing x_{JT}, bottom–top) the simple diffraction pattern of the cubic aristotype gradually decreases in intensity, and a more complex pattern associated with the tetragonal CJT structure type emerges. Small shifts in peak positions and variation in peak widths are also observed. (b) The effective lattice parameters $a_{eff} = \sqrt[3]{4V/Z}$ extracted from the data in (a) using Rietveld refinement, and the corresponding JT compositions x_{JT} estimated from Vegard's law. Data points corresponding to cubic (undistorted) phases are shown in magenta, and those of tetragonal (distorted) phases are shown in blue. These data show the existence of a miscibility gap. (c) Coarse-grained MC simulations driven by the strain model shown in Fig. 4.2 give ground-state structures with varying degrees of CJT order (top) and residual strain (bottom, solid line). The isotropic strain broadening measured in our Rietveld refinements of the data in panel (a) are shown as open circles, and are coloured according to the presence (blue) or absence (magenta) of long-range JT order. The thin horizontal line denotes the accessible thermal energy at room temperature for $J = 5\,\mathrm{kJ\,mol^{-1}}$. Standard uncertainties in the data shown in panels (b) and (c) are smaller than the symbols.

energies as a measure both of the enthalpic cost of solid-solution formation and of the residual strain arising from elastic mismatch between short and long-range CJT effects within the mixed-composition phase. The phase-segregation behaviour of $Cu_xMn_{1-x}[Pt(CN)_6]$ could then be rationalised if $J \sim 5\,\mathrm{kJ\,mol^{-1}}$, whereby the available thermal energy during synthesis would allow access only to a JT-dilute undistorted phase, a JT-rich long-range-ordered phase, or mixtures thereof. It is difficult to validate this energy scale directly using *e.g.* DFT calculations by virtue of the size and complexity of JT-dilute PBA configurations, but we note that it is consistent with expectation from the elastic moduli of PBAs.[356] Some variation in the magnitude of J will occur amongst different PBA systems, in turn broadening or narrowing the miscibility gap accordingly.

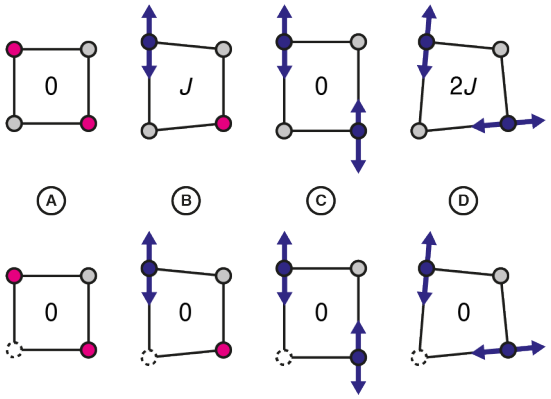


Figure 4.5: Strain-only model: incorporation of a vacancy in a network window relieves all strain. Note that the cyanides are not shown. M′-site ions, which are JT-inactive, are shown as grey circles, vacant M′-sites are shown as dotted circles, JT-inactive/JT-axis out-of-plane M-site ions are shown as magenta circles, JT-active M-site ions with in-plane elongation are shown as blue filled circles with the JT elongation axes shown as blue double-headed arrows.

4.5.3 $Cs_xCu[Fe(CN)_6]_{(2+x)/3}$: varying vacancy content

Our next step was to consider the effect of incorporating hexacyanometallate vacancies on the emergence of CJT order.

Initial model: strain-only

Our next set of simulations involved varying M′-site vacancy content within a fully-JT-active configuration. Arguably the simplest way in which to incorporate the effect of vacancies within a strain model is to assume that the presence of a vacancy relieves all strain in the neighbouring windows. Such a modification was easily implemented within our MC simulations by saying that when there is an M′-site vacancy within a network window, all angular strain within that window relieved and gives a strain contribution of zero (Fig. 4.5).

The key results of these simulations are shown in Fig. 4.6, and we note that the $x_{\mathrm{vac}} = 0$ run here is identical to the $x_{\mathrm{JT}} = 1$ system given above. Again, at high temperatures, there is a disordered arrangement of JT axes, and for compositions below a critical vacancy fraction, there is a phase transition below a critical temperature to a state with long-range CJT order (Fig. 4.6(a)). Increasing the vacancy

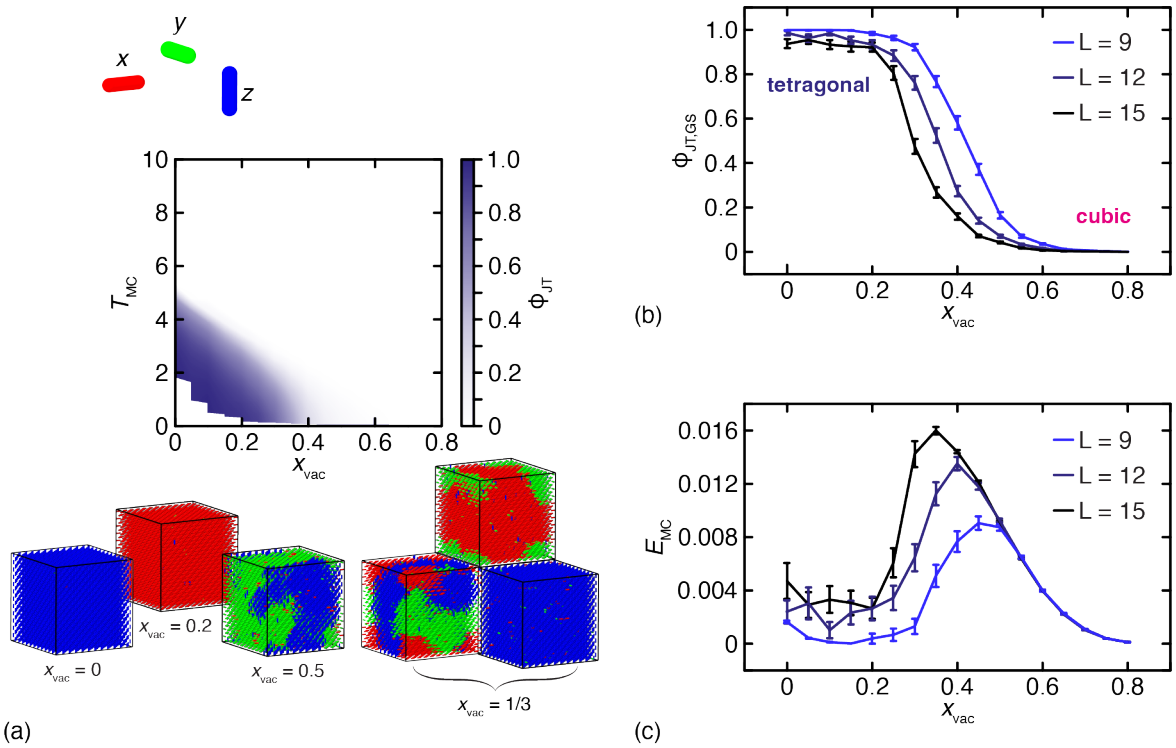


Figure 4.6: Evolution of long-range CJT order in partially-vacant JT-active PBAs. (a) Simulated annealing for $12 \times 12 \times 12$ supercells. JT order as function of $T_{\rm MC} = \frac{T}{J}$ and $x_{\rm vac}$. (b) Compositional-dependent ground-state order parameter $\phi_{\rm GS}$ as a function of system size L. (c) The ground-state average strain per window as a function of $x_{\rm vac}$ (also shown for different supercell dimensions).

fraction lowers the JT-ordering transition temperature (Fig. 4.6(a)). We found that ground-state long-range CJT order vanishes with increasing vacancy concentration (Fig. 4.3(b)). We again tested for finite size effects (Fig. 4.6(b)), and we saw that the critical vacancy fraction below which long-range CJT order emerges decreases with increasing box size—$x_{\rm vac} \approx 0.54, 0.45$, and 0.37 for $9 \times 9 \times 9$, $12 \times 12 \times 12$, and $15 \times 15 \times 15$ supercells, respectively. The reduction of the critical vacancy fraction for long-range CJT order with larger simulation boxes reflects the easier formation of domains as system size grows.

In principle, one expects the ground-state energies of all these MC configurations to be identically zero, since coalignment of all JT axes will give zero strain energy in all cases. In practice, the formation of domains near the critical composition gives rise to a very small residual energy, which is consequently box-size dependent

(Fig. 4.6(c)). Note that this energy scale is two or three orders of magnitude smaller than that of the residual strain plot shown in Fig. 4.3(c).

$Cu[Co(CN)_6]_{2/3}$, with $x_{\text{vac}} = 0.33$, is experimentally known to be cubic with no long-range CJT order;[134] however, long-range CJT order was more resilient than this in our model. Examples of $12 \times 12 \times 12$ ground-state MC configurations with $x_{\text{vac}} = 0.33$ are shown in Fig. 4.6(a); there is considerable variation between independent MC configurations, which is expected for critical fluctuations. Whilst configurations with long-range CJT order occasionally emerge, how often they emerge decreases as system size increases (Fig. B3.10), reflecting the greater propensity for domain formation as box size increases. So, whilst it might appear that $x_{\text{vac}} = 0.33$ is on the cusp of long-range CJT order for $15 \times 15 \times 15$ supercells—the critical vacancy fraction for long-range CJT order for $15 \times 15 \times 15$ supercells was $x_{\text{vac}} \approx 0.37$—the pictures of CJT order in these $x_{\text{vac}} = 0.33$ compositions often reflect large domains of short-range CJT order. Hence, long-range CJT order persists to higher vacancy fractions than observed in practice.

Correlated vacancies

We next considered the possibility that the high critical vacancy fraction predicted by these MC simulations ($x_{\text{vac}} \simeq 0.5$) might reflect the fact that a random distribution of vacancies was used in these MC simulations. The possibility of vacancy correlations, at least in single-crystal PBA samples, was established in Ref. 102, hence we wanted to determine whether the vacancy arrangement affects the propensity for long-range CJT order.

We carried out a further series of MC simulations in which the vacancy distributions were not assigned randomly, but rather determined by a parent MC simulation carried out as described in Ref. 102. The vacancy correlation Hamiltonian given in Ref. 102 was modified to allow for different vacancy fractions. In the same study, it was noted that varying the nature of the M′-site cation (*e.g.* from Co^{3+} to Mn^{3+})

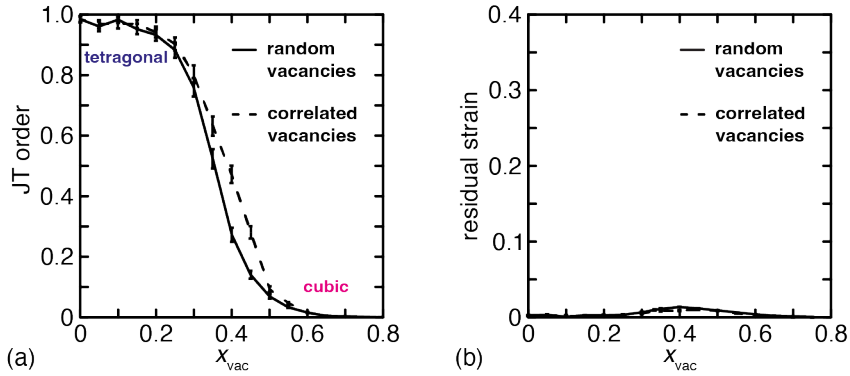


Figure 4.7: Dependence of (a) ground-state CJT order and (b) ground-state residual strain on M′-site vacancy concentration determined using MC simulations. The black data points correspond to simulations driven only by the strain model illustrated in Fig. 4.5. Data connected by solid lines correspond to random vacancy distributions, and data connected by dashed lines correspond to configurations in which vacancies were distributed with the correlations determined for single-crystal samples in Ref. 102. Standard uncertainties in the data shown are smaller than the symbols.

had no obvious effect on phase behaviour, and with this in mind we expect the numerical results for M′ = Co to apply also to our systems with M′ = Fe. Having assigned vacancy distributions according to the correlated-vacancy model of Ref. 102, we proceeded to carry out our own JT-orientation MC simulations as described above. All simulations were carried out using $12 \times 12 \times 12$ supercells.

We found similar behaviour in our MC simulations for both random- and correlated-vacancy distributions (Fig. 4.7), suggesting that the incorporation of vacancy correlations has little material effect on the evolution and nature of CJT order in our MC simulations. Instead, the robustness of CJT order in this simple model likely reflects the high topological connectivity of the underlying face-centred cubic net. While we show here the behaviour for the specific case $x_{\mathrm{JT}} = 1$, similar results were obtained for all combinations of x_{JT}, x_{vac} tested.

Extended model: inclusion of crystal-field

The obvious ingredient missing in our microscopic model was to consider how the presence of a vacancy might influence JT-axis orientations of neighbouring sites. It is known from the layered structure of $CuNi(CN)_4$,[357] for example, that the fully-

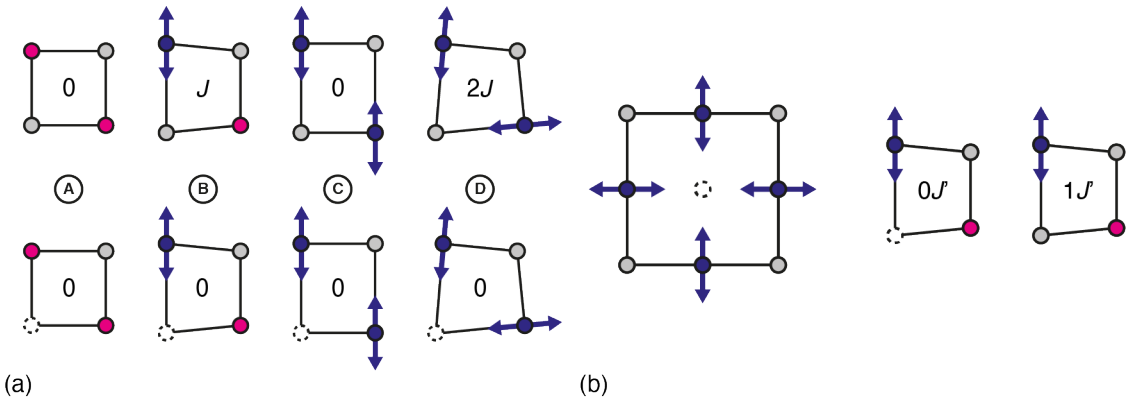


Figure 4.8: (a) Strain-only model. (b) Updated vacancy model. Note that the cyanides are not shown. M′-site ions, which are JT-inactive, are shown as grey circles, vacant M′-sites are shown as dotted circles, JT-inactive/JT-axis out-of-plane M-site ions are shown as magenta circles, JT-active M-site ions with in-plane elongation are shown as blue filled circles with the JT elongation axes shown as blue double-headed arrows.

occupied e_g^* orbital of Cu^{2+} is always oriented orthogonal to its planar N_4 coordination environment—*i.e.* towards the vacancies in its coordination shell. Likewise, in a recent DFT study of copper hexacyanoferrates,[135] the JT axes of Cu^{2+} ions were found to point towards vacancies, irrespective of whether or not the relevant coordination site was occupied by water. This anisotropy is ultimately a crystal-field effect: both H_2O and vacancies are weaker-field ligands than N-bound cyanide.[358]

Consequently, we introduced an additional crystal-field term in our MC Hamiltonian that penalised JT orientations pointing towards an occupied site (Fig. 4.8(b)). In practice, this term was introduced into our MC simulations by attaching an additional energy cost J' to any JT-active M-site ion whose JT axis pointed directly at an occupied M′ site.

We repeated our MC simulations of the evolution of CJT order in partially-vacant JT-active PBA systems including this additional crystal-field term; a summary of the key results is given in Fig. 4.9. Here we show the effect of three different values of J': the $J' = 0$ case is of course identical to the original model without crystal-field terms, the $J' = J$ series is the case on which we focus, and $J' = 2J$ is included for additional context. Again, at high temperatures, there is a disordered arrangement

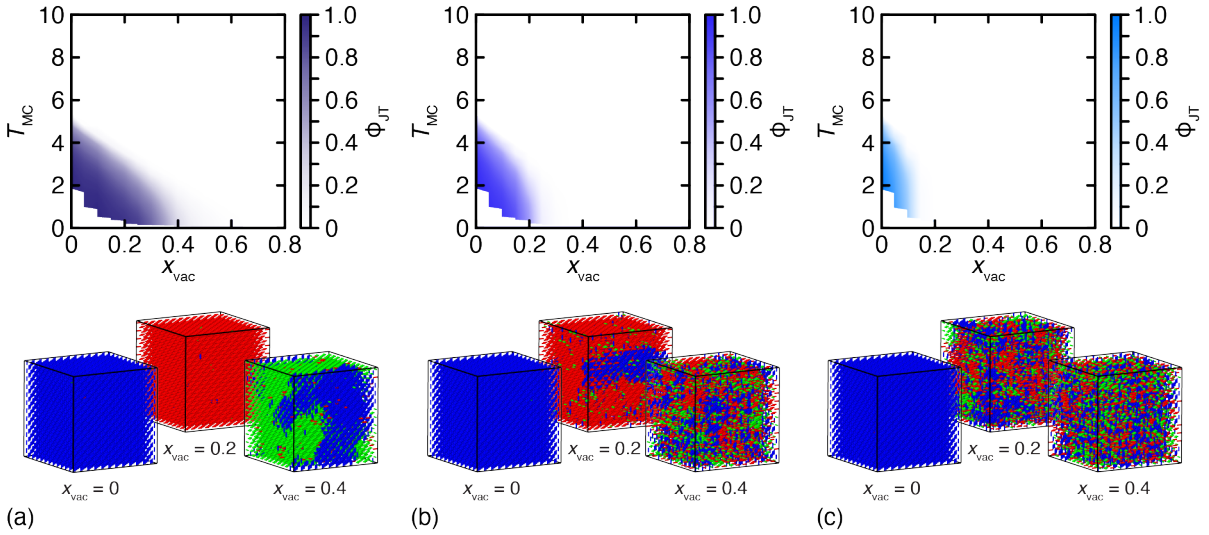


Figure 4.9: Summary of the effect of the crystal-field term on the evolution of CJT order in JT-active PBAs. (a) $J' = 0$ (these are the same data shown in Fig. 4.6, reproduced here for ease of comparison). (b) $J' = J$ is the case where crystal-field and strain effects are of similar energy scales, and is the situation on which the main text focuses. The ground-state order parameter values are those shown in Fig. 4.10. (c) As the crystal-field term is increased further to $J' = 2J$, CJT order is suppressed more quickly on vacancy incorporation.

of JT axes, and for compositions below a critical vacancy fraction, there is a phase transition on cooling to a state with long-range CJT order. MC simulations incorporating this additional crystal-field term showed a lower critical vacancy fraction for vacancy order (Fig. 4.9), and again was independent of vacancy correlations (Fig. 4.10). Varying the relative strengths of crystal-field and strain terms simply shifts the critical vacancy fraction at which CJT order emerges/disappears, so we expect this threshold to differ slightly amongst different PBA families. The key point is that long-range CJT order is suppressed more quickly on vacancy incorporation by increasing the strength of the crystal-field term (J'); when $J' = 0$, the critical vacancy fraction is ≈ 0.45 for a $12 \times 12 \times 12$ supercell, whereas when $J' = 1$, the critical vacancy fraction is ≈ 0.28. Hence, when $J' = 1$, the $x_{\text{vac}} = 0.33$ composition is predicted to be cubic with no long-range CJT order. Given that $Cu[Co(CN)_6]_{2/3}$ is cubic experimentally, the addition of this crystal-field term is critical.

Importantly, in the $x_{\text{vac}} = 0.33$ composition, the strain-only model ($J' = 0$) produced configurations that sometimes showed long-range CJT order and sometimes

showed domains of short-range CJT order (Fig. 4.10), whereas no configurations showed long-range CJT order with the inclusion of the crystal-field term (when $J' = 1$) (Fig. B3.11). Whilst the $J' = 1$ $x_{\text{vac}} = 0.33$ configurations did not show long-range CJT order, the arrangement of the JT-distortion axes within the configurations were not random (Fig. 4.10). The principal effect of introducing the crystal-field term is to favour reorientation of the JT-axis directions around vacancies, which acts in competition with the coalignment naturally favoured by strain alone (Fig. 4.10(inset)). This competition introduces a nontrivial texture to the local CJT order, even within configurations that show no long-range CJT order. Hence, the JT texture in the disordered ground states is very different from the domains in the $J' = 0$ configurations.

The parameters J and J' are independent, but from here on we focus on the simplest case $J = J'$ to minimise the number of variables in our parameterisation and since varying J' gives qualitatively similar behaviour.

Experimentally, we explored this point by characterising the diffraction behaviour of the $Cs_xCu[Fe(CN)_6]_{(2+x)/3}$ PBA family, for which the concentration of JT-active Cu^{2+} is constant and maximal. As expected, the vacancy-free material $CsCu[Fe(CN)_6]$ is tetragonally distorted, reflecting long-range CJT order of the Cu^{2+} ions. On increasing the $[Fe(CN)_6]^{3-}$ vacancy fraction $x_{\text{vac}} = \frac{1-x}{3}$, CJT order eventually disappeared such that the limiting composition $Cu[Fe(CN)_6]_{2/3}$ adopted a distortion-free cubic structure. As the 220 reflections are split in the tetragonal CJT-ordered phase but not in the cubic JT-disordered phase, looking at this region of the X-ray diffraction patterns of the $Cs_xCu[Fe(CN)_6]_{(2+x)/3}$ series can help us to determine the critical vacancy fraction for long-range CJT order (Fig. 4.11(a)). The critical vacancy fraction for CJT order appears to be around $x_{\text{vac}} \simeq 20\,\%$, where the Bragg reflections in the X-ray diffraction patterns show particularly strong anisotropic peak broadening (Fig. 4.11(a)). This broadening likely involves contributions from lattice strain, some compositional variations amongst

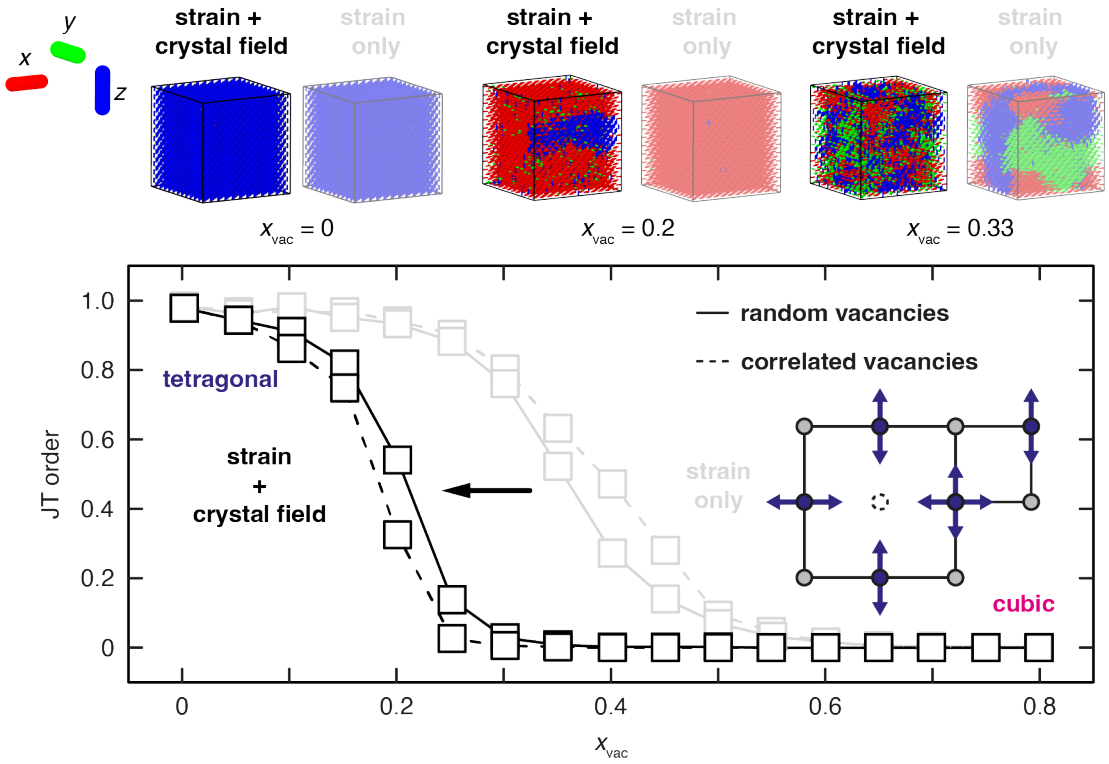


Figure 4.10: Dependence of ground-state CJT order on M′-site vacancy concentration determined using MC simulations on $12 \times 12 \times 12$ supercells. The grey data points correspond to simulations driven only by the strain model illustrated in Fig. 4.8(a); the black data points correspond to the model which also takes into account the crystal-field preference for JT orientations to point towards vacancies (Fig. 4.8(b)). Data connected by solid lines correspond to random vacancy distributions, and data connected by dashed lines correspond to configurations in which vacancies were distributed with the correlations determined for single-crystal samples in Ref. 102. Standard uncertainties in the data shown are smaller than the symbols. Representative configurations from the strain-only model and strain + crystal field model are shown for comparison.

crystallites, and also diffuse scattering as observed elsewhere at morphotropic phase boundaries.[359,360]

With the view to compare the experimental results directly against the MC simulations, the regions of the experimental diffraction patterns around the (220) reflection were isolated (*i.e.* near 13° in 2θ), a linear background subtracted, and the centre-of-mass determined in order to deconvolute the effect of composition-dependent variations in the experimental unit cell parameters. The data were then transformed from scattering angle to reciprocal lattice units such that the centre of mass occurred at the high-symmetry position $2\sqrt{2}$. Converting the MC-predicted

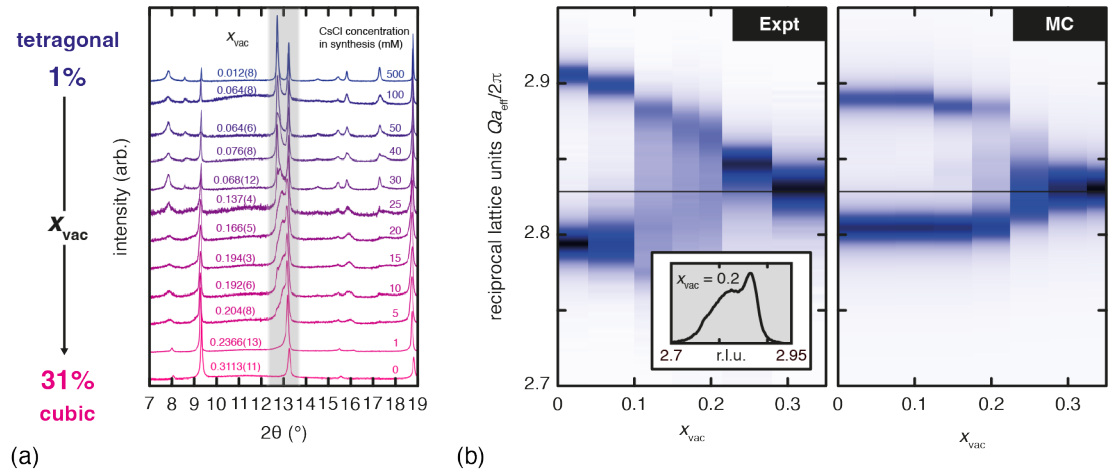


Figure 4.11: Vacancy-driven CJT melting in $Cs_xCu[Fe(CN)_6]_{(2+x)/3}$. (a) Synchrotron X-ray powder diffraction patterns ($\lambda = 0.826060$ Å) of $Cs_xCu[Fe(CN)_6]_{(2+x)/3}$. (b) The region of the X-ray diffraction patterns of $Cs_xCu[Fe(CN)_6]_{(2+x)/3}$ spanning the 220 reflections, which are split in the tetragonal CJT-ordered phase but not in the cubic JT-disordered phase. The thin horizontal line at $2\sqrt{2}$ reciprocal lattice units indicates the high-symmetry 220 position. The left-hand panel shows experimental data: a transition from CJT order to disorder is observed around $x_{\mathrm{vac}} \simeq 0.2$, with strong broadening at critical compositions (inset). The right-hand panel shows the results from MC simulations driven by a combined strain + crystal-field model.

lattice parameters to reciprocal lattice units allowed us to determine that the MC simulations incorporating the additional crystal-field term showed a critical vacancy fraction for long-range CJT order very close to experiment (Fig. 4.11(b)). Our simulations also reproduced qualitatively the strain observed at the order/disorder transition. Crucially, if the $x_{\mathrm{vac}} = 0.33$ composition contained domains of CJT order as predicted by the strain-only model, there would be a signature of this in the corresponding diffraction pattern—the 220 reflections would appear as two broad reflections with reciprocal lattice units centred around two separate values, whereas the strain + crystal field model predicts just the one (Fig. 4.11(b)). Hence, the strain + crystal field model better describes the experimental data.

4.5.4 Determination of a generic PBA phase map

Having identified these two ingredients of strain and crystal-field effects, we were able to map a generalised ground-state phase diagram for PBAs (Fig. 4.12). We carried out a manifold of simulated-annealing MC simulations corresponding to a finely-distributed grid of $x_{\rm JT}$ and $x_{\rm vac}$ values. In all cases, the MC energy was determined using the combined strain/crystal-field model with $J' = J$. For each ground-state configuration, we determined the degree of CJT order, the residual MC energy, and also the residual strain. The MC energies for a given ($x_{\rm JT}$,$x_{\rm vac}$) parameterisation were normalised relative to that of the corresponding two-phase mixture

$$\begin{aligned} E_{\rm MC}^{\rm norm}(x_{\rm JT},x_{\rm vac}) &= E_{\rm MC}(x_{\rm JT},x_{\rm vac}) - x_{\rm JT}\times E_{\rm MC}(1,x_{\rm vac}) + (1-x_{\rm JT})\times E_{\rm MC}(0,x_{\rm vac}) \\ &= E_{\rm MC}(x_{\rm JT},x_{\rm vac}) - x_{\rm JT}\times E_{\rm MC}(1,x_{\rm vac}) \end{aligned} \quad (4.6)$$

to capture the energy penalty associated with solid-solution formation. Our results are shown in Fig. 4.12 along with representations of representative MC configurations at various key compositions.

One prediction of our model is that vacancies stabilise solid solutions of partial JT activity, such that the miscibility gap observed for stoichiometric PBAs (e.g. the hexacyanoplatinates) is eventually closed. Long-range CJT order appears stable only in a relatively small region of the phase diagram—*cf.* the manganites, where orbital order is similarly only found in a relatively small region of its phase diagram[156] (Fig. 1.20(c))—corresponding to low vacancy concentrations and high fractions of JT activity. The crystal-field term has the interesting effect of breaking the symmetry of ground-state strain with respect to JT composition observed in vacancy-free compositions, such that one expects greater residual strain in JT-rich compositions once vacancies are incorporated.

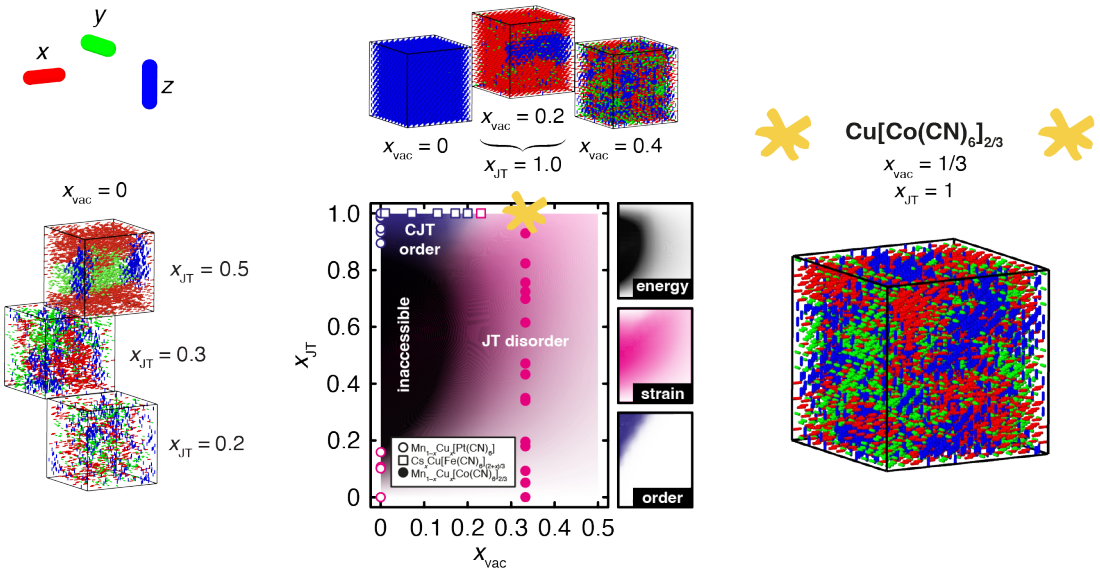


Figure 4.12: Generic ground-state phase map for PBAs. MC simulations driven by strain and crystal-field terms give ground-state structures whose energies, residual strain, and degree of CJT order vary systematically as a function of M-site JT activity and $[M'(CN)_6]^{n-}$ vacancy concentration. The single parameter of this model, J, determines the scales of the energy and strain terms, but affects neither the emergence of CJT order nor the basic form of the features shown here. CJT order is expected only for PBA samples with high fractions of JT-active M-sites and low M′ vacancy concentrations (blue region in top-left). Low-vacancy phases with intermediate x_{JT} fractions are unstable with respect to segregation into JT-poor and JT-rich phases, giving rise to an inaccessible region of phase space (coloured black). The boundary of this region is sensitive to the magnitude of J, which may vary from PBA family to PBA family. Likewise the relative strengths of strain and crystal-field effects determine the vacancy fraction at which CJT order emerges (*i.e.* extent of the blue region), which again may vary amongst PBA families. The phase map is dominated by a continuous region of JT-disordered states, many with large residual strains (shown in pink). JT orientations are not random in these states, but are governed by the competing effects of strain (which favours JT coalignment) and crystal-field (which favours reorientation of JT axes towards vacancies). The coordinates corresponding to each of the systems for which we have experimental X-ray diffraction measurements are shown as data points coloured magenta if the corresponding structure is cubic (no CJT order) or blue if tetragonal (CJT order). Representative MC configurations at different JT/vacancy fractions are shown as small boxes, with the three different local JT orientations shown in red, green, and blue. The location of $Cu[Co(CN)_6]_{2/3}$, the structure of which we study using PDF measurements, is indicated by a yellow star.

4.5.5 $Cu_xMn_{1-x}[Co(CN)_6]_{2/3}$: varying JT content in a partially-vacant series

As a test of these general predictions, we interrogated the structural behaviour of a third and final PBA family of composition $Cu_xMn_{1-x}[Co(CN)_6]_{2/3}$. These materials share a common hexacyanometallate vacancy fraction of $\frac{1}{3}$ but vary systematically in the degree of M-site JT activity. Our experimental X-ray diffraction measurements are summarised in Fig. 4.13(a). In contrast to the phase-segregation behaviour of $Cu_xMn_{1-x}[Pt(CN)_6]$, and as anticipated from our MC results, we observed a series of solid-solutions with cubic symmetry throughout this partially-vacant family. Hence experiment and simulation both demonstrate that vacancy incorporation acts to suppress CJT order and stabilise phases with stronger JT mixing. For intermediate compositions, our data showed unusual peakshapes that reflected a mixture of crystallites with slightly different compositions; decent fits to these data could be obtained using a two-phase model, with the compositional difference between these two phases now relatively small. Our Rietveld refinements allowed us once again to estimate the compositional dependence of isotropic strain, and we found excellent qualitative agreement between experiment and the residual (ground-state) strain anticipated from MC simulations—in particular we recovered the compositional asymmetry highlighted above (Fig. 4.13(b)). So in all respects the structural behaviour of this family is well captured by our simple strain/crystal-field model.

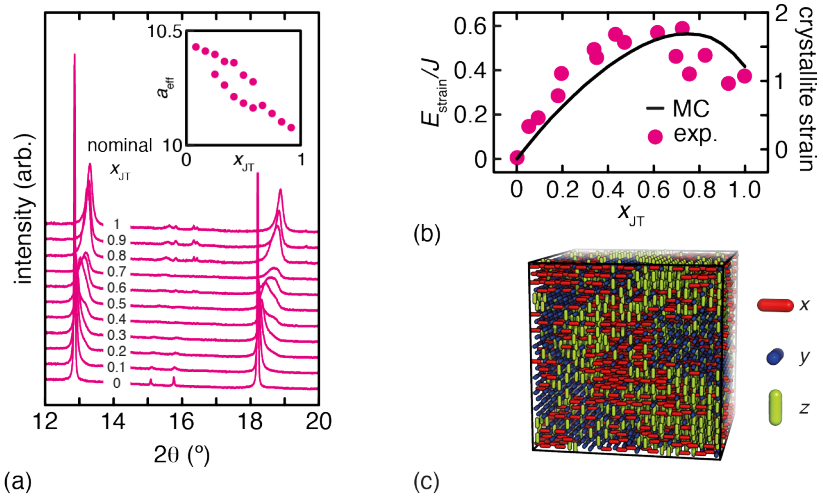


Figure 4.13: Structural behaviour of $Cu_xMn_{1-x}[Co(CN)_6]_{2/3}$ PBAs. (a) Representative regions of the X-ray diffraction patterns ($\lambda = 0.82507$ Å) measured as a function of M-site JT activity. The inset shows the variation in cubic lattice parameter as a function of x_{JT} determined using Pawley refinements. (b) The variation in isotropic crystal strain determined in these refinements (magenta data points) showed an asymmetric dependence on JT fraction that was consistent with expectation from our MC model (black line). Standard uncertainties in the data shown in panels (a) and (b) are smaller than the symbols. (c) Coarse-grained representation of the JT axis orientations in one such MC model, with the different directions of axial elongation shown using rods of different colours. The complex texture that emerges reflects the tension between coalignment and vacancy-driven reorientations governing JT orientations.

4.6 Pair distribution function refinements

Our final step is to test whether the non-trivial texture of JT disordered states predicted by the strain + crystal field model is consistent with experimental measurements. The particular experiment we use is a pair distribution function (PDF) measurement.

4.6.1 Initial small-box PDF refinements of $Cu[Co(CN)_6]_{2/3}$

We first tried to fit the PDF of a $Cu[Co(CN)_6]_{2/3}$ sample using the 'real-space Rietveld' approach implemented in TOPAS.[341] The fits from a joint PDF + Bragg small-box average structure refinement are shown in Fig. 4.14, and gave R_{wp} values of 53.30% for the PDF fit and 9.45% for the Bragg fit. Similar to our conventional small-box average structure fits of $Mn[Pt(CN)_6]$ and $Cu[Pt(CN)_6]$ in Chapter 3 (Subsection 3.5.1), we encountered the issue that the mixture of sharp and weak features in the PDF observed experimentally could not be accounted for satisfactorily. The key obstacle was that the peak widths of the experimental PDF do not increase monotonically with increasing distance r and hence made it difficult to fit both the low-r and high-r regions of the PDF simultaneously. This is a common difficulty associated with PBAs as atom pairs at similar distances can be correlated to very different extents (*e.g.* inter- *vs* intra-polyhedral atom-pairs) and was discussed in more detail in Chapter 3.[329]

Hence, we next decided to use the MC-driven 'interaction-space' PDF refinement approach developed in Chapter 3 to achieve a better description of the changes in peak widths across the PDF; we hoped that this would allow us to test different pictures of local JT order to check whether our predicted non-trivial texture of JT disordered states is consistent with PDF measurements.

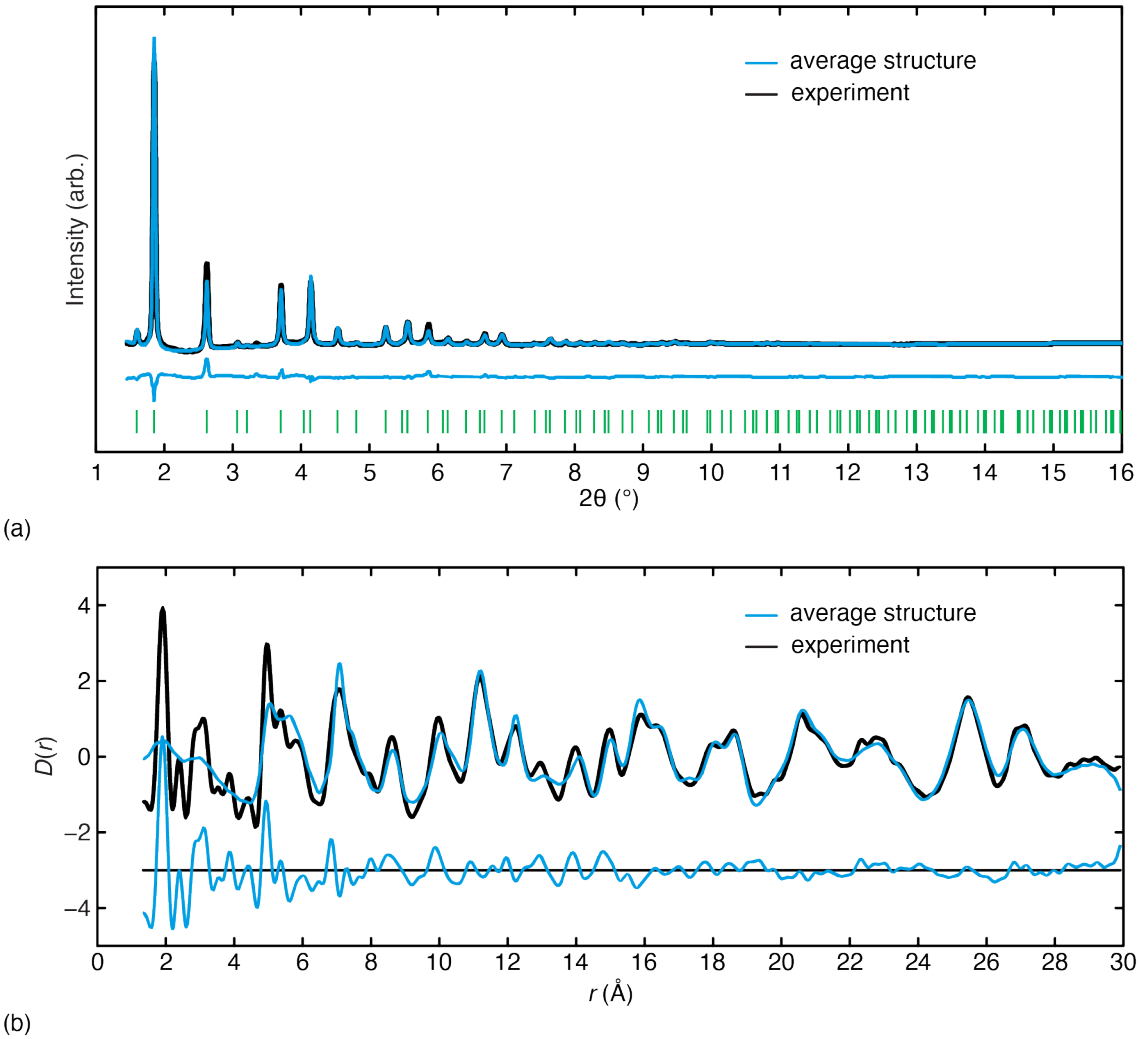


Figure 4.14: The best combined (a) Bragg and (b) PDF fit possible using a conventional small-box Rietveld approach implemented in TOPAS. The experimental data are shown in black, the fits are shown in blue, the difference curves (data−model) are shown in blue shifted vertically, and the tick marks are shown in green.

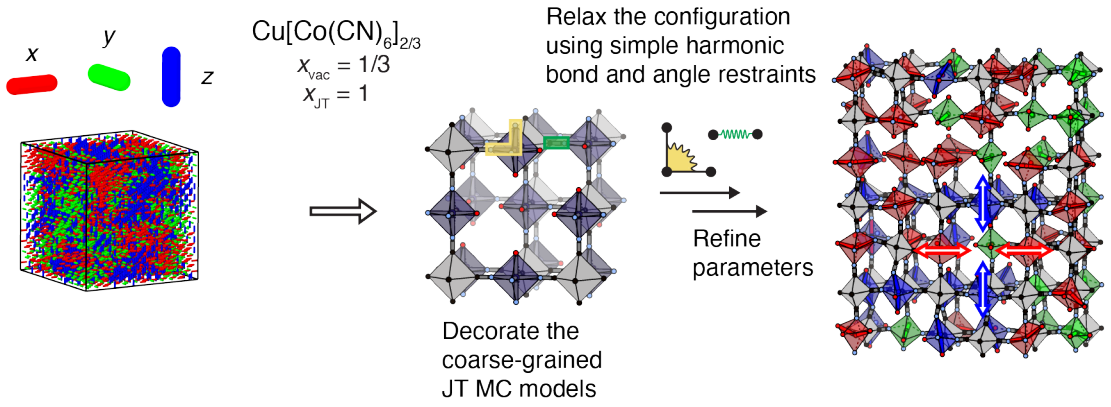


Figure 4.15: An illustration of the process of decorating a coarse-grained JT MC model and then using simple harmonic bond and angle restraints to relax an atomistic representation. A coarse-grained JT MC configuration with $x_{\mathrm{vac}} = \frac{1}{3}$ and $x_{\mathrm{JT}} = 1$ is identified (left). A starting atomistic representation of the PBA structure is then produced (middle), which is then relaxed using simple harmonic bond (green) and angle (yellow) restraints, using Eq. 3.1 as the MC Hamiltonian. A portion of an atomistic representation of $\mathrm{Cu[Co(CN)_6]_{2/3}}$ is shown (right).

4.6.2 Atomistic modelling of $\mathrm{Cu[Co(CN)_6]_{2/3}}$ from coarse-grained MC configurations

Access to coarse-grained representations of JT orientations in JT-dilute and/or partially-vacant PBAs allowed us—for the first time—to construct atomistic models of the local structure in these systems. We illustrate this point with the single representative example of $\mathrm{Cu[Co(CN)_6]_{2/3}}$, chosen because it has at once both high JT activity and high vacancy content. To develop an atomistic model of the local structure in this system, we used the JT arrangements from the relevant MC simulation (*i.e.* as carried out above) to decorate a suitable lattice-dynamical model as described in Chapter 3 and Ref. 329 and illustrated in Fig. 4.15. The model included coordinated water molecules (treated as an O atom) for $\mathrm{Cu^{2+}}$ ions adjacent to vacancies, but did not include zeolitic nor interstitial water. Because our experimental data were measured using X-rays, we omitted H atoms from our model. $6 \times 6 \times 6$ supercells were used, containing a total of 10,080 atoms. The model parameters (equilibrium bond lengths, effective force constants) were systematically varied to best fit the experimental X-ray PDF.

Table 4.1: Empirical parameters used to model the X-ray PDFs of $Cu[Co(CN)_6]_{2/3}$, together with their refined values.

Parameter	Value	Parameter	Value
r(C–N) (Å)	1.15	k_θ(C–Co–C) (eV/rad^2)	0.16
r_e(Co–C) (Å)	1.80	k_θ(N_{eq}–Cu–N_{eq}) (eV/rad^2)	17.12
r_e(Cu–N_{eq}) (Å)	1.99	k_θ(N_{eq}–Cu–N_{ax}) (eV/rad^2)	0.17
r_e(Cu–N_{ax}) (Å)	2.38	k_θ(O_{eq}–Cu–O_{eq}) (eV/rad^2)	0.17
r_e(Cu–O_{eq}) (Å)	1.95	k_θ(O_{eq}–Cu–O_{ax}) (eV/rad^2)	0.17
r_e(Cu–O_{ax}) (Å)	2.38	k_θ(N_{eq}–Cu–O_{eq}) (eV/rad^2)	0.86
k_r(Co–C) (eV/Å^2)	17.12	k_θ(O_{eq}–Cu–N_{ax}) (eV/rad^2)	8.60
k_r(Cu–N_{eq}) (eV/Å^2)	49.3	k_θ(N_{eq}–Cu–O_{ax}) (eV/rad^2)	0.05
k_r(Cu–N_{ax}) (eV/Å^2)	8.56	k_θ(Cu–N_{eq}–C) (eV/rad^2)	0.17
k_r(Cu–O_{eq}) (eV/Å^2)	34	k_θ(Cu–N_{ax}–C) (eV/rad^2)	0.03
k_r(Cu–O_{ax}) (eV/Å^2)	171		

4.6.3 Empirical potential refinements

The quality of fit was monitored independently for both Bragg and PDF components through the corresponding R_{wp} values, with final refinements converging to values of about 9.5% and 30%, respectively; whilst this empirical potential big-box approach gave a similar fit to the reciprocal space Bragg data as the more conventional small-box average structure refinement (9.5% versus 9.4%, respectively), the empirical potential big-box approach gave a much better fit to the real-space PDF data than the conventional small-box average structure approach (30% versus 53%, respectively). The final set of lattice dynamical parameters from which our fits are obtained is given in Table 4.1. It is important to note that we do not attach any particular physical significance to the specific values determined in this parameter set. These values represent one possible parameterisation capable of producing configurations that match both PDF and Bragg intensities, but it was shown in Ref. 329 and Section 3.5.2 that the sensitivity of the data to some parameters can be negligible.

Representative fragments of the local structure of a strain-only model ($J' = 0$) and a strain + crystal-field model ($J' = 1$) obtained using the empirical potential refinement methodology are shown in Fig. 4.16(b),(c). The atomistic representation

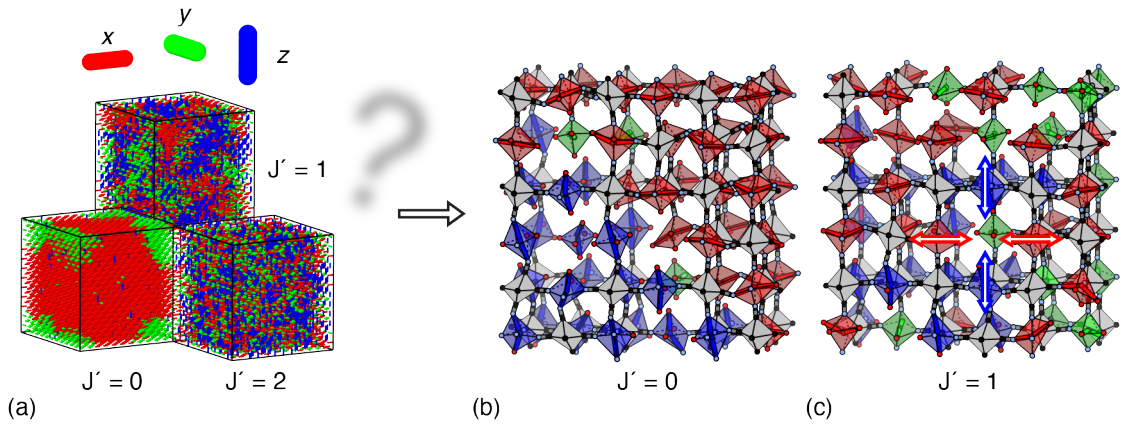


Figure 4.16: (a) Coarse-grained representations of the different pictures of local JT order predicted by the strain-only model ($J' = 0$) and strain + crystal-field model ($J' = 1, 2$). Atomistic representations of the (b) strain-only model ($J' = 0$) and (c) strain + crystal-field model ($J' = 1$) obtained using the empirical potential refinement methodology.

of the strain-only model ($J' = 0$) shown in Fig. 4.16(b) illustrates the tendency of this model to form domains of short-range CJT order, whilst the atomistic representation of the strain + crystal-field model ($J' = 1$) (Fig. 4.16(c)) captures how the presence of vacancies drives reorientation of the JT elongation axes to give a local structure distinct from that found in the fully-ordered state (cf. Fig. 4.2). This picture extends the phenomenology of orbital disordered states—which are notoriously difficult to study experimentally[162]—beyond that of dense phases such as perovskites[192] and transition-metal oxides.[361]

We next wanted to test the sensitivity of the PDF to MC models with different descriptions of short-range JT order (Fig. 4.16(a)) (by varying the value of J') and also the sensitivity to random versus correlated vacancy arrangements (using the Hamiltonian described in Ref. 102 to produce initial correlated vacancy arrangements); again, we have chosen $Cu[Co(CN)_6]_{2/3}$ as a test case. The empirical potential refinement methodology was used to produce an atomistic representation from a coarse-grained MC model with random JT orientations and random vacancies, as well as to produce atomistic representations from coarse-grained MC models with

Table 4.2: A comparison of the goodness-of-fit $R_{\rm wp}$ values obtained from joint X-ray PDF + Bragg refinements of various models of JT order in $Cu[Co(CN)_6]_{2/3}$.

JT model	Vacancy model	PDF $R_{\rm wp}$ (%)	Bragg $R_{\rm wp}$ (%)	Combined $R_{\rm wp}$ (%)
random	random	32.24	10.01	42.25
$J' = 0$	random	28.90	9.76	38.65
$J' = 1$	random	30.58	9.68	40.27
$J' = 2$	random	30.83	9.72	40.55
$J' = 1$	correlated	31.28	9.59	40.87

values of $J' = 0, 1, 2$ and random vacancy arrangements; additionally, an atomistic representation of a coarse-grained MC model with $J' = 1$ and a correlated vacancy arrangement was produced. The big-box atomistic models were used to calculate the PDFs shown in Fig. 4.17(a),(b); the Bragg patterns were also calculated from their collapsed (average) structure. A comparison of the goodness-of-fit $R_{\rm wp}$ values of both the PDF and Bragg components of combined PDF + Bragg refinements of the various models are shown in Table 4.2.

What Table 4.2 and the PDFs in Fig. 4.17 serve to illustrate is an apparent insensitivity of the PDF and Bragg pattern to different descriptions of CJT order and vacancy arrangements, with all the models tested producing similar fits to both the PDF and Bragg data. This highlights the need for a coupled approach to differentiate between models, *e.g.* by understanding the energetics of the system and not just measuring a PDF and hoping to determine the structure. In our work, tracking the evolution of the 220 reflections of the $Cs_xCu[Fe(CN)_6]_{(2+x)/3}$ series allowed us to determine that the strain + crystal field (J') model, with a non-trivial JT texture, gives the closer match to experiment in terms of the critical composition for long-range CJT order than the strain-only model ($J' = 0$), with domains of short-range JT order. Whilst we are unable to see any significant differences between the different pictures of local JT order from their calculated PDFs (Fig. 4.17(a),(b)) nor between random versus correlated vacancy arrangements (Fig. 4.17(c)), what is key is that the MC-driven 'interaction-space' big-box refinement approach is able to produce atomistic configurations that are consistent with the PDF data.

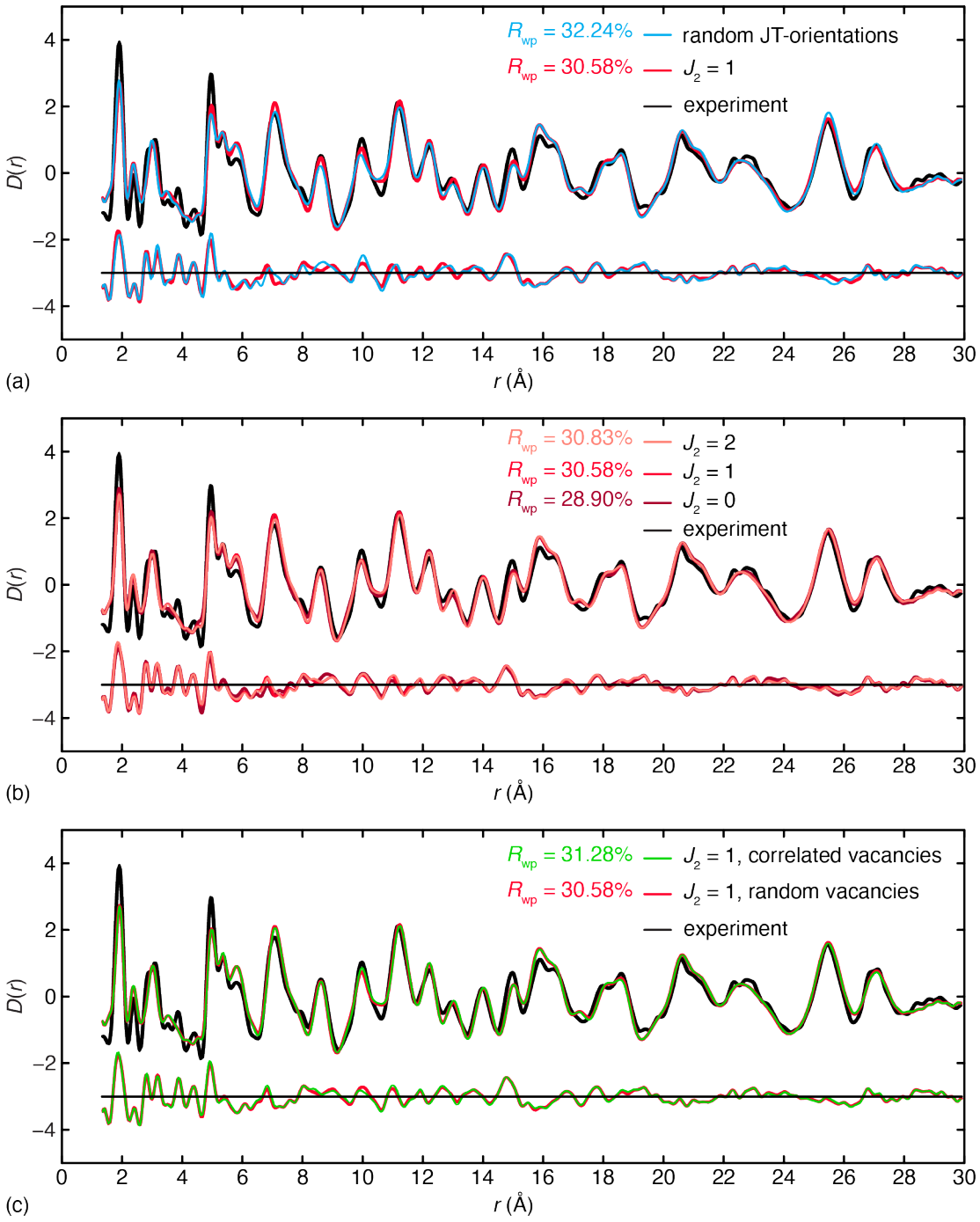


Figure 4.17: (a), (b) Sensitivity of the PDF to varying degrees of local CJT order. (c) Sensitivity of the PDF to random vs correlated vacancy arrangements.

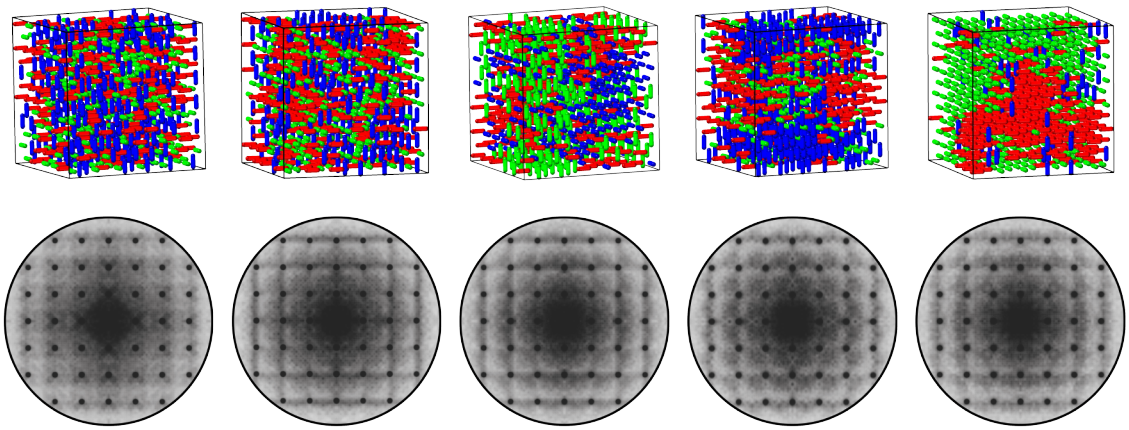


Figure 4.18: Variation in single-crystal X-ray diffuse scattering patterns of models of $Cu[Co(CN)_6]_{2/3}$ with different pictures of local JT order. In each case the supercell size was $6 \times 6 \times 6$ with a random vacancy distribution. Note that the coarse-grained JT MC models are shown for clarity, but the single-crystal diffuse scattering patterns are calculated from their respective atomistic representations.

4.6.4 Single-crystal X-ray diffraction simulations

Whilst it was not possible to use the PDF measurements to differentiate between different local JT pictures, the empirical potential refinement approach could be used to produce atomistic configurations that are consistent with the PDF data, and from these atomistic configurations, it is possible to calculate single-crystal diffuse scattering patterns, which do indeed show differences (Fig. 4.18).

Electron diffraction techniques may soon offer the ability to measure accurate single-crystal diffuse scattering patterns even from polycrystalline PBA samples. With this in mind, we include in Fig. 4.19 some simple calculations of $(hk0)$ scattering from atomistic $Cu[Co(CN)_6]_{2/3}$ configurations; we consider four cases: with and without vacancy correlations, and with and without the crystal-field term in the underlying JT-orientation Hamiltonian. The underlying configuration sizes for these simulations were $12 \times 12 \times 12$ supercells, and Laue symmetry was applied.

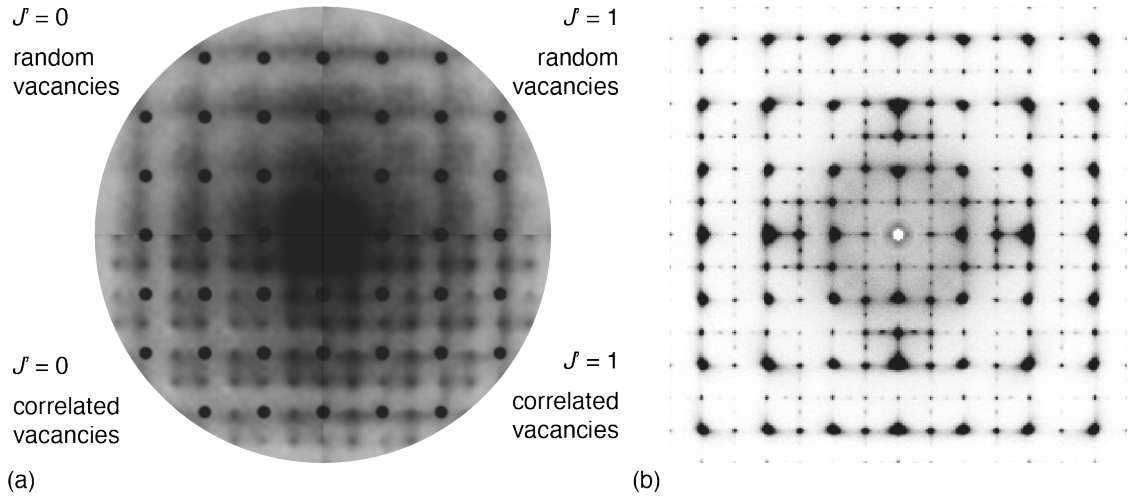


Figure 4.19: (a) Single-crystal X-ray diffuse scattering patterns for the $(hk0)$ plane, calculated from four different atomistic models of $Cu[Co(CN)_6]_{2/3}$ with random/correlated vacancy distributions and strain-only $(J' = 0)$/strain + crystal field $(J' = 1)$ CJT models. In each case the supercell size was $12 \times 12 \times 12$. (b) Experimental reconstructed $(hk0)$ scattering plane for $Cu[Co(CN)_6]_{2/3}$ $(-6 < |h|, |k| < 6)$, reproduced from Ref. 102 with permission from Springer Nature.

4.7 Conclusions

The distinction between long- and short-range CJT order in PBAs is reminiscent of the complexity of orbital order in the manganite perovskites.[162] In $La_{1-x}Ca_xMnO_3$, for example, the C-type Mn^{3+} orbital order of La-rich compositions quickly melts on Ca doping to give a complex polaron liquid/glass phase from which the stripe charge/orbital order of $La_{0.5}Ca_{0.5}MnO_3$ eventually emerges.[156,201,206,362] Of course, charge ordering is less relevant to the PBAs we have studied here, but the interplay between JT dilution and orbital orientations will nonetheless affect other electronic properties—*e.g.* magnetism[363] or photoinduced charge-transfer processes[256]—in a conceptually similar way. In PBAs, the anisotropy that competes with strain to introduce nontrivial CJT textures arises from crystal-field effects, and while we cannot rule out exchange mechanisms (*e.g.* Kugel–Khomskii), we have not needed to invoke these in order to explain our experimental measurements. An implication of this role of crystal field is that the use of different capping ligands in partially-vacant PBAs may provide a mechanism for (de)stabilising CJT order, *e.g.* to avoid phase transitions during electrochemical cycling. Mechanically, JT disorder appears to strengthen PBAs relative to JT-inactive analogues,[364] which may be a consequence of nontrivial JT textures frustrating soft mode instabilities.[365]

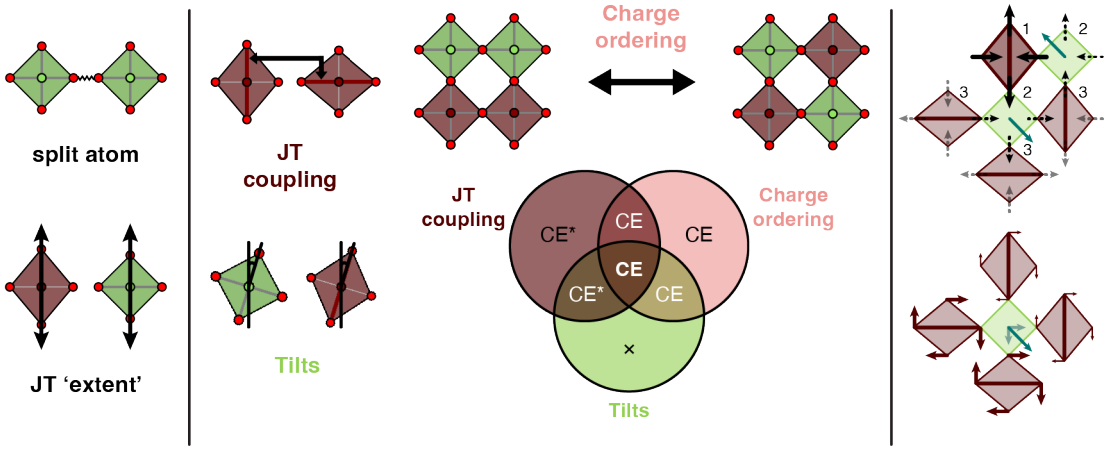
The apparent insensitivity of our results to the presence and nature of vacancy correlations is perhaps surprising, but ultimately helpful. It is not yet clear, for example, whether the vacancy correlations known to occur in PBA single crystals[102] are actually relevant to polycrystalline samples—such as those studied here or as found in functional PBA-based devices. The advent of electron diffraction techniques for characterising correlated disorder in polycrystalline samples[366,367] may offer further experimental sensitivity to the nature of local CJT order in PBAs, and in this spirit we have included in Section 4.6.4 some calculations of diffuse scattering patterns based on the model developed in our study.

The interplay of strain and crystal-field effects that governs CJT order in PBAs is likely to be relevant also to similar phenomenology in other hybrid framework materials. In the formate perovskites, for example, CJT order can couple with cooperative tilting to break inversion symmetry,[119,126] and so manipulation of local CJT order may allow the design of relaxor-like phases containing polar nanoregions.[368,369] Likewise in thiocyanates, where CJT order is crucial in stabilising low-dimensional quantum magnetism.[370] What differs amongst these various systems is the geometry of the lattice on which JT-active ions sit and the rules governing vacancy incorporation.[115] Hence the calculation (and validation) of ground-state phase maps for these various geometries of the kind shown in Fig. 4.12 is an obvious priority in generalising the results of this study beyond PBAs. What is already clear is that molecular frameworks can support nontrivial CJT textures that—at least in the case of PBAs—can now be rationalised, and hence controlled in terms of relatively simple microscopic ingredients.

Chapter 5

The interplay between Jahn–Teller distortions and structural degrees of freedom in manganite perovskites

5.1 Overview



The manganite perovskites are known to show a complex interplay between various degrees of freedom, including orbital, charge, lattice, and spin degrees of freedom; this interplay is implicated in the emergence of various interesting electronic and magnetic properties, including the useful property of colossal magnetoresistance. Cooperative Jahn–Teller (CJT)/orbital effects, in the context of dense transition-metal compounds, have typically been understood in terms of vibronic coupling or electronic exchange mechanisms. However, having explored the possibility of using simple geometric modelling to understand the nature of CJT order in Prussian blue analogues (PBAs) (Chapter 4), this chapter aims to determine the extent to

which simple geometric considerations of the kind developed for PBAs might help rationalise CJT and charge order in the manganite perovskites. Using a simple geometric approach, implemented through Monte Carlo simulations, it is shown that coupling between orbital, tilt, and shear strain modes in the $LaGa_{1-x}Mn_xO_3$ system is responsible for the pseudocubic to orthorhombic phase transition. Distortion mode analysis of the $LaGa_{1-x}Mn_xO_3$ series is used to verify the MC results by comparison to experimental data. The simple geometric model is then developed to show how the *CE* structure of $La_{0.5}Ca_{0.5}MnO_3$ might arise from the coupling between charge, orbital, tilt, shift, and shear strain degrees of freedom. This simple geometric approach offers a way to explore the nature of coupling between various degrees of freedom that can otherwise be difficult to disentangle using conventional structure-determining techniques.

5.2 Acknowledgements

This project was carried out in collaboration with Ben Tragheim and Mark Senn (University of Warwick). The synthesis and characterisation of the $LaGa_{1-x}Mn_xO_3$ compositional series were carried out by Ben Tragheim, and is described in Ref. 371. The initial sample characterisation to assess phase purity was performed via the Warwick X-ray Research Technology Platform. We are grateful to the STFC for the provision of synchrotron beam time at I11, Diamond Light Source, under the block allocation grant award (CY32893), and to the ILL for neutron beam time at D2B under the proposal number 5-24-693 (DOI: 10.5291/ILL-DATA.5-24-693). This work was published in *Physical Review B* and was chosen as the Editor's Suggestion:

B. R. M. Tragheim, E. A. Harbourne, C. Ritter, A. L. Goodwin, M. S. Senn, "The interplay between Jahn–Teller distortions and structural degrees of freedom in pseudocubic states in manganite perovskites",
Phys. Rev. B **2025**, *112*, 115119.

5.3 Introduction

Coupling between orbital, spin, charge, and tilt degrees of freedom in the manganite perovskites drives the emergence of various interesting electronic and magnetic properties, including colossal magnetoresistance (CMR).[17–20] Hence, to optimise CMR in these materials, obtaining an accurate microscopic understanding of how the different charge and orbital ordering phenomena control CMR will be important. When degrees of freedom are strongly coupled, it can be difficult to understand their individual roles in driving a particular phenomenon; in such cases, prototype systems are often used to isolate individual degrees of freedom as much as possible.[25] For example, substituting JT-active high-spin Mn^{3+} (0.645 Å in an octahedral coordination environment)[372] in $LaMnO_3$ with the similarly-sized JT-inactive Ga^{3+} (0.62 Å)[372] minimises additional octahedral rotations and isolates tolerance factor effects as much as possible; hence, the solid solution $LaGa_{1-x}Mn_xO_3$ (LGMO) (Fig. 5.1(a)) is an ideal prototype system for investigating the coupling between orbital, tilt, and shear strain degrees of freedom that have been shown to drive its orthorhombic ($b > a > c/\sqrt{2}$) ($x \gtrsim 0.5$) to pseudocubic ($b \approx a \approx c/\sqrt{2}$) ($x \lesssim 0.5$) phase transition.[371] The orthorhombic solid solution end member $LaMnO_3$ shows long-range C-type orbital order[16]—where the d_{z^2} orbitals align in a perpendicular manner within the orthorhombic $Pbnm$ $\boldsymbol{a}$-$\boldsymbol{b}$ plane and layer along the $\boldsymbol{c}$ axis (Fig. 5.1(b))—and below a critical composition ($x \sim 0.5$), long-range cooperative Jahn–Teller (CJT) order dissolves to give a pseudocubic state.[371,373,374]

To provide insight into how each structural distortion contributes to changes in orbital ordering in the LGMO series as a function of JT content, Ref. 371 performed a symmetry-driven crystallographic distortion-mode analysis (subsection 2.3.5). With respect to the aristotype $Pm\bar{3}m$ ABO_3 perovskite structure, and choosing the A site as the origin, the unique structural distortions in the $Pbnm$ perovskite transform as eight different irreps (Fig. 5.2(a)): R_4^-, R_5^-, X_5^-, M_2^+, and M_3^+

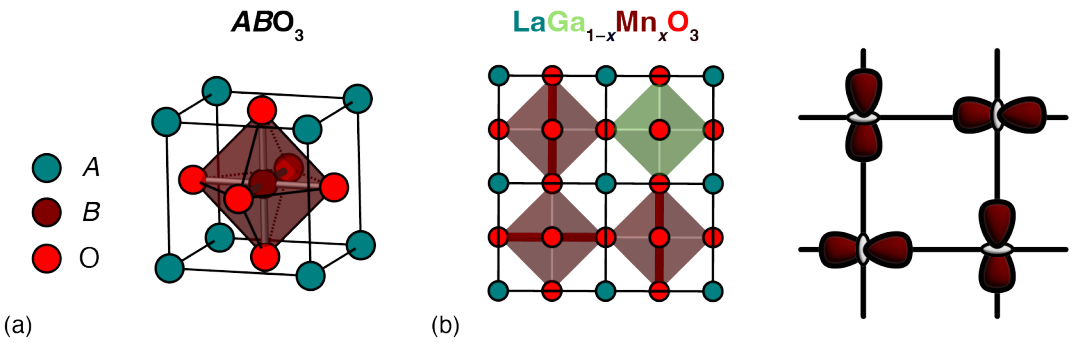
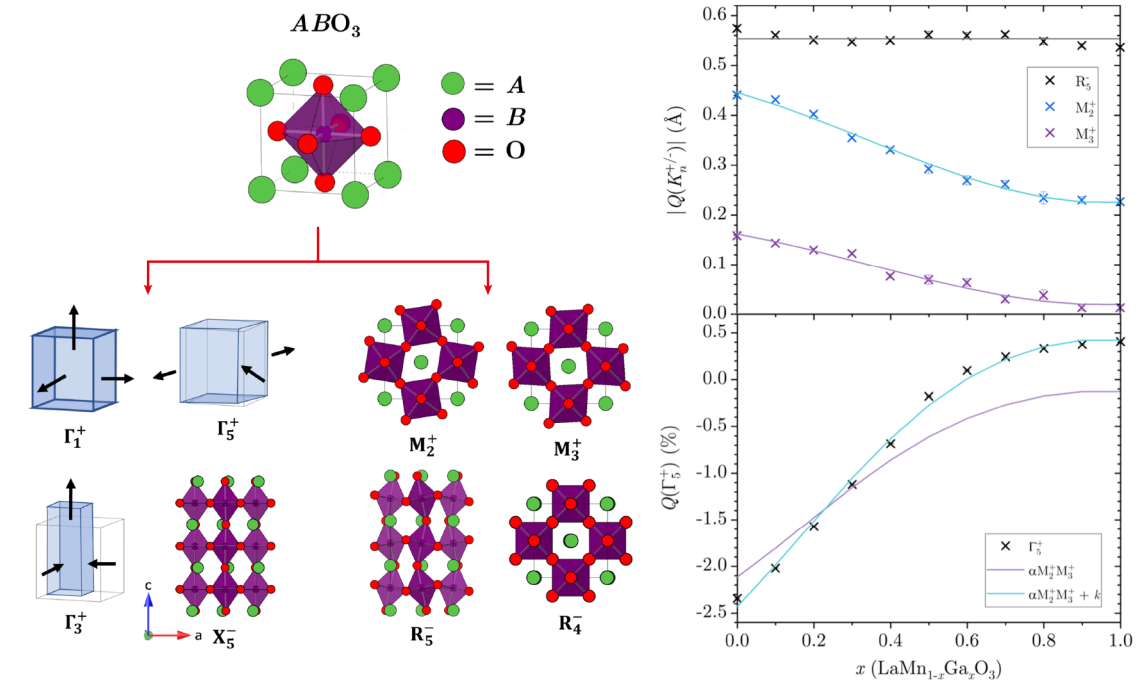


Figure 5.1: (a) $LaGa_{1-x}Mn_xO_3$ $Pm\bar{3}m$ aristotype. (b) In this system, CJT order results in C-type orbital order:[16] d_{z^2} orbitals alternate directions within the $Pbnm$ **a**-**b** plane whilst they layer along the **c** axis.

(describing atomic displacements) and Γ_1^+, Γ_3^+, and Γ_5^+ (describing unit cell strain). Ref. 371 showed by symmetry-adapted distortion-mode Rietveld analysis[288] of variable composition synchrotron X-ray and neutron powder diffraction data that the trilinear coupling term ($\Gamma_5^+M_2^+M_3^+$) between shear strain (Γ_5^+), octahedral rotation (M_2^+), and the C-type orbital ordering (M_3^+) modes drives the orthorhombic to pseudocubic phase transition in LGMO (Fig. 5.2(b)).

Whilst orbital ordering phenomena are typically thought to arise in dense ceramics through either vibronic coupling[125] or electronic exchange pathways,[351,352] given the relative success that simple geometric considerations had in rationalising the emergence and nature of CJT order in Prussian blue analogues in Chapter 4, we wanted to see whether simple geometric ideas of the kind developed in Chapter 4 might help rationalise CJT order in the manganite perovskites as well. This chapter explores the extent to which simple geometric considerations can replicate the experimental results of Ref. 371, specifically the coupling between JT, tilt, and shear strain modes that drives the orthorhombic to pseudocubic phase transition in LGMO. This chapter then goes on to extend the simple geometric model developed for the LGMO series to see whether the same kind of geometric considerations can account for and rationalise the charge and orbital order of the *CE* structure of $La_{0.5}Ca_{0.5}MnO_3$.



(a) (b)

Figure 5.2: (a) Schematic of the eight distortion modes spanning the structural distortions of the $Pbnm$ ABO_3 perovskite with respect to the $Pm\bar{3}m$ aristotype. Strain irreps: Γ_1^+, Γ_3^+ and Γ_5^+. Distortion modes describing atomic displacements: R_4^-, R_5^-, X_5^-, M_2^+ and M_3^+. (b) Experimental distortion mode analysis of the $LaMn_{1-x}Ga_xO_3$ series. Figure adapted from Ref. 371, which is licensed under a Creative Commons Attribution 4.0 International.

5.4 $LaGa_{1-x}Mn_xO_3$: Monte Carlo simulations

The following section aims to determine whether geometric constraints of corner-sharing JT-active and JT-inactive polyhedra can explain the emergence of CJT order and/or the coupling to strain observed experimentally in the $LaGa_{1-x}Mn_xO_3$ perovskites. Our two-dimensional model is based on corner-sharing rhombuses that are allowed to tilt, stretch, and shift. A Monte Carlo Hamiltonian is developed to penalise individual rhombuses from breaking their connectivity at their corners, to penalise departures from ideal JT distortion geometries for JT-active rhombuses, to penalise departures from a rhombus' ideal tilt angle, and to favour alternation of JT distortion axes between neighbouring rhombuses as observed in the C-type orbital ordering of $LaMnO_3$.

5.4.1 The basic model and simulation implementation

A series of Monte Carlo (MC) simulations were performed to gain a better understanding of the local ordering that gives rise to the average structural distortions observed crystallographically in the solid solution $LaGa_{1-x}Mn_xO_3$ as a function of JT-active content (x). Since the CJT order in the fully JT-active system ($x = 1$, *i.e.* $LaMnO_3$) can be described by alternating directions of d_{z^2} orbitals within the *Pbnm* ***a***-***b*** plane (Fig. 5.1(b)), the problem was reduced to two-dimensions (2D), considering 10×10 arrays of corner-sharing rhombuses. Each rhombus was assigned randomly as JT active or JT inactive subject to a predefined overall composition x, given by $LaGa_{1-x}Mn_xO_3$. These rhombuses approximate the cross-section of corner-sharing MnO_6 and GaO_6 octahedra. Each rhombus has four degrees of freedom: its horizontal and vertical position, its tilt angle θ, and a JT distortion magnitude ϕ. The equilibrium value of θ for a JT-active (9.2005°) and a JT-inactive rhombus (4.6305°) were obtained from the corresponding in-plane tilts in the end members of $LaMnO_3$ and $LaGaO_3$, respectively. The value of ϕ was set to zero for every rhombus assigned as JT inactive, meaning all Ga–O bond lengths within an individual rhombus remained as 1.954 Å (as observed for $LaGaO_3$) throughout the simulations. For rhombuses assigned as JT active, the value of ϕ was allowed to vary from a starting value of zero (corresponding to a Mn–O bond length of 2.016 Å) with an equilibrium magnitude of 1. The actual rhombic distortion given by $\phi = 1$ (Mn–O(JT) = 2.143 Å, Mn–O(non-JT) = 1.889 Å) was set to mimic the JT distortion magnitude (projected in the plane) observed in $LaMnO_3$ itself.

The MC energy term contained four terms: (i) a split-atom term[310] that acts to maintain sensible connectivity of neighbouring rhombuses, (ii) a JT term that penalised departures from ideal JT distortion geometries for JT-active sites, (iii) a JT coupling term that favoured alternation of JT distortion axes on neighbouring sites, and (iv) a tilt term that penalised departures from a site's ideal tilt angle.

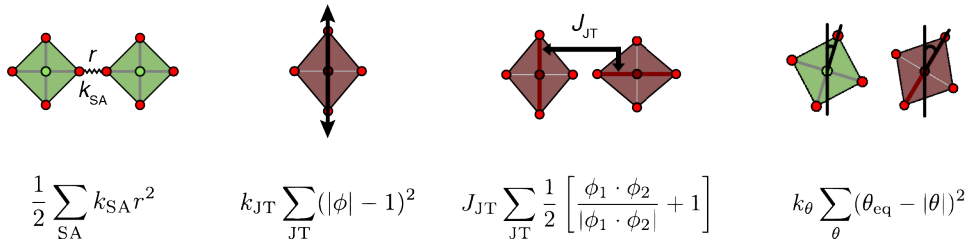


Figure 5.3: Energy penalties used in the Monte Carlo simulation.

The MC energy can be given by:

$$E_{\mathrm{MC}} = \frac{1}{2}\sum_{\mathrm{SA}} k_{\mathrm{SA}} r^2 + k_{\mathrm{JT}}\sum_{\mathrm{JT}}(|\phi|-1)^2 + J_{\mathrm{JT}}\sum_{\mathrm{JT}}\frac{1}{2}\left[\frac{\phi_1\cdot\phi_2}{|\phi_1\cdot\phi_2|}+1\right] + k_\theta\sum_\theta(\theta_{\mathrm{eq}}-|\theta|)^2. \tag{5.1}$$

The spring constants assigned to these various terms (Fig. 5.3) were varied to ensure sensible convergence of the MC simulations; their absolute values did not affect the ground-state structures that emerged. The values of the spring constants used in the simulations presented here were $k_{\mathrm{SA}} = 0.2\,\text{Å}^{-2}$, $k_{\mathrm{JT}} = 1$, $J_{\mathrm{JT}} = 1$, $k_\theta = 1\,\mathrm{deg}^{-2}$. Note that the MC temperature is relative, and so we focus only on ground-state configurations for which the absolute value of temperature is not relevant.

A simulated annealing approach was employed, starting with a MC temperature, $T_{\mathrm{i}} = \frac{10E_{\mathrm{i}}}{n_{\mathrm{tot}}}$, where E_{i} is the initial energy of the configuration, and n_{tot} is the total number of cells in the supercell. Simulations proceeded by selecting a JT-active or JT-inactive ion site at random. If a JT-inactive ion was selected, one of two types of moves was proposed at random such that each of the two types of moves was proposed roughly 50% of the time. The first type of move changed the horizontal and vertical positions of the rhombus individually by $\frac{-0.01}{an_{\mathrm{cells}}} \leq \Delta x, \Delta y < \frac{0.01}{an_{\mathrm{cells}}}$, where n_{cells} is the number of cells in each of the x- and y-directions, and an_{cells} is the lattice parameter, lpa, of the supercell, with a given by $a = 3.895\,\text{Å} + 0.086x_{\mathrm{JT}}$ (linear interpolation of the corresponding end members $LaMnO_3$ and $LaGaO_3$), where x_{JT} is the fraction of JT-active sites. The second type of move changed the tilt angle θ by $-1^\circ \leq \Delta\theta < 1^\circ$. For a JT-active ion, a third type of move could be proposed with an

equal likelihood as the first two. The third type of move changed the JT distortion magnitude ϕ by $-0.3 \leq \Delta\phi < 0.3$. Moves were accepted or rejected according to the usual Metropolis algorithm.[321] Simulations were continued at each temperature until equilibrium was achieved, which was determined by allowing 500 accepted moves for each site in the supercell. We found this to be a suitable balance between safe convergence and computational expense. Following equilibration, the system temperature was reduced by a factor of 0.01. Below a MC effective temperature of 5×10^{-4}, moves where the simulation box was allowed to shear (*i.e.* the box may itself become a rhombus) represented $\sim 10\%$ of the proposed moves. Note that no explicit term involving shear was introduced into the MC Hamiltonian. Instead, a proposed 'shear move' involved changing the lattice parameters of the box, *lpa* and *lpb* (previously fixed and equal to each other), by $-0.001an_{\text{cells}} \leq \Delta lpa, \Delta lpb < 0.001an_{\text{cells}}$, and also changing the supercell angle, γ (previously fixed to 90°), by $-2.865 \times 10^{\circ} < \Delta\gamma \leq 2.865 \times 10^{-3\circ}$. The simulations were continued until a final MC temperature of $\sim 1 \times 10^{-5}$ was reached. The parameters mentioned here were chosen to ensure sensible convergence of the MC simulations.

5.4.2 Results and discussion

In a first set of simulations, geometric relaxation of the box was not allowed, and hence the shear strain was identically zero. These initial simulations did capture a degree of coupling between the average tilt and rotation observed as a function of x, but it is clear from their high residual ground state energies that they are highly strained (Fig. C1.12(c),(d)). Consequently, further simulations were performed that allowed the simulation box to shear (*i.e.* it may itself become a rhombus). For values of x greater than about 0.5, this additional degree of freedom serves to reduce the residual ground state energy significantly, producing results where the majority of rhombuses are able to satisfy their preferred local geometry within a sheared box. Representative $x = 0.3, 0.5, 0.8$ and 1 configurations are given in Fig. 5.4, showing

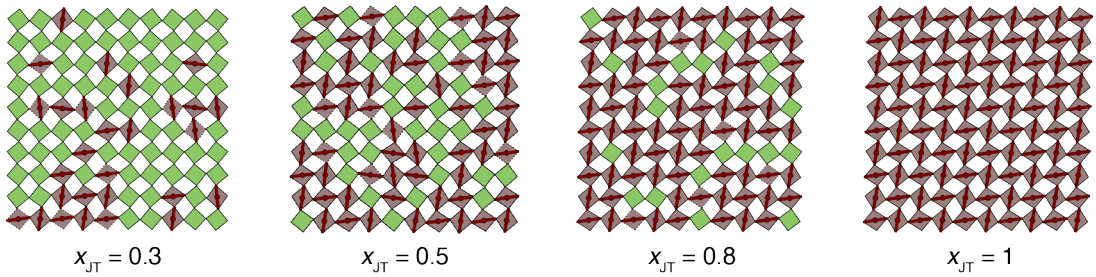


Figure 5.4: A representative relaxed configuration for each of the compositions x = 0.3, 0.5, 0.8, and 1, showing the development of long-range CJT order and shearing of the MC supercell.

the development of long-range CJT order and how the supercells become become more sheared with increasing x. It is important to note that this shearing arises spontaneously from our simple Hamiltonian that captures only the desire for the rhombuses to rotate and distort while remaining connected at their corners and should hence be thought of as the microscopic origin behind the trilinear terms $\Gamma_5^+\mathrm{M}_2^+\mathrm{M}_3^+$ that have been identified through invariants analysis.[371] In particular, there was no explicit term involving shear in the MC Hamiltonian.

Next, in order to check that our simple geometric model produces configurations that are consistent with experiment, the MC configurations were collapsed down to create an average $Pbnm$ unit cell from which the evolution of the M_3^+ (JT), M_2^+ (tilt), and Γ_5^+ (shear strain) amplitudes could be determined as a function of composition and hence compared to the experimental values shown earlier in Fig. 5.2(b). Amplitudes of each of the distortion modes are given in terms of absolute A_p values, which refer to the aristotype-cell-normalised amplitude of a particular distortion, and were determined using the webtool ISODISTORT by comparing the collapsed MC configurations with the parent $Pm\bar{3}m$ aristotype cell at each composition.[288] Values of M_3^+, M_2^+ and Γ_5^+ given in Fig. 5.5 are the averages over 100 independent simulations, and error bars denote the standard uncertainty in the error of each measurement. Fig. 5.5 also shows the values of M_3^+, M_2^+ and Γ_5^+ for each of the 100 independent simulations to show the variation at each composition.

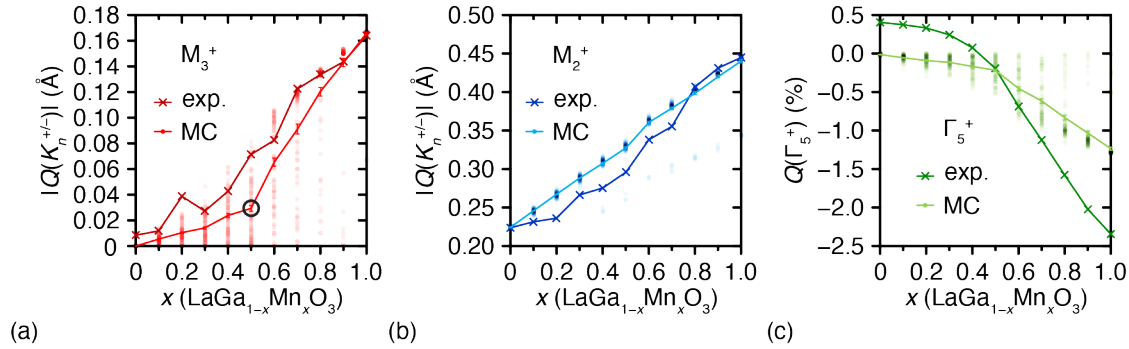


Figure 5.5: The evolution of the (a) M_3^+ (JT), (b) M_2^+ (tilt), and (c) Γ_5^+ (shear strain) modes extracted from the relaxed MC simulations. Averages over 100 independent simulations are given, along with error bars denoting the standard uncertainty in the error of each average. The values of M_3^+, M_2^+ and Γ_5^+ for each of the 100 independent simulations are shown as coloured, semi-transparent circles.

Fig. 5.5(a), depicting the evolution of the M_3^+ (JT) mode, shows that the MC simulations produce configurations that possess long-range CJT order from $x = 1$ down to $\sim x = 0.5$, which is the theoretical JT bond percolation limit in a square lattice. Configurations corresponding to high values of x often developed domain structures containing domains of opposite JT-order phase (Figs. 5.6(a) and C1.13 and) or opposite tilt phase (Figs. 5.6(b) and C1.14). This behaviour is typical of 2D MC simulations based on local moves.[324] The presence of multiple domains results in reduced order parameters when the MC configuration is collapsed onto a single subcell (Fig. 5.5(a),(b)). In such cases the magnitude of the cell shear was also reduced (Fig. 5.5(c)), reflecting the link between the evolution of CJT order, tilts, and macroscopic shear.

The average evolution of M_3^+ (JT) (Fig. 5.5(a)) and M_2^+ (tilt) (Fig. 5.5(b)) are in excellent agreement with those observed experimentally down to $x = 0.5$. Whilst the MC simulation undergoes a phase transition to a JT-disordered state below $x = 0.5$ (Fig. 5.5(a)), the diffraction data show a continuous evolution as a function of x. This discrepancy is due to the fact that the shear strain (Γ_5^+) only arises in the MC simulations as a consequence of long-range coupling between M_3^+ (JT) and M_2^+ (tilt), while in a real *Pbnm* perovskite it is ever-present through the coupling

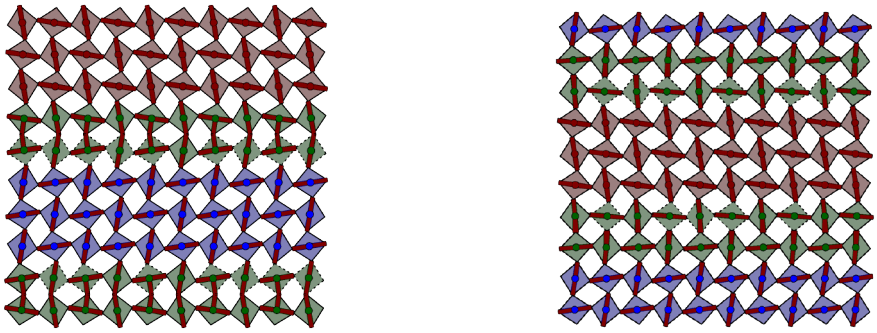


Figure 5.6: Tendency for domain formation in MC configurations with high x. (a) Domains of opposite JT-order phase, and (b) domains of opposite tilt phase in the $x = 1$ configuration.

to the out-of-phase BO_6 tilt ($\Gamma_5^+(R_5^-)^2$) that is necessarily ignored in the 2D MC simulations. Indeed, the evolution of Γ_5^+ (Fig. 5.5(c)) has a similar trend as the experimental model in which the constant term arising from the coupling to R_5^- was ignored.[371]

The present results therefore strongly suggest that far from the shear strain tending to zero (*i.e.* the occurrence of the pseudocubic state) being a symptom of orbital disorder in other systems, it is more likely to be a cause. For example, perovskite systems adopting shear strain states that are predisposed to a strong coupling between M_3^+ and M_2^+ will tend to exhibit CJT ordering even below the percolation threshold. On the other hand, in a perovskite that is highly resistant to shearing in the correct manner, long-range CJT order will be suppressed even above the percolation threshold.

In order to investigate further the link between shear strain, CJT order, and tilts, a further set of simulations were carried out to explore whether imposing shear strain on an otherwise JT-disordered system with tilts can induce long-range CJT order. To do this, a shear strain term ($k_\gamma(\gamma - \gamma_{eq})^2$) was added to the MC Hamiltonian to favour a sheared state; an ideal supercell angle $\gamma_{eq} = 89°$ was chosen to reflect the average supercell angle $\gamma_{avg} = 89.01°$ for the long-range orbital-ordered $x_{JT} = 1$ composition from the previous set of simulations. The simulation box was allowed

to shear from the start of the simulated annealing process. Additionally, rhombuses assigned as JT inactive, with their JT distortion magnitude ϕ previously set to zero, were now allowed to vary from a starting value of zero with an equilibrium magnitude of zero (*i.e.* favouring a JT-undistorted site). The updated MC energy can be given by:

$$E_{\mathrm{MC}} = \frac{1}{2}\sum_{\mathrm{SA}} k_{\mathrm{SA}} r^2 + J_{\mathrm{JT}} \sum_{\mathrm{JT}} \frac{1}{2}\left[\frac{\phi_1 \cdot \phi_2}{|\phi_1 \cdot \phi_2|} + 1\right] + k_\theta \sum_{\theta} (\theta_{\mathrm{eq}} - |\theta|)^2 + k_{\mathrm{JT}} \sum_{\mathrm{JT}} (|\phi| - \phi_{\mathrm{eq}})^2 + k_\gamma (\gamma - \gamma_{\mathrm{eq}})^2, \tag{5.2}$$

where $\gamma_{\mathrm{eq}} = 89°$ and $\phi_{\mathrm{eq}} \in 0, 1$ for a JT-inactive and JT-active site, respectively. The spring constants assigned to these various terms were varied and it was found that for $k_{\mathrm{SA}} = 0.2$, $k_{\mathrm{JT}} = 1$, $J_{\mathrm{JT}} = 1$, and $k_\theta = 1$ (the set of spring constants used in the previous simulations), setting $k_\gamma = 100000$ ensured that $\gamma_{\mathrm{eq}} = 89°$ was closely obeyed (Fig. 5.7(b)). However, applying the updated Hamiltonian (Eq. 5.2) and this set of spring constants to the previously JT-disordered $x_{\mathrm{JT}} = 0.3$ composition (Fig. 5.5(a)) did not induce long-range CJT order (Fig. 5.7(b)). It was observed that with increasing k_{SA}, some JT order could be induced (Fig. 5.7(c),(d)), though a long-range JT-ordered state was not achieved.

To explore further whether perovskite systems adopting shear strain states might tend to show long-range CJT ordering even below the percolation threshold, the effect of adopting a sheared state was investigated across the full composition range (Fig. 5.8). Values of M_3^+ (CJT order), M_2^+ (tilts), and Γ_5^+ (shear strain) given in Fig. 5.8(a) for the simulations under the application of shear strain with $k_{\mathrm{SA}} = 0.2, 20$ are the averages over 20 independent simulations, and error bars denote the standard uncertainty in the error of each measurement. Fig. 5.8(b),(c) also show the values of M_3^+ and M_2^+ for each of the 20 independent simulations under the application of shear strain with $k_{\mathrm{SA}} = 20$. The average evolution of M_3^+ (C-type orbital order) (Fig. 5.8(b)) is in excellent agreement with those observed experimentally, whilst

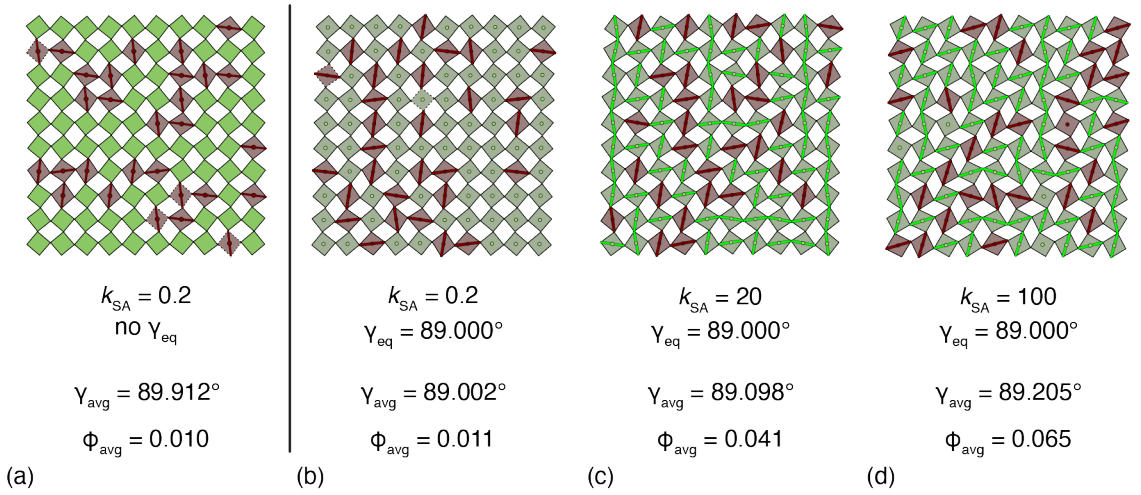


Figure 5.7: $x_{\mathrm{JT}} = 0.3$. (a) no $k_\gamma(\gamma - \gamma_{\mathrm{eq}})^2$ term in Hamiltonian (*i.e.* no shear strain applied) and JT-inactive sites are rigid squares. (b) $k_\gamma(\gamma - \gamma_{\mathrm{eq}})^2$ term in Hamiltonian with $\gamma_{\mathrm{eq}} = 89.000°$ (*i.e.* shear strain applied), varying k_{SA}, and JT-inactive sites are now allowed to stretch and become rhombuses ($k_{\mathrm{JT}} \sum_{\mathrm{JTI}} (|\phi| - \phi_{\mathrm{eq}})^2$, $\phi_{\mathrm{eq}} = 0$). We can start to see JT order emerging through the application of shear strain when k_{SA} is large enough.

the effect of increasing the split-atom constant (k_{SA}) is to deviate away from the linear increase in M_2^+ with increasing x_{JT}, with intermediate compositions tilting more.

It can be seen in Fig. 5.8(a) that the application of shear strain, even with a reasonably large split-atom spring constant $k_{\mathrm{SA}} = 20$, did not shift the percolation threshold for long-range CJT order. However, through the application of shear strain, short-range CJT order can be achieved in systems that do not show long-range CJT order; indeed, even in the $x_{\mathrm{JT}} = 0$ composition, $\mathrm{M}_3^+ \neq 0$, hence some short-range CJT order can be observed (Fig. 5.8(b)). This effect parallels that seen for ferroelectric materials, which show a spontaneous non-zero electric polarisation even when the applied electric field is zero;[11,375] the spontaneous polarisation arises because the material's crystal structure breaks spatial inversion symmetry.[376,377] For these LGMO systems, the application of a shear strain necessarily lowers the (pseudo)cubic symmetry to orthorhombic, such that with the nature of the trilinear coupling term between tilts, shear strain, and CJT order, since the system has both tilts and shear strain present, JT-inactive cations have to 'stretch' to produce some

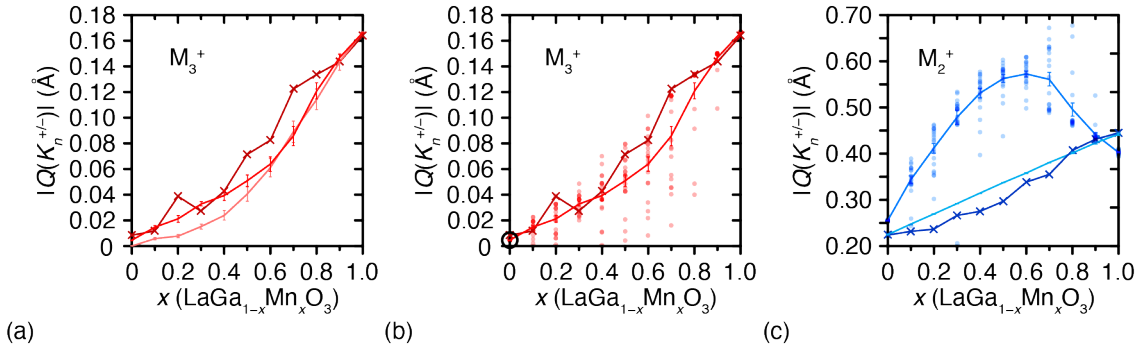


Figure 5.8: Distortion mode analysis of configurations produced by MC simulations with shear strain. The evolution of the (a), (b) M_3^+ (JT) mode and (c) M_2^+ (tilt) mode as a function of composition x. Averages over 20 independent simulations are given, along with error bars denoting the standard uncertainty in the error of each average. The values of (b) M_3^+ and (c) M_2^+ for each of the 20 independent simulations are shown as coloured, semi-transparent circles. The dark-coloured lines show the evolution of the experimental values, the medium-coloured lines show the evolution of the MC configurations with $k_{\mathrm{SA}} = 20$, and the light-coloured lines show the evolution of the MC configurations with $k_{\mathrm{SA}} = 0.2$.

short-range CJT order, even at $x_{\mathrm{JT}} = 0$ (Fig. 5.8(b)); note that in this sense, the stretching of the JT-inactive cations is not electronic in nature.

From these MC simulations, it is clear that there is an interplay between the C-type orbital ordering (M_3^+), tilt (M_2^+), and shear (Γ_5^+) modes that gives rise to the trilinear coupling term, $\Gamma_5^+ M_2^+ M_3^+$. In the MC simulations that omitted shear strain from the Hamiltonian, shear strain (Γ_5^+) arises as a consequence of long-range coupling between M_3^+ (C-type orbital ordering) and M_2^+ (tilts). In the MC simulations with a shear strain term included in the Hamiltonian, short-range orbital order could be induced in compositions below the percolation threshold for long-range orbital order as a consequence of the coupling between shear strain (Γ_5^+) and tilts (M_2^+). Taken together, perhaps these results suggest that the ability for the system to shear is required in order to observe long-range C-type orbital ordering, but perhaps is not enough to drive long-range orbital order itself.

5.5 $La_{0.5}Ca_{0.5}MnO_3$: Monte Carlo simulations

A related challenge that we are now set up to address is the extent to which geometric considerations can account for charge and orbital order in the CMR family $La_{1-x}Ca_xMnO_3$ (LCMO). The focus of the following section is on one well-studied member—$La_{0.5}Ca_{0.5}MnO_3$—with the eventual motivation to extend to different stoichiometries in subsequent work. Given the success of the simple geometric model in rationalising the trilinear coupling term between JT (M_3^+), tilt (M_2^+), and shear strain (Γ_5^+) modes that drives the orthorhombic↔pseudocubic phase transition in the $LaGa_{1-x}Mn_xO_3$ series, our hypothesis is that the same kind of geometric considerations likely play a strong role in governing the *CE* structure of the $La_{0.5}Ca_{0.5}MnO_3$ system.

5.5.1 Model and simulation implementation

To understand better the coupling between orbital order, tilts, charge, and shear strain in driving the *CE* structure of $La_{0.5}Ca_{0.5}MnO_3$, a series of MC simulations were performed. In order to capture the *CE* structure of $La_{0.5}Ca_{0.5}MnO_3$,[203] the MC model developed in the previous section (Section 5.4) for $LaGa_{1-x}Mn_xO_3$ was extended. Two additional terms were added to the MC Hamiltonian (Eq. 5.1) developed in Subsection 5.4.1: (i) a charge-order term that favours checkerboard charge order (CO) of Mn^{3+} and Mn^{4+} sites (Fig. 5.9(b)), and (ii) a next-nearest neighbour JT coupling term that favours alternation of Mn^{3+} JT distortion axes that are separated by a JT-inactive Mn^{4+} site (Fig. 5.9(c)). The MC energy, E_{MC}, can be given by:

$$E_{\mathrm{MC}} = \frac{1}{2}\sum_{\mathrm{SA}} k_{\mathrm{SA}} r^2 + k_{\mathrm{JT}} \sum_{\mathrm{JT}} (|\phi| - \phi_{\mathrm{eq}})^2 + J_{\mathrm{JT}} \sum_{\mathrm{JT}} \frac{1}{2}\left[\frac{\phi_1 \cdot \phi_2}{|\phi_1 \cdot \phi_2|} + 1\right] + k_\theta \sum_{\theta} (\theta_{\mathrm{eq}} - |\theta|)^2 + J_{\mathrm{c}} \sum_{n} \frac{1}{2}\left[\frac{\epsilon_1 \cdot \epsilon_2}{|\epsilon_1 \cdot \epsilon_2|} + 1\right] + J_{\mathrm{nnJT}} \sum_{\mathrm{nnJT}} \frac{1}{2}\left[\frac{\phi_1 \cdot \phi_2}{|\phi_1 \cdot \phi_2|} + 1\right], \tag{5.3}$$

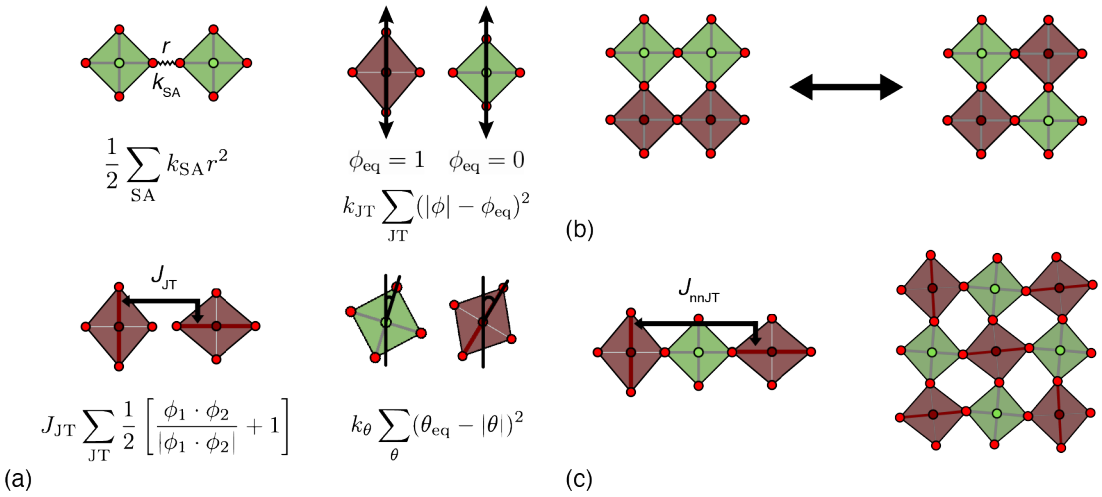


Figure 5.9: Energy penalties used in the Monte Carlo simulations of $La_{0.5}Ca_{0.5}MnO_3$. (a) Original terms in the Hamiltonian: split-atom, JT-distortion magnitude, JT coupling, and tilt. Additional (b) charge-ordering term and (c) next-nearest Jahn–Teller coupling.

where $\phi_{eq} \in 0, 1$ and $\epsilon \in -1, 1$ for a JT-inactive and JT-active site, respectively. The values of the spring constants (Fig. 5.9(b)) used in the simulations presented in this section were $k_{JT} = 1$, $J_{JT} = 1$, $k_\theta = 1$, $J_c = 1$, $J_{nnJT} = 1$; the value of k_{SA} was varied, so the value of k_{SA} used to produce a specific (set of) configuration(s) will be specified later as appropriate.

2D simulations of 20×20 arrays of corner-sharing rhombuses were considered. Each rhombus was assigned randomly as JT active (Mn^{3+}) or JT inactive (Mn^{4+}) subject to the predefined overall composition, $La_{0.5}Ca_{0.5}Mn^{3+}_{0.5}Mn^{4+}_{0.5}O_3$. Each rhombus still has four degrees of freedom (as for the previous LGMO MC simulations): its horizontal and vertical position, its tilt angle θ, and a JT-distortion magnitude ϕ. For rhombuses assigned as JT active, the value of ϕ was allowed to vary from a starting value of zero (corresponding to a Mn^{3+}–O bond length of 1.97675 Å) with an equilibrium magnitude of 1. The actual rhombic distortion given by $\phi = 1$ (Mn^{3+}–O(long) = 2.0465 Å, Mn^{3+}–O(short) = 1.907 Å)* was set to mimic the (average) JT distortion magnitude (projected onto the 2D plane) observed in $La_{0.5}Ca_{0.5}MnO_3$

*The in-plane JT distortion magnitude for $La_{0.5}Ca_{0.5}MnO_3$ is 0.1395 Å, whilst for $LaMnO_3$, it was 0.254 Å.

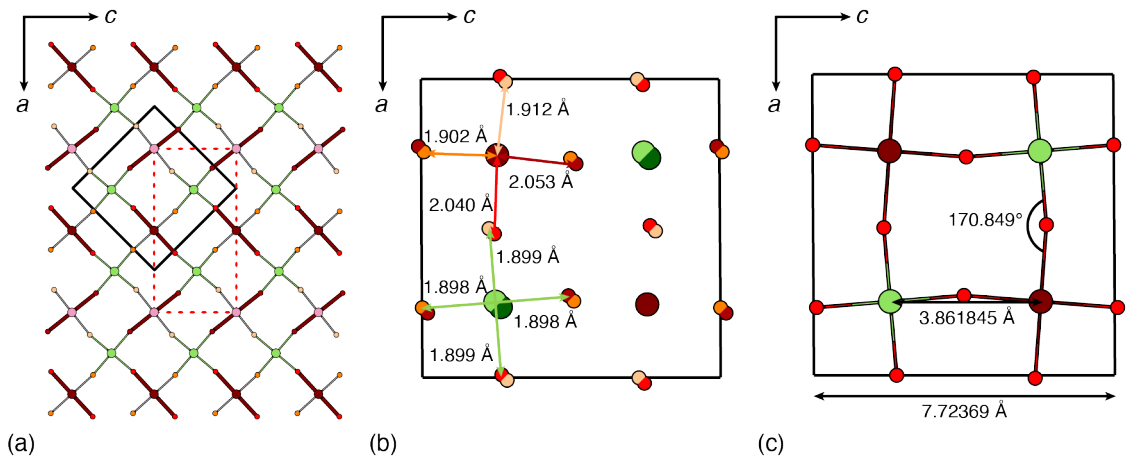


Figure 5.10: The *CE* structure of $La_{0.5}Ca_{0.5}MnO_3$ as given in Ref. 203. The red dashed box in (a) shows the minimum repeating unit to describe the $P21/m$ *CE* structure. The black box shows the sub-cell that MC configurations will be collapsed onto. Included is an illustration of the collapsed *CE* structure in the **a**-**c** plane, showing (b) the bond lengths used in the MC configurations and (c) the unit-cell parameter and ideal tilt value.

(Fig. 5.10(b)).[203] For rhombuses assigned as JT inactive, the value of ϕ was allowed to vary from a starting value of zero (corresponding to an average Mn^{4+}–O bond length of 1.8985 Å, Fig. 5.10(b)) with an equilibrium magnitude of zero. The equilibrium value of $\theta_{eq} = 4.5755°$, assigned to both a JT-active and JT-inactive rhombus, was obtained from the average Mn tilt in the structure of $La_{0.5}Ca_{0.5}MnO_3$ reported by Radaelli *et al.* (Fig. 5.10(c)).[203]

A simulated annealing approach was employed, starting with a MC temperature, $T_i = \frac{5E_i}{n_{tot}}$, where E_i is the initial energy of the configuration, and n_{tot} is the total number of cells in the supercell. Simulations proceeded by selecting a JT-active or JT-inactive ion site at random and randomly proposing one of four types of moves such that each of the four types of moves was proposed roughly 25% of the time. The first type of move changed the horizontal and vertical position of the rhombus by $\frac{-0.01}{an_{cells}} \leq \Delta x, \Delta y < \frac{0.01}{an_{cells}}$, where n_{cells} is the number of cells in each of the x- and y-directions, and an_{cells} $(= bn_{cells})$ is the lattice parameter of the supercell, with $a = 3.862$ Å (half the unit cell length shown in Fig. 5.10(c) to reflect the subcell in these MC simulations containing one MnO_4 rhombus). The

second type of move changed the tilt angle θ by $-1^\circ \leq \Delta\theta < 1^\circ$. The third type of move changed the JT distortion magnitude ϕ by $-0.3 \leq \Delta\phi < 0.3$. The fourth, and new, type of move for these LCMO MC simulations involved selecting a second site of the opposite type at random (*i.e.* if a JT-active site was initially chosen, then the second site chosen would be a JT-inactive ion and vice versa) and proposing that the JT distortion preference ϕ_{eq} of the two sites are swapped. Moves were accepted or rejected according to the usual Metropolis algorithm.[197,321] Simulations were continued at each temperature until equilibrium was achieved, which was determined by allowing 500 accepted moves for each site in the supercell. Following equilibration, the system temperature was reduced by a factor of 0.01. Below a MC effective temperature of 5×10^{-4}, moves where the simulation box was allowed to shear (*i.e.* the box may itself become a rhombus) represented 10% of the proposed moves. Note that no explicit term involving shear was introduced into the MC Hamiltonian. Instead, a proposed 'shear move' involved changing the lattice parameters of the box, *lpa* and *lpb* (previously fixed and equal to each other above a MC effective temperature of 5×10^{-4}), by $-0.001an_{\text{cells}} \leq \Delta a, \Delta b < 0.001an_{\text{cells}}$, and also changing the supercell angle, γ (previously fixed to 90°), by $-2.865 \times 10^{-3\circ} < \Delta\gamma \leq 2.865 \times 10^{-3\circ}$. The simulations were continued until a final MC temperature of $\sim 1 \times 10^{-5}$ was reached.

5.5.2 Results and discussion

In a first set of simulations [Fig. 5.11], each rhombus had access to all four degrees of freedom (its horizontal and vertical position, tilt angle, and a JT distortion magnitude), and all six terms in the MC energy defined in Eq. 5.3 were explicitly included. This MC Hamiltonian was able to produce the *CE*-type ordering (Fig. 5.11(a)), with a checkerboard CO of Mn^{3+} JT-active and Mn^{4+} JT-inactive sites accompanied by orbital order resulting from the JT distortion of the Mn^{3+} sites forming zig-zag chains along one diagonal (*e.g.* [101] in the unit cell setting

shown in Fig. 5.10(b)) and a parallel alignment of JT distortion axes along the other (*e.g.* $[10\bar{1}]$). As can be seen from the Mn^{4+} sublattice shown in Fig. 5.11(b), the *CE* structure is accompanied by shift displacements of Mn^{4+} JT-inactive rhombuses in alternate directions along the $[10\bar{1}]$ diagonal, which is consistent with the transverse modulation proposed by Radaelli *et al.*.[203] Additionally, it is worth noting that whilst the Mn^{4+} JT-inactive rhombuses showed one tilt angle ($\phi_{\text{avg}} = 4.66°$ across 5 configurations), the Mn^{3+} JT-active rhombuses showed a splitting of their tilts: for sites with their JT-distortion axis pointing along *e.g.* the vertical direction, they had one tilt angle ($|\phi_{\text{avg}}| = 2.48°$ across 5 configurations), whilst for sites with their JT-distortion axes pointing along *e.g.* the horizontal direction, they had a different tilt angle ($|\phi_{\text{avg}}| = 6.51°$ across 5 configurations). The Mn^{3+}, Mn^{4+}, and O sublattices and their respective simulated single-crystal scattering patterns can be seen in Fig. C2.15.

In order to gain a better understanding of the microscopic origin of the *CE* structure, a further set of MC simulations were performed to investigate the interplay between charge order, JT order, tilts, shifts, and strain in driving the *CE* structure. This set of MC simulations involved varying the set of terms included in the MC Hamiltonian (Fig. 5.12) in order to see which ingredients, or combination of ingredients, are necessary to achieve the *CE* structure. In all of these MC simulations, the rhombuses had access to all degrees of freedom—the horizontal and vertical position, *i.e.* the 'shift' degree of freedom, tilt, and a JT distortion—as well as being able to swap JT-distortion preference with another site of the opposite kind. As the aim was to explore the microscopic origin of the *CE* structure, the next-nearest neighbour JT coupling term ($J_{\text{nnJT}} \sum_{\text{nnJJT}} \frac{1}{2} \left[\frac{\phi_1 \cdot \phi_2}{|\phi_1 \cdot \phi_2} + 1 \right]$) was not included in the MC Hamiltonian in order to determine whether the other ingredients are sufficient to produce the correct nearest-neighbour JT ordering. The 'JT extent' term ($k_{\text{JT}} \sum_{\text{JT}} (|\phi| - \phi_{\text{eq}})^2$) and the 'split-atom' term ($\frac{1}{2} \sum_{\text{SA}} k_{\text{SA}} r^2$) were both always present in the MC Hamiltonian (Fig. 5.12(a)). However, whether the direct-nearest neighbour JT coupling

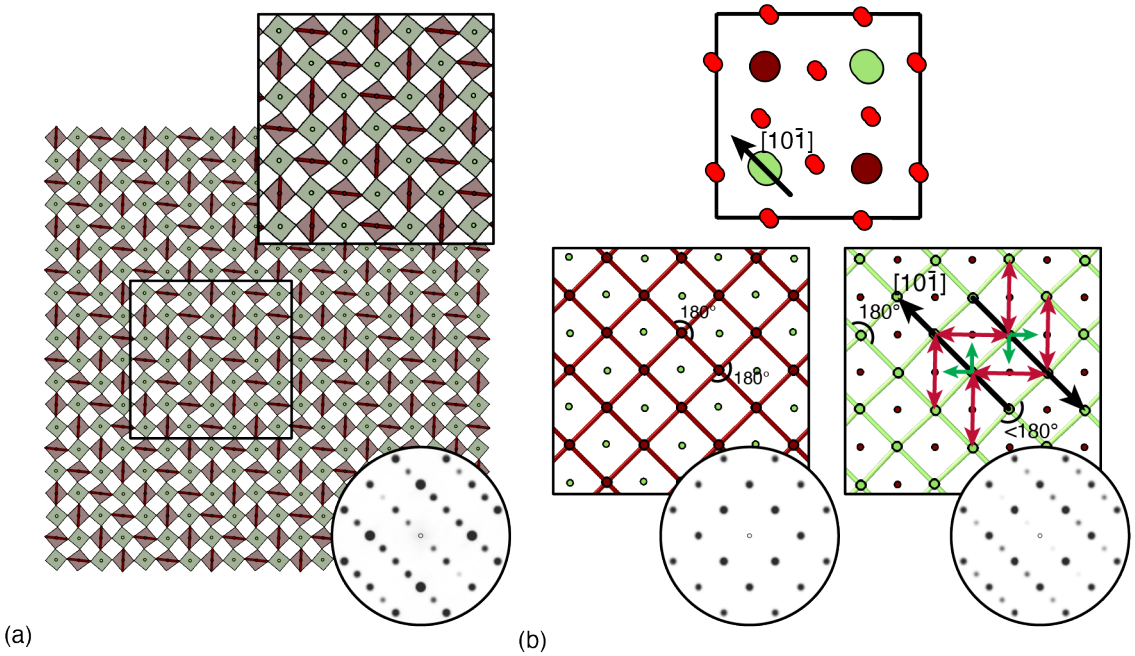


Figure 5.11: (a) A 20×20 supercell of the $La_{0.5}Ca_{0.5}MnO_3$ structure produced using the MC Hamiltonian as given in Eq. 5.3 and $k_{SA} = 100$. The *CE* structure is observed, with checkerboard charge order, zig-zag chains of JT order along the [101] direction, and an alternating parallel alignment of JT distortion axes along the $[10\bar{1}]$ direction. (b) A portion of the Mn^{3+} sub-lattice (JT-active sites) is shown in red and a portion of the Mn^{4+} sub-lattice (JT-inactive sites) is shown in green. The collapsed cell is also shown, highlighting the displacements of the $Mn^{4+}O_4$ rhombuses along the $[10\bar{1}]$ direction. The simulated single-crystal diffuse scattering patterns (averaged over five configurations) of the full structure, the Mn^{4+}, and Mn^{3+} sub-lattices are included, which highlight the displacements of JT-inactive (Mn^{4+}) rhombuses along the $[10\bar{1}]$ direction.

term ($J_{JT} \sum_{JT} \frac{1}{2} \left[\frac{\phi_1 \cdot \phi_2}{|\phi_1 \cdot \phi_2} + 1 \right]$), checkerboard CO term ($J_c \sum_n \frac{1}{2} \left[\frac{\epsilon_1 \cdot \epsilon_2}{|\epsilon_1 \cdot \epsilon_2|} + 1 \right]$), or tilt term ($k_\theta \sum_\theta (\theta_{eq} - |\theta|)^2$) were included in the MC Hamiltonian was varied, as well as the various combinations of these three terms (Fig. 5.12(b)). Additionally, the simulation box was allowed to shear below a MC effective temperature of 5×10^{-4}, but no explicit shear strain term was included in the Hamiltonian.

The first combination of ingredients checked for the ability to produce the *CE* ordering was the combination of all three terms highlighted in the previous paragraph: JT coupling, checkerboard CO, and tilts [Fig. 5.13]. When the split-atom spring constant is small ($k_{SA} = 0.2$), configurations have some local JT coupling between next-nearest neighbours despite the absence of a next-nearest neighbour

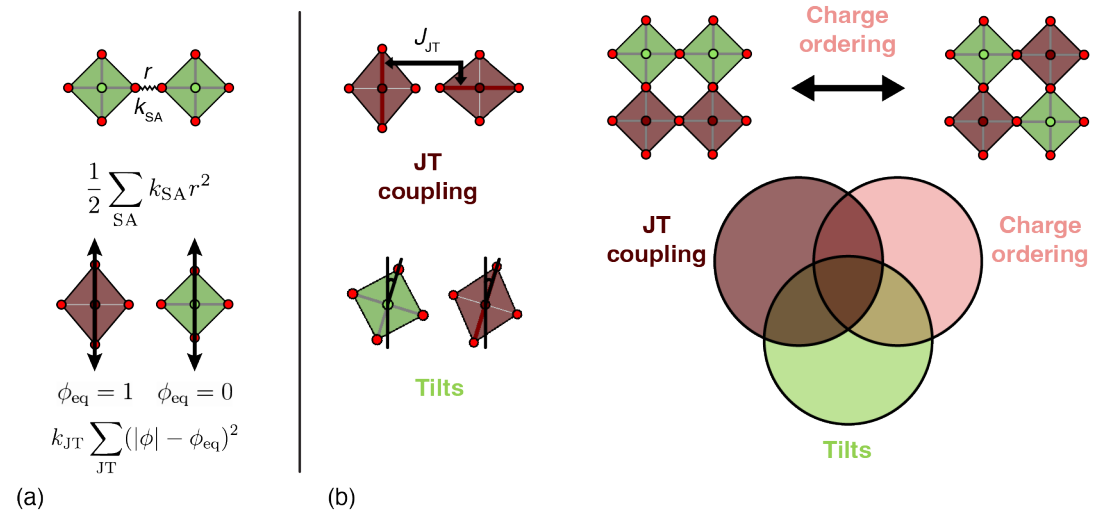


Figure 5.12: $La_{0.5}Ca_{0.5}MnO_3$ simple model: energy penalties in the MC Hamiltonian. (a) The split-atom term and JT-distortion magnitude term are always included in the MC Hamiltonian. (b) Which additional terms needs to be included in the MC Hamiltonian to still achieve the *CE* structure can be represented by the Venn diagram of JT coupling, tilts, and charge ordering terms.

JT coupling term from the Hamiltonian (Fig. 5.13(a)). As the split-atom spring constant is increased ($k_{SA} = 20$), this JT order becomes increasingly long range, with small domains of JT order appearing along both the [101] and [10$\bar{1}$] diagonals (Fig. 5.13(b)); this is reflected in the simulated single-crystal scattering pattern, which shows streaks along both directions (Fig. 5.13(b), Fig. C2.16(a)–(c)). Increasing the split-atom spring constant further ($k_{SA} = 100$) produces configurations that show long-range JT order, however, they also contain domain boundaries (Fig. 5.13(c), Fig. C2.16(d)–(f)). For all values of k_{SA} tested, checkerboard CO was achieved, so it can be said that when k_{SA} is large enough, the *CE* structure starts to emerge, but with the presence of JT domains.

In order to check whether the domain structure is a lower energy configuration than the fully-ordered *CE* structure or whether the formation of domains was a kinetic effect of the MC, a further set of MC simulations was performed. Each site was given a JT-distortion magnitude to match either the structure with domains or the fully-ordered *CE* structure, and above a certain temperature, sites were only

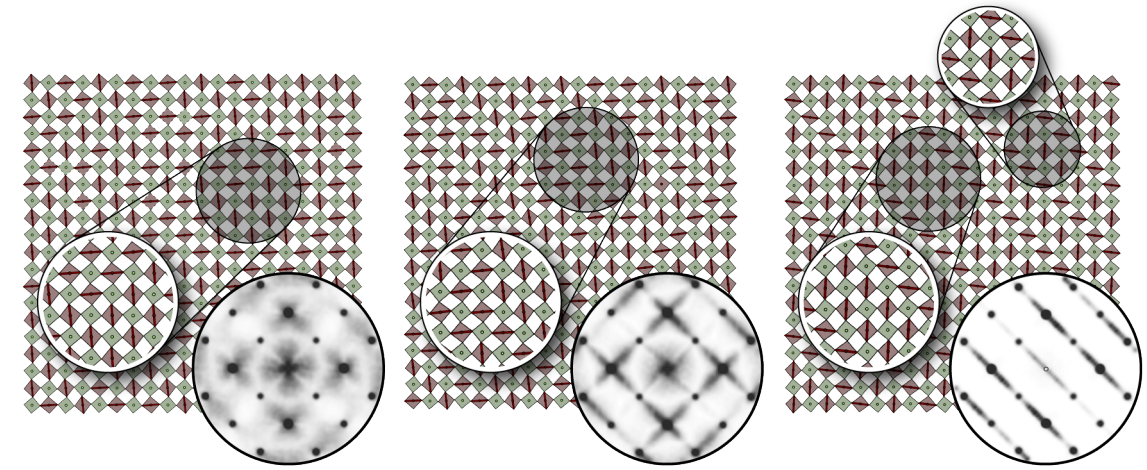


Figure 5.13: 20×20 supercells where JT coupling, checkerboard charge order, and tilt terms have all been included in the MC Hamiltonian but no next-nearest JT coupling is included. As k_{SA} is increased—(a) $k_{\mathrm{SA}} = 0.2$, (b) $k_{\mathrm{SA}} = 20$, and (c) $k_{\mathrm{SA}} = 100$—domains of next-nearest JT ordering start to appear, such that when $k_{\mathrm{SA}} = 100$, the CE structure with domain walls emerges. The corresponding simulated single-crystal diffuse scattering patterns (averaged over five configurations) are shown—the diffuse features sharpen into streaks along the $[10\bar{1}$ direction as k_{SA} increases.

allowed to tilt and shift, and below the certain temperature, sites then had access to all degrees of freedom (shift, tilt, swap JT-distortion preference, change JT-distortion magnitude, box shear). Before the simulation box was allowed to shear, the energy of the configuration with domains was far greater than that without domains (dominated by the split-atom term), but once the box was allowed to shear, the (final) energy of the configuration with domains and the fully-ordered configuration were essentially the same. This explains why the MC simulations tended to form configurations with domains: there are simply far more ways to form configurations with domains than a configuration without domains, and so the domain configurations are statistically more likely to be found in the MC simulation. This also highlights that the energy penalty of forming a domain wall is low, and the energy cost of flipping domains is far greater.

Having seen that the combination of all three of nearest-neighbour JT coupling, checkerboard CO, and tilt terms produces CE-type order (albeit with domains),

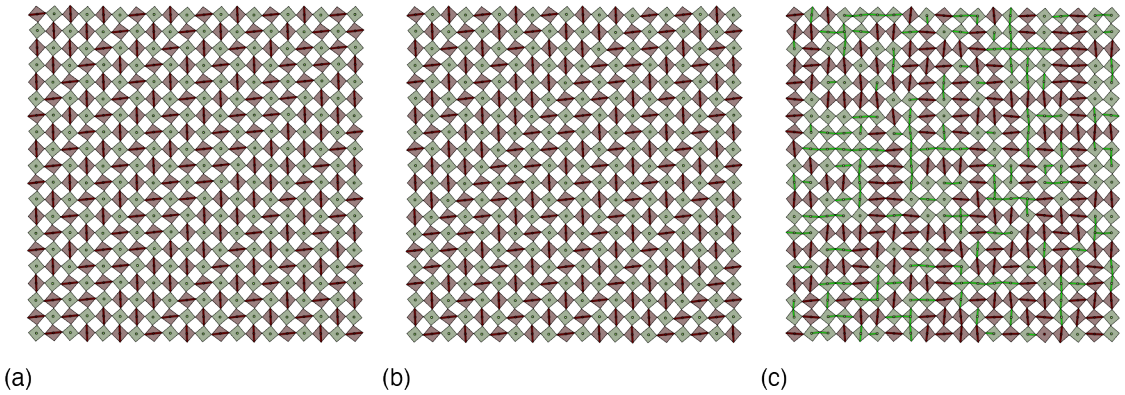


Figure 5.14: Investigating which of the charge order, nearest-neighbour JT coupling, and tilt terms needs to be included in the MC Hamiltonian to give the *CE* structure. 20×20 supercells where the split-atom and JT-distortion-magnitude terms are included in the MC Hamiltonian in addition to the (a) checkerboard charge ordering term, (b) nearest-neighbour JT coupling term, and (c) tilt term.

the next question would be to ask what the minimum number of terms needed to achieve the *CE*-type order might be (Fig. 5.15(a)); this should allow us to identify how these degrees of freedom couple to drive the *CE*-type order.

Interestingly, if only the checkerboard CO term is included in the MC Hamiltonian whilst sites are free to tilt, shift, swap, and change their JT-distortion magnitude as they wish, the same Mn^{3+} and Mn^{4+} tilt distortions identified earlier and the correct JT ordering are both still observed (again with domains) despite not providing the MC simulations with this information (Fig. 5.14(a)). Similarly, including only the nearest-neighbour JT coupling term in the MC Hamiltonian produces the *CE* structure with domains (note that more accepted moves was needed in this particular case) (Fig. 5.14(b)). However, the tilt term by itself is not able to produce the *CE* structure (Fig. 5.14(c)). This suggests that there is a coupling between charge order and JT order that gives the other.

To understand the geometric origin of the coupling between charge order and JT order (Fig. 5.15(a)), an illustration is provided in Fig. 5.15(b). When there is checkerboard CO and the direction of JT distortion is set for one Mn^{3+} site (labelled '1' in Fig. 5.15(b)), as a Mn^{4+} ion would preferentially shift rather than become 'JT

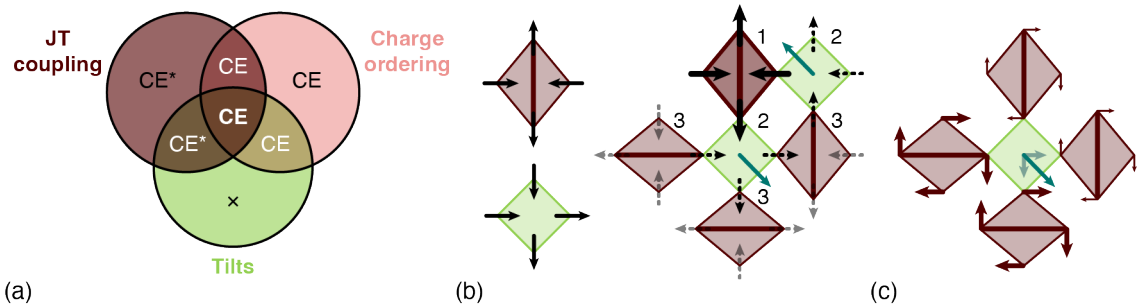
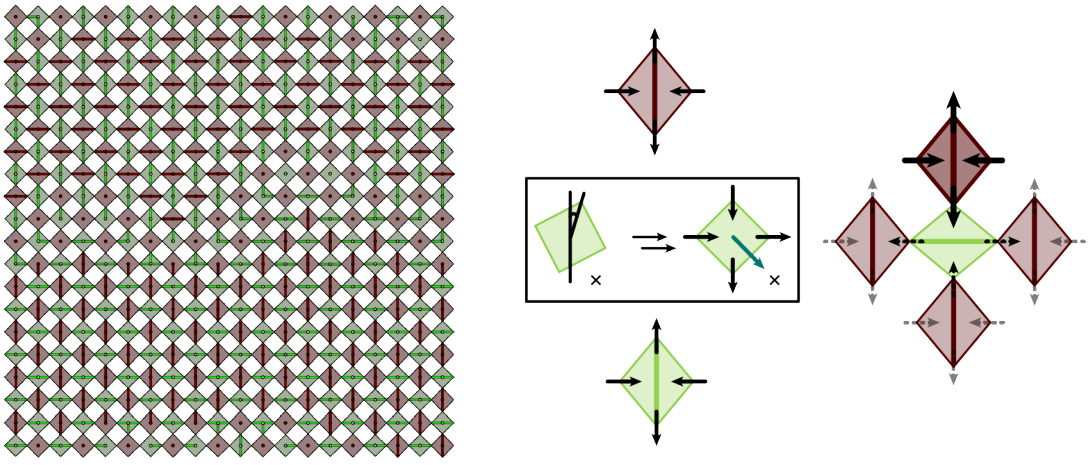


Figure 5.15: The coupling of degrees of freedom in the *CE* structure of $La_{0.5}Ca_{0.5}MnO_3$. (a) A Venn diagram showing which of the JT coupling, checkerboard charge ordering, and tilt terms need to be included in the MC Hamiltonian to produce the *CE* structure (with domains). (b) An illustration of the coupling between charge order and JT order: given the preference of Mn^{3+} rhombuses to stretch and Mn^{4+} rhombuses to shift rather than stretch (*i.e.* become JT active), once the direction of the first JT-distortion axis is set ('1'), the shift directions of the neighbouring JT-inactive rhombuses ('2') is set, which in turn set the JT-distortion direction of its neighbouring JT-active rhombuses ('3'). (c) An illustration of how the splitting of the tilts of the JT-active $Mn^{3+}O_4$ rhombuses facilitates the diagonal shift displacements of the $Mn^{4+}O_4$ rhombuses.

active', the direction of the shift degree of freedom is necessarily set for the four nearest Mn^{4+} sites (labelled '2'). It can then be seen how this gives rise to the alternating shifts of the Mn^{4+} sites along one cell diagonal ($[10\bar{1}]$ in Fig. 5.15(b)), specifically the diagonal along which the JT-distortion axes align parallel. Once the shift direction of the Mn^{4+} sites ('2') is determined, the JT-distortion axes of the four nearest Mn^{3+} sites (labelled '3') are also necessarily determined. Hence, on a lattice with checkerboard CO, once the direction of the JT-distortion axis is determined for the first site, the direction of the JT-distortion axes of all the remaining JT-active sites is necessarily determined through coupling to the Mn^{4+} shift displacements.

Having established the coupling between charge and JT order, it is perhaps not immediately clear what role the tilts play in obtaining *CE* order. To explore the role of the tilts, MC simulations in which the rhombuses were prevented from tilting were performed. Even if checkerboard CO (Fig. 5.16(a)) and/or the nearest-neighbour JT coupling terms (Fig. C2.17(a)–(b)) are included in the MC Hamiltonian, the *CE* structure is not observed if rhombuses are prevented from tilting. This suggests that tilts are a crucial degree of freedom needed to observe the *CE* structure.



(a) (b)

Figure 5.16: The requirement of tilts to achieve the *CE* structure of $La_{0.5}Ca_{0.5}MnO_3$. (a) A 20×20 supercell where the checkerboard charge-order term has been included in the MC Hamiltonian as well as the split-atom term and JT-distortion magnitude term, but crucially, the rhombuses have been prevented from tilting. The *CE* structure is not observed. (b) An illustration to show how when rhombuses are prevented from tilting, they appear to lose access to the shift degree of freedom, and so the only option left for $Mn^{4+}O_4$ rhombuses is to stretch.

When rhombuses are prevented from tilting, they appear to lose access to the shift degree of freedom (Fig. 5.16(a)); this suggests that the tilts must play a role in facilitating the diagonal shift displacements of the Mn^{4+} sites that we have already seen are crucial to coupling JT-distortion axes. Since the alternate shift displacements cannot be accommodated by shearing connecting Mn^{3+} rhombuses themselves, it must be the case that the tilts are what facilitate the Mn^{4+} shift displacements. It then becomes clear why there are two different tilt magnitudes of the Mn^{3+} JT-active sites: to accommodate the vector acting on the Mn^{4+} sites along the diagonal (dark green arrow in Fig. 5.15(b)), the Mn^{3+} sites with JT-distortion axes pointing in one direction must tilt more than the sites with JT-distortion axes pointing along the other direction. Hence, without access to the tilt degree of freedom, the diagonal shift displacements cannot be accommodated, and consequently the *CE* JT ordering cannot be observed (Fig. 5.16(b)). So, whilst the tilts might not drive the *CE* structure itself (Fig. 5.14(c)), the ability for rhombuses to tilt is required in order to facilitate the shift degree of freedom that couples JT-distortion

axes together on a checkerboard CO lattice. This is reminiscent of the role of shear strain in $LaGa_{1-x}Mn_xO_3$, where it was concluded that the ability for the system to shear is required in order to observe long-range *C*-type orbital ordering, but the application of shear strain cannot drive otherwise orbitally disordered compositions to long-range orbital order. So, as long as rhombuses in $La_{0.5}Ca_{0.5}MnO_3$ are free to tilt, including either checkerboard CO or nearest-neighbour JT coupling in the Hamiltonian is sufficient to get the other for 'free' and hence to achieve the *CE* structure.

From these $La_{0.5}Ca_{0.5}MnO_3$ MC simulations, we have seen how charge order, JT order, shifts, and tilts couple to drive the *CE* structure, but the role that shear strain plays has not yet been addressed. Throughout these simulations, the simulation box was allowed to shear but no explicit shear strain term was included in the MC Hamiltonian. These configurations did not show a strong desire to shear, having an average cell $\gamma \sim 89.93°$, hence with the other ingredients discussed, the *CE* structure can still be obtained in the absence of significant shearing. Introducing an explicit shear strain term ($k_\gamma(\gamma - \gamma_{eq})^2$) and setting the ideal cell γ_{eq} to 89.69° (the cell γ reported by Radaelli *et al.*)[203] did not produce significantly different configurations (Fig. C2.18). Although significant shearing is not observed in these MC simulations, allowing the system to shear does allow the system to relax to a significantly lower-strain state. Hence, whilst shear strain does not seem to help drive the *CE* structure itself, coupling to shear strain reduces the overall energy of the system and happens spontaneously without needing to add an explicit shear-strain term to the Hamiltonian.

The work of this chapter has demonstrated that simple geometric considerations of corner-sharing JT-active and JT-inactive polygons can be used to rationalise the coupling between JT, tilt, and shear strain modes that drives the orthorhombic to pseudocubic transition in the $LaGa_{1-x}Mn_xO_3$ series.[371] Additionally, extending the simple model for the $La_{0.5}Ca_{0.5}MnO_3$ system revealed how charge order, JT order,

shifts, and tilts couple to drive the *CE* structure. What these results hopefully demonstrate is the power that simple modelling can have in understanding complex phenomena involving an interplay of multiple degrees of freedom that can be hard to disentangle using perhaps more conventional techniques.

5.6 Conclusions and future directions

Having used simple geometric modelling to rationalise the coupling between degrees of freedom that give rise to the *C*-type orbital order of $LaMnO_3$ and the *CE* structure of $La_{0.5}Ca_{0.5}MnO_3$, the next step for this model is to see whether it has the essential ingredients to explain the competition between *C* and *CE* type distortion modes that gives rise to a 1:3 orbital order:charge disorder striping in the manganite quadruple perovskites $AMn_3Mn_4O_{12}$ (A=$Ca_{1-x}Na_x$,$Hg_{1-x}Na_x$);[25,206] using the $R_{5/8}Ca_{3/8}MnO_3$ (R = rare-earth cation) prototype systems, it has been shown that the optimal doping level for CMR coincides with the point of closest proximity to this orbital order:charge disorder state,[362] *i.e.* the point at which the *C* and *CE* orbital order arrangements have the strongest competition.

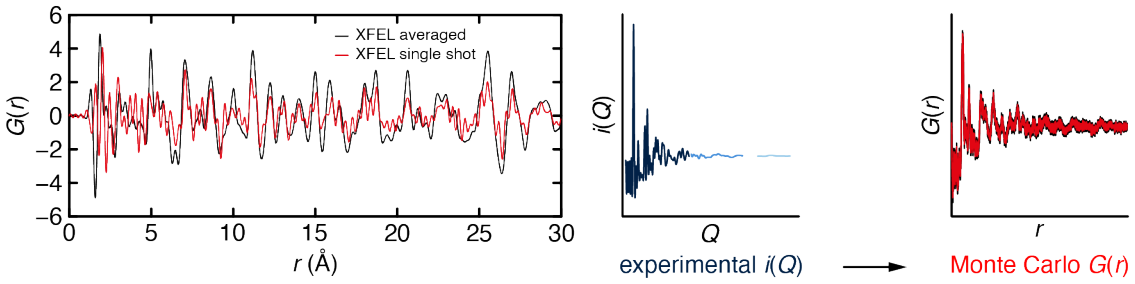
The fact that simple geometric considerations have been able to rationalise the emergence and nature of CJT effects in both PBAs (Chapter 4) and now also the $LaGa_{1-x}Mn_xO_3$ and $La_{0.5}Ca_{0.5}MnO_3$ manganite perovskites begs the question: can geometric considerations of the kind developed in these past two chapters be extended to model CJT effects in other systems? The layered A_xMO_2 materials, with both charge and CJT order within MO_2 layers,[378–380] seem an ideal candidate. Li_2MnO_3 is the characteristic example of in-layer honeycomb charge ordering with a 2:1 ratio of Mn^{4+} and Li^+ ions;[379] the $Na_{2.8}ZnIr_2O_6$ system shows a similar honeycomb charge ordering pattern.[380] In the $Na_{0.67}MnO_2$ battery cathode material, cycling between JT-active high-spin Mn^{3+} and JT-inactive Mn^{4+} switches on and off long-range CJT order,[378] and is implicated in reducing the efficiency of the battery; doping with JT-inactive Mg^{2+} in $Na_{0.67}Mn_xMg_{1-x}O_2$ seems a potential solution

for widening the voltage window by suppressing long-range CJT order and hence preventing damaging CJT-driven symmetry breaking.[378] The $Na_{0.67}Mn_{0.72}Mg_{0.28}O_2$ composition shows in-layer honeycomb ordering of the Mg/Mn cations[381] as the ratio of Mn^{4+} to Mg^{2+} approaches the ideal 2:1 ratio. Hence, the simple geometric model developed in this chapter could be extended to model the in-layer CJT order and honeycomb order in the $Na_{0.67}Mn_xMg_{1-x}O_2$ system as a function of composition x ($0.667 \leq x \leq 1$).

Chapter 6

Measuring pair distribution functions with X-ray free-electron lasers: ultra-fast studies of disorder in Prussian blue analogues

6.1 Overview



So far in this thesis, pair distribution function (PDF) analysis has been used to help with understanding the local structure and dynamics in the effectively defect-free transition-metal hexacyanoplatinate Prussian blue analogues (PBAs) (Chapter 3), particularly the key phonons responsible for their negative thermal expansion. PDF analysis was also used in Chapter 4 to obtain an atomistic local structure representation of a more complex PBA, $Cu[Co(CN)_6]_{2/3}$, containing local JT distortions within a globally undistorted cubic structure. Hence, PDF techniques can be a powerful tool for studying the local structure of materials. However, to capture the ultra-fast atomic changes that occur during *e.g.* photoinduced charge transfer

in PBAs, tools with femtosecond resolution will be required, something that current synchrotron sources do not provide. X-ray free-electron lasers (XFELs) are capable of producing femtosecond-pulsed X-ray radiation, however, current XFEL technologies do not possess the real-space resolution that many advanced structural studies require. Hence, the work of this chapter concerns the efforts made by a consortium to develop high-quality ultra-fast total scattering/PDF data at the European XFEL in Hamburg. The hope within the aims of this thesis is that XFEL technologies can be used to characterise the local structure of complex PBAs, *e.g.* those with JT distortions/vacancies; the longer-term hope is that the development of XFEL techniques will allow the characterisation of processes that occur on the timescale of femtoseconds, *e.g* photoinduced charge transfer in PBAs. Finally, the possibility of using a simple inverse Monte Carlo method to generate a PDF from reciprocal space data that is missing information is explored.

6.2 Acknowledgements

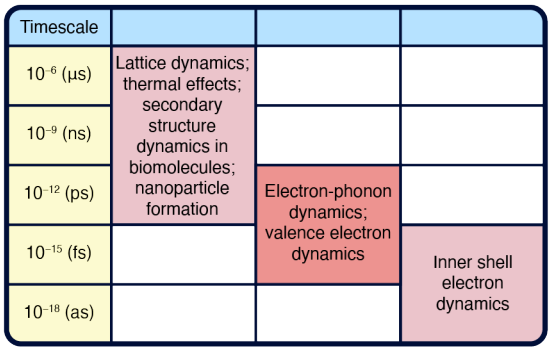
This work forms part of a community long-term project, headed by David Keen, to establish high-quality ultra-fast total scattering/pair distribution function techniques at the European XFEL, Hamburg. The group's work was published in *IUCrJ*[382] and this chapter includes work from the wider group. My contributions include the synthesis of the $Cu[Co(CN)_6]_{2/3}$ Prussian blue analogue (PBA) sample, data analysis and modelling of the PBA data, attendance at all three beamtimes—two on the High Energy Density (HED) beamline and one on the Materials Imaging and Dynamics (MID) beamline—and (exploring methods for) mounting capillary, flat plate, and thin-film powder samples. I am grateful to John Cattermull and Hunter Windsor for providing additional PBA samples to measure, and data for a few of these samples are presented in Appendix D1.

A. F. Sapnik, P. A. Chater, D. S. Keeble, J. S. O. Evans, F. Bertolotti, A. Guagliardi, L. J. Støkler, E. A. Harbourne, A. B. Borup, R. S. Silberg,

A. Descamps, C. Prescher, B. D. Klee, A. Phelipeau, I. Ullah, K. G. Medina, T. A. Bird, V. Kaznelson, W. Lynn, A. L. Goodwin, B. B. Iversen, C. Crepisson, E. S. Bozin, K. M. Ø. Jensen, E. E. McBride, R. B. Neder, I. Robinson, J. S. Wark, M. Andrzejewski, U. Boesenberg, E. Brambrink, C. Camarda, V. Cerantola, S. Goede, H. Höppner, O. S. Humphries, Z. Konopkova, N. Kujala, T. Michelat, M. Nakatsutsumi, A. Pelka, T. R. Preston, L. Randolph, M. Roeper, A. Schmidt, C. Strohm, M. Tang, P. Talkovski, U. Zastrau, K. Appel, D. A. Keen,
"High-quality ultra-fast total scattering and pair distribution function data using an X-ray free-electron laser",
IUCrJ. **2025**, *12*, 531–547.

6.3 Introduction

Total scattering/pair distribution function (PDF) techniques can provide an excellent handle on the local structure of PBAs. PDF analysis was performed in Chapter 3 to interrogate the local structure and dynamics of the $MPt(CN)_6$ Prussian blue analogues (PBAs), particularly the key phonons responsible for negative thermal expansion in these materials. PDF measurements were used again in Chapter 4 to provide an atomistic representation of the local structure of a more complex PBA, $Cu[Co(CN)_6]_{2/3}$, containing an interplay between cooperative Jahn–Teller effects and hexacyanometallate vacancies. The big-box models of these two structures represent a snapshot of their structures, since the interaction between the X-ray (or neutron) and the sample occurs on a timescale far faster than that of atomic vibrations. Hence, both static and dynamic (dis)order can be captured by total scattering measurements. Recently, there has been a growing interest in studying (dis)ordering processes themselves, *e.g.* crystallisation and amorphisation, as well as ultra-fast responses to external stimuli such as light.[383–385] In the context of PBAs, there is an interest in understanding the mechanism of photoinduced charge transfer;[257–261] recently, an initial photoinduced spin-state transition that pre-empts charge transfer



(a)

Source	Q_{max} (Å^{-1}) (r-resolution~π/Q_{max})	Timescale for measurement	Year method started
Cu/Mo X-ray	~ 16	~ days	1930s
Neutron	~ 40	~ hours	1990s
Synchrotron X-ray	~ 26	~ seconds	2000s
XFELs	~ 8	~ 100fs	2010s
XFELs (our work)	~ 20	~ 30fs	2023

(b)

Figure 6.1: XFELs within the context of total scattering measurements. (a) The timescales upon which various (dis)ordering processes take place. (b) The $Q_{\max}$ values and data acquisition times currently achievable using in-house Cu/Mo X-ray, neutron spallation, synchrotron X-ray, and X-ray free-electron setups.

in $Cs_{0.7}Co[Fe(CN)_6]_{0.9}$ has been identified, with the spin-state transition occurring over 50 fs and charge-transfer over 200 fs.[262] Since the PDF captures the instantaneous structure, it should be possible to use PDF techniques to probe local structure changes that happen during (dis)ordering processes themselves. Many (dis)ordering processes happen on timescales ranging from hours to femtoseconds [Fig. 6.1(a)], hence capturing atomic changes associated with many of these processes will require instrumentation with ultra-fast data acquisition capabilities. Whilst synchrotron-based diffractometers are capable of providing high real-space resolution (with $Q_{\max}$ values of around 25 Å^{-1}) [Fig. 6.1(b)], typical synchrotron measurements take seconds to minutes [Fig. 6.1(b)], and hence do not possess the temporal resolution required to capture ultra-fast atomic changes.

X-ray free-electron lasers (XFELs) are an emerging technology capable of capturing ultra-fast atomic changes.[295–297] One early study to make use of XFEL total scattering measurements was a pump–probe study of the formation of gold trimers in solution, which achieved $Q_{\max} \approx 6.5$ Å^{-1} for difference structure factors $\Delta S(Q)$ ($S(Q)$ after pumping minus $S(Q)$ before pumping) with 15 keV X-rays;[386] such $Q_{\max}$ values will not provide the real-space resolution required to probe *e.g.* structural changes in complex materials such as PBAs. Only limited progress has been achieved

in terms of improving the real-space resolution, with a $Q_{\max} = 12.6\,\text{Å}^{-1}$ (real-space resolution $\sim 0.5\,\text{Å}$) for $\Delta S(Q)$ possibly the highest recorded.[265] Hence, in order to make use of the temporal resolution of XFELs to *e.g.* study the ultra-fast mechanism of photoinduced changes in PBAs, the real-space resolution of XFEL PDF instruments will first need to be improved.

This chapter presents the efforts of a large group of people to make it possible to attain high-quality, ultra-fast total scattering and PDF data at the High Energy Density (HED) scientific instrument at the European XFEL.[382] The experimental setup, which makes use of a tilted detector geometry to maximise $Q_{\max}$, will be described. Additionally, the data processing and reduction pipeline will be outlined, with more details available in the published paper (Ref. 382). The results of some standard crystalline materials are included to show the possibility of measuring high-quality ultra-fast total scattering data. This chapter then goes on to assess the quality of XFEL PDFs of PBAs by comparison with synchrotron PDF data, before exploring whether XFEL PDFs can be used to characterise structural complexity in PBAs, *e.g.* those containing JT-active cations and hexacyanometallate vacancies. Finally, the possibility of using an inverse Monte Carlo method to calculate a PDF from reciprocal-space total scattering data with gaps in Q is explored in the context of weighing up the pros and cons of maximising $Q_{\max}$ at the expense of a continuous coverage in Q space.

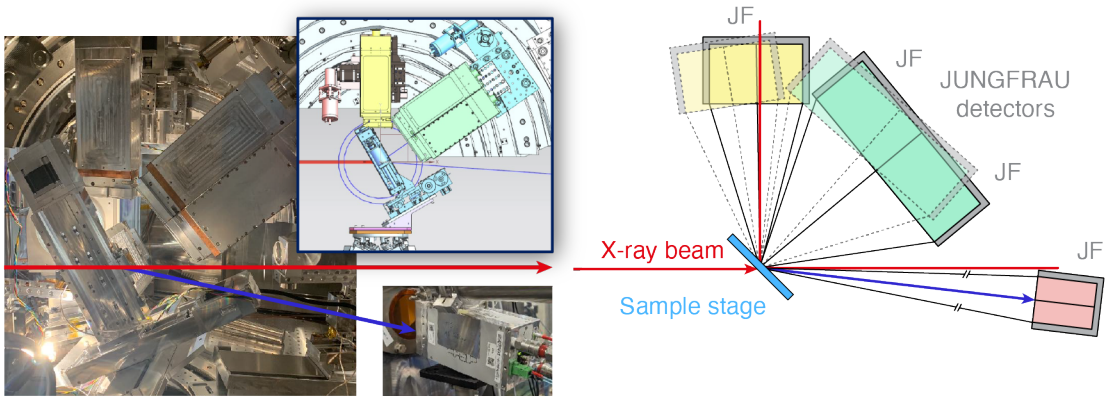
6.4 Pair distribution function measurements at the EuXFEL

6.4.1 Methods

The following section describes the key features of the two different setups we developed for measuring total scattering/PDF data at the High Energy Density (HED)[278] scientific instrument at the European XFEL in Hamburg. Only a brief overview of the key features is given—further technical details can be found in the published paper (Ref. 382). Both experiments were carried out in interaction chamber one (IC1)[278] under a $< 10^{-4}$ mbar vacuum to eliminate background contributions from air scattering. The incident X-ray energy in both experiments was ~ 24 keV.

EuXFEL HED Interaction Chamber 1 (IC1): setup 1

Our aim at the first experiment was to collect data to $Q_{\text{max}} \approx 20\,\text{Å}^{-1}$. To achieve this, we arranged four JUNGFRAU detectors[387,388] around the sample in the vertical plane [Fig. 6.2]; three were placed within the vacuum chamber above the horizontal plane/X-ray beam (red line in Fig. 6.2) and measured scattering up to $2\theta \sim 110°$, the fourth detector (pink in Fig. 6.2(b)) was placed outside the vacuum chamber below the horizontal plane/X-ray beam to measure some of the low-2θ angles not captured by the three detectors within the vacuum chamber. To access these higher 2θ angles, the sample stage (blue in Fig. 6.2(b)) was positioned at an angle of 120° to the horizontal plane/X-ray beam such that the normal to the plane of the sample stage was pointing at $2\theta = 30°$. This first setup achieved a $Q_{\text{max}} = 19.9\,\text{Å}^{-1}$, much higher than typical Q_{max} values at XFEL facilities;[389–391] however, this high Q_{max} value came at the expense of two gaps in Q coverage between $7.56 < Q < 7.77\,\text{Å}^{-1}$ and $13.63 < Q < 15.32\,\text{Å}^{-1}$. The JUNGFRAU detectors were mounted on movable arms, so one could in theory explore moving the detectors to cover the gaps.



(a) (b)

Figure 6.2: Overview of the first setup used on the EuXFEL HED IC1 beamline. (a) Experimental setup and CAD drawing and (b) schematic of the arrangement of the four JUNGFRAU detectors. The fourth detector (shown in pink), which was placed below the horizontal plane/X-ray beam outside the IC1 vacuum chamber, is not shown in the CAD drawing in (a). CAD drawing adapted from Ref. 382, which is licensed under a Creative Commons Attribution 4.0 International License, and part (b) remade in the style of Ref. 382.

EuXFEL HED Interaction Chamber 1 (IC1): setup 2

The aim of the second experiment was to design a setup with as high $Q_{\max}$ as possible with no gaps in Q coverage; this second setup provided a continuous coverage over approximately $0.35 \lesssim Q \lesssim 16.6\,\text{Å}^{-1}$. A schematic illustration of the setup is shown in Fig. 6.3. A key feature of this setup was an inclined ($2\theta \approx 75°$) (Varex 4343CT) detector arrangement [Fig. 6.3(a)],[392] which has several advantages. Firstly, this arrangement places the detector closer to the sample at higher scattering angles, and hence maximises the detector solid angle at these higher scattering angles where the sample scattering will be weakest. Secondly, since the detector is further away from the sample at lower scattering angles, the detector's resolution for these lower 2θ Bragg peaks will be higher, and reduces the chance of saturating the detector. Thirdly, this inclined detector arrangement significantly increases the range of scattering angles that can be measured compared to placing the detector perpendicular to the X-ray beam. Other features of the setup include a set of clean-up slits and a stainless steel shield placed before the sample stage to reduce background scattering,

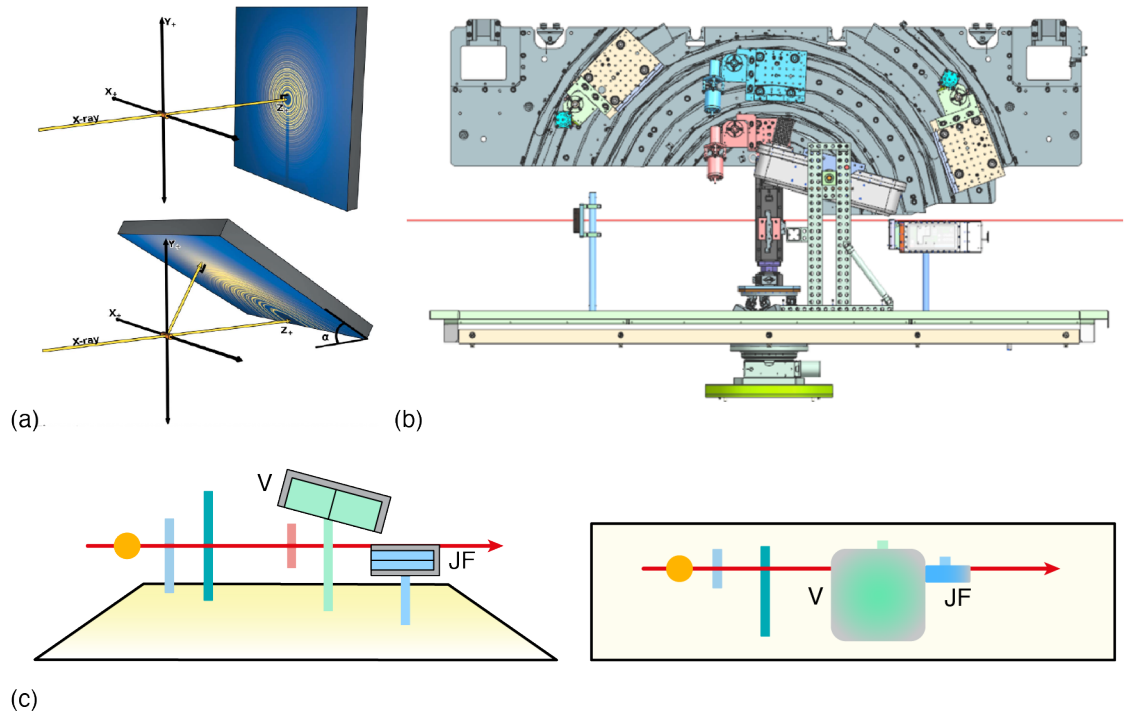


Figure 6.3: Overview of the second setup developed on the EuXFEL HED IC1 beamline. (a) An inclined area detector for total scattering.[392] (b) Technical CAD drawing of the setup. (c) Schematic of the main diffractometer components (left: side view, right: plan view). The path of the X-ray beam is shown as a red horizontal line. A diamond monitor is shown in orange, clean-up slits are shown in light blue, a steel shield is shown in teal, the sample stage is shown in pink. The Varex detector is labelled 'V', with the active areas highlighted in green. The JUNGFRAU detector is labelled 'JF', with its active areas highlighted in blue. Part (b) reprinted from Ref. 382, which is licensed under a Creative Commons Attribution 4.0 International License. Part (c) remade in the style of Ref. 382.

and the use of a JUNGFRAU detector to cover scattering angles $1° \lesssim 2\theta \lesssim 14.5°$ (the Varex detector covers $9° \lesssim 2\theta \lesssim 89°$).

Sample preparation and mounting

Samples were mounted onto EUCALL[393,394] standard sample holders, consisting of an outer and inner frame [Fig. 6.4(a)]. Various different target mount plates—designed to hold flat-plate samples, thin film samples, and capillaries [Fig. 6.4(b)]—could be mounted onto the inner frame. Capillaries were glued and/or taped directly to the capillary mount plates, which came in two separate sizes such that capillaries of lengths up to $\sim 40\,\text{mm}$ and $\sim 70\,\text{mm}$ could be accommodated. Flat-plate samples

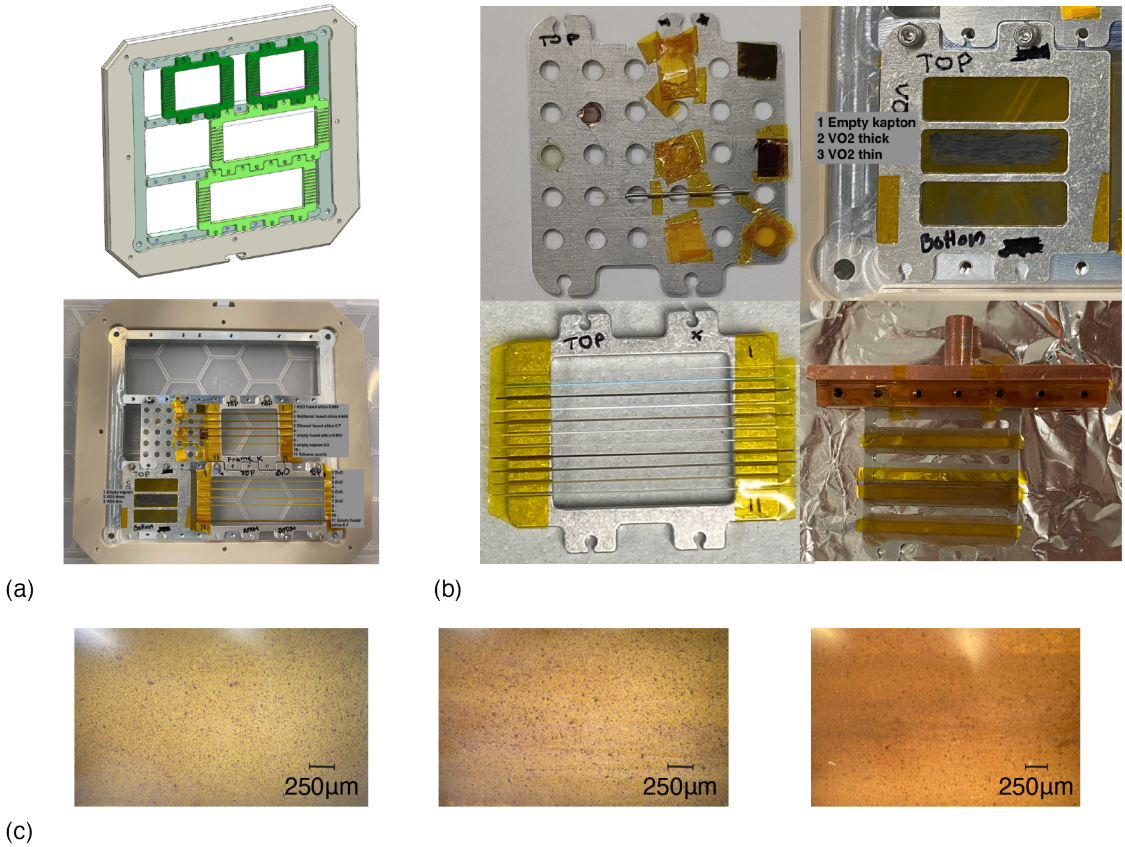


Figure 6.4: Sample mounting at the EuXFEL. (a) Technical CAD drawing (top) of the EUCALL sample holder used in the HED experiments, which have bespoke (green) frames that can hold capillaries of varying length and diameter. Flat-plate samples and thin films can also be mounted, and an example frame holding samples is shown (bottom). (b) A closer look at how flat-plate samples (top-left), capillaries (bottom-left) and thin film samples (right) can be mounted onto sub-frames. Note that the top-right thin films were mounted onto the HED sample holder in (a), and the bottom-right thin films were mounted onto the sample holder used on the MID beamline. (c) Microscope images of thin film samples of $RbMn[Fe(CN)_6]$ PBA prepared with different thicknesses of layers of powder.

were prepared by spreading powders between two layers of Kapton tape to create a 'sandwich'. Thin film samples were prepared by suspending powder in a solvent (*e.g.* ethanol, isopropanol), pipetting the suspension onto the non-sticky side of a piece of Kapton tape, and evaporating off the solvent to leave a thin layer of powder. Different thicknesses of sample could be prepared by adding more layers [Fig. 6.4(c)].

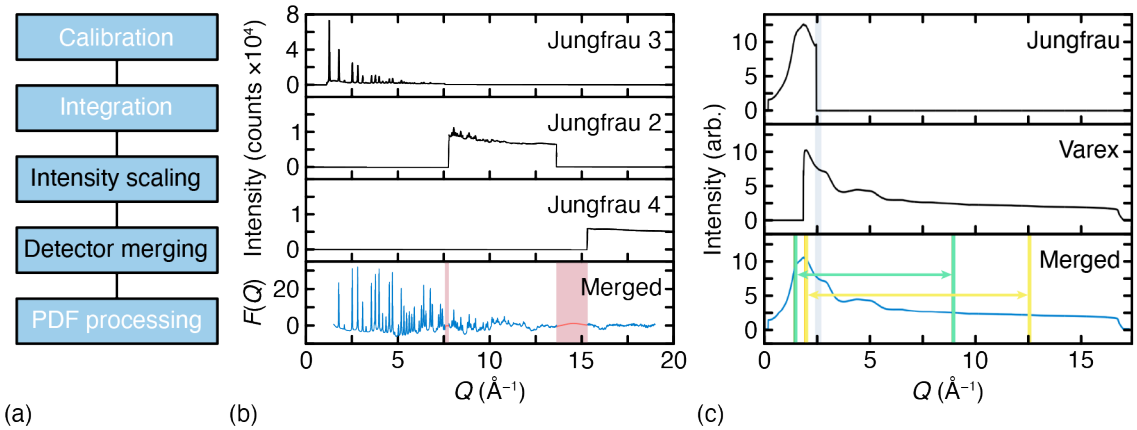


Figure 6.5: (a) Overview of the data processing pipeline. (b) Example of processed data from JUNGFRAU 3, 2, and 4 detectors collected using setup 1 on HED IC1. Data collected for $Cu[Co(CN)_6]_{2/3}$ PBA in a borosilicate capillary is given as an example. The merged $F(Q)$ data is also shown, with interpolation into the Q-gaps highlighted by pink shaded regions. (c) Example of processed data from the Varex and JUNGFRAU detectors collected using setup 2 on HED IC1. The fully merged data, using water in a fused silica capillary is also given. The values of $Q_{\min}$ and $Q_{\max}$ achieved at recent XFEL experiments making use of $S(Q)$[390] and $\Delta S(Q)$[265] measurements are shown as green and yellow vertical lines, respectively. The region where data from the JUNGFRAU and Varex detectors are merged is highlighted by a grey shaded region. Parts (a) and (c) adapted from Ref. 382, which is licensed under a Creative Commons Attribution 4.0 International License.

6.4.2 Data processing

An important aim of this long-term community project was to achieve *high-quality* and *quantitative* XFEL total scattering/PDF data. Hence, the group aimed to develop a robust data-processing procedure for obtaining high-quality PDFs from XFEL total scattering data. The main steps of the procedure are as follows (outlined in Fig. 6.5(a)): (i) calibration using a flat-plate sample of NIST CeO_2 SRM 674b powder; (ii) azimuthal integration of the data from the individual detectors—the four JUNGFRAU detectors of setup 1 [Fig. 6.5(b)] or the JUNGFRAU and Varex detector of setup 2 [Fig. 6.5(c)]—to yield the intensity as a function of Q, $I_x(Q)$; (iii) scaling and (iv) merging of the $I_x(Q)$ from each detector to give a merged $I_{\text{merged}}(Q)$; (v) subtraction of background scattering and subsequent Fourier transform of $I_{\text{merged}}(Q)$ to yield the PDF. Further technical details of each of these steps can be found in the published paper (Ref. 382).

6.4.3 Results and discussion: EuXFEL HED IC1 setup 2

Given the aim of establishing high-quality XFEL total scattering that are reliable, reproducible and robust for a wide range of different types of materials, the group chose to pursue setup 2 primarily [Fig. 6.3] as it did not have the added complication of how to deal with the gaps in Q coverage during data processing. The results for setup 2 are therefore given first. Approaches for treating the Q gaps in data obtained using setup 1 are discussed after.

First, highly crystalline powders (Si, CeO_2, LaB_6 and Ag behenate) were investigated to show that quantitative total scattering data over a wide Q range can be obtained. Finally, and most pertinent to this thesis, a range of PBA samples with different compositions were measured; this chapter focuses on XFEL PDF data of $Cu[Co(CN)_6]_{2/3}$ so that comparisons can be made with synchrotron (I15-1) PDF data that were used in Chapter 4.

Crystalline standards

Highly crystalline powders—certified standard reference materials (SRMs) Si, CeO_2, LaB_6, and Ag behenate from the US National Institute of Standards and Technology (NIST)—were measured in capillary and flat-plate geometries to determine the diffractometer characteristics ('calibration'). The reciprocal space diffraction pattern of NIST Si 640b SRM [Fig. 6.6(a)] showed narrow, symmetric peaks and a high signal-to-noise ratio, even at the highest angles. The PDFgetX3 software[395] was used to calculate a PDF from the normalised NIST Si 640b reciprocal-space data over the Q range $1.76 \leq Q \leq 16\,\text{Å}^{-1}$. The PDF contained sharp peaks, as expected for a highly crystalline material. The PDF also showed minimal damping at high r, suggesting negligible instrumental contributions from this setup. A small-box Rietveld refinement was performed using the PDFgui software[189], and a reasonable fit was achieved ($R_\text{p} = 13.7\%$) [Fig. 6.6(b)], though there was some oscillatory behaviour in the difference curve, which may be an artefact from the Fourier transform

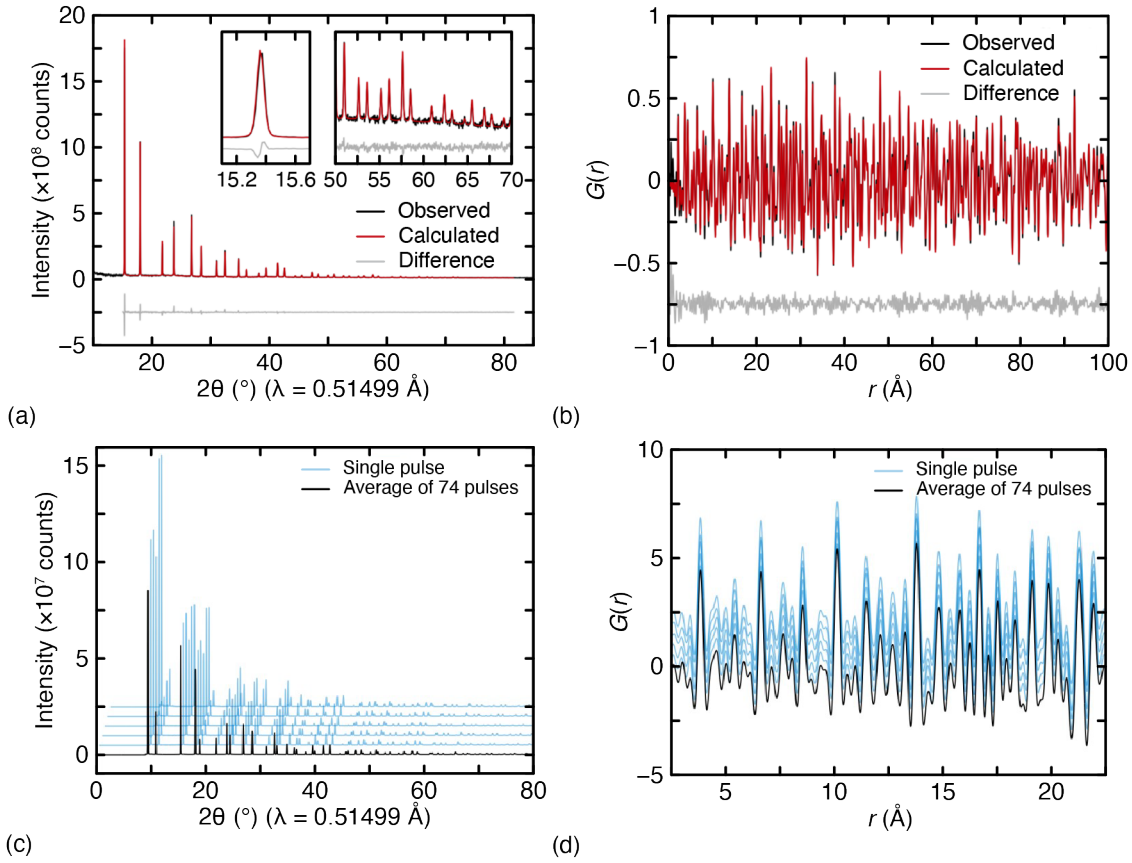


Figure 6.6: EuXFEL HED IC1 setup 2: Rietveld refinements and PDFs of crystalline standards. (a) NIST Si 640b Rietveld refinement of averaged normalised powder diffraction data. (b) NIST Si 640b small-box PDF 'real-space Rietveld' refinement. (c) A comparison of representative single pulse powder diffraction patterns (blue lines) of NIST CeO_2 and the averaged pattern (black line). (d) A comparison of single pulse PDF data (blue lines) of NIST CeO_2 with the average PDF (black line) (offset vertically). Figure adapted from Ref. 382, which is licensed under a Creative Commons Attribution 4.0 International License.

of the merged region of the Q data ($1.89 < Q < 2.49\,\text{Å}^{-1}$). Overall, the Rietveld and PDF fits of NIST Si 640b SRM show that it is possible to obtain quantitative total scattering data across a wide Q range using an XFEL source.

To assess whether high-quality and quantitative total scattering data can be obtained in a single XFEL pulse—critical for future time-resolved studies—NIST CeO_2 674 SRM powder was measured in a fused silica capillary using single XFEL pulses ($\sim$ 30 fs) of only 10% of the full X-ray beam intensity. Remarkably, the diffraction patterns of various single pulses once again showed sharp Bragg peaks and a high signal-to-noise ratio [Fig. 6.6(c)], whilst their PDFs showed little variation,

indicating high reproducibility [Fig. 6.6(d)].

Total scattering data from a Prussian blue analogue

Finally for setup 2, the XFEL PDF obtained from a PBA, $Cu[Co(CN)_6]_{2/3}$, is shown in Fig. 6.7(a); data were Fourier transformed using PDFgetX3[395] over the Q-range $0.25 \leq Q \leq 15.6\,\text{Å}^{-1}$. Note that sometimes with area detectors, there is a need for oblique incidence[396] or parallax effect[397] corrections. The PDF obtained from this same $Cu[Co(CN)_6]_{2/3}$ sample at the I15-1 beamline at Diamond Light Source is shown for comparison [Fig. 6.7(a)]; data were Fourier transformed using PDFgetX3[395] over the Q-range $0.35 \leq Q \leq 19\,\text{Å}^{-1}$. There appears to be a reasonable agreement between the XFEL PDF and I15-1 PDF, with key peaks appearing in similar places. Both PDFs show a mixture of sharp and broad peaks, which is characteristic of PBAs where atom pairs can be correlated to different extents at similar distances (*e.g.* inter- *vs* intra-polyhedral atom-pairs).[329] The width of peaks at low r appear similar in the two PDFs; however, at high r, the widths of the XFEL peaks appear narrower and more clearly resolved despite a lower Q_{max}, though it is not immediately clear how much of this might be noise. Additionally, the XFEL PDF appears to show less damping at high r than the I15-1 PDF, suggesting there were fewer instrumental contributions from the XFEL setup.

An interesting area to look at more closely in order to assess whether (some) differences may arise from changes in the sample itself is the $3 < r < 5$ Å region. Broad peaks in this $3 < r < 5$ Å region typically correspond to correlations with zeolitic and interstitial water within the cavities of the framework structure, but there are also peaks corresponding to C–(Co)–C (linear) (~ 3.6 Å), N–(Cu)–N (linear) (~ 4.1 Å), and C–(Co)–C (bent) (~ 4.5 Å). The three features in this $3 < r < 5$ Å region appear to have noticeably different intensities in the I15-1 and XFEL setup 2 PDFs. Hence, it is possible that these differences may arise from changes to the sample between March 2022 and November 2024, or possibly caused by beam dam-

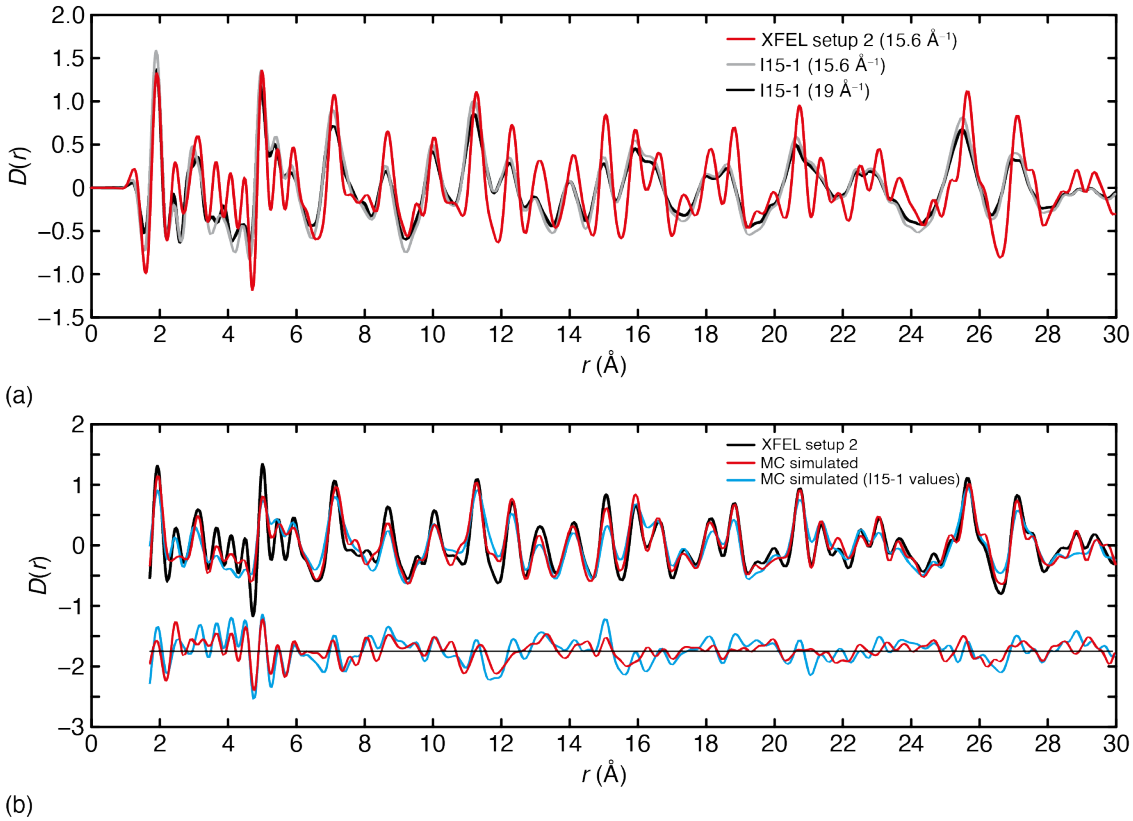


Figure 6.7: (a) Comparison between XFEL and synchrotron PDF data of $Cu[Co(CN)_6]_{2/3}$ PBA obtained using the PDFgetX3 software.[395] The XFEL data are shown in red ($Q_{max} = 15.6 Å^{-1}$), and the I15-1 data are shown in grey ($Q_{max} = 15.6 Å^{-1}$) and black ($Q_{max} = 19 Å^{-1}$) with two different Q_{max} values used to aid with comparison. (b) PDF fits of the XFEL data using the MC-driven big-box modelling technique developed in Chapter 3. XFEL experimental data are shown as a black line and two different fits are shown with red and blue lines. Difference curves (data−model) are shown in the same colours, shifted vertically.

age. To check what differences arise from the different Q_{max} values achieved by the XFEL ($15.6\,Å^{-1}$) and I15-1 setups ($19\,Å^{-1}$), the PDF obtained from Fourier transforming the I15-1 data over the Q-range $0.35 \leq Q \leq 15.6\,Å^{-1}$ is also shown in Fig. 6.7(a); there are only minor differences in the I15-1 PDFs obtained with Q_{max} values of $15.6\,Å^{-1}$ and $19\,Å^{-1}$, however there is a slight change in the $3 < r < 5\,Å$ region, with two of the peaks appearing to merge into one. Hence, it is difficult to determine the relative extent to which real changes in the sample vs differences in the setups may contribute to the observed differences between the XFEL and I15-1 PDFs.

To test whether XFEL PDF data may be used to characterise the local structure

Table 6.1: Empirical parameters used to model the X-ray PDFs of $Cu[Co(CN)_6]_{2/3}$ [Fig. 6.7(d)], together with their refined values.

Parameter	I15-1 value	XFEL value	Parameter	I15-1 value	XFEL value
r(C–N) (Å)	1.15	1.16	k_θ(C–Co–C) (eV/rad^2)	0.16	2.57
r_e(Co–C) (Å)	1.800	1.925	k_θ(N_{eq}–Cu–N_{eq}) (eV/rad^2)	17.12	2.57
r_e(Cu–N_{eq}) (Å)	1.990	1.925	k_θ(N_{eq}–Cu–N_{ax}) (eV/rad^2)	0.17	0.26
r_e(Cu–N_{ax}) (Å)	2.380	2.230	k_θ(O_{eq}–Cu–O_{eq}) (eV/rad^2)	0.17	0.26
r_e(Cu–O_{eq}) (Å)	1.950	1.880	k_θ(O_{eq}–Cu–O_{ax}) (eV/rad^2)	0.17	0.26
r_e(Cu–O_{ax}) (Å)	2.380	2.230	k_θ(N_{eq}–Cu–O_{eq}) (eV/rad^2)	0.86	0.51
k_r(Co–C) (eV/Å^2)	17.12	51.36	k_θ(O_{eq}–Cu–N_{ax}) (eV/rad^2)	8.60	5.14
k_r(Cu–N_{eq}) (eV/Å^2)	49.3	25.68	k_θ(N_{eq}–Cu–O_{ax}) (eV/rad^2)	0.05	0.05
k_r(Cu–N_{ax}) (eV/Å^2)	8.56	5.14	k_θ(Cu–N_{eq}–C) (eV/rad^2)	0.17	0.051
k_r(Cu–O_{eq}) (eV/Å^2)	34	102.72	k_θ(Cu–N_{ax}–C) (eV/rad^2)	0.03	0.051
k_r(Cu–O_{ax}) (eV/Å^2)	171	2054.37			

of complex PBA materials, the Monte Carlo (MC)-driven 'interaction-space' big-box modelling technique—developed in Chapter 3 on the $M[Pt(CN)_6]$ PBAs and used again in Section 4.6.2 to develop an atomistic representation of $Cu[Co(CN)_6]_{2/3}$ from a coarse-grained representation of local JT orientations—was applied to the XFEL PDF data [Fig. 6.7(b)]. Using the values of the parameters of the lattice-dynamical model refined on the I15-1 data ($R_{wp} = 31\%$) in Section 4.6.2 gave the fit to the XFEL PDF data ($R_{wp} = 52\%$) shown in blue in Fig. 6.7(b). A better fit, shown in red in Fig. 6.7(b), was obtained ($R_{wp} = 39\%$) using the values given in Table 6.1; these values represent one possible parameterisation and it is likely that others exist that may produce an even better fit. The goodness-of-fit values obtained from the I15-1 and XFEL data are remarkably similar (31% vs 39%, respectively), suggesting that XFEL PDFs may have the potential to characterise the local structure of complex PBAs.

To check whether any differences may be arising due to possible changes in water content between the time the I15-1 PDF was measured (March 2022) and the time the XFEL PDF was measured (November 2024), models with varying degrees of hydration were produced; no zeolitic nor interstitial water were included in the MC model that gave the less good fit shown in blue in Fig. 6.7(b), whereas some zeolitic and interstitial water were included in the MC model that gave the better fit shown

in red. Including zeolitic/interstitial water mostly seems to increase the intensity of the three peaks in the $3 < r < 5\,\text{Å}$ region rather than drastically change the intensity of these peaks relative to each other. Hence, it is possible that there is a variation in the water content of the PBA between the times the I15-1 and XFEL PDFs were measured, but this change is likely not responsible for the differences in peak positions/shape observed in this $3 < r < 5\,\text{Å}$ region in the XFEL vs I15-1 PDFs shown in Fig. 6.7(a). So, the differences between the I15-1 and XFEL setup 2 PDFs in this $3 < r < 5\,\text{Å}$ region appear to reflect differences from the setups, though other sample changes cannot be ruled out.

In Chapter 3 and Chapter 4, PDFs obtained at the I15-1 beamline were used to model the local structure of PBAs. However, the I15-1 PDF of $Cu[Co(CN)_6]_{2/3}$ did not appear to have the sensitivity to differentiate between models with varying degrees of short-range JT order. Hence, PDFs with a high Q_{max} are likely to be vital when seeking to characterise the local structure of many complex PBAs. Hence, we wanted to see whether it might be possible to make use of the higher $Q_{\text{max}} \sim 20\,\text{Å}^{-1}$ offered by setup 1 compared to setup 2 ($Q_{\text{max}} \sim 16\,\text{Å}^{-1}$).

6.4.4 Results and discussion: EuXFEL HED IC1 setup 1

Whilst a higher $Q_{\text{max}} \approx 20\,\text{Å}^{-1}$ was achieved using setup 1 [Fig. 6.2], limitations on space and geometry meant that there were two gaps in the Q range ($7.56 < Q < 7.77\,\text{Å}^{-1}$ and $13.63 < Q < 15.32\,\text{Å}^{-1}$) [Fig. 6.5(b)]. A couple of options for how to interpolate into the Q gaps were explored by the group; for some highly crystalline samples, interpolation had a relatively small impact on the PDF [Fig. 6.7], however for samples with more significant diffuse scattering, reliable interpolation proved more challenging and impacted the PDF more significantly. Details regarding the normalisation and interpolation procedures are given next in the context of their reliability for processing PBA total scattering data.

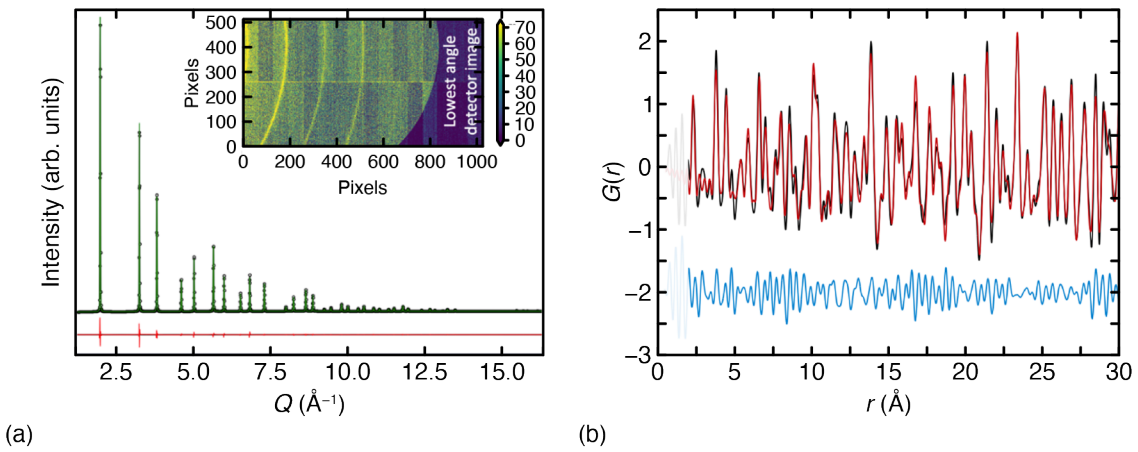


Figure 6.8: EuXFEL HED IC1 setup 1. (a) A Rietveld refinement (green line) of a NIST Si 640b sample. The difference is shown as a red line shifted vertically. A 2D image of the data collected by the fourth (lowest angle) detector from scattering by Ag behenate (crystalline standard) is shown as an inset. (b) Small-box PDF refinement of NIST SI 640b using averaged data. Figure adapted from Ref. 382, which is licensed under a Creative Commons Attribution 4.0 International License.

Data processing procedure as demonstrated by PBA samples

The first challenge was how to carry out primary beam normalisation. The reliability of normalising the scattering intensity as measured by the detector to the OGT-IPM monitoring device—a quadrant detector placed after attenuators—was explored [Fig. 6.9(a)]: whilst normalising to the OGT-IPM device seems reasonable for some samples, it works less reliably for others [Fig. 6.9(a), left]. It appears that this normalisation procedure is highly sample dependent and reflects individual sample behaviour: if during a run the sample deteriorates or some of the run is hitting an empty capillary during a 'fly scan'—where measurements are taken at regular separations along a capillary to minimise the effects of potential beam damage and also so that scattering from across the capillary can be averaged for better statistics—then a non-linear response between the detector and the OGT-IPM monitor will be observed. This is particularly noticeable for run 274 ($Mn[Co(CN)_6]_{2/3}$), where it appears that there are two clusters, one with more intensity than the other for a given OGT-IPM sum [Fig. 6.9(a), middle]. Plotting intensity as a function of train number [Fig. 6.9(a), right], we can see these two clusters as a function of time. The

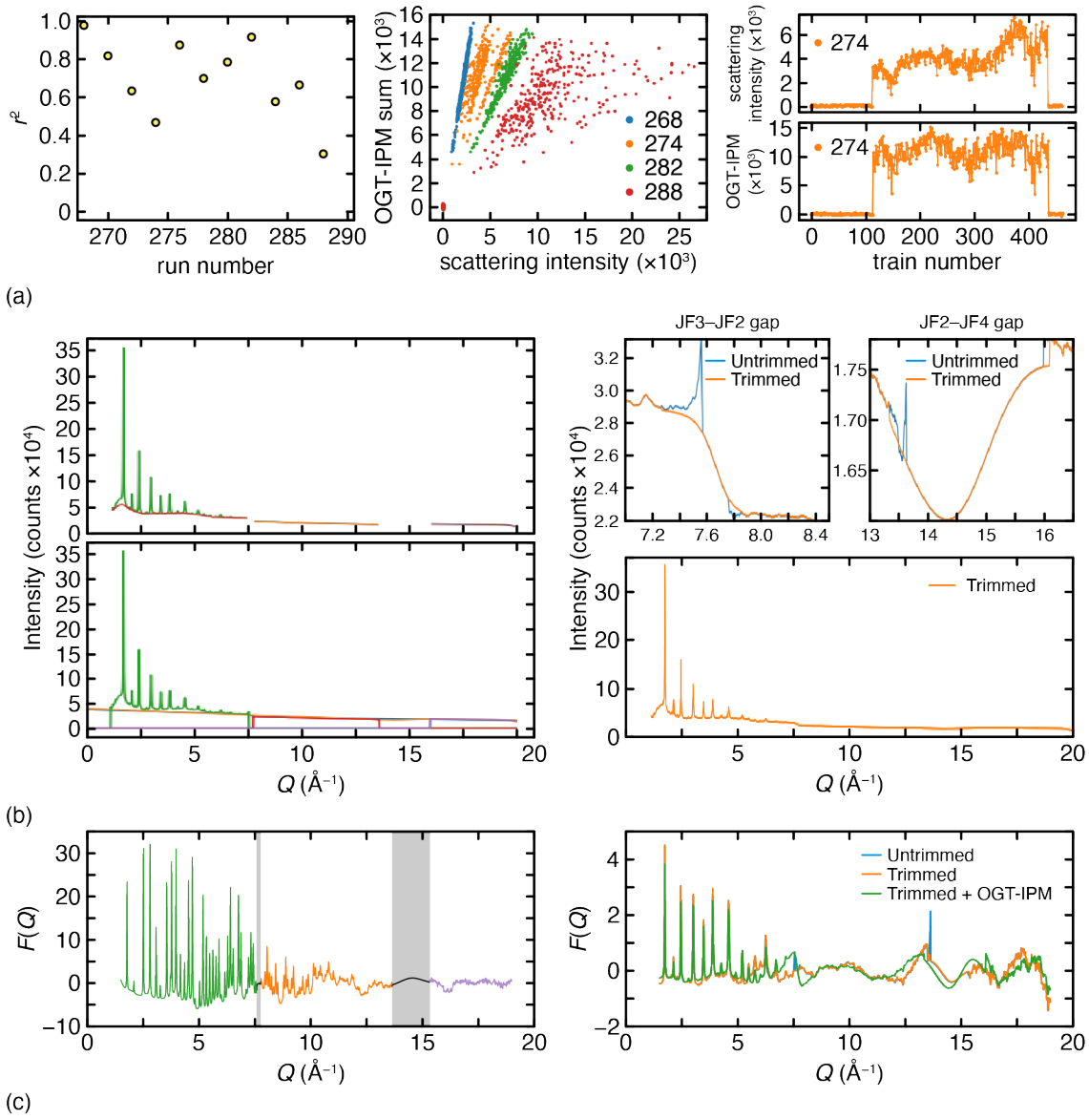


Figure 6.9: EuXFEL HED IC1 setup 1: data processing. (a) Normalisation. (b) Intensity scaling and interpolation. (c) Example processed data: $Cu[Co(CN)_6]_{2/3}$ (run number 270) (left) and $Rb_2Mn[Fe(CN)_6]$ (run number 288) (right).

first $\sim$ 200 trains (once the shutter is open) have one scaling, then the scattering intensity starts to increase towards the end. In this case, the variation in scattering intensity likely reflects different sample packing density along the capillary as well as the possibility that the sample may be redistributing within the capillary. This suggests that normalising to the OGT-IPM device will not necessarily always give a reliable scale.

How to treat the two gaps in Q coverage ($7.56 < Q < 7.77\,\text{Å}^{-1}$ and $13.63 < Q < 15.32\,\text{Å}^{-1}$) presented another challenge. An interpolation procedure was developed [Fig. 6.9(b), left], which involved (i) fitting a background function to each of the detector modules, (ii) extrapolating these background functions into the gaps; (iii) scaling the data so that the extrapolated backgrounds intersect at the halfway point; (iv) combining the two extrapolated backgrounds in a smooth way to form a gap-filling dataset; (v) combining the real data with the extrapolated gap-fillers. When a detector edge coincides with the middle of a Bragg peak, complications with the interpolation arise [Fig. 6.9(b), right]. In such cases, the data can be 'trimmed', choosing the number of Q-points to trim from either side of both detector gaps. It is also possible to choose the number of points from the baseline to extrapolate into the gap, and when fitting the background, the number of points to ignore from the edges. Finally, it is also possible to change the smoothness of the background functions, ranging from essentially linear to something that will follow most diffuse scattering.

The normalisation and interpolation procedures made it possible to tailor data processing to each sample individually. To assess the reliability of these procedures given the number of parameters at play, examples of processed data for two different samples, $Cu[Co(CN)_6]_{2/3}$ (run 270) and $Rb_2Mn[Fe(CN)_6]$ (run number 288), are shown in Fig. 6.9(c). Whilst the $Cu[Co(CN)_6]_{2/3}$ sample (run 270) appears better behaved, processing the $Rb_2Mn[Fe(CN)_6]$ data (run number 288) is much trickier; normalising to the OGT-IPM appears particularly unreliable in this case, and how much data to trim around the detector edges and what values to use for interpolation parameters is not straightforward. Finally, to assess the impact of the normalisation and interpolation procedures on the PDF data, a comparison is given between $F(Q)$ data for $Cu[Co(CN)_6]_{2/3}$ (run 270) that have not been trimmed nor normalised to the OGT-IPM, with an $F(Q)$ that has been trimmed and normalised to the OGT-IPM [Fig. 6.10(a)]. The normalisation and interpolation procedure seemed to have

a noticeable impact on the low-r region of the PDF, bringing the reliability of this data processing into question.

Ultimately, the long-term goal is to be able to use XFEL techniques to probe local structure changes that happen on ultra-fast timescales; in the context of PBAs, there is interest in understanding the mechanism behind photoinduced charge transfer, which has been shown to take place over 200 fs.[262] Hence, obtaining high-quality PDFs from single (30 fs) XFEL shots will be important. In each of the PBA measurements, a 'fly scan' on each capillary was measured, with scattering from each shot summed and averaged to improve statistics. The PDFs of $Cu[Co(CN)_6]_{2/3}$ (run 270) from two separate shots and the averaged PDF are shown in Fig. 6.10(b). Whilst the PDFs from the single shots contain significant noise, structural peaks can still be observed that match the features of the averaged PDF, though there seems to be a greater variation in the $3 < r < 5$ Å region highlighted in previous sections compared to other regions. The two single-shot PDFs of $Cu[Co(CN)_6]_{2/3}$ measured in a capillary appear to have a much lower signal-to-noise ratio than the single-shot PDFs of a flat-plate sample of the NIST CeO_2 standard shown in Fig. 6.6 from setup 2. This difference in signal-to-noise ratio may potentially reflect the variation in powder packing density in flat-plate vs capillary samples, the latter of which sometimes had regions that were visibly more densely packed than others; hence, you might expect a greater variation in signal-to-noise ratio from shot to shot as you move along a capillary from an area of greater density of powder to a lower density of powder—giving greater variation from shot-to-shot—as well as an overall lower signal-to-noise ratio if primarily hitting a less well-packed area. This suggests that for future time-resolved studies, using densely-packed flat-plate geometries may be preferable.

To assess the quality of the averaged PDF data for this experimental setup (setup 1)—with $Q_{max} = 19\,\text{Å}^{-1}$ but with gaps in Q coverage—a comparison with the averaged data for experimental setup 2—with $Q_{max} = 15.6\,\text{Å}^{-1}$ but with a

continuous Q coverage—as well as with synchrotron data (I15-1, Diamond Light Source)—with $Q_{\mathrm{max}} = 19\,\mathrm{Å}^{-1}$—is given in Fig. 6.10(c). It should be noted that the same batch of sample of $Cu[Co(CN)_6]_{2/3}$ was used for the I15-1 (2022), XFEL setup 1 (2023), and XFEL setup 2 (2024) experiments, as the stability of this particular PBA—as is the case for many other PBAs—is high. Both of the XFEL PDFs appear to show less damping at high r than the I15-1 PDF, suggesting there were fewer instrumental contributions from both XFEL setups compared to the instrumentation from the I15-1 beamline. At low r, the widths of the peaks are remarkably similar between the three PDFs, whereas at high r, the widths of the peaks in both XFEL PDFs appear narrower and more clearly resolved. The most noticeable differences between the three PDFs again appear to occur in the $3 < r < 5\,\mathrm{Å}$ region.

To check whether the differences between the two XFEL PDFs and the I15-1 synchrotron PDF might be due to noise or artefacts arising from the interpolation procedure applied to the XFEL setup 1 data, the MC-driven big-box 'interaction-space' PDF refinement approach was used to produce an atomistic representation from the XFEL PDF from setup 1 [Fig. 6.10(d)], and hence to determine which peaks arise from pair correlations within the big-box structure and which do not. Initially, the values of the parameters of the lattice-dynamical model refined using the I15-1 data (Section 4.6.2) were used as a starting point and produced the fit shown in green in Fig. 6.10(d) ($R_{\mathrm{wp}} = 57\%$). A better fit ($R_{\mathrm{wp}} = 47\%$) to the XFEL setup 1 PDF data was obtained using the values given in Table 6.1. The goodness-of-fits of both of these MC big-box models to the XFEL setup 1 data are not as good as to the XFEL setup 2 data [Fig. 6.7(b)] despite the higher $Q_{\mathrm{max}} = 19\,\mathrm{Å}^{-1}$ of setup 1 compared to setup 2 ($Q_{\mathrm{max}} = 15.6\,\mathrm{Å}^{-1}$). This suggests that the interpolation procedure may have a significant impact on the reliability of the XFEL setup 1 PDF. However, it is not immediately clear from Fig. 6.10 exactly where the interpolated data might be affecting the resultant PDF.

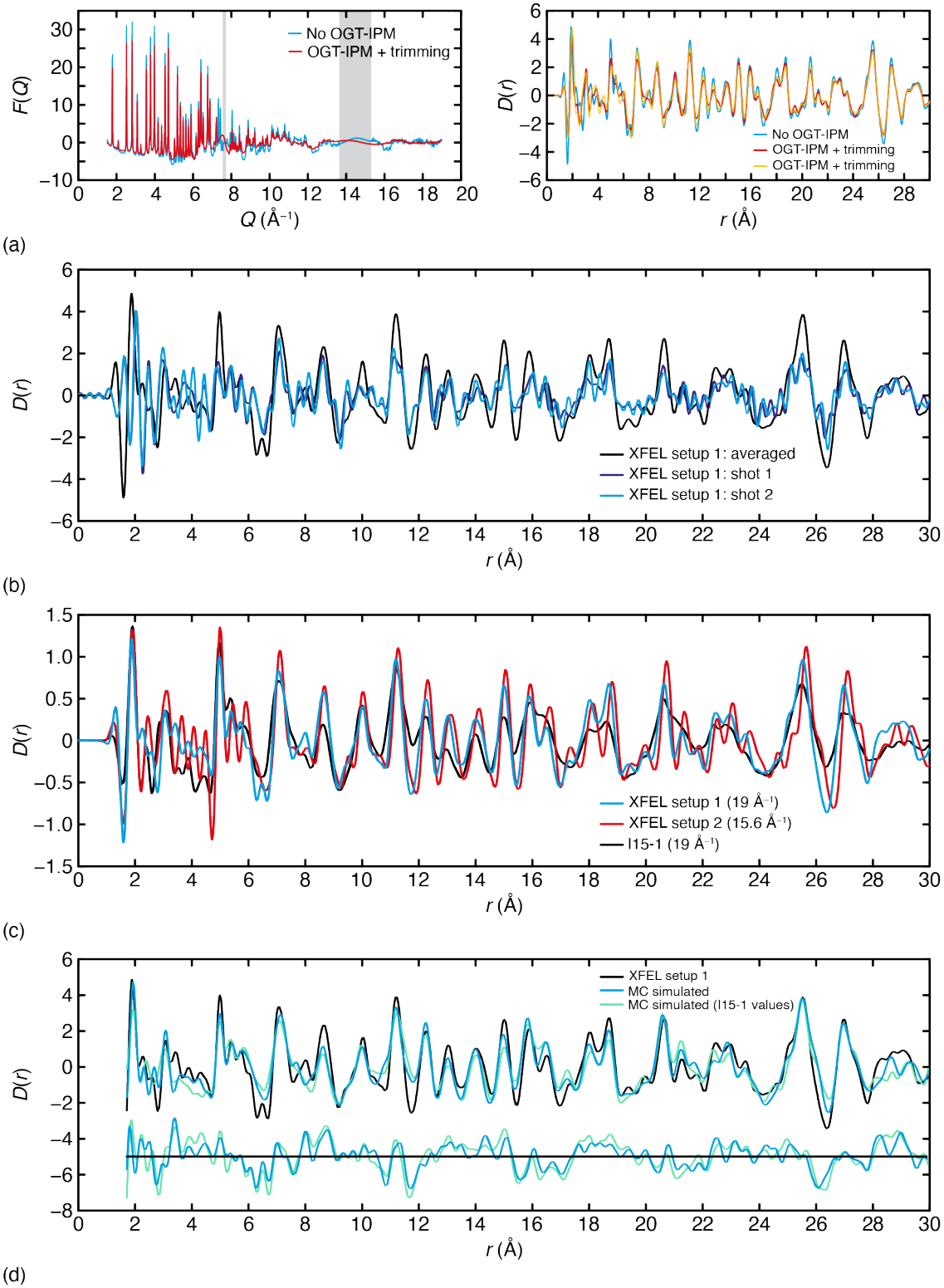


Figure 6.10: $Cu[Co(CN)_6]_{2/3}$ PDFs. (a) (Left) Comparison between $F(Q)$ data that have (red) and have not (blue) been normalised to the OGT-IPM device (blue). The corresponding PDFs are shown on the right. (b) A comparison between the averaged PDF (black) and the PDF from separate single shots (blue). (c) A comparison between the I15-1 (black), XFEL setup 1 (blue), and XFEL setup 2 (red) PDFs all obtained using the PDFgetX3 software.[395] Note that a scale factor of 0.25 has been applied to the XFEL setup 1 data (blue). (d) MC fits (blue, green) of $6 \times 6 \times 6$ supercells to the XFEL setup 1 PDF data (black) using the values of the parameters from the lattice-dynamical models given in Table 6.1.

6.5 Monte Carlo $G(r)$

Since PDFs measured with a high $Q_{\max}$ are likely to be vital to characterise the local structure of many complex PBAs, ideally we would make use of the higher $Q_{\max} \sim 20\,\text{Å}^{-1}$ offered by setup 1 compared to setup 2 ($Q_{\max} \sim 16\,\text{Å}^{-1}$). However, the reliability of the procedure for interpolating between the two detector gaps ($7.56 < Q < 7.77\,\text{Å}^{-1}$ and $13.63 < Q < 15.32\,\text{Å}^{-1}$) and the reproducibility of success from sample to sample first needs to be addressed. Hence, in the following section, a simple Monte Carlo (MC) method is explored for generating a PDF from reciprocal space data;[398,399] importantly, this MC method uses only the $i(Q)$ data that has actually been measured experimentally, avoiding the need for interpolation altogether. When assessing whether it might be better to sacrifice a higher $Q_{\max}$ for a continuous Q range, or to make use of a higher $Q_{\max}$ but with gaps in Q, it is important to consider what impact the two detector gaps might have on the resultant PDF; if minimal, making use of the data with higher $Q_{\max}$ seems the more desirable choice.

In this last past of my results section, the Monte Carlo $G(r)$ (MCGR) method[398,399] will first be tested on a dummy dataset to show that the method can reproduce an existing $G(r)$. After, that sections in the $i(Q)$ data corresponding to the two Q gaps of the XFEL data will be artificially removed from the dummy data to assess their individual impacts on the resultant PDF. Finally, the MCGR method is applied to the XFEL setup 1 total scattering data to generate a PDF where no interpolation into the Q gaps has been required.

6.5.1 Simulation implementation

The MCGR approach[398,399] is an inverse MC transformation method where a numerical form of the PDF is generated and adjusted until its Fourier transform ($i_{\text{model}}(Q)$) is in best agreement with the experimental data ($i_{\text{exp}}(Q)$). The goodness-of-fit of

the model $i_{\mathrm{model}}(Q)$ to the experimental $i_{\mathrm{exp}}(Q)$ is given by

$$\chi^2 = \sum_j \left| i_{\mathrm{model}}(Q) - i_{\mathrm{exp}}(Q) \right|^2 / \sigma^2, \tag{6.1}$$

where σ is a weighting function, which could encompass the actual experimental errors if these are known. Throughout this section, $\sigma = 0.01$ is arbitrarily assigned to all Q data points. The MC simulation proceeds by randomly selecting a point of the model $G(r)$ and adjusting its value by a random value between $-0.05 \leq \Delta G(r) < 0.05$. Moves are accepted or rejected according to the Metropolis algorithm[197] where χ^2 (Eq. 6.1) is used as an energy function to allow the model $G(r)$ to give a better fit of $i_{\mathrm{model}}(Q)$ to $i_{\mathrm{exp}}(Q)$.

There are a number of advantages inherent to the MCGR approach. Firstly, it is possible to apply constraints to the form of $G(r)$, *e.g* to values at low r. Secondly, the use of the inverse transformation method ensures that there are no transformation ripples, hence no smoothing function needs to be applied. Finally, and most importantly, there is no requirement for a continuous Q range in experimental $i(Q)$ data—the model $i_{\mathrm{model}}(Q)$ can be computed from the model $G(r)$ at the Q values of the experimental $i_{\mathrm{exp}}(Q)$ data, and only the agreement of these points are calculated using Eq. 6.1. Hence, it is possible to calculate a model $G(r)$ using only the data points for which $i(Q)$ has been measured, avoiding the need for any interpolation.

Testing the MCGR method

In theory, the MCGR method should be able to produce a numerical model $G(r)$ that (more or less) reproduces a pre-existing $G(r)$. To illustrate this, a pre-existing $G(r)$ [Fig. 6.11(a)] calculated from a big-box model of $Cu[Co(CN)_6]_{2/3}$ (see section 4.6.2) was Fourier transformed to give what acts as the 'experimental' $i(Q)$ [Fig. 6.11(b)]. A numerical form of $G(r)$, the 'model' $G(r)$ [Fig. 6.11(c)], was then adjusted until its Fourier transform, the 'model' $i(Q)$ [Fig. 6.11(d)], was in best agreement with the 'experimental' $i_{\mathrm{exp}}(Q)$ data [Eq. 6.1]. The Metropolis algo-

rithm[197] was run for approximately 100 accepted moves per r point for convergence. To aid comparison between the model $G(r)$ and the pre-existing $G(r)$ (from the big-box model of $Cu[Co(CN)_6]_{2/3}$), the model $G(r)$ was computed at the same r points as the pre-existing $G(r)$ ($0 \leq r \leq 29.91\,\text{Å}$ in steps of $0.01994\,\text{Å}$). Both the 'experimental' (dummy) $i_{\text{exp}}(Q)$ and model $i_{\text{model}}(Q)$ were calculated between $0.35272 \leq Q \leq 18.98433\,\text{Å}^{-1}$ with $\Delta Q = 0.01357\,\text{Å}^{-1}$.

The final model $G(r)$ after performing the MCGR process once is shown in Fig. 6.11(c); however, the $G(r)$ can be averaged over multiple independent runs to reduce statistical noise. A comparison between an averaged (300 independent runs) model $G(r)$ (blue) and the dummy pre-existing $G(r)$ (black) is shown in [Fig. 6.11(e)]. There appears to be a good match between the model $G(r)$ and the pre-existing 'dummy' $G(r)$; however, there was some noise at low r ($\lesssim 1.5\,\text{Å}$). As mentioned, an advantage of the MCGR approach is that constraints can be applied to the form of the $G(r)$; restricting low-r values ($< 1.45562\,\text{Å}$) to a value of -1 improved the fit [Fig. 6.11(e), red]. Hence, since the MCGR method can successfully recreate an existing $G(r)$, this suggests that the MCGR method is an effective approach for generating a numerical $G(r)$ from experimental $i(Q)$ data and hence could be applied to the XFEL setup 1 data.

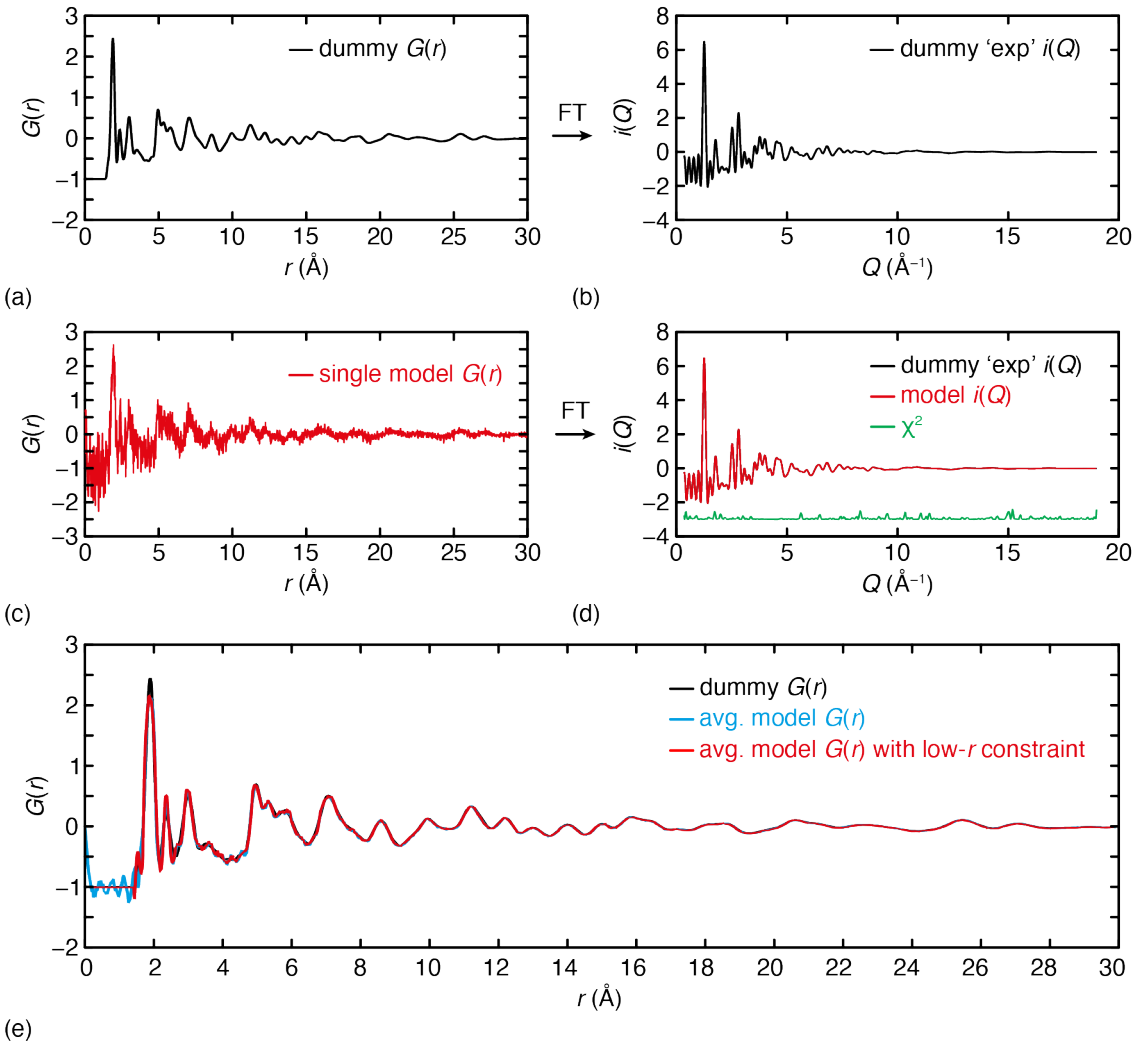


Figure 6.11: An overview of the MCGR process using dummy data with no gaps in Q range. (a) A pre-existing $G(r)$ was Fourier transformed to give (b) a dummy 'experimental' $i_{\mathrm{exp}}(Q)$. (c) The model $G(r)$ was adjusted point by point until its (d) Fourier transform, $i_{\mathrm{model}}(Q)$ (red), was in best agreement with $i_{\mathrm{exp}}(Q)$ (black). (e) The $G(r)$ can be averaged across multiple independent MC runs (blue), and constraints can be applied to the form of $G(r)$, such as to its value at low r (red). The MCGR process appears to recreate the dummy $G(r)$ well.

Before applying the MCGR method to the XFEL setup 1 $i(Q)$ data, the MCGR method can first be used to check the impact that gaps in Q might have on the resultant PDF by introducing gaps into the dummy 'experimental' $i(Q)$. To investigate what effect both the low-Q gap ($7.56 < Q < 7.77\,\text{Å}^{-1}$) and high-$Q$ gap ($13.63 < Q < 15.32\,\text{Å}^{-1}$) have on the PDF, these regions of the dummy 'experimental' $i(Q)$ data were removed. Initially, the impact of the low-Q gap ($7.56 < Q < 7.77\,\text{Å}^{-1}$) was explored [Fig. D2.20]; this low-Q gap appeared to have only a minimal impact, with there being very few differences between the model $G(r)$ generated from a continuous $i(Q)$ dataset and one with this low-Q gap. The high-Q gap appeared to have some effect on the low-r region of the PDF [Fig. D2.21], seemingly creating three more prominent peaks between $3.5 < r < 4.5\,\text{Å}$—and shifting them slightly to lower r—and changing the shape of the features between $5 < r < 6\,\text{Å}$. When both Q gaps are introduced together [Fig. 6.12(b)], the model $G(r)$ [Fig. 6.12(c)] reflects the differences caused by the wider high-Q gap.

An advantage of the MCGR method is that it is possible to calculate standard errors [Fig. 6.12(e),(f)]; these errors will take into account both the standard error arising from averaging over multiple repeats ('MC errors'), but will also theoretically take into account experimental data point errors (σ) if these are known. Hence, the standard errors can be used to give an indication of the confidence in each $G(r)$ data point, and so can be used to explore whether there are any trends—*e.g.* periodic fluctuations—that might be arising from introducing gaps in the experimental $i(Q)$ data. There do not appear to be any noticeable differences in the standard errors between $G(r)$ data points computed from $i(Q)$ data with gaps versus data with no gaps [Fig. 6.12(e),(f)]. This perhaps suggests that the Q gaps do not appear to introduce any significant oscillatory artefacts in the model $G(r)$.

Although the model $i_{\text{model}}(Q)$ is only compared to the existing data points of the 'experimental' $i_{\text{exp}}(Q)$ during the goodness-of-fit calculation (Eq. 6.1), the model $i_{\text{model}}(Q)$ can still be calculated into the Q gaps to see how well the gaps are re-

produced [Fig. 6.12(h)]. The narrower low-Q gap ($7.56 < Q < 7.77\,\text{Å}^{-1}$) in $i(Q)$ appears to be recreated well, suggesting that the information within this gap can be provided from the rest of the $i(Q)$ data. However, the wider high-Q gap is not recreated so well, suggesting that this gap contains information that the rest of the $i(Q)$ data does not provide. This again suggests that the impact of the narrower low-Q gap is minimal, and the wider high-Q gap is more significant. Hence, when seeking to push Q_{max}, it may be possible to sacrifice the data points within the narrower low-Q gap but the effects of the wider high Q-gap should be considered; for this $Cu[Co(CN)_6]_{2/3}$ PBA sample, the $3.5 < r < 4.5\,\text{Å}$ and $5 < r < 6\,\text{Å}$ regions appear to be most affected, and whilst the $3.5 < r < 4.5\,\text{Å}$ region is unlikely to be particularly helpful in characterising local JT order, the $5 < r < 6\,\text{Å}$ region is likely key.

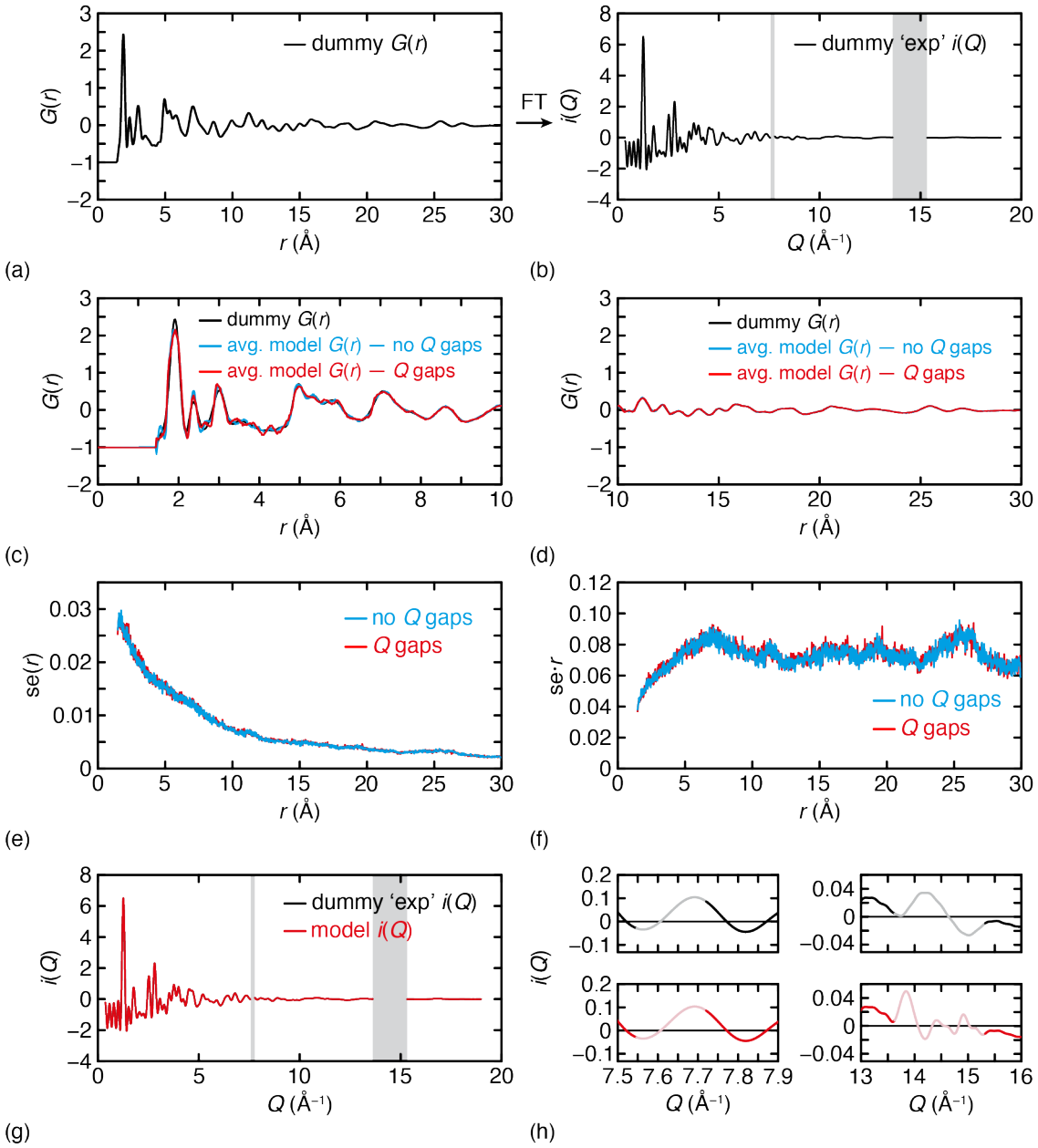


Figure 6.12: Investigating the effect of both a narrow low-Q gap and a wider high-Q gap using dummy data. (a) A pre-existing $G(r)$ was Fourier transformed to give a dummy 'experimental' $i_{\mathrm{exp}}(Q)$ where the $i(Q)$ data in the two gaps ($7.56 < Q < 7.77\,\text{Å}^{-1}$ and $13.63 < Q < 15.32\,\text{Å}^{-1}$) was then removed. The (c) low-r region and (d) high-r region of the averaged model $G(r)$, showing the impact that Q gaps in the 'experimental' $i_{\mathrm{exp}}(Q)$ data has on the model $G(r)$. The standard error of each data point in the model $G(r)$ can be calculated: (e) shows the variation of the standard error as a function of r for $i_{\mathrm{exp}}(Q)$ data with gaps and no gaps, and (f) shows the variation of the standard error multiplied by r. (g) Whilst the model $i_{\mathrm{model}}(Q)$ is only compared to the $i_{\mathrm{exp}}(Q)$ at the data points present in $i_{\mathrm{exp}}(Q)$, (h) the values of $i_{\mathrm{model}}(Q)$ at the missing Q points can be calculated (pink) and compared to the original dummy $i(Q)$ data points (grey) before the data was chopped out.

6.5.2 XFEL total scattering data: HED setup 1

Having shown that it is possible to use the MCGR method to calculate a PDF from experimental $i(Q)$ data, and explored the effects of Q gaps on the resultant PDF, the final step is to apply the MCGR method to the XFEL setup 1 data. The model $G(r)$ was computed between $0 \leq r \leq 30\,\text{Å}$ in steps of $0.02\,\text{Å}$. The Metropolis algorithm[197] was run for approximately 250 accepted moves per r point for convergence. The model $i_{\text{model}}(Q)$ was calculated at the Q points present in the experimental $i_{\text{exp}}(Q)$ data: between $1.50925 \leq Q \leq 18.99051\,\text{Å}^{-1}$ with $\Delta Q = 0.01\,\text{Å}^{-1}$ but with gaps between $7.56 < Q < 7.77\,\text{Å}^{-1}$ and $13.63 < Q < 15.32\,\text{Å}^{-1}$.

The results of applying the MCGR method to the XFEL setup 1 data are shown in Fig. 6.13. The pre-existing $G(r)$ and the model $G(r)$ of the dummy data with the same gaps in Q from the previous section are shown for comparison [Fig. 6.13(c),(d)]. The model $G(r)$ of the XFEL setup 1 data is particularly noisy at low r, but the key structural features can still be observed. This noise likely arises from the fact that the XFEL setup 1 $i(Q)$ data is missing the most intense peak at $\sim 1.25\,\text{Å}^{-1}$ [Fig. 6.13(b)]. Additionally, no resolution corrections were applied.

When using real experimental data, instrumental resolution corrections should be incorporated, since the experimental measurement, $S^E(Q)$, is actually

$$S^E(Q) = R(Q) \otimes S(Q), \tag{6.2}$$

where $R(Q)$ is the instrument resolution function. In the MCGR method, the model $i_{\text{model}}(Q)$ can be convolved, point by point, with a model $R_{\text{model}}(Q)$, with the convolution of $i_{\text{model}}(Q) \otimes R_{\text{model}}(Q)$ compared with the experimental $i_{\text{exp}}(Q)$ using Eq. 6.1.

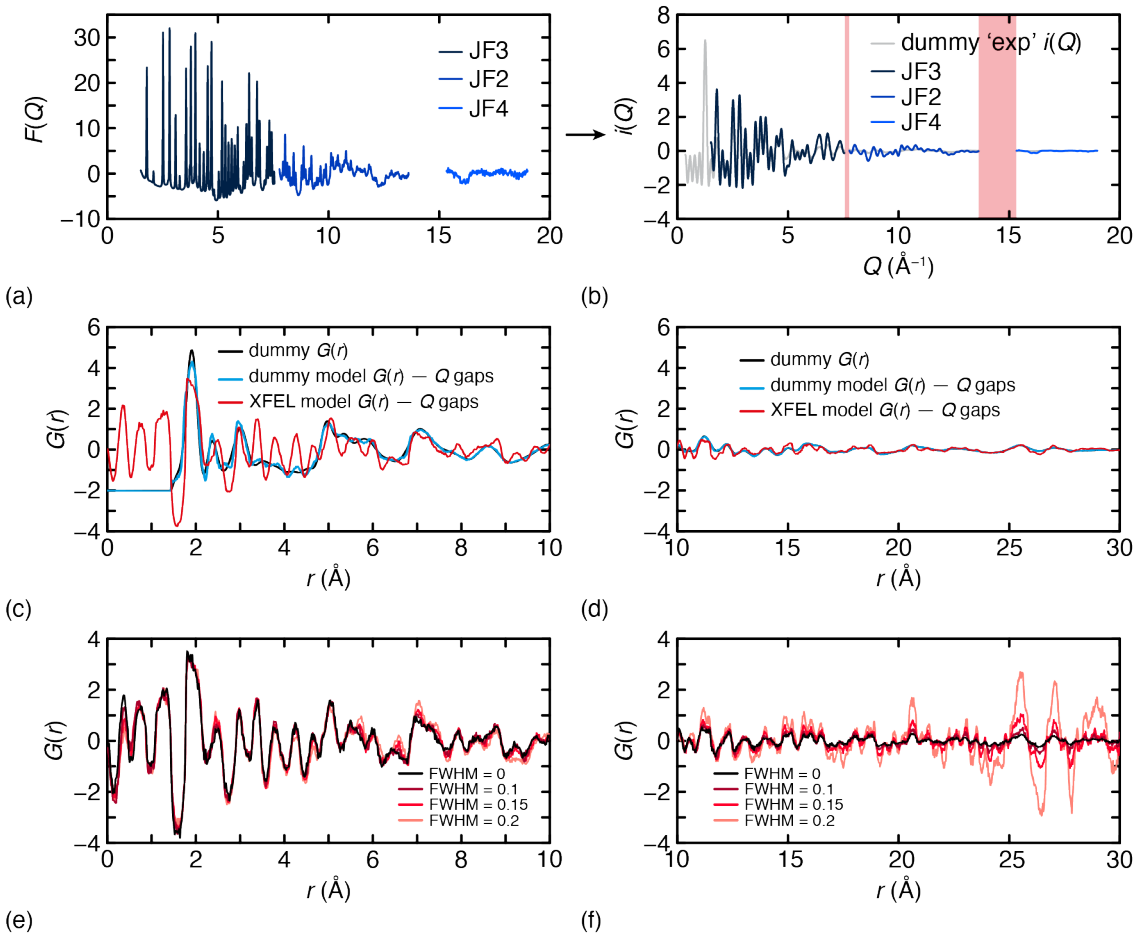


Figure 6.13: Results from applying the MCGR approach to XFEL setup 1 data. The XFEL setup 1 experimental (a) $F(Q)$ data was transformed to (b) $i(Q)$ (blue). The dummy $i(Q)$ data from the big-box model of $Cu[Co(CN)_6]_{2/3}$ is shown for comparison. The (c) low-r region and (d) high-r region of the XFEL averaged model $G(r)$ (red). The averaged model $G(r)$ (blue) of the dummy data and the pre-existing $G(r)$ dummy data (black) are shown for comparison. The (e) low-r region and (f) high-r region of the XFEL averaged model $G(r)$ where a Gaussian resolution function with varying FWHM has been applied.

To start off with, a Gaussian resolution function was applied. The resolution corrected model $i_R(Q_j)$ at point j is given by

$$i_R(Q_j) = \sum_k i(Q_k) R(Q_j - Q_k) \mathrm{d}Q, \tag{6.3}$$

where the sum is over all Q points, k. $R(Q)$ for a Gaussian function is given by

$$R(Q) = \frac{1}{\sigma\sqrt{2\pi}} \exp\left(-\frac{(Q_j - Q_k)^2}{2\sigma^2}\right), \tag{6.4}$$

where σ is the standard deviation, given by

$$\sigma = \frac{\text{FWHM}}{\sqrt{8 \ln 2}}. \tag{6.5}$$

Here, FWHM is the full width at half-maximum, and the effect of varying the FWHM can be seen in Fig. 6.13(e),(f). There were no significant differences at low r, and increasingly greater differences with increasing FWHM at high r. Only small differences between applying no Gaussian resolution function (FWHM = 0) and a small FWHM (FWHM = 0.1) were observed, which may suggest that instrumental contributions are small; this may reflect the minimal damping at high r seen in the XFEL PDF where interpolation was performed [Fig. 6.10(b)]. Ideally, a Rietveld refinement of a standard crystalline material should be performed in order to determine *e.g.* a TCHZ peak shape that could be incorporated accurately into the MCGR process.

Whilst there is still work that can be done with respect to these MCGR XFEL PDFs, what this last results section has shown is that a relatively simple approach such as this inverse MC transformation method can be used to generate a $G(r)$ from experimental $i(Q)$ data that does not have a continuous Q range, avoiding the need for interpolation and hence only using real experimental values.

6.6 Conclusions and future directions

A key achievement of the consortium, of which I was a member of, was to show that quantitative total scattering data can be obtained over a wide range of Q values using XFEL instrumentation. A Q_{max} above 16 Å^{-1}, achieved in this work, is significantly higher than what is currently routine for XFEL setups.[389–391] Additionally, a further result of this work is that it is possible to obtain quantitative total scattering and PDFs from single $\sim$ 30 fs X-ray pulses. Hence, with upgrades to XFEL sources to increase the energy of the X-ray beams, it can be envisioned that PDFs with

sufficient real-space resolution for quantitative studies of (dis)ordering processes should become attainable. It was also shown in section 6.4.4 that a higher $Q_{\mathrm{max}} \approx 20\,\mathrm{\AA}^{-1}$ is achievable with X-ray beams of 24 keV energy, but this was only possible by using a detector arrangement that did not provide a continuous coverage over the full Q-range. To make use of this higher $Q_{\mathrm{max}} \sim 20\,\mathrm{\AA}^{-1}$, the possibility of using a Monte Carlo method (MCGR) to produce PDFs from $i(Q)$ data without needing to interpolate data between gaps in Q was explored [Section 6.4.4]. Whilst it was shown that the smaller, lower-Q gap ($7.56 < Q < 7.77\,\mathrm{\AA}^{-1}$) theoretically has little impact on the resultant PDF, the larger, higher-Q gap ($13.63 < Q < 15.32\,\mathrm{\AA}^{-1}$) may introduce some noise. Hence, measuring high-quality total scattering data with Q_{max} greater than $16\,\mathrm{\AA}^{-1}$ might therefore only be realistic following XFEL source upgrades to increase X-ray beam energy.

Having established the potential of XFEL sources to provide high-quality quantitative total scattering/PDF data, the next step is to link the instrumentation developed in this work to pump–probe techniques with femtosecond delays (and longer) to study ultra-fast responses to external stimuli or (dis)ordering processes themselves. $\mathrm{Rb}_x\mathrm{Mn}_x\mathrm{Co}_{1-x}[\mathrm{Fe(CN)}_6]_{0.98}$ with $x = 0.94$ is a PBA that undergoes photoinduced charge transfer with a wide thermal hysteresis centred at room temperature, which results from coupled charge transfer and symmetry breaking [Fig. 6.14(b)]. Hervé *et al.* found that the major changes in this PBA occur within the first $\sim 100\,\mathrm{ps}$;[400] hence, XFEL technologies seem ideally suited to studying the local structural changes associated with charge transfer in PBAs such as $\mathrm{RbMn[Fe(CN)}_6]$.

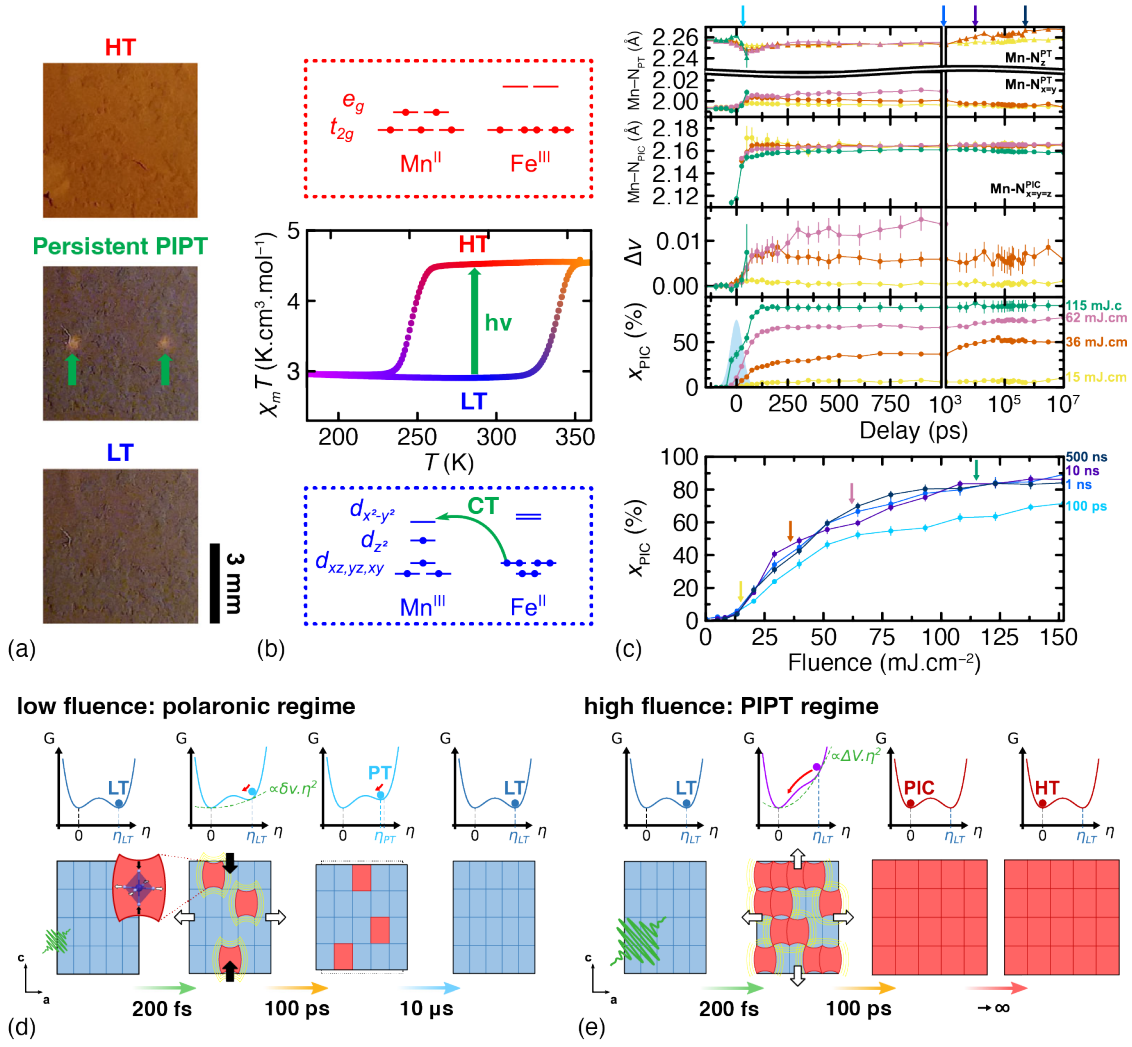


Figure 6.14: Photoinduced charge transfer in $Rb_xMn_xCo_{1-x}[Fe(CN)_6]_{0.98}$. Figure adapted from Ref. 400, which is licensed under a Creative Commons Attribution 4.0 International License.

Chapter 7

Conclusion and Outlook

This final chapter reflects on the aims of this thesis as given in Section 1.5, and highlights the key results of each chapter. The following key themes emerge: (i) the power of relatively simple models in helping to understand complex (dis)ordering processes; (ii) the ability of simple models to help interpret PDF data; and (iii) the development of new techniques/methodologies. This chapter offers some general remarks and thoughts for future directions.

7.1 Conclusions

Chapter 1 set out to highlight how Prussian blue analogues (PBAs) and the manganite perovskites can contain a wide variety of different distortions and defect structures[1] that can impact their performance as functional materials. The original aim of this thesis (Section 1.5) was to gain a better understanding of the interplay between the various degrees of freedom in these materials, with the idea being that this will ultimately give us a better idea of how to control/mitigate them to suit our functional needs. Section 1.3 identified the versatility of Monte Carlo (MC) modelling in testing the underlying physical and/or chemical interactions governing various ordering phenomena, as well as the usefulness of total scattering/pair distribution function (PDF) techniques as a local structure probe owing to its simultaneous sensitivity to both the local and average structures. Hence, using both MC modelling and/or PDF techniques seemed to offer a potentially powerful strategy for studying complex (dis)ordering processes in PBAs and the manganite perovskites.

Before exploring the interplay of cooperative Jahn–Teller (CJT) order and hexacynometallate vacancy incorporation in PBAs—relevant especially to the $K_xMn[Fe(CN)_6]_y$ cathode material where CJT-driven symmetry breaking causes

structural damage from repeated cycling between different phases[245]—there was a need to understand the local structure of the simpler higher-symmetry PBAs first. Chapter 3 aimed to exploit the link between local structure and dynamics in the negative thermal expansion (NTE) $MPt(CN)_6$ PBAs—where the local structure can be described by thermal (phonon-driven) displacements away from the average structure—in order to develop a method for producing atomistic representations of PBAs from pair distribution function (PDF) data; this Monte Carlo (MC)-driven big-box modelling method is based on the optimisation of harmonic force constants of a lattice-dynamical model to reproduce the experimentally-determined pair correlations. Not only does this method seem to capture the variation in peak widths observed for PBAs better than conventional small-box PDF refinement methods, it also allows the calculation of Grüneisen parameters from the refined harmonic potentials and ultimately the identification of the key modes responsible for NTE in these materials—correlated octahedral tilts. Hence, this intentionally simplistic PDF refinement approach seems to offer a powerful and simple way to obtain atomistic representations of the local structure of PBAs, something that is typically hard computationally due to the open-framework structure of PBAs and the complexity arising from the presence of *e.g.* H_2O, vacancies, JT distortions *etc.* and their correlations.

Having obtained a local structure picture of the more simple PBAs, Chapter 4 sought to develop models of the local structure of more complex PBAs containing JT-active cations and hexacyanometallate vacancies. Whilst the rules governing CJT order have conventionally been studied in dense ceramics, where CJT order is generally thought to arise either through vibronic coupling or electronic exchange mechanisms, the mechanism responsible for driving CJT order in PBAs is not well understood. Hence, Chapter 4 aimed to explore the rules governing CJT order in PBAs. The approach was again intentionally simple, with the model based on the competition between strain and crystal-field effects; this model can account for the

experimental stability, extent of CJT order, and crystallite strain and gives us an idea of how to tune JT dilution and vacancy concentration to control the emergence and nature of CJT effects. It was then shown that the MC-driven 'interaction-space' PDF refinement approach developed in Chapter 3 can be used to produce an atomistic representation of the local structure of these more complex PBAs, highlighting the generality of this method. What emerged from the coarse-grained MC models is that PBAs without long-range CJT order may contain short-range JT order of a non-trivial texture, which may have functional consequences on *e.g.* mechanical stability.[364,365] This highlights how JT (dis)order may be important in materials without long-range symmetry as well as those with long-range symmetry breaking. What the coarse-grained JT MC models also suggested is that PBAs may possess a complex interplay between compositional, orbital, and structural degrees of freedom not unlike that of the strongly-correlated manganite perovskites.

Whilst orbital effects in dense ceramics are typically understood to arise from either vibronic coupling[125] or electronic exchange mechanisms,[351,352] given the relative success of the simple model developed in Chapter 4 in rationalising CJT effects in PBAs, Chapter 5 aimed to explore whether a similarly simple geometric model of the kind developed for the PBAs could also be used to explain the emergence and nature of CJT effects in the manganite perovskites. This simple geometric approach was successful in identifying the coupling between JT, tilt, and shear strain modes that is responsible for driving the pseudocubic to orthorhombic phase transition in $LaGa_{1-x}Mn_xO_3$ as well as to show how charge, JT, tilt, shift, and strain degrees of freedom couple to give rise to the *CE* structure of $La_{0.5}Ca_{0.5}MnO_3$. What the success of simple geometric models in explaining the CJT effects in both PBAs and manganite perovskites serves to show is the power that relatively simple geometric models can have in understanding complex (dis)ordering processes that are often difficult to study using perhaps more conventional methods.

Having used synchrotron powder PDF measurements to aid in characterising

the local structure of JT/vacancy models in PBAs (Chapter 4), Chapter 6 aimed to explore whether PDFs obtained at an X-ray free-electron laser (XFEL) facility can be used to characterise the local structure of these same PBAs. Ultimately, it is hoped that XFEL PDFs may be used to characterise disorder that happens on far shorter timescales, *e.g.* atomic changes associated with photoinduced charge transfer in PBAs. A lot of the work of Chapter 6 was concerned with developing XFEL PDFs to maximise the real-space resolution, and involved exploring different detector setups. The first detector setup achieved a $Q_{\mathrm{max}} \sim 20\,\mathrm{\AA}^{-1}$ but had gaps in Q coverage, whereas the second detector setup achieved a continuous Q coverage but with the sacrifice of a lower $Q_{\mathrm{max}} \sim 16\,\mathrm{\AA}^{-1}$. Given that PDFs measured with a high Q_{max} are likely to be crucial for characterising the local structure of many complex PBAs, Chapter 6 went on to explore whether a simple inverse MC method can be used to calculate a PDF from the Q-data available that does not require interpolating into the gaps in Q; this simple method also theoretically allows errors to be calculated for individual points in the PDF, if the experimental errors are known. Again, this highlights the power of simple models in helping interpret PDF data.

7.2 Outlook

Given the success of simple geometric considerations in accounting for CJT effects in both PBAs and manganite perovskites, the natural question to ask seems to be whether such simple considerations can also be applied to understand CTJ/orbital ordering in other systems beyond PBAs and the manganite perovskites. For example, one can envisage that the competition between strain and crystal-field effects that governs CJT order in PBAs might be relevant to other hybrid framework materials. Whilst the model for the PBAs was developed for an FCC lattice, it would be simple enough to extend the model for systems with primitive cubic lattices, *e.g.* $[\mathrm{C(NH_2)_3}]\mathrm{Mn}_{1-x}\mathrm{Cu}_x(\mathrm{HCOO})_3$. So, when designing simple geometric models for sys-

tems beyond PBAs and the manganite perovskites, consideration would need to be given to the geometry of the lattice on which the JT-active ions sit, as well as the rules governing any other degrees of freedom the system may have, *e.g.* vacancies, tilts, charge ordering patterns, known JT ordering patterns (*e.g.* antiferrodistortive), strain etc..

In this vein, it may be possible to use similar geometric approaches to understand other (dis)ordering processes or the interplay between degrees of freedom not involving CJT effects. For example, whilst the emphasis of the thesis has been on understanding the interplay between CJT order and vacancies, as well as the contribution of conventional octahedral tilts and columnar shift distortions in driving NTE, PBAs can contain a variety of other distortions and defect structures not explored in this thesis, including hydration, magnetism, and A-site slide distortions.[1] For example, in the case of the proton conducting materials $Co[Cr(CN)_6]_{2/3} \cdot zH_2O$, conductivity is found to vary by nearly five orders of magnitude with varying degree of hydration; moreover, proton conduction via the pore network is mediated by correlated octahedral tilts.[401] Hence, whilst this thesis has focussed on the role of structural complexity in PBA NTE and battery materials, it also likely affects the performance of other functional PBA materials with applications in *e.g.* proton conductivity,[401] spin-crossover,[402,403] cooperative magnetism,[404,405] and gas storage.[89]

A recurring theme of this thesis is the power of simple models to aid in understanding (dis)ordering processes in complex materials as well as to help with interpreting PDF data. A notable reflection on the PDF work of Chapter 4 is the lack of sensitivity of the PDF data to different CJT order models. This highlighted that whilst the PDF data can be used to show that a coarse-grained JT MC model is consistent with experimental PDF data, it would have been insufficient, at least in this case, to simply measure a PDF and hope to determine the structure from it with certainty. A similar issue was encountered in the work of Ref. 162, where they showed that a range of meaningfully different local orbital arrangement models of the orbital

disorder phase of $LaMnO_3$ can give similar fits to the experimental PDF. This issue was also encountered in studies of orbital disorder in the spin glass $Y_2Mo_2O_7$, where again, very different models produced almost-equivalent PDF fits.[406,407] In this particular case, the issue of orbital disorder was only resolvable since the temperatures involved were much lower than in the case of $LaMnO_3$. What this highlights is the issue of lack of uniqueness will likely pose more of a problem at high temperatures and for more complex structures. What allowed the differentiation between different pictures of local JT order in Chapter 4 was using a coupled approach of powder X-ray diffraction measurements, MC modelling, and PDF measurements. This highlights the need to pair information gained from PDF modelling with other information *e.g.* the energetics of the system; in the case of Chapter 4, what was key was analysing the energetics of the various compositions through the residual strain from MC simulations and the experimentally-observed crystallite strain determined from Rietveld refinements, and tracking the splitting/broadening of lattice parameters/key reflections in the Bragg pattern of both experimental samples and MC configurations as a function of composition. In Chapter 3, the empirically-derived phonon dispersion curves were compared with those derived by density functional theory. Hence, whilst powder PDFs can offer insight into the local structure, they are perhaps best used in combination with other approaches, especially in systems with greater complexity where PDF modelling can be difficult. Depending on the material and the local structure problem, PDF analysis could be paired with other local structure probes—*e.g.* nuclear magnetic resonance (NMR), extended X-ray absorption fine structure (EXAFS), or infrared (IR) spectroscopy—or compared with computational results from *e.g.* DFT, mean-field formulations, or molecular dynamics simulations.

Bibliography

[1] Cattermull, J.; Pasta, M.; Goodwin, A. L. *Mater. Horiz.* **2021,** *8,* 3178-3186.

[2] Coey, J. M. D. *Adv. Phys.* **1999,** *48,* 167-293.

[3] Khomskii, D. I.; Kugel, K. I. *Phys. Rev. B* **2003,** *67,* 134401.

[4] Goodenough, J. B. *Rep. Prog. Phys.* **2004,** *67,* 1915-1993.

[5] Hotta, T.; Malvezzi, A. L.; Dagotto, E. *Phys. Rev. B* **2000,** *62,* 9432-9452.

[6] Goldschmidt, V. M. *Naturwiss.* **1926,** *14,* 477-485.

[7] Li, C.; Soh, K. C. K.; Wu, P. *J. Alloys Compd.* **2004,** *372,* 40-48.

[8] Howard, C. J.; Stokes, H. T. *Acta Crystallogr. B* **1998,** *54,* 782-789.

[9] Bednorz, J. G.; Müller, K. A. *Rev. Mod. Phys.* **1988,** *60,* 585-600.

[10] Maeno, Y.; Hashimoto, H.; Yoshida, K.; Nishizaki, S.; Fujita, T.; Bednorz, J. G.; Lichtenberg, F. *Nature* **1994,** *372,* 532-534.

[11] Cohen, R. E. *Nature* **1992,** *358,* 136-138.

[12] Rondinelli, J. M.; Fennie, C. J. *Adv. Mater.* **2012,** *24,* 1961-1968.

[13] Kobayashi, K.-I.; Kimura, T.; Sawada, H.; Terakura, K.; Tokura, Y. *Nature* **1998,** *395,* 677-680.

[14] Rao, C. N. R.; Cheetham, A. K. *Science* **1996,** *272,* 369-370.

[15] Bokov, A. A.; Protsenko, N. P.; Ye, Z.-G. *J. Phys. Chem. Solids* **2000,** *61,* 1519-1527.

[16] Goodenough, J. B. *Phys. Rev.* **1955,** *100,* 564-573.

[17] Raveau, B.; Maignan, A.; Martin, C.; Hervieu, M. *Chem. Mater.* **1998,** *10,* 2641-2652.

[18] Bishop, A. R.; Röder, H. *Curr. Opin. Solid State Mater. Sci.* **1997,** *2,* 244-251.

[19] Millis, A. J.; Mueller, R.; Shraiman, B. I. *Phys. Rev. B* **1996,** *54,* 5405-5417.

[20] Millis, A. J.; Littlewood, P. B.; Shraiman, B. I. *Phys. Rev. Lett.* **1995,** *74,* 5144-5147.

[21] Azuma, M.; Oka, K.; Nabetani, K. *Sci. Technol. Adv. Mater.* **2015,** *16,* 034904.

[22] Robels, U.; Herbiet, R.; Arlt, G. *Ferroelectrics* **1989,** *93,* 95-103.

[23] Shirane, G.; Suzuki, K.; Takeda, A. *J. Phys. Soc. Jpn.* **1952,** *7,* 12-18.

[24] Rao, C. N. *J. Phys. Chem. B* **2000,** *104,* 5877-5889.

[25] Tragheim, B. R.; Simpson, S.; Liu, E. P.; Senn, M. S.; Chen, W. T. *Phys. Rev. B* **2024,** *110,* 245123.

[26] Senn, M. S.; Bristowe, N. C. *Acta Cryst. A* **2018,** *74,* 308-321.

[27] Knapp, M. C.; Woodward, P. M. *J. Solid State Chem.* **2006,** *179,* 1076-1085.

[28] King, G.; Woodward, P. M. *J. Mater. Chem.* **2010,** *20,* 5785-5796.

[29] Vasala, S.; Karppinen, M. *Prog. Solid State Chem.* **2015,** *43,* 1-36.

[30] Ebbinghaus, S. G.; Abicht, H.-P.; Dronskowski, R.; Müller, T.; Reller, A.; Weidenkaff, A. *Progr. Solid St. Chem.* **2009,** *37,* 173-205.

[31] Kermoun, H.; Benziada-Taïbi, L. *J. Fluorine Chem.* **1999,** *99,* 119-122.

[32] Senn, M. S.; tin Chen, W.; Saito, T.; García-Martín, S.; Attfield, J. P.; Shimakawa, Y. *Chem. Mater.* **2014,** *26,* 4832-4837.

[33] Howard, C. J.; Kennedy, B. J.; Woodward, P. M. *Acta Crystallogr. B* **2003,** *59,* 463-471.

[34] Karen, P.; Woodward, P. M.; Lindén, J.; Vogt, T.; Studer, A.; Fischer, P. *Phys. Rev. B* **2001,** *64,* 214405.

[35] Karen, P.; Kjekshus, A.; Huang, Q.; Karen, V. L.; Lynn, J. W.; Rosov, N.; Sora, I. N.; Santoro, A. *J. Solid State Chem.* **2003,** *174,* 87-95.

[36] Solana-Madruga, E.; Arévalo-López, Á. M.; Santos-García, A. J. D.; Urones-Garrote, E.; Ávila-Brande, D.; Sáez-Puche, R.; Attfield, J. P. *Angew. Chem. Int. Ed.* **2016,** *55,* 9340-9344.

[37] Yang, M.; Oró-Solé, J.; Rodgers, J. A.; Jorge, A. B.; Fuertes, A.; Attfield, J. P. *Nat. Chem.* **2011,** *3,* 47-52.

[38] Retuerto, M.; de la Calle, C.; Martínez-Lope, M. J.; Porcher, F.; Krezhov, K.; Menéndez, N.; Alonso, J. A. *J. Solid State Chem.* **2012,** *185,* 18-24.

[39] Terai, T.; Murata, T.; Kakeshita, T. *J. Magn. Magn. Mater.* **2007,** *310,* 768-770.

[40] Millange, F.; Caignaert, V.; Domengès, B.; Raveau, B.; Suard, E. *Chem. Mater.* **1998,** *10,* 1974-1983.

[41] Raveau, B.; Seikh, M. M. *Z. Anorg. Allg. Chem.* **2015,** *641,* 1385-1394.

[42] Cox, D. E.; Sleight, A. W. *Acta Crystallogr. B* **1979,** *35,* 1-10.

[43] Yamada, I.; Takata, K.; Hayashi, N.; Shinohara, S.; Azuma, M.; Mori, S.; Muranaka, S.; Shimakawa, Y.; Takano, M. *Angew. Chem. Int. Ed.* **2008,** *47,* 7032-7035.

[44] Senn, M. S.; Wright, J. P.; Attfield, J. P. *Nature* **2012,** *481,* 173-176.

[45] Kajimoto, R.; Yoshizawa, H.; Tomioka, Y.; Tokura, Y. *Phys. Rev. B* **2001,** *63,* 212407.

[46] Hervieu, M.; Malo, S.; Perez, O.; Beràn, P.; Martin, C.; Baldinozzi, G.; Raveau, B. *Chem. Mater.* **2003,** *15,* 523-527.

[47] Williams, A. J.; Attfield, J. P. *Phys. Rev. B* **2005,** *72,* 024436.

[48] Attfield, J. P. *Solid State Sci.* **2006,** *8,* 861-867.

[49] Billinge, S. J. L.; DiFrancesco, R. G.; Kwei, G. H.; Neumeier, J. J.; Thompson, J. D. *Phys. Rev. Lett.* **1996,** *77,* 715-718.

[50] Larochelle, S.; Mehta, A.; Kaneko, N.; Mang, P. K.; Panchula, A. F.; Zhou, L.; Arthur, J.; Greven, M. *Phys. Rev. Lett.* **2001,** *87,* 95502.

[51] van den Brink, J.; Khomskii, D. I. *J. Phys.: Condens. Matter* **2008,** *20,* 434217.

[52] Taskin, A. A.; Ando, Y. *Phys. Rev. Lett.* **2007,** *98,* 207201.

[53] Bristowe, N. C.; Varignon, J.; Fontaine, D.; Bousquet, E.; Ghosez, P. *Nat. Commun.* **2015,** *6,* 6677.

[54] Towler, M. D.; Dovesi, R.; Saunders, V. R. *Phys. Rev. B* **1995,** *52,* 10150-10159.

[55] Wenger, O. S.; Güdel, H. U. *J. Chem. Phys.* **2001,** *114,* 5832-5841.

[56] Jahn, H. A.; Teller, E. *Proc. R. Soc. A* **1937,** *161,* 220-235.

[57] Bersuker, I. B. *Chem. Rev.* **2001,** *101,* 1067-1114.

[58] Housecroft, C. E.; Sharpe, A. G. *Inorganic Chemistry;* Pearson: Harlow, 2012.

[59] Tokura, Y.; Nagaosa, N. *Science* **2000,** *288,* 462-468.

[60] Hemberger, J.; von Nidda, H.-A. K.; Fritsch, V.; Deisenhofer, J.; Lobina, S.; Rudolf, T.; Lunkenheimer, P.; Lichtenberg, F.; Loidl, A.; Bruns, D.; Büchner, B. *Phys. Rev. Lett.* **2003,** *91,* 66403.

[61] Blake, G. R.; Palstra, T. T. M.; Ren, Y.; Nugroho, A. A.; Menovsky, A. A. *Phys. Rev. Lett.* **2001,** *87,* 245501.

[62] Burdett, J. K. *Inorg. Chem.* **1981,** *20,* 1959-1962.

[63] Vleck, J. H. V. *J. Chem. Phys.* **1939,** *7,* 72-84.

[64] Goodenough, J. B. *Annu. Rev. Mater. Sci.* **1998,** *28,* 1-27.

[65] Rodriguez-Carvajal, J.; Hennion, M.; Moussa, F.; Moudden, A. H.; Pinsard, L.; Revcolevschi, A. *Phys. Rev. B* **1998,** *57,* R3189-3192.

[66] Mellan, T. A.; Corà, F.; Grau-Crespo, R.; Ismail-Beigi, S. *Phys. Rev. B* **2015,** *92,* 085151.

[67] Gehring, G. A.; Gehring, K. A. *Rep. Prog. Phys.* **1975,** *38,* 1-89.

[68] Fauth, F.; Suard, E.; Caignaert, V.; Domengès, B.; Mirebeau, I.; Keller, L. *Eur. Phys. J. B* **2001,** *21,* 163-174.

[69] Carpenter, M. A.; Howard, C. J. *Acta Crystallogr. B* **2009,** *65,* 134-146.

[70] dos Santos, A. M.; Cheetham, A. K.; Atou, T.; Syono, Y.; Yamaguchi, Y.; Ohoyama, K.; Chiba, H.; Rao, C. N. R. *Phys. Rev. B* **2002,** *66,* 64425.

[71] Kanamori, J. *J. Phys. Chem. Solids* **1959,** *10,* 87-98.

[72] Anderson, P. W. *Phys. Rev.* **1959,** *115,* 2-13.

[73] Woodward, P. M. *Acta Crystallogr. B* **1997,** *53,* 32-43.

[74] Dove, M. T.; Heine, V.; Hammonds, K. D. *Mineral. Mag.* **1995,** *59,* 629-639.

[75] Burns, G.; Glazer, A. M. *Space Groups for Solid State Scientists;* Academic Press, Oxford: 2013.

[76] Glazer, A. M. *Acta Crystallogr. B* **1972,** *28,* 3384-3392.

[77] Lufaso, M. W.; Woodward, P. M. *Acta Crystallogr. B* **2001,** *57,* 725-738.

[78] Geller, S. *J. Chem. Phys.* **1956,** *24,* 1236-1239.

[79] Benedek, N. A.; Rondinelli, J. M.; Djani, H.; Ghosez, P.; Lightfoot, P. *Dalton Trans.* **2015,** *44,* 10543-10558.

[80] Lau, C.; Kim, Y.; Albright, S.; Char, K.; Ahn, C. H.; Walker, F. J. *APL Mater.* **2019,** *7,* 031108.

[81] Hill, N. A. *J. Phys. Chem. B* **2000,** *104,* 6694-6709.

[82] Aken, B. B. V.; Palstra, T. T. M.; Filippetti, A.; Spaldin, N. A. *Nat. Mater.* **2004,** *3,* 164-170.

[83] Mizokawa, T.; Khomskii, D. I.; Sawatzky, G. A. *Phys. Rev. B* **1999,** *60,* 7309-7313.

[84] v. Zimmermann, M.; Hill, J. P.; Gibbs, D.; Blume, M.; Casa, D.; Keimer, B.; Murakami, Y.; Tomioka, Y.; Tokura, Y. *Phys. Rev. Lett.* **1999,** *83,* 4872-4875.

[85] Hurlbutt, K.; Wheeler, S.; Capone, I.; Pasta, M. *Joule* **2018,** *2,* 1950-1960.

[86] Verdaguer, M.; Girolami, G. S. *Magnetic Prussian Blue Analogs;* Wiley Online Books: 2004 Magnetism: Molecules to Materials V (eds J.S. Miller and M. Drillon).

[87] Pintado, S.; Goberna-Ferrón, S.; Escudero-Adán, E. C.; Galán-Mascarós, J. R. *J. Am. Chem. Soc.* **2013,** *135,* 13270-13273.

[88] Madshus, K.; Strömme, A. *Z. Naturforsch* **1968,** *23,* 391-392.

[89] Kaye, S. S.; Long, J. R. *J. Am. Chem. Soc.* **2005,** *127,* 6506-6507.

[90] Kojima, A.; Teshima, K.; Shirai, Y.; Miyasaka, T. *J. Am. Chem. Soc.* **2009,** *131,* 6050-6051.

[91] Sletten, E.; Jensen, L. H. *Acta Crystallogr. B* **1973,** *29,* 1752-1756.

[92] Bever, A. K. V. *Recl. Trav. Chim. Pays-Bas* **1938,** *57,* 1259-1268.

[93] Her, J.-H.; Stephens, P. W.; Kareis, C. M.; Moore, J. G.; Min, K. S.; Park, J.-W.; Bali, G.; Kennon, B. S.; Miller, J. S. *Inorg. Chem.* **2010,** *49,* 1524-1534.

[94] Goodwin, A. L. *Phys. Rev. B* **2006,** *74,* 134302.

[95] Feng, F.; Chen, S.; Zhao, S.; Zhang, W.; Miao, Y.; Che, H.; Liao, X.-Z.; Ma, Z.-F. *Chem. Eng. J.* **2021,** *411,* 128518.

[96] Gebert, F.; Cortie, D. L.; Bouwer, J. C.; Wang, W.; Yan, Z.; Dou, S.-X.; Chou, S.-L. *Angew. Chem. Int. Ed.* **2021,** *60,* 18519-18526.

[97] Escax, V.; Moulin, C.; Villain, F.; Champion, G.; Itié, J.-P.; Münsch, P.; Michel, V.; Bleuzen, A. *Comptes Rendus Chim.* **2003,** *6,* 1165-1173.

[98] Buser, H. J.; Schwarzenbach, D.; Petter, W.; Ludi, A. *Inorg. Chem.* **1977,** *16,* 2704-2710.

[99] Adak, S.; Daemen, L. L.; Hartl, M.; Williams, D.; Summerhill, J.; Nakotte, H. *J. Solid State Chem.* **2011,** *184,* 2854-2861.

[100] Roque, J.; Reguera, E.; Balmaseda, J.; Rodríguez-Hernández, J.; Reguera, L.; del Castillo, L. F. *Micropor. Mesopor. Mater.* **2007,** *103,* 57-71.

[101] Balmaseda, J.; Reguera, E.; Rodríguez-Hernández, J.; Reguera, L.; Autie, M. *Micropor. Mesopor. Mater.* **2006,** *96,* 222-236.

[102] Simonov, A.; Baerdemaeker, T. D.; Boström, H. L. B.; Gómez, M. L. R.; Gray, H. J.; Chernyshov, D.; Bosak, A.; Bürgi, H.-B.; Goodwin, A. L. *Nature* **2020,** *578,* 256-260.

[103] Flambard, A.; Köhler, F. H.; Lescouëzec, R. *Angew. Chem. Int. Ed.* **2009,** *48,* 1673-1676.

[104] Franz, P.; Ambrus, C.; Hauser, A.; Chernyshov, D.; Hostettler, M.; Hauser, J.; Keller, L.; Krämer, K.; Stoeckli-Evans, H.; Pattison, P.; Bürgi, H.-B.; Decurtins, S. *J. Am. Chem. Soc.* **2004,** *126,* 16472-16477.

[105] Pauling, L. *The Nature of the Chemical Bond and the Structure of Molecules and Crystals: An Introduction to Modern Structural Chemistry;* Cornell Univ. Press: 1960.

[106] Sharpe, A. G. *The Chemistry of Cyano Complexes of the Transition Metals;* Academic Press: London: 1976.

[107] Siebert, H.; Jentsch, W. *Z. Naturforsch. B* **1981,** *36,* 123-124.

[108] Rodríguez-Hernández, J.; Reguera, E.; Lima, E.; Balmaseda, J.; Martínez-García, R.; Yee-Madeira, H. *J. Phys. Chem. Solids* **2007,** *68,* 1630-1642.

[109] Duyker, S. G.; Hill, J. A.; Howard, C. J.; Goodwin, A. L. *J. Am. Chem. Soc.* **2016,** *138,* 11121-11123.

[110] Boström, H. L. *CrystEngComm* **2020,** *22,* 961-968.

[111] Howard, C. J.; Stokes, H. T. *Acta Crystallogr. B* **2004,** *60,* 674-684.

[112] Howard, C. J.; Stokes, H. T. *Acta Crystallogr. A* **2005,** *61,* 93-111.

[113] Boström, H. L. B.; Hill, J. A.; Goodwin, A. L. *Phys. Chem. Chem. Phys.* **2016,** *18,* 31881-31894.

[114] Kareis, C. M.; Lapidus, S. H.; Her, J.-H.; Stephens, P. W.; Miller, J. S. *J. Am. Chem. Soc.* **2012,** *134,* 2246-2254.

[115] Boström, H. L.; Bruckmoser, J.; Goodwin, A. L. *J. Am. Chem. Soc.* **2019,** *141,* 17978-17982.

[116] Fiore, M.; Wheeler, S.; Hurlbutt, K.; Capone, I.; Fawdon, J.; Ruffo, R.; Pasta, M. *Chem. Mater.* **2020,** *32,* 7653-7661.

[117] Kieslich, G.; Sun, S.; Cheetham, A. K. *Chem. Sci.* **2014,** *5,* 4712-4715.

[118] Lee, J.-H.; Bristowe, N. C.; Lee, J. H.; Lee, S.-H.; Bristowe, P. D.; Cheetham, A. K.; Jang, H. M. *Chem. Mater.* **2016,** *28,* 4259-4266.

[119] Boström, H. L. B.; Senn, M. S.; Goodwin, A. L. *Nat. Commun.* **2018,** *9,* 2380.

[120] Goodwin, A. L.; Chapman, K. W.; Kepert, C. J. *J. Am. Chem. Soc.* **2005,** *127,* 17980-17981.

[121] Chapman, K. W.; Chupas, P. J.; Kepert, C. J. *J. Am. Chem. Soc.* **2006,** *128,* 7009-7014.

[122] Margadonna, S.; Prassides, K.; Fitch, A. N. *Angew. Chem., Int. Ed.* **2004,** *43,* 6316-6319.

[123] Matsuda, T.; Kim, J. E.; Ohoyama, K.; Moritomo, Y. *Phys. Rev. B* **2009,** *79,* 172302.

[124] Gao, Q.; Sun, Y.; Shi, N.; Milazzo, R.; Pollastri, S.; Olivi, L.; Huang, Q.; Liu, H.; Sanson, A.; Sun, Q.; Liang, E.; Xing, X.; Chen, J. *Scr. Mater.* **2020,** *187,* 119-124.

[125] Bersuker, I. B. *Symmetry* **2021,** *13,* 1577.

[126] Stroppa, A.; Jain, P.; Barone, P.; Marsman, M.; Perez-Mato, J. M.; Cheetham, A. K.; Kroto, H. W.; Picozzi, S. *Angew. Chem. Int. Ed* **2011,** *50,* 5847-5850.

[127] Tan, J. C.; Cheetham, A. K. *Chem. Soc. Rev.* **2011,** *40,* 1059-1080.

[128] Kostakis, G. E.; Hewitt, I. J.; Ako, A. M.; Mereacre, V.; Powell, A. K. *Phil. Trans. Soc. A* **2010,** *368,* 1509-1536.

[129] Reguera, L.; Krap, C.; Balmaseda, J.; Reguera, E. *J. Phys. Chem. C* **2008,** *112,* 15893-15899.

[130] Hu, K. L.; Kurmoo, M.; Wang, Z.; Gao, S. *Chemistry - A European Journal* **2009,** *15,* 12050-12064.

[131] Nifontova, G. A.; Filipenko, O. S.; Astakhova, A. S.; Lavrent'ev, I. P.; Atovmyan, L. O. *Koord. Khim.* **1990,** *16,* 218-224.

[132] Shang, R.; Chen, S.; Wang, B.; Wang, Z.; Gao, S. *Angew. Chem. Int. Ed.* **2016,** *55,* 2097-2100.

[133] Moritomo, Y.; Kato, K.; Kuriki, A.; Takata, M.; Sakata, M.; Tokoro, H.; ichi Ohkoshi, S.; Hashimoto, K. *J. Phys. Soc. Jpn* **2002,** *71,* 2078-2081.

[134] Boström, H. L. B.; Collings, I. E.; Cairns, A. B.; Romao, C. P.; Goodwin, A. L. *Dalton Trans.* **2019,** *48,* 1647-1655.

[135] Wang, X.; Ta, A. T.; Quemerais, S.; Grandjean, A.; zur Loye, H. C.; Phillpot, S. R. *Chem. Mater.* **2024,** *36,* 6731-6739.

[136] Cattermull, J.; Roth, N.; Cassidy, S. J.; Pasta, M.; Goodwin, A. L. *J. Am. Chem. Soc.* **2023,** *145,* 24249-24259.

[137] Cattermull, J.; Pasta, M.; Goodwin, A. L. *J. Am. Chem. Soc.* **2023,** *145,* 24471-24475.

[138] Welberry, T. R.; Goossens, D. J.; Edwards, A. J.; David, W. I. F. *Acta Cryst. A* **2001,** *57,* 101-109.

[139] Welberry, T. R.; Goossens, D. J. *IUCrJ* **2014,** *1,* 550-562.

[140] Ising, E. *Z. Phys.* **1925,** *31,* 253-258.

[141] McKenzie, S. *J. Phys. C: Solid State Phys.* **1983,** *16,* 2509.

[142] Anderson, P. W. *Phys. Rev.* **1956,** *102,* 1008-1013.

[143] Potts, R. B. *Proc. Camb. Phil. Soc.* **1952,** *48,* 106-109.

[144] Ahmed, M. R.; Gehring, G. A. *J. Phys. A: Math. Gen.* **2005,** *38,* 4047-4067.

[145] Ahmed, M. R.; Gehring, G. A. *Phys. Rev. B* **2006,** *74,* 014420.

[146] Coates, C. S.; Goodwin, A. L. *Mater. Horiz.* **2019,** *6,* 211-218.

[147] Šimėnas, M.; Balčiūnas, S.; Mączka, M.; Banys, J.; Tornau, E. E. *Phys. Chem. Chem. Phys.* **2016,** *18,* 18528-18535.

[148] Joyce, G. S. *Phys. Rev.* **1967,** *155,* 478-491.

[149] Cairns, A. B.; Cliffe, M. J.; Paddison, J. A. M.; Daisenberger, D.; Tucker, M. G.; Coudert, F.-X.; Goodwin, A. L. *Nat. Chem.* **2016,** *8,* 442-447.

[150] Rasche, B.; Isaeva, A.; Ruck, M.; Borisenko, S.; Zabolotnyy, V.; Büchner, B.; Koepernik, K.; Ortix, C.; Richter, M.; van den Brink, J. *Nat. Mater.* **2013,** *12,* 422-425.

[151] Keen, D. A.; Goodwin, A. L. *Nature* **2015,** *521,* 303-309.

[152] Welberry, T. R.; Paściak, M. *Metall. Mater. Trans. A* **2011,** *42,* 6-13.

[153] Paddison, J. A. M.; Stewart, J. R.; Manuel, P.; Courtois, P.; McIntyre, G. J.; Rainford, B. D.; Goodwin, A. L. *Phys. Rev. Lett.* **2013,** *110,* 267207.

[154] Nakatsuji, S. *et al. Science* **2012,** *336,* 559-563.

[155] Lacroix, C.; Mendels, P.; Mila, F. *Introduction to Frustrated Magnetism: Materials, Experiments, Theory;* Springer: 2011.

[156] Lynn, J. W.; Argyriou, D. N.; Ren, Y.; Chen, Y.; Mukovskii, Y. M.; Shulyatev, D. A. *Phys. Rev. B* **2007,** *76,* 014437.

[157] Shintani, H.; Tanaka, H. *Nat. Phys.* **2006,** *2,* 200-206.

[158] Ahmed, M. R.; Gehring, G. A. *Phys. Rev. B* **2009,** *79,* 174106.

[159] Tanaka, T.; Matsumoto, M.; Ishihara, S. *Phys. Rev. Lett.* **2005,** *95,* 267204.

[160] Zhou, J.-S.; Goodenough, J. B. *Phys. Rev. B* **1999,** *60,* R15002.

[161] Qiu, X.; Proffen, T.; Mitchell, J. F.; Billinge, S. J. *Phys. Rev. Lett.* **2005,** *94,* 177203.

[162] Thygesen, P. M.; Young, C. A.; Beake, E. O.; Romero, F. D.; Connor, L. D.; Proffen, T. E.; Phillips, A. E.; Tucker, M. G.; Hayward, M. A.; Keen, D. A.; Goodwin, A. L. *Phys. Rev. B* **2017,** *95,* 174107.

[163] Chatterji, T.; Fauth, F.; Ouladdiaf, B.; Mandal, P.; Ghosh, B. *Phys. Rev. B* **2003,** *68,* 052406.

[164] Wu, F. Y. *Rev. Mod. Phys.* **1982,** *54,* 235-268.

[165] Nussinov, Z.; Brink, J. V. D. *Rev. Mod. Phys.* **2015,** *87,* 1.

[166] Kitaev, A. *Ann. Phys.* **2006,** *321,* 2-111.

[167] Tanaka, T.; Ishihara, S. *Phys. Rev. B* **2009,** *79,* 035109.

[168] Senn, M. S.; Keen, D. A.; Lucas, T. C. A.; Hriljac, J. A.; Goodwin, A. L. *Phys. Rev. Lett.* **2016,** *116,* 207602.

[169] Brivio, F.; Frost, J. M.; Skelton, J. M.; Jackson, A. J.; Weber, O. J.; Weller, M. T.; Goñi, A. R.; Leguy, A. M. A.; Barnes, P. R. F.; Walsh, A. *Phys. Rev. B* **2015,** *92,* 144308.

[170] Keiber, T.; Bridges, F.; Sales, B. C. *Phys. Rev. Lett.* **2013,** *111,* 95504.

[171] Wright, A. C.; Clare, A. G.; Grimley, D. I.; Sinclair, R. N. *J. Non-Cryst. Solids* **1989,** *112,* 33-47.

[172] Sapnik, A. F.; Geddes, H. S.; Reynolds, E. M.; Yeung, H. H.-M.; Goodwin, A. L. *Chem. Commun.* **2018,** *54,* 9651-9654.

[173] Lonsdale, K. Y.; Smith, H. *Proc. R. Soc. A.* **1941,** *179,* 8-50.

[174] Misawa, M.; Price, D. L.; Suzuki, K. *J. Non-Cryst. Solids* **1980,** *37,* 85-97.

[175] Dove, M. T.; Tucker, M. G.; Keen, D. A. *Eur. J. Mineral.* **2002,** *14,* 331-348.

[176] Young, C. A.; Goodwin, A. L. *J. Mater. Chem.* **2011,** *21,* 6464-6476.

[177] Billinge, S. J. L.; Kanatzidis, M. G. *Chem. Commun.* **2004,** 749-760.

[178] Mancini, A.; Malavasi, L. *Chem. Commun.* **2015,** *51,* 16592-16604.

[179] Weber, T.; Simonov, A. *Z. Kristallogr.* **2012,** *227,* 238-247.

[180] Simonov, A.; Weber, T.; Steurer, W. *J. Appl. Crystallogr.* **2014,** *47,* 2011-2018.

[181] Kobas, M.; Weber, T.; Steurer, W. *Phys. Rev. B* **2005,** *71,* 224205.

[182] Grandjean, F.; Samain, L.; Long, G. J. *Dalton Trans.* **2016,** *45,* 18018-18044.

[183] Pasciak, M.; Welberry, T. R.; Kulda, J.; Kempa, M.; Hlinka, J. *Phys. Rev. B* **2012,** *85,* 224109.

[184] Battle, P. D.; Evers, S. I.; Hunter, E. C.; Westwood, M. *Inorg. Chem.* **2013,** *52,* 6648-6653.

[185] Keen, D. A. *J. Appl. Crystallogr.* **2001,** *34,* 172-177.

[186] Egami, T.; Billinge, S. J. L. *Underneath the Bragg peaks: structural analysis of complex materials;* Pergamon Elsevier, Oxford: 2003.

[187] Billinge, S. J. L.; Levin, I. *Science* **2007,** *316,* 561-565.

[188] Jensen, K. M. Ø.; Christensen, M.; Juhas, P.; Tyrsted, C.; Bøjesen, E. D.; Lock, N.; Billinge, S. J. L.; Iversen, B. B. *J. Am. Chem. Soc.* **2012,** *134,* 6785-6792.

[189] Farrow, C. L.; Juhas, P.; Liu, J. W.; Bryndin, D.; Božin, E. S.; Bloch, J.; Proffen, T.; Billinge, S. J. L. *J. Phys.: Condens. Matter* **2007,** *19,* 335219.

[190] Božin, E. S.; Sartbaeva, A.; Zheng, H.; Wells, S. A.; Mitchell, J. F.; Proffen, T.; Thorpe, M. F.; Billinge, S. J. L. *J. Phys. Chem. Solids* **2008,** *69,* 2146-2150.

[191] Božin, E. S.; Qiu, X.; Schmidt, M.; Paglia, G.; Mitchell, J. F.; Radaelli, P. G.; Proffen, T.; Billinge, S. J. L. *Phys. B: Condens. Matter* **2006,** *385-386,* 110-112.

[192] Bozin, E. S.; Schmidt, M.; DeConinck, A. J.; Paglia, G.; Mitchell, J. F.; Chatterji, T.; Radaelli, P. G.; Proffen, T.; Billinge, S. J. *Phys. Rev. Lett.* **2007,** *98,* 137203.

[193] Proffen, T.; Billinge, S. J. L. *Appl. Phys. A* **2002,** *74,* s1770-s1772.

[194] Billinge, S. J. L.; Petkov, V.; Proffen, T.; Kwei, G. H.; Sarrao, J. L.; Shastri, S. D.; Kycia, S. *MRS Online Proc. Libr.* **1999,** *602,* 177-182.

[195] McGreevy, R. L. *J. Phys.: Condens. Matter* **2001,** *13,* R877-R913.

[196] McGreevy, R. L.; Pusztai, L. *Mol. Simul.* **1988,** *1,* 359-367.

[197] Metropolis, N.; Ulam, S. *J. Am. Stat. Assoc.* **1949,** *44,* 335-341.

[198] Sartbaeva, A.; Wells, S. A.; Thorpe, M. F.; Božin, E. S.; Billinge, S. J. *Phys. Rev. Lett.* **2007,** *99,* 155503.

[199] Tucker, M. G.; Keen, D. A.; Dove, M. T.; Goodwin, A. L.; Hui, Q. *J. Phys.: Condens. Matter* **2007,** *19,* 335218.

[200] Soper, A. K. *Chem. Phys.* **1996,** *202,* 295-306.

[201] Wollan, E. O.; Koehler, W. C. *Phys. Rev.* **1955,** *100,* 545.

[202] Bochu, B.; Chenavas, J.; Joubert, J. C.; Marezio, M. *J. Solid State Chem.* **1974,** *11,* 88-93.

[203] Radaelli, P. G.; Cox, D. E.; Marezio, M.; Cheong, S.-W. *Phys. Rev. B* **1997,** *55,* 3015-3023.

[204] Schiffer, P.; Ramirez, A. P.; Bao, W.; Cheong, S.-W. *Phys. Rev. Lett.* **1995,** *75,* 3336-3339.

[205] Fäth, M.; Freisem, S.; Menovsky, A. A.; Tomioka, Y.; Aarts, J.; Mydosh, J. A. *Science* **1999,** *285,* 1540-1542.

[206] Chen, W. T.; Wang, C. W.; Cheng, C. C.; Chuang, Y. C.; Simonov, A.; Bristowe, N. C.; Senn, M. S. *Nat. Commun.* **2021,** *12,* 6319.

[207] Radaelli, P. G.; Cox, D. E.; Marezio, M.; Cheong, S. W.; Schiffer, P. E.; Ramirez, A. P. *Phys. Rev. Lett.* **1995,** *75,* 4488-4491.

[208] Evans, J. S. O. *J. Chem. Soc., Dalton Trans.* **1999,** 3317-3326.

[209] Dove, M. T.; Fang, H. *Rep. Prog. Phys.* **2016,** *79,* 066503.

[210] Evans, J. S. O.; David, W. I. F.; Sleight, A. W. *Acta Crystallogr. B* **1999,** *55,* 333-340.

[211] Taylor, D. *Br. Ceram. Trans. J.* **1988,** *87,* 39-45.

[212] Evans, J. S. O.; Mary, T. A.; Sleight, A. W. *J. Solid State Chem.* **1997,** *133,* 580-583.

[213] Tao, J. Z.; Sleight, A. W. *J. Solid State Chem.* **2003,** *173,* 45-48.

[214] Chapman, K. W.; Chupas, P. J.; Kepert, C. J. *J. Am. Chem. Soc.* **2005,** *127,* 11232-11233.

[215] Goodwin, A. L.; Kepert, C. J. *Phys. Rev. B* **2005,** *71,* 140301(R).

[216] Margadonna, S.; Prassides, K.; Fitch, A. N. *J. Am. Chem. Soc.* **2004,** *126,* 15390-15391.

[217] Goodwin, A. L.; Keen, D. A.; Tucker, M. G.; Dove, M. T.; Peters, L.; Evans, J. S. O. *J. Am. Chem. Soc.* **2008,** *130,* 9660-9661.

[218] Pannhorst, W. *J. Non-Cryst. Solids* **1997,** *219,* 198-204.

[219] Versluis, A.; Douglas, W. H.; Sakaguchi, R. L. *Dent. Mater.* **1996,** *12,* 290-294.

[220] Jakubinek, M. B.; O'Neill, C.; Felix, C.; Price, R. B.; White, M. A. *Dent. Mater.* **2008,** *24,* 1468-1476.

[221] Fleming, D. A.; Johnson, D. W.; Lemaire, P. J. "Article Comprising a Temperature Compensated Optical Fiber Refractive Index Grating", 1997.

[222] Mittal, R.; Gupta, M. K.; Chaplot, S. L. *Prog. Mater. Sci.* **2018,** *92,* 360-445.

[223] Miller, W.; Smith, C. W.; Mackenzie, D. S.; Evans, K. E. *J. Mater. Sci.* **2009,** *44,* 5441-5451.

[224] Barrera, G. D.; Bruno, J. A. O.; Barron, T. H. K.; Allan, N. L. *J. Phys: Condens. Matter* **2005,** *17,* R217.

[225] Chen, J.; Hu, L.; Deng, J.; Xing, X. *Chem. Soc. Rev.* **2015,** *44,* 3522-3567.

[226] Attfield, J. P. *Front. Chem.* **2018,** *6,* 371.

[227] Heine, V.; Welche, P. R. L.; Dove, M. T. *J. Am. Ceram. Soc.* **1999,** *82,* 1793-1802.

[228] Pryde, A. K. A.; Hammonds, K. D.; Dove, M. T.; Heine, V.; Gale, J. D.; Warren, M. C. *J. Phys.: Condens. Matter* **1996,** *8,* 10973.

[229] Rodriguez, E. E.; Llobet, A.; Proffen, T.; Melot, B. C.; Seshadri, R.; Littlewood, P. B.; Cheetham, A. K. *J. Appl. Phys.* **2009,** *105,* 114901.

[230] Tucker, M. G.; Dove, M. T.; Keen, D. A. *J. Phys.: Condens. Matter* **2000,** *12,* L425.

[231] Bordet, P. *C. R. Phys.* **2018,** *19,* 561-574.

[232] Chapman, K. W.; Chupas, P. J.; Kepert, C. J. *J. Am. Chem. Soc.* **2005,** *127,* 15630-15636.

[233] Chapman, K. W.; Beyer, K. A.; Zhao, H.; Chupas, P. J. *CrystEngComm* **2013,** *15,* 9377-9381.

[234] Ma, N.; Ohtani, R.; Le, H. M.; Sørensen, S. S.; Ishikawa, R.; Kawata, S.; Bureekaew, S.; Kosasang, S.; Kawazoe, Y.; Ohara, K.; Smedskjaer, M. M.; Horike, S. *Nat. Commun.* **2022,** *13,* 4023.

[235] Goodwin, A. L. *Nat. Commun.* **2019,** *10,* 4461.

[236] Schmidt, E. M.; Bulled, J. M.; Goodwin, A. L. *IUCrJ* **2022,** *9,* 21-30.

[237] Cattermull, J.; Sada, K.; Hurlbutt, K.; Cassidy, S. J.; Pasta, M.; Goodwin, A. L. *Chem. Mater.* **2022,** *34,* 5000-5008.

[238] Brant, W. R.; Mogensen, R.; Colbin, S.; Ojwang, D. O.; Schmid, S.; Häggström, L.; Ericsson, T.; Jaworski, A.; Pell, A. J.; Younesi, R. *Chem. Mater.* **2019,** *31,* 7203-7211.

[239] Deng, L.; Qu, J.; Niu, X.; Liu, J.; Zhang, J.; Hong, Y.; Feng, M.; Wang, J.; Hu, M.; Zeng, L.; Zhang, Q.; Guo, L.; Zhu, Y. *Nat. Commun.* **2021,** *12,* 2167.

[240] Dhir, S.; Jagger, B.; Maguire, A.; Pasta, M. *Nat. Commun.* **2023,** *14,* 3833.

[241] Dhir, S.; Cattermull, J.; Jagger, B.; Schart, M.; Olbrich, L. F.; Chen, Y.; Zhao, J.; Sada, K.; Goodwin, A.; Pasta, M. *Nat. Commun.* **2024,** *15,* 7580.

[242] Wessells, C. D.; Huggins, R. A.; Cui, Y. *Nat. Commun.* **2011,** *2,* 550.

[243] Wheeler, S.; Hurlbutt, K.; Pasta, M. *Chem* **2018,** *4,* 666-668.

[244] Dhir, S.; Wheeler, S.; Capone, I.; Pasta, M. *Chem* **2020,** *6,* 2442-2460.

[245] Bie, X.; Kubota, K.; Hosaka, T.; Chihara, K.; Komaba, S. *J. Mater. Chem. A* **2017,** *5,* 4325-4330.

[246] Cattermull, J.; Jagger, B.; Cassidy, S. J.; Dhir, S.; Allan, P. K.; Pasta, M.; Goodwin, A. L. *Sci. Adv.* **2026,** *12,* 1629.

[247] Matsuda, T.; Moritomo, Y. *Appl. Phys. Express* **2011,** *4,* 047101.

[248] Jiang, L.; Lu, Y.; Zhao, C.; Liu, L.; Zhang, J.; Zhang, Q.; Shen, X.; Zhao, J.; Yu, X.; Li, H.; Huang, X.; Chen, L.; Hu, Y. S. *Nat. Energy* **2019,** *4,* 495-503.

[249] Zhou, A.; Xu, Z.; Gao, H.; Xue, L.; Li, J.; Goodenough, J. B. *Small* **2019,** *15,* 1902420.

[250] Moritomo, Y.; Igarashi, K.; Kim, J.; Tanaka, H. *Appl. Phys. Express* **2009,** *2,* 085001.

[251] Yang, D.; Xu, J.; Liao, X. Z.; He, Y. S.; Liu, H.; Ma, Z. F. *Chem. Commun.* **2014,** *50,* 13377-13380.

[252] McCusker, J. K. *Science* **2019,** *363,* 484-488.

[253] Canton, S. E. *et al. Nat. Commun.* **2015,** *6,* 6359.

[254] Sato, O.; Iyoda, T.; Fujishima, A.; Hashimoto, K. *Science* **1996,** *272,* 704-705.

[255] ichi Ohkoshi, S.; Tokoro, H. *Acc. Chem. Res.* **2012,** *45,* 1749-1758.

[256] Azzolina, G.; Tokoro, H.; Imoto, K.; Yoshikiyo, M.; ichi Ohkoshi, S.; Collet, E. *Angew. Chem. Int. Ed.* **2021,** *60,* 23267-23273.

[257] Asahara, A.; Nakajima, M.; Fukaya, R.; Tokoro, H.; ichi Ohkoshi, S.; Suemoto, T. *Phys. Rev. B* **2012,** *86,* 195138.

[258] Moritomo, Y.; Wakaume, K.; Takachi, M.; Zhu, X.; Kamioka, H. *J. Phys. Soc. Jpn.* **2013,** *82,* 094710.

[259] Johansson, J. O.; Kim, J.-W.; Allwright, E.; Rogers, D. M.; Robertson, N.; Bigot, J.-Y. *Chem. Sci.* **2016,** *7,* 7061-7067.

[260] van Veenendaal, M. *Sci. Rep.* **2017,** *7,* 6672.

[261] Watanabe, S.; Sawada, Y.; Nakaya, M.; Yoshino, M.; Nagasaki, T.; Kameyama, T.; Torimoto, T.; Inaba, Y.; Takahashi, H.; Takeshita, K.; Onoe, J. *J. Appl. Phys.* **2016,** *119,* 235102.

[262] Cammarata, M.; Zerdane, S.; Balducci, L.; Azzolina, G.; Mazerat, S.; Exertier, C.; Trabuco, M.; Levantino, M.; Alonso-Mori, R.; Glownia, J. M.; Song, S.; Catala, L.; Mallah, T.; Matar, S. F.; Collet, E. *Nat. Chem.* **2021,** *13,* 10-14.

[263] Newton, M. A.; Chapman, K. W.; Thompsett, D.; Chupas, P. J. *J. Am. Chem. Soc.* **2012,** *134,* 5036-5039.

[264] Georgescu, I. *Nat. Rev. Phys.* **2020,** *2,* 345.

[265] Griffiths, J.; Suzana, A. F.; Wu, L.; Marks, S. D.; Esposito, V.; Boutet, S.; Evans, P. G.; Mitchell, J. F.; Dean, M. P. M.; Keen, D. A.; Robinson, I.; Billinge, S. J. L.; Bozin, E. S. *Nat. Mater.* **2024,** *23,* 1041-1047.

[266] Clegg, W. *Crystal Structure Determination;* Oxford University Press: Oxford, 1998.

[267] Blake, A. J.; Clegg, W.; Cole, J. M.; Evans, J. S. O.; Main, P.; Parsons, S.; Watkin, D. J. *Crystal Structure Analysis: Principles and Practice;* Oxford University Press: Oxford, 2009.

[268] Dove, M. T. *Introduction to Lattice Dynamics;* Cambridge Univ. Press: Cambridge, 1993.

[269] of Crystallography, I. U. *International Tables for Crystallography, Volume A: Space-Group Symmetry;* Wiley (ed M. I. Aroyo): 6th ed.; 2016.

[270] Bragg, W. L. *Proc. Camb. Phil. Soc.* **1912,** *17,* 43-57.

[271] Bragg, W. H.; Bragg, W. L. *Proc. R. Soc. A* **1913,** *88,* 428-438.

[272] Bradley, G. J.; Cracknell, A. P. *The Mathematical Theory of Symmetry in Solids;* Clarendon Press, Oxford: 1972.

[273] Karle, J.; Hauptman, H. *Acta Crystallogr.* **1950,** *3,* 181-187.

[274] Patterson, A. L. *Z. Kristallogr.* **1935,** *90,* 517-542.

[275] Sayre, D. *Acta Crystallogr.* **1952,** *5,* 60-65.

[276] Palatinus, L.; Chapuis, G. *J. Appl. Crystallogr.* **2007,** *40,* 786-790.

[277] Tschentscher, T.; Bressler, C.; Grünert, J.; Madsen, A.; Mancuso, A. P.; Meyer, M.; Scherz, A.; Sinn, H.; Zastrau, U. *Appl. Sci.* **2017,** *7,* 592.

[278] Zastrau, U. *et al. J. Synchrotron Rad.* **2021,** *28,* 1393-1416.

[279] Abeghyan, S.; Bagha-Shanjani, M.; Chen, G.; Englisch, U.; Karabekyan, S.; Li, Y.; Preisskorn, F.; Wolff-Fabris, F.; Wuenschel, M.; Yakopov, M.; Pflueger, J. *J. Synchrotron Rad.* **2019,** *26,* 302-310.

[280] Decking, W. *et al. Nat. Photonics* **2020,** *14,* 391-397.

[281] Scholz, M.; Zhao, Z. T. MOA04. In *Proceedings of the 39th International Free-Electron Laser Conference (FEL2019)*; Hamburg, Germany, 2019.

[282] Coelho, A. A. *TOPAS-Academic version 6;* Coelho Software: Brisbane: 2016.

[283] Toby, B. H. *Powder Diffr.* **2006,** *21,* 67-70.

[284] Pawley, G. S. *J. Appl. Crystallogr.* **1981,** *14,* 357-361.

[285] Thompson, P.; Cox, D. E.; Hastings, J. B. *J. Appl. Crystallogr.* **1987,** *20,* 79-83.

[286] Rietveld, H. M. *J. Appl. Crystallogr.* **1969,** *2,* 65-71.

[287] Stephens, P. W. *J. Appl. Crystallogr.* **1999,** *32,* 281-289.

[288] Campbell, B. J.; Stokes, H. T.; Tanner, D. E.; Hatch, D. M. *J. Appl. Crystallogr.* **2006,** *39,* 607-614.

[289] Stokes, H. T.; Hatch, D. M.; Campbell, B. J. *ISODISTORT, ISOTROPY Software Suite;* iso.byu.edu.

[290] Warren, B. E. *X-ray diffraction;* Reading: Addison-Wesley (reprinted by Dover, New York): 1990.

[291] Wagner, C. N. J. *J.Non-Cryst. Solids* **1985,** *76,* 29-42.

[292] Wright, A. C. *Advances in Structure Research by Diffraction Methods;* volume 5 Oxford: Pergamon Press: 1974.

[293] Debye, P. *Ann. Phys.* **1915,** *351,* 809-823.

[294] Farrow, C. L.; Billinge, S. J. *Acta Crystallogr. A* **2009,** *65,* 232-239.

[295] Støckler, L. J.; Krause, L.; Svane, B.; Tolborg, K.; Richter, B.; Takahashi, S.; Fujita, T.; Kasai, H.; Sugahara, M.; Inoue, I.; Nishibori, E.; Iversen, B. B. *IUCrJ* **2023,** *10,* 103-117.

[296] Nakano, M.; Miyashita, O.; Jonic, S.; Song, C.; Nam, D.; Joti, Y.; Tama, F. *J. Synchrotron Rad.* **2017,** *24,* 727-737.

[297] Obara, Y.; Ito, H.; Ito, T.; Kurahashi, N.; Thürmer, S.; Tanaka, H.; Katayama, T.; Togashi, T.; Owada, S.; ichi Yamamoto, Y.; Karashima, S.; Nishitani, J.; Yabashi, M.; Suzuki, T.; Misawa, K. *Struct. Dyn.* **2017,** *4,* 044033.

[298] Dove, M. *Collection SFN* **2011,** *12,* 123-159.

[299] Dove, M. D. *Structure and Dynamics: An Atomic View of Materials;* Oxford University Press: Oxford, 2003.

[300] Debye, P. *Ann. Phys.* **1913,** *348,* 49-92.

[301] Waller, I. *Z. Phys.* **1923,** *17,* 398-408.

[302] Raunio, G.; Almqvist, L.; Stedman, R. *Phys. Rev.* **1969,** *178,* 1496-1501.

[303] Newnham, R. E. *Properties of Materials: Anisotropy, Symmetry, Structure;* Oxford University Press: Oxford, 2005.

[304] Grüneisen, E. *Thermische Eigenschaften der Stoffe;* volume 10 Springer: Berlin (eds H. Geiger and K. Scheel): 1926.

[305] Ducamp, M.; Coudert, F. X. *J. Phys. Chem. C* **2021,** *125,* 15647-15658.

[306] Megaw, H. D. *Mat. Res. Bull.* **1971,** *6,* 1007-1018.

[307] Panda, M. K.; Runčevski, T.; Sahoo, S. C.; Belik, A. A.; Nath, N. K.; Dinnebier, R. E.; Naumov, P. *Nat. Commun.* **2014,** *5,* 4811.

[308] Barron, T. H. K. *Lond. Edinb. Dub. Phil. Mag.* **1955,** *46,* 720-734.

[309] Barron, T. H. K. *Ann. Phys.* **1957,** *1,* 77-90.

[310] Giddy, A. P.; Dove, M. T.; Pawley, G. S.; Heine, V. *Acta Cryst. A* **1993,** *49,* 697-703.

[311] Hammonds, K. D.; Dove, M. T.; Giddy, A. P.; Heine, V.; Winkler, B. *Am. Mineral.* **1996,** *81,* 1057-1079.

[312] Dove, M. T.; Hammonds, K. D.; Heine, V.; Withers, R. L.; Xiao, Y.; Kirkpatrick, R. J. *Phys. Chem. Miner.* **1996,** *23,* 56-62.

[313] Dove, M. T.; Pryde, A. K. A.; Heine, V.; Hammonds, K. D. *J. Phys: Condens. Matter* **2007,** *19,* 275209.

[314] Li, C. W.; Tang, X.; Muñoz, J. A.; Keith, J. B.; Tracy, S. J.; Abernathy, D. L.; Fultz, B. *Phys. Rev. Lett.* **2011,** *107,* 195504.

[315] Occhialini, C. A.; Guzmán-Verri, G. G.; Handunkanda, S. U.; Hancock, J. N. *Front. Chem.* **2018,** *6,* 545.

[316] Dove, M. T.; Du, J.; Wei, Z.; Keen, D. A.; Tucker, M. G.; Phillips, A. E. *Phys. Rev. B* **2020,** *102,* 094105.

[317] Dove, M. T.; Wei, Z.; Phillips, A. E.; Keen, D. A.; Refson, K. *APL Mater.* **2023,** *11,* 041130.

[318] Tan, L.; Heine, V.; Li, G.; Dove, M. T. *Rep. Prog. Phys.* **2024,** *87,* 126501.

[319] Dove, M. T. *Phil. Trans. R. Soc. A* **2019,** *377,* 20180222.

[320] Tealdi, C.; Lavrentiev, M. Y.; Mohn, C. E.; Allan, N. L. *J. Struct. Chem.* **2016,** *57,* 257-266.

[321] Metropolis, N.; Rosenbluth, A. W.; Rosenbluth, M. N.; Teller, A. H.; Teller, E. *J. Chem. Phys.* **1953,** *21,* 1087-1092.

[322] Kirkpatrick, S.; Gelatt, C. D.; Vecchi, M. P. *Science* **1983,** *220,* 671-680.

[323] Ferrenberg, A. M.; Swendsen, R. H. *Phys. Rev. Lett.* **1988,** *61,* 2635-2638.

[324] Landau, D. P.; Binder, K. *A Guide to Monte Carlo Simulations in Statistical Physics;* Cambridge University Press: Cambridge, 2015.

[325] Wilde, R. E.; Ghosh, S. N.; Marshall, B. J. *Inorg. Chem.* **1970,** *9,* 2512-2516.

[326] Siebert, H.; Weise, M. *Z. Naturforsch. B* **1975,** *30,* 33-39.

[327] Boström, H. L. B.; Brant, W. R. *J. Mater. Chem. C* **2022,** *10,* 13690-13699.

[328] Pasta, M.; Wang, R. Y.; Ruffo, R.; Qiao, R.; Lee, H. W.; Shyam, B.; Guo, M.; Wang, Y.; Wray, L. A.; Yang, W.; Toney, M. F.; Cui, Y. *J. Mater. Chem. A* **2016,** *4,* 4211-4223.

[329] Harbourne, E. A.; Barker, H.; Guéroult, Q.; Cattermull, J.; Nagle-Cocco, L. A. V.; Roth, N.; Evans, J. S. O.; Keen, D. A.; Goodwin, A. L. *Chem. Mater.* **2024,** *36,* 5796-5804.

[330] Soper, A. K. *Phys. Rev. B* **2005,** *72,* 104204.

[331] Tucker, M. G.; Goodwin, A. L.; Dove, M. T.; Keen, D. A.; Wells, S. A.; Evans, J. S. O. *Phys. Rev. Lett.* **2005,** *95,* 255501.

[332] Conterio, M. J.; Goodwin, A. L.; Tucker, M. G.; Keen, D. A.; Dove, M. T.; Peters, L.; Evans, J. S. O. *J. Phys.: Condens. Matter* **2008,** *20,* 255225.

[333] Soper, A. K.; Barney, E. R. *J. Appl. Crystallogr.* **2011,** *44,* 714-726.

[334] Gale, J. D. *J. Chem. Soc., Faraday Trans.* **1997,** *93,* 629-637.

[335] Gale, J. D.; Rohl, A. L. *Mol. Simul.* **2003,** *29,* 291-341.

[336] Clark, S. J.; Segall, M. D.; Pickard, C. J.; Hasnip, P. J.; Probert, M. I. J.; Refson, K.; Payne, M. C. *Z. Kristallogr.* **2005,** *220,* 567-570.

[337] Togo, A.; Chaput, L.; Tadano, T.; Tanaka, I. *J. Phys.: Condens. Matter* **2023,** *35,* 353001.

[338] Togo, A. *J. Phys. Soc. Jpn.* **2023,** *92,* 012001.

[339] Fair, R.; Jackson, A.; Voneshen, D.; Jochym, D.; Le, D.; Refson, K.; Perring, T. *J. Appl. Crystallogr.* **2022,** *55,* 1689-1703.

[340] Chapman, K. W.; Hagen, M.; Kepert, C. J.; Manuel, P. *Phys. B: Condens. Matter* **2006,** *385-386 I,* 60-62.

[341] Coelho, A.; Chater, P.; Kern, A. *J. Appl. Crystallogr.* **2015,** *48,* 869-875.

[342] Keen, D. A.; Tucker, M. G.; Dove, M. T. *J. Phys.: Condens. Matter* **2005,** *17,* S15.

[343] Playford, H. Y.; Owen, L. R.; Levin, I.; Tucker, M. G. *Annu. Rev. Mater. Res.* **2014,** *44,* 429-449.

[344] Cope, E. R.; Dove, M. T. *J. Appl. Crystallog.* **2007,** *40,* 589-594.

[345] Jeong, I.-K.; Proffen, T.; Mohiuddin-Jacobs, F.; Billinge, S. J. L. *J. Phys. Chem. A* **1999,** *103,* 921-924.

[346] Goodwin, A. L.; Tucker, M. G.; Dove, M. T.; Keen, D. A. *Phys. Rev. Lett.* **2004,** *93,* 075502.

[347] Goodwin, A. L.; Tucker, M. G.; Cope, E. R.; Dove, M. T.; Keen, D. A. *Phys. Rev. B* **2005,** *72,* 214304.

[348] Tallentire, S. E.; Child, F.; Fall, I.; Vella-Zarb, L.; Evans, I. R.; Tucker, M. G.; Keen, D. A.; Wilson, C.; Evans, J. S. O. *J. Am. Chem. Soc.* **2013,** *135,* 12849-12856.

[349] Wang, L.; Lu, Y.; Liu, J.; Xu, M.; Cheng, J.; Zhang, D.; Goodenough, J. B. *Angew. Chem. Int. Ed.* **2013,** *52,* 1964-1967.

[350] Maiti, N.; Meena, S. S.; Bhatt, P. *The Chemical Record* **2026,** e70187.

[351] Kugel, K. I.; Khomskiĭ, D. I. *Sov. Phys. Usp.* **1982,** *25,* 231-256.

[352] Khomskii, D.; Streltsov, S. *Chem. Rev.* **2021,** *121,* 2992-3030.

[353] Millis, A. J. *Nature* **1998,** *392,* 147-150.

[354] Halperin, B.; Englman, R. *Phys. Rev. B* **1971,** *3,* 1698-1708.

[355] Englman, R.; Halperin, B. *Phys. Rev. B* **1970,** *2,* 75-94.

[356] Félix, G.; Mikolasek, M.; Shepherd, H. J.; Long, J.; Larionova, J.; Guari, Y.; Itié, J.-P.; Chumakov, A. I.; Nicolazzi, W.; Molnár, G.; Bousseksou, A. *Eur. J. Inorg. Chem.* **2018,** *2018,* 443-448.

[357] Chippindale, A. M.; Hibble, S. J.; Marelli, E.; Bilbe, E. J.; Hannon, A. C.; Zbiri, M. *Dalton Trans.* **2015,** *44,* 12502-12506.

[358] Figgis, B. N.; Hitchman, M. A. *Ligand Field Theory and Its Applications;* WILEY-VCH: New York, 2000.

[359] Zhang, N.; Yokota, H.; Glazer, A. M.; Ren, Z.; Keen, D. A.; Keeble, D. S.; Thomas, P. A.; Ye, Z. G. *Nat. Commun.* **2014,** *5,* 5231.

[360] Zhang, N.; Yokota, H.; Glazer, A. M.; Keen, D. A.; Gorfman, S.; Thomas, P. A.; Ren, W.; Ye, Z. G. *IUCrJ* **2018,** *5,* 73-81.

[361] Browne, A. J.; Kimber, S. A.; Attfield, J. P. *Phys. Rev. Mater.* **2017,** *1,* 052003(R).

[362] Tragheim, B. R. M.; Ritter, C.; Senn, M. S. *Phys. Rev. B* **2024,** *110,* 235141.

[363] Tokoro, H.; Ohkoshi, S. I.; Matsuda, T.; Hashimoto, K. *Inorg. Chem.* **2004,** *43,* 5231-5236.

[364] Boström, H. L.; Cairns, A. B.; Chen, M.; Daisenberger, D.; Ridley, C. J.; Funnell, N. P. *Chem. Sci.* **2024,** *15,* 3155-3164.

[365] Meekel, E. G.; Partridge, P.; Paraoan, R. A.; Levinsky, J. J.; Slater, B.; Hobday, C. L.; Goodwin, A. L. *Nat. Mater.* **2024,** *23,* 1245-1251.

[366] Schmidt, E. M.; Klar, P. B.; Krysiak, Y.; Svora, P.; Goodwin, A. L.; Palatinus, L. *Nat. Commun.* **2023,** *14,* 6512.

[367] Poppe, R.; Roth, N.; Neder, R. B.; Palatinus, L.; Iversen, B. B.; Hadermann, J. *IUCrJ* **2024,** *11,* 82-91.

[368] Evans, N. L.; Thygesen, P. M.; Boström, H. L.; Reynolds, E. M.; Collings, I. E.; Phillips, A. E.; Goodwin, A. L. *J. Am. Chem. Soc.* **2016,** *138,* 9393-9396.

[369] Donlan, E. A.; Boström, H. L.; Geddes, H. S.; Reynolds, E. M.; Goodwin, A. L. *Chem. Commun.* **2017,** *53,* 11233-11236.

[370] Cliffe, M. J.; Lee, J.; Paddison, J. A. M.; Schott, S.; Mukherjee, P.; Gaultois, M. W.; Manuel, P.; Sirringhaus, H.; Dutton, S. E.; Grey, C. P. *Phys. Rev. B* **2018,** *97,* 144421.

[371] Tragheim, B. R. M.; Harbourne, E. A.; Ritter, C.; Goodwin, A. L.; Senn, M. S. *Phys. Rev. B* **2025,** *112,* 115119.

[372] Shannon, R. D. *Acta Cryst. A* **1976,** *32,* 751-767.

[373] Goodenough, J. B.; Wold, A.; Arnott, R. J.; Menyuk, N. *Phys. Rev.* **1961,** *124,* 373-384.

[374] Blasco, J.; García, J.; Campo, J.; Sánchez, M. C.; Subías, G. *Phys. Rev. B* **2002,** *66,* 174431.

[375] Cross, L. E. *Ferroelectrics* **1987,** *76,* 241-267.

[376] Lines, M. E.; Glass, A. M. *Principles and Applications of Ferroelectrics and Related Materials;* Clarendon Press: Oxford, 1977.

[377] Neumann, F. E.; Meyer, O. E. Vorlesungen über die Theorie der Elastizität der festen Körper und des Lichtäthers. In ; Leipzig, O. E. M.; Teubner-Verlag, B. G., Eds.; 1885.

[378] Clément, R. J.; Billaud, J.; Armstrong, A. R.; Singh, G.; Rojo, T.; Bruce, P. G.; Grey, C. P. *Energy Environ. Sci.* **2016,** *9,* 3240-3251.

[379] Lee, S.; Choi, S.; Kim, J.; Sim, H.; Won, C.; Lee, S.; Kim, S. A.; Hur, N.; Park, J.-G. *J. Phys.: Condens. Matter* **2012,** *24,* 456004.

[380] Baroudi, K. *et al. J. Solid State Chem.* **2014,** *210,* 195-205.

[381] Boivin, E.; House, R. A.; Pérez-Osorio, M. A.; Marie, J.-J.; Maitra, U.; Rees, G. J.; Bruce, P. G. *Joule* **2021,** *5,* 1267-1280.

[382] Sapnik, A. F. *et al. IUCrJ* **2025,** *12,* 531-547.

[383] Terban, M. W.; Billinge, S. J. *Chem. Rev.* **2022,** *122,* 1208-1272.

[384] Christiansen, T. L.; Cooper, S. R.; Jensen, K. M. Ø. *Nanoscale Adv.* **2020,** *2,* 2234-2254.

[385] Proffen, T. *Rev. Mineral. Geochem.* **2006,** *63,* 255-274.

[386] Kim, K. H. *et al. Nature* **2015,** *518,* 385-389.

[387] Redford, S. *et al. J. Instrum.* **2018,** *13,* C01027.

[388] Redford, S. *et al. J. Instrum.* **2020,** *15,* C02025.

[389] Kraus, D. *et al. Nature* **2025,** *642,* 351-355.

[390] Gorman, M. G. *et al. J. Appl. Phys.* **2024,** *135,* 165902.

[391] Støckler, L. J.; Christensen, R. S.; Kløve, M.; Bertelsen, A. D.; Borup, A. B.; Krause, L.; Takahashi, S.; Fujita, T.; Kasai, H.; Inoue, I.; Nishibori, E.; Iversen, B. B. *ChemPhysChem* **2023,** *24,* e202300407.

[392] Burns, N.; Rahemtulla, A.; Annett, S.; Moreno, B.; Kycia, S. *J. Appl. Crystallogr.* **2023,** *56,* 510-518.

[393] Appleby, G. A.; Pascarelli, S.; Pahl, D.; Tschentscher, T. *Synchrotron Radiat. News* **2017,** *30,* 6-8.

[394] Prencipe, I. *et al. High Power Laser Sci. Eng.* **2017,** *5,* e17.

[395] Juhás, P.; Davis, T.; Farrow, C.; Billinge, S. *J. Appl. Crystallogr.* **2013,** *46,* 560-566.

[396] Skinner, L. B.; Benmore, C. J.; Parise, J. B. *Nucl. Instrum. Methods Phys. Res. A* **2012,** *662,* 61-70.

[397] Marlton, F.; Ivashko, O.; Zimmerman, M. V.; Gutowski, O.; Dippel, A. C.; Jørgensen, M. R. V. *J. Appl. Crystallogr.* **2019,** *52,* 1072-1076.

[398] Tucker, M. G.; Dove, M. T.; Keen, D. A. *J. Appl. Crystallogr.* **2001,** *34,* 780-782.

[399] Pusztai, L.; McGreevy, R. L. *Phys. B: Condens. Matter* **1997,** *234-236,* 357-358.

[400] Hervé, M.; Privault, G.; Trzop, E.; Akagi, S.; Watier, Y.; Zerdane, S.; Chaban, I.; Ramírez, R. G. T.; Mariette, C.; Volte, A.; Cammarata, M.; Levantino, M.; Tokoro, H.; ichi Ohkoshi, S.; Collet, E. *Nat. Commun.* **2024,** *15,* 267.

[401] Ohkoshi, S. I.; Nakagawa, K.; Tomono, K.; Imoto, K.; Tsunobuchi, Y.; Tokoro, H. *J. Am. Chem. Soc.* **2010,** *132,* 6620-6621.

[402] Kosaka, W.; Nomura, K.; Hashimoto, K.; ichi Ohkoshi, S. *J. Am. Chem. Soc.* **2005,** *127,* 8590-8591.

[403] Boström, H. L. B.; Cairns, A. B.; Liu, L.; Lazor, P.; Collings, I. E. *Dalton Trans.* **2020,** *49,* 12940-12944.

[404] ichi Ohkoshi, S.; Tokoro, H.; Hashimoto, K. *Coord. Chem. Rev.* **2005,** *249,* 1830-1840.

[405] Ferlay, S.; Mallah, T.; Ouahès, R.; Veillet, P.; Verdaguer, M. *Nature* **1995,** *378,* 701-703.

[406] Thygesen, P. M. M.; Paddison, J. A. M.; Zhang, R.; Beyer, K. A.; Chapman, K. W.; Playford, H. Y.; Tucker, M. G.; Keen, D. A.; Hayward, M. A.; Goodwin, A. L. *Phys. Rev. Lett.* **2017,** *118,* 067201.

[407] Greedan, J. E.; Gout, D.; Lozano-Gorrin, A. D.; Derahkshan, S.; Proffen, T.; Kim, H.-J.; Božin, E.; Billinge, S. J. L. *Phys. Rev. B* **2009,** *79,* 014427.

[408] Matsuda, T.; Kim, J.; Moritomo, Y. *Dalton Trans.* **2012,** *41,* 7620-7623.

Appendix A: Local structure and dynamics in $MPt(CN)_6$ Prussian blue analogues

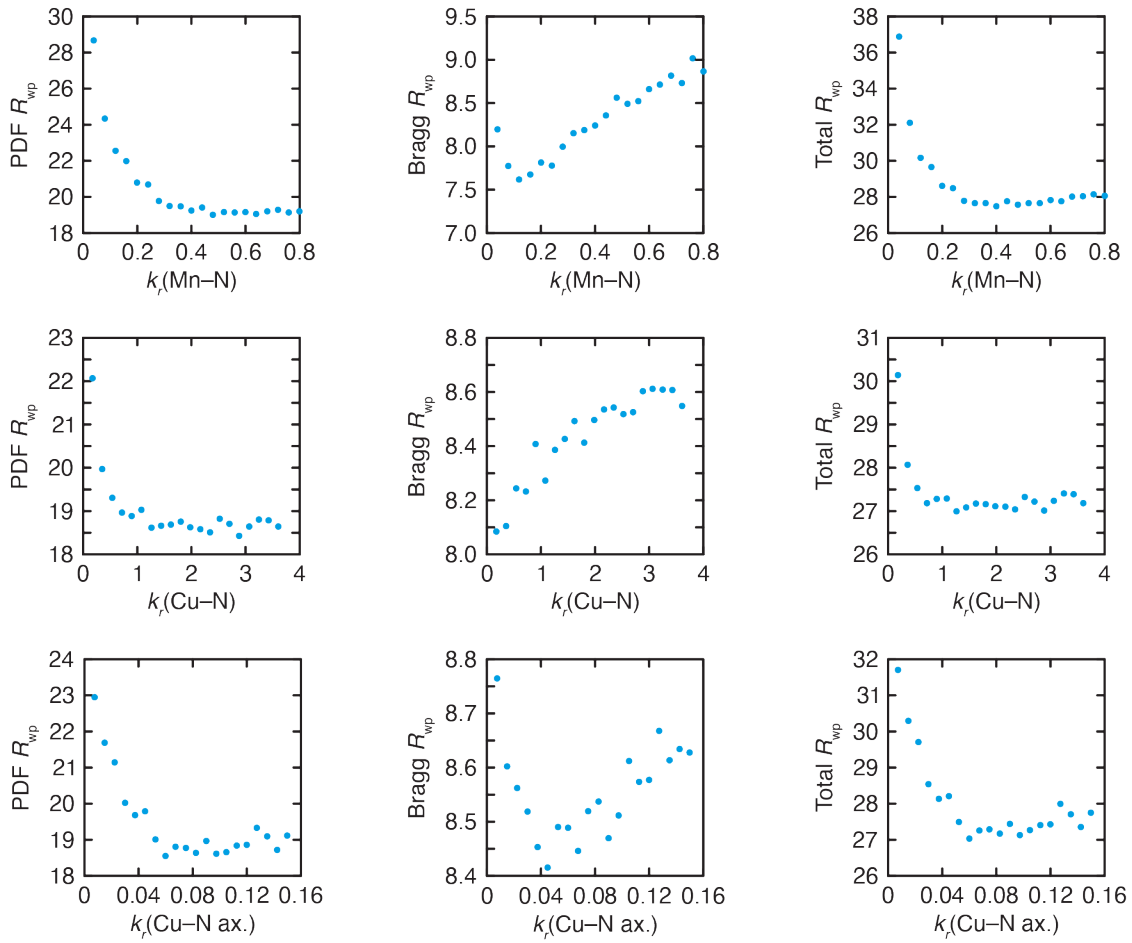


Figure A0.1: Goodness-of-fit as a function of k_r(M–N).

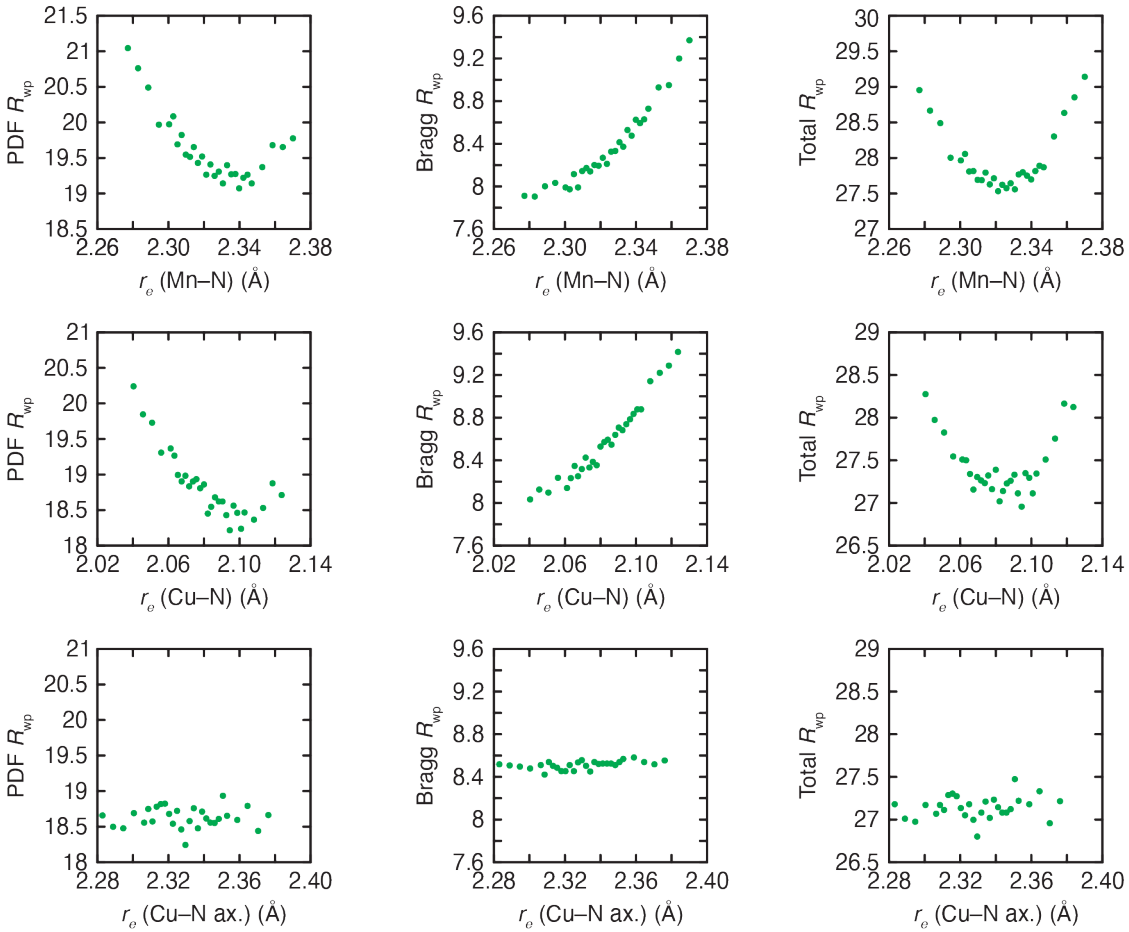


Figure A0.2: Goodness-of-fit as a function of r_{e}(M–N).

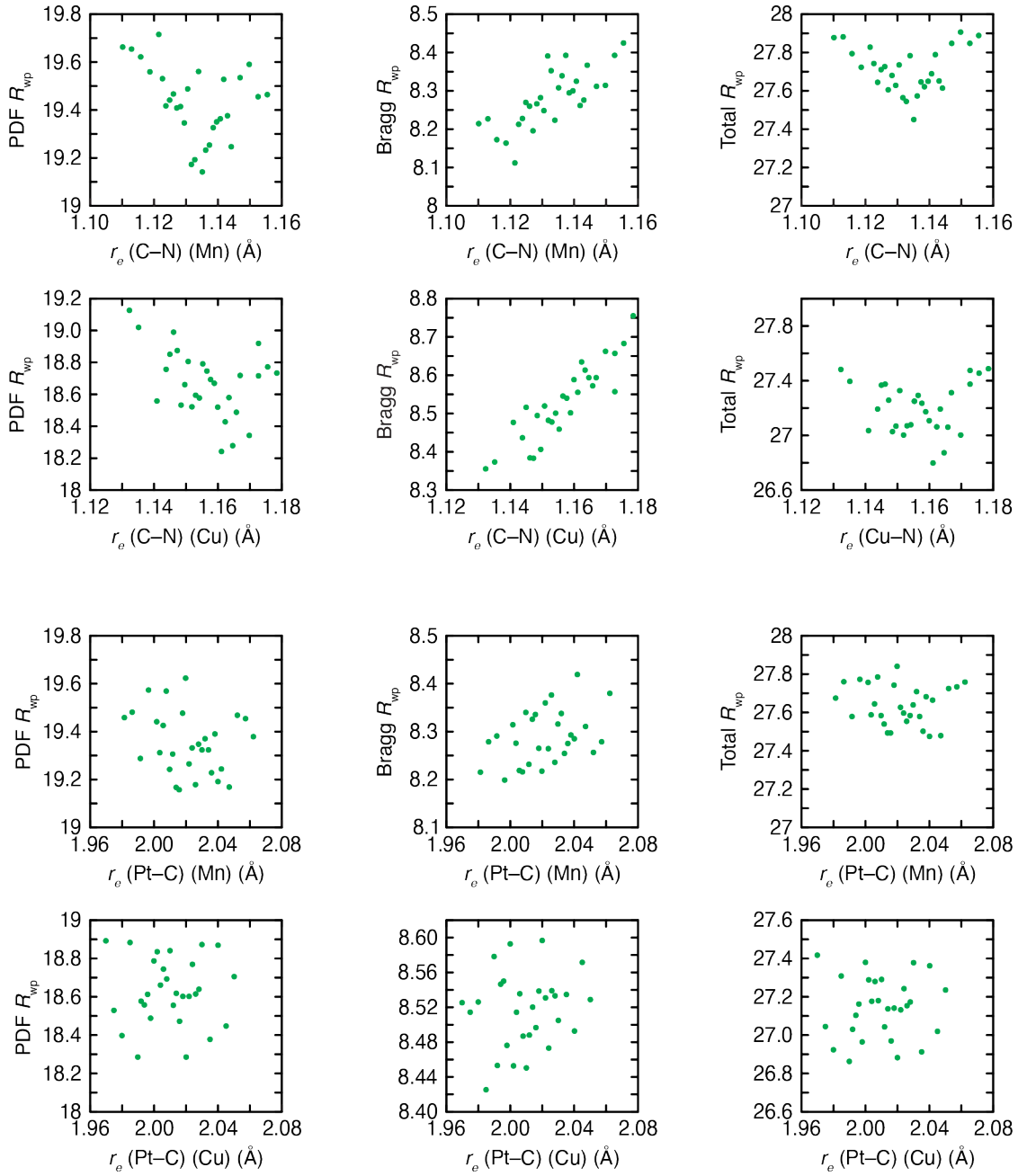


Figure A0.3: Goodness-of-fit as a function of r_{e}(C–X).

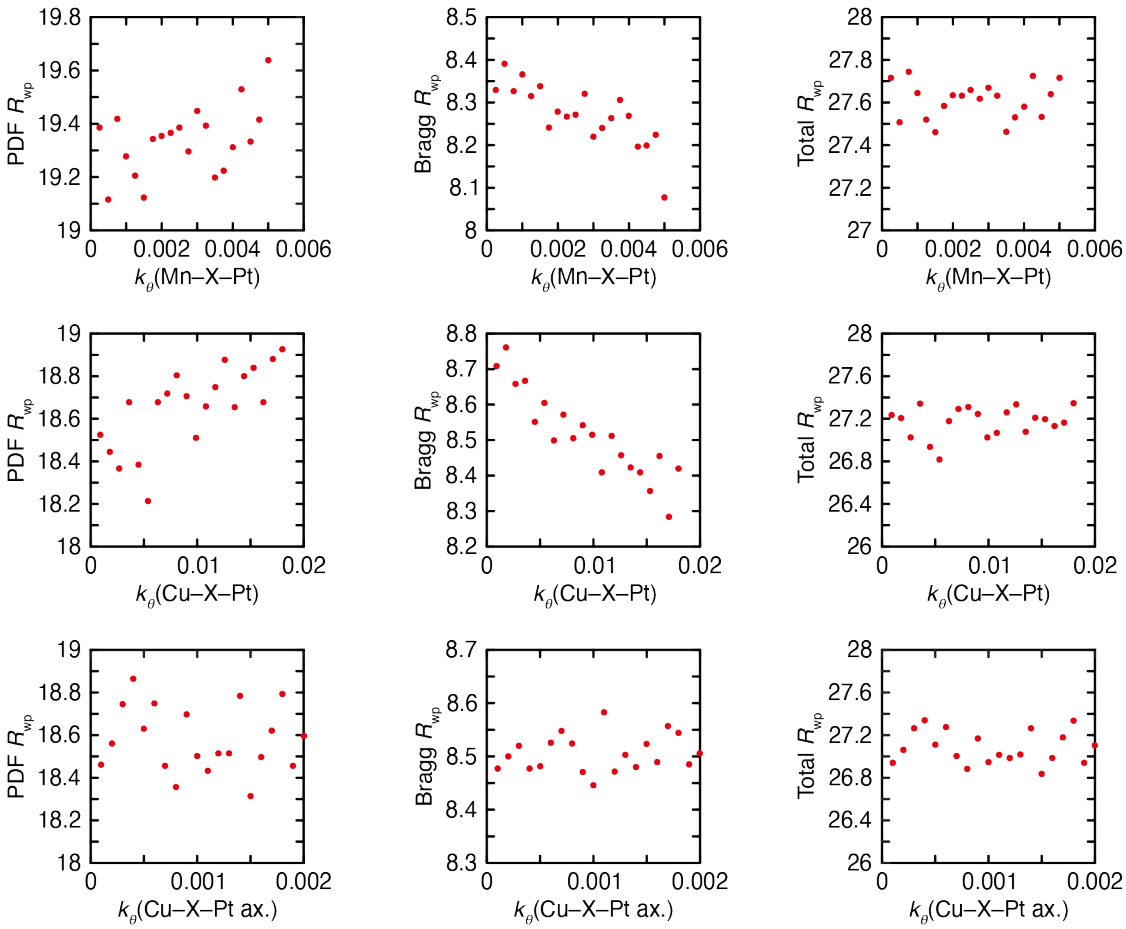


Figure A0.4: Goodness-of-fit as a function of k_θ(M–X–Pt).

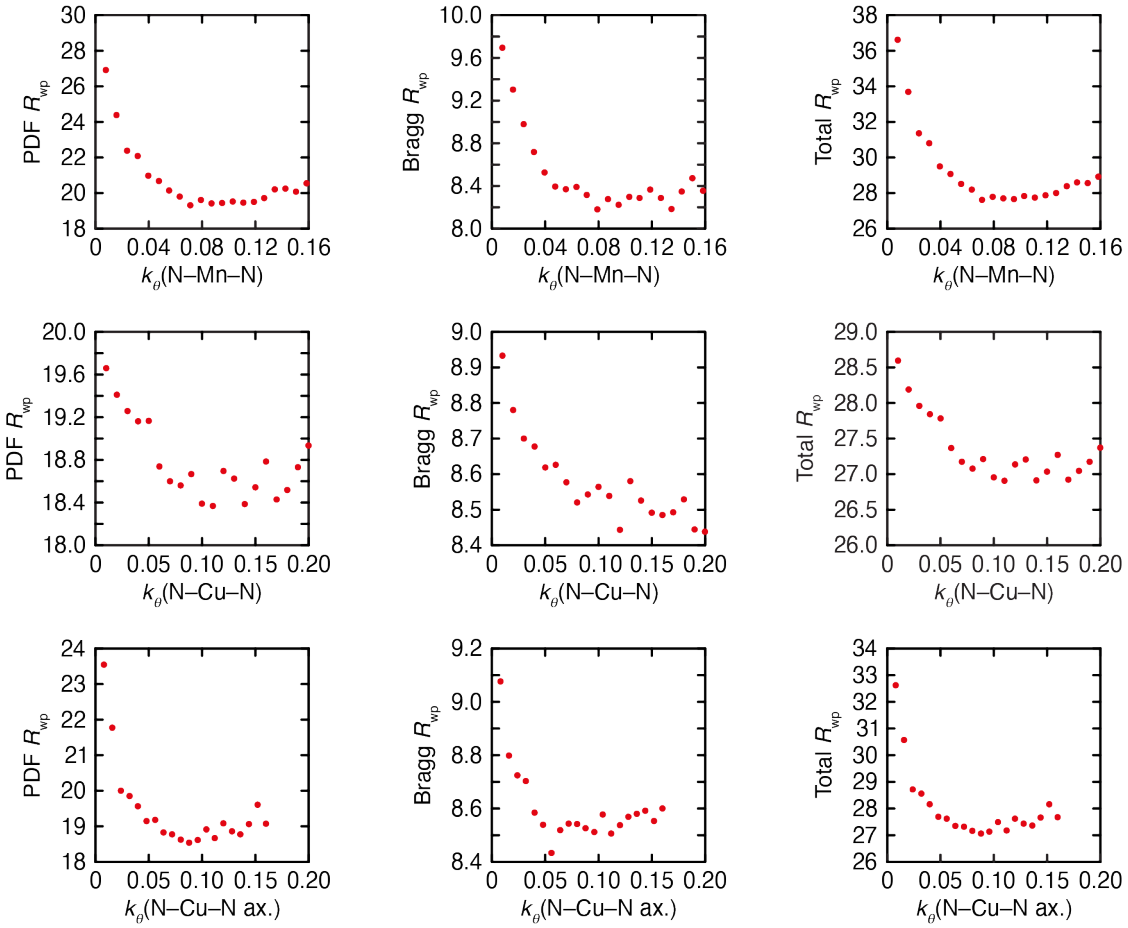


Figure A0.5: Goodness-of-fit as a function of k_θ(N–M–N).

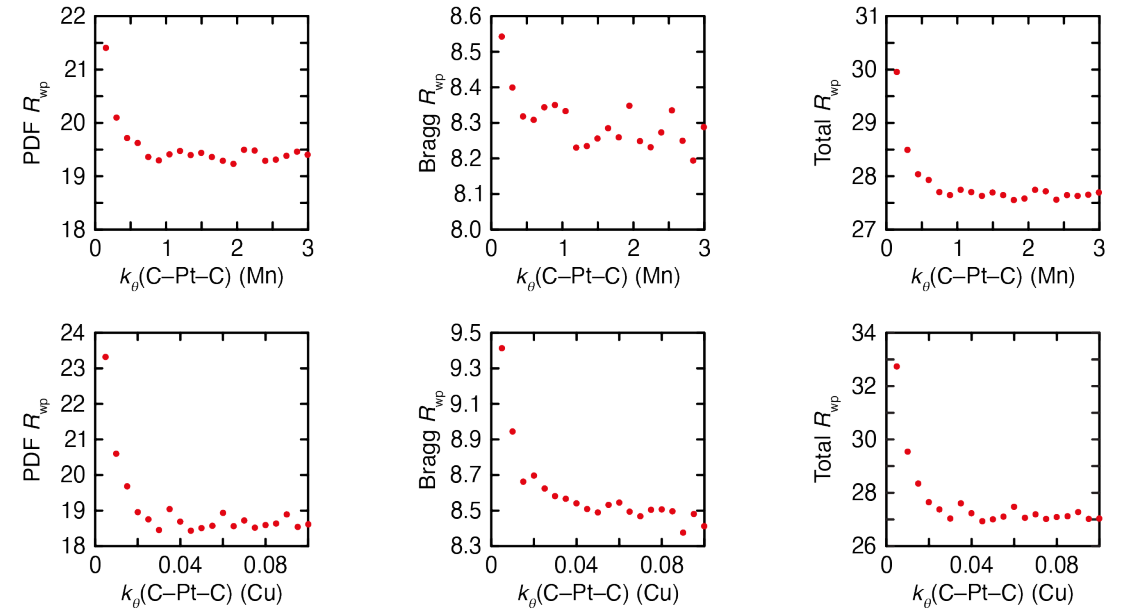


Figure A0.6: Goodness-of-fit as a function of k_θ(C–Pt–C).

Crystallographic details of the average structures formed by projections of these MC configurations are described in Tables A0.1 and A0.2. For the case of $CuPt(CN)_6$ we give our results in terms of the standard space-group setting $I4/mmm$, but note that our refinements were carried out using the non-standard $F4/mmm$ setting as described in the text.

Table A0.1: Crystallographic parameters for the structure of $MnPt(CN)_6$ at ambient temperature and pressure. The experimental data were collected at I15-1 beamline, Diamond Light Source, using a wavelength of $\lambda = 0.1617$ Å.

Space group	$Fm\bar{3}m$								
a/Å	10.74419(11)								
V/Å^3	1240.28(4)								
Z	4								
R_{wp}/% (Bragg)	8.31								
R_{wp}/% (PDF)	19.14								
Atom	x		y	z	U_{11}/Å^2	U_{22}/Å^2	U_{33}/Å^2	U_{23}/Å^2	U_{13}/Å^2	U_{12}/Å^2
Pt	0		0	0	0.00961(9)	0.00961	0.00961	0	0	0
Mn	0.5		0	0	0.01118(11)	0.01118	0.01118	0	0	0
C	0.18642(7)		0	0	0.01016(10)	0.0417(3)	0.0417	0	0	0
N	0.29122(7)		0	0	0.01029(10)	0.0884(6)	0.0884	0	0	0

Table A0.2: Crystallographic parameters for the structure of $CuPt(CN)_6$ at ambient temperature and pressure. The experimental data were collected at I15-1 beamline, Diamond Light Source, using a wavelength of $\lambda = 0.1617$ Å.

Space group	$I4/mmm$								
a/Å	7.27638(11)								
c/Å	11.0245(3)								
V/Å^3	583.70(2)								
Z	2								
R_{wp}/% (Bragg)	8.31								
R_{wp}/% (PDF)	19.14								
Atom	x	y	z	U_{11}/Å^2	U_{22}/Å^2	U_{33}/Å^2	U_{23}/Å^2	U_{13}/Å^2	U_{12}/Å^2
Pt	0	0	0	0.00784(9)	0.00784	0.0196(3)	0	0	0
Cu	0.5	0.5	0	0.00822(10)	0.00822	0.0211(4)	0	0	0
C1	0.19091(7)	0.19091	0	0.0229(2)	0.0229	0.0435(5)	0	0	−0.0151(2)
N1	0.30286(7)	0.30286	0	0.0466(5)	0.0466	0.0840(9)	0	0	−0.0388(5)
C2	0	0	0.18109(16)	0.0340(4)	0.0340	0.0210(4)	0	0	0
N2	0	0	0.28569(16)	0.0745(8)	0.0745	0.0211(4)	0	0	0

Appendix B: Rules governing Jahn–Teller order in Prussian blue analogues

B1 Synthesis and characterisation

B1.1 $Cu_xMn_{1-x}[Pt(CN)_6]$ series

Polycrystalline samples of $Cu_xMn_{1-x}[Pt(CN)_6]$ were prepared by the dropwise addition of aqueous solutions of $CuSO_4 \cdot nH_2O$ and $MnSO_4 \cdot nH_2O$ (total of 0.5 mmol, 0.5 mL) to an aqueous solution containing $K_2[Pt(CN)_6]$ (0.5 mmol, 0.5 mL). A precipitate instantly formed and the reaction mixture was stirred for 2 h at 60°C and 2 h at room temperature. The product was isolated as a fine powder by filtration in vacuo and dried in air. The sample colour varied from white to blue-green as a function of the Cu^{2+} content. In order to determine sample compositions, atomic absorption spectroscopy (AAS) was performed on all samples using a Varian AA240FS spectrometer, equipped with Perkin Elmer ATOMAX hollow cathode lamps. The lamp current was 5–10 mA and the fuel a mixture of air and acetylene. The samples were dissolved in small amounts of concentrated hydrochloric acid and diluted with deionised water. The metal concentration of each sample was determined against a calibration curve prepared using at least four reference solutions, which had been

diluted from the appropriate stock solution ($1\,\mathrm{g\,L^{-1}}$). Each sample was measured at least three times per metal and the uncertainties calculated based on the standard deviation of the repeated measurements. The compositions so determined are given in Table B1.3.

Table B1.3: Atomic absorption spectroscopy data for each $Cu_xMn_{1-x}[Pt(CN)_6]$ sample, together with the corresponding compositions determined in Rietveld refinements of X-ray powder diffraction measurements.

x_{nom}	x_{AAS}	x_{PXRD}
0	0	0
0.1	0.005(19)	−0.00043(2)
0.2	0.371(10)	0.490(6)
0.3	0.480(8)	0.646(6)
0.4	0.563(8)	0.698(5)
0.5	0.691(18)	0.828(5)
0.6	0.976(2)	0.982(2)
0.7	0.988(3)	0.995(2)
0.8	0.991(2)	0.986(2)
0.9	0.997(2)	1.013(4)
1	1	1

B1.2 $Cs_xCu[Fe(CN)_6]_{(2+x)/3}$ series

The synthesis of $Cs_xCu[Fe(CN)_6]_{(2+x)/3}$ followed the method of Ref. 408. Samples were prepared by the dropwise addition of an aqueous solution of $CuSO_4 \cdot nH_2O$ (0.5 mmol, 100 mL) to an aqueous solution containing $K_3Fe(CN)_6$ (0.5 mmol, 100 mL). Both solutions also contained an amount of CsCl that determined the amount of Cs in the final product. CsCl concentrations of 0, 1, 5, 10, 15, 20, 25, 30, 40, 50, 100, 500 $\mathrm{mmol\,L^{-1}}$ were used to prepare the series of samples. A precipitate instantly formed and the reaction mixture was stirred for 24 h at room temperature. The product was isolated as a fine powder by centrifugation and dried in air. The colour of the hexacyanoferrates varied from dark brown to yellowish brown with increasing Cs concentration and lower vacancy concentration.

The composition—and, hence, vacancy content—of the samples was verified by inductively coupled plasma mass spectrometry (ICP-MS). Each sample was digested

in concentrated HCl and then diluted in 2% nitric acid to target a final Cu concentration of approximately 70 parts per billion (ppb). Calibration for Cu, and Fe compositions was achieved through a series of standard nitrate solutions (Certipur, Merck) of known compositions; we used final concentrations of 0, 5, 10, 20, 40, 60, 80, 100 ppb. For our samples and for each standard solution, the corresponding Cu and Fe compositions were determined using a Shimadzu ICPMS-2030 spectrometer coupled with a mini torch and an AS-10 autosampler. A helium collision cell was used to remove interfering polyatomic species. Measurements were performed in triplicate, with washing runs carried out between successive measurements. The measured ICP-MS intensities for the $Cs_xCu[Fe(CN)_6]_{(2+x)/3}$ samples are given in Table B1.4, along with the concentration of CsCl used in the synthesis. The ratio of Fe/Cu gives an estimate of $(2 + x)/3$ in $Cs_xCu[Fe(CN)_6]_{(2+x)/3}$. The samples with low vacancy content were more challenging to digest which is reflected in the lower concentrations of metals found.

Table B1.4: Average ICP-MS data for each $Cs_xCu[Fe(CN)_6]_{(2+x)/3}$ sample. All measurements were made in triplicate, and errors correspond to the corresponding uncertainty in the mean value. For the single measurement marked with an asterisk, all three measurements gave the same numerical result so we do not quote an uncertainty here.

CsCl concentration ($\mathrm{mmol\,L^{-1}}$)	ρ(Cu 65) ($\mu\mathrm{g\,L^{-1}}$)	ρ(Fe 56) ($\mu\mathrm{g\,L^{-1}}$)	x	x_{vac}
0	68.37(6)	40.57(6)	0.066(3)	0.3113(11)
1	69.33(12)	45.60*	0.290(4)	0.2366(13)
5	59.1(5)	40.5(2)	0.39(2)	0.204(8)
10	63.5(4)	44.2(3)	0.424(18)	0.192(6))
15	63.1(2)	43.8(1)	0.418(9)	0.194(3)
20	60.9(2)	43.8(2)	0.502(15)	0.166(5)
25	59.4(3)	44.2(1)	0.589(12)	0.137(4)
30	55.7(5)	44.7(4)	0.80(4)	0.068(12)
40	50.7(1)	40.4(3)	0.77(2)	0.076(8)
50	35.9(2)	29.0(2)	0.808(18)	0.064(6)
100	37.5(2)	30.2(2)	0.81(2)	0.064(8)
500	33.5(2)	28.5(2)	0.96(2)	0.012(8)

B1.3 $Cu_xMn_{1-x}[Co(CN)_6]_{2/3}$ series

Polycrystalline $Cu_xMn_{1-x}[Co(CN)_6]_{2/3}$ samples were prepared by the dropwise addition of an aqueous solution of $CuSO_4 \cdot nH_2O$ and $MnSO_4 \cdot nH_2O$ in the required ratio (total of 0.5 mmol, 0.5 mL) to an aqueous solution containing $K_3Co(CN)_6$ (0.33 mmol, 0.5 mL). A precipitate instantly formed and the reaction mixture was stirred for 1 h at 60°C and 1 h at room temperature. The product was isolated as a fine powder by filtration *in vacuo* and dried in air. The colour of the hexacyanocobaltates varied from white to blue with increasing Cu^{2+} concentration. Because the series formed a solid solution, the Mn/Cu compositions were estimated using Vegard's law following Rietveld refinement of X-ray powder diffraction patterns.

B2 Powder X-ray diffraction

B2.1 Measurements

Our powder X-ray diffraction data made use of the synchrotron X-ray source on the I11 beamline at Diamond Light Source, UK. The diffraction patterns of the sample were collected in capillary transmission geometry. A room temperature X-ray diffraction pattern was collected using the Mythen2 Position Sensitive Detector (PSD), two data collections of 20 seconds each were taken at angles 0.25 degrees apart, then summed to account for gaps in the detector coverage. The X-ray wavelengths used were 0.826060 and 0.825070 Å.

B2.2 Refinement details: $Cu_xMn_{1-x}[Pt(CN)_6]$ series

The structural refinements for the $Cu_xMn_{1-x}[Pt(CN)_6]$ samples series were performed using Rietveld refinement in TOPAS software.[282] The PXRD patterns for each end member ($Mn[Pt(CN)_6]$ and $Cu[Pt(CN)_6]$) were refined using the reported structures from Ref.[134] as a starting point. Lattice parameters and the positions

Table B2.5: Crystallographic details for the $Fm\bar{3}m$ structure of $Mn[Pt(CN)_6]$

a(Å)	10.75392(3)			
V (Å^3)	1243.655(10)			
Z	4			
Atom	x	y	z	B_{eq} (Å^2)
C	0.1959(5)	0.0	0.0	0.614(14)
Mn	0.5	0.0	0.0	0.614(14)
N	0.2977(5)	0.0	0.0	0.614(14)
Pt	0.0	0.0	0.0	0.614(14)

Table B2.6: Crystallographic details for the $I4/mmm$ structure of $Cu[Pt(CN)_6]$

a(Å)	7.276060(14)			
c(Å)	11.02880(4)			
V (Å^3)	583.876(3)			
Z	2			
Atom	x	y	z	B_{eq} (Å^2)
C1	0.3050(5)	0.3050(5)	0.0	0.452(11)
C2	0.0	0.0	0.3189(6)	0.452(11)
Cu	0.0	0.0	0.0	0.452(11)
N1	0.1944(3)	0.1944(3)	0.0	0.452(11)
N2	0.0	0.0	0.2125(5)	0.452(11)
Pt	0.5	0.5	0.0	0.452(11)

of the C and N atoms were allowed to refine. A common atomic displacement parameter for all atoms was also refined along with a Thompson Cox pseudo-Voigt peakshape model. The structures are reported in Tables B2.5 and B2.6.

The powder X-ray diffraction patterns for the intermediate compositions were refined using a constrained mixed phase model. The structures for the end members were used as starting points where the lattice parameters were allowed to refine. The resulting cell volume was used to constrain the Cu/Mn composition in each structure subject to the following equation:

$$\begin{aligned} \mathrm{Occ}_{\mathrm{Cu}} &= \frac{V_{x=0} - V_x}{V_{x=0} - V_{x=1}}, \\ \mathrm{Occ}_{\mathrm{Mn}} &= 1 - \mathrm{Occ}_{\mathrm{Cu}}. \end{aligned} \tag{B2.1}$$

The resulting total Cu compositions, determined from these occupancies and the corresponding phase fractions, are compared against AAS values in Table B1.3.

For each unit cell, the C and N positions were refined, a common B_{eq} was used for all atoms, and a Lorentzian strain term was used to account for isotropic strain broadening from the fixed Thompson Cox pseudo-Voigt peakshape model. The resulting fits obtained using Rietveld refinement are shown in Fig. B2.7.

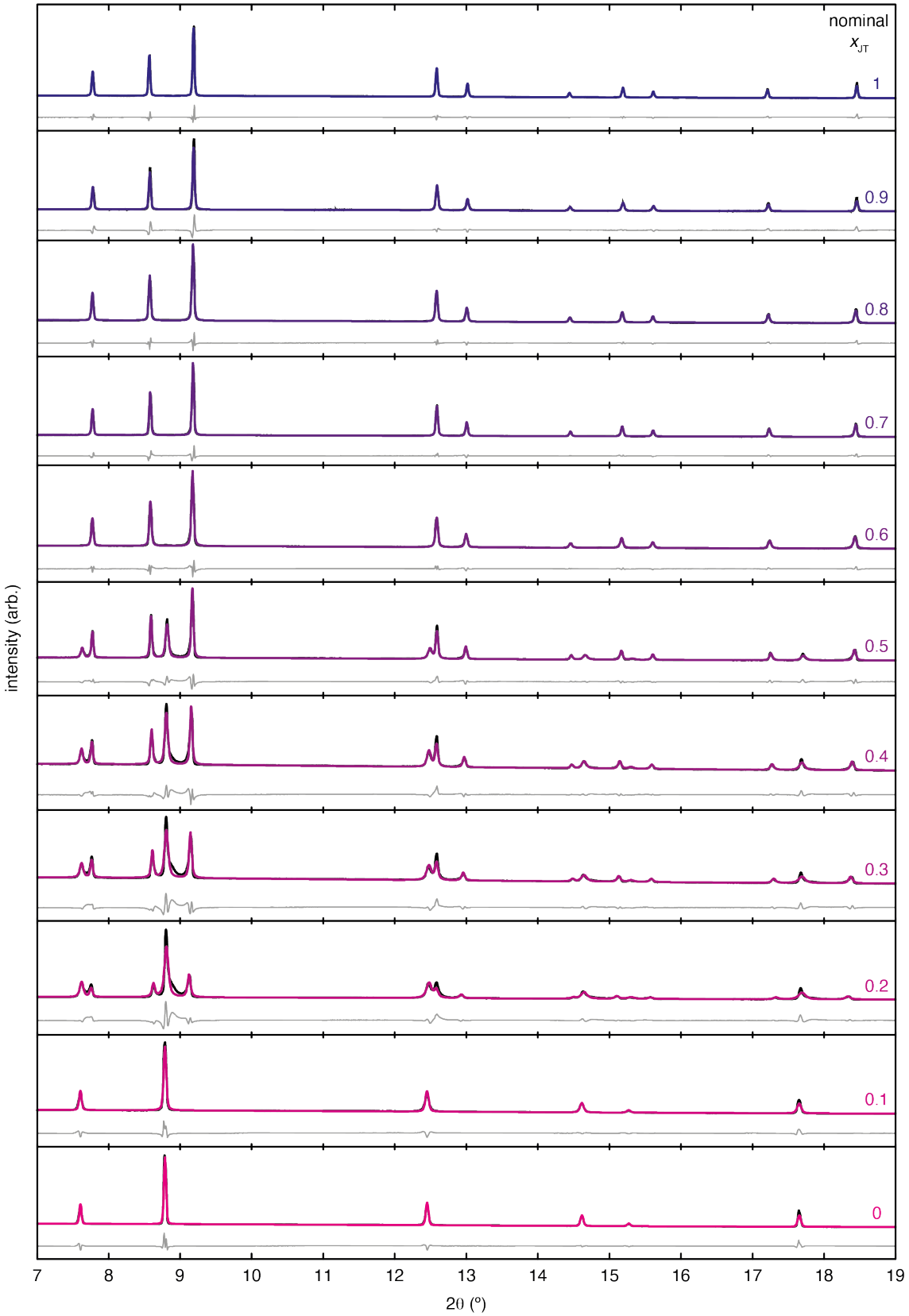


Figure B2.7: Synchrotron X-ray powder diffraction patterns ($\lambda = 0.825070\,\text{Å}$) of $Cu_xMn_{1-x}[Pt(CN)_6]$ (black lines) and corresponding Rietveld fits (coloured lines). The difference (data−fit) is shown as a grey curve shifted vertically.

B2.3 Refinement details: $Cu_xMn_{1-x}[Co(CN)_6]_{2/3}$ series

The structural refinements for the $Cu_xMn_{1-x}[Co(CN)_6]_{2/3}$ series were performed using Pawley refinement in TOPAS software.[282] All PXRD patterns were refined using cubic unit cell(s) in the $Fm\bar{3}m$ space group, as previously reported in Ref.[134]. Lattice parameters and a Thompson Cox pseudo-Voigt peakshape were allowed to refine for $Mn[Co(CN)_6]_{2/3}$, the sharpest diffraction pattern. For all other compositions, a Lorentzian strain term was used to account for variation in peakshape broadening, and in the case of $0.2 \leq x_{\mathrm{JT}} \leq 0.6$ two unit cells were refined. The resulting fits are shown in Fig. B2.8.

B2.4 Powder diffraction patterns of $Cs_xCu[Fe(CN)_6]_{(2+x)/3}$

The X-ray powder diffraction patterns measured for $Cs_xCu[Fe(CN)_6]_{(2+x)/3}$ samples are shown in Fig. B2.9. Given the complexity of the peak shapes, we do not report Rietveld refinements here. The diffraction patterns are consistent with a solid-solution of cubic and tetragonal PBA phases, albeit with some severe peak broadening as discussed at the critical compositions for CJT order. In order to generate the peak profiles shown in Fig. 4.11 in Chapter 4, the regions of the diffraction patterns around the (220) reflection were isolated (*i.e.* near 13° in 2θ), a linear background subtracted, and the centre-of-mass determined. The data were then transformed from scattering angle to reciprocal lattice units such that the centre of mass occurred at the high-symmetry position $2\sqrt{2}$. This processing allowed us to deconvolute the effect of composition-dependent variations in unit cell parameters for direct comparison against the MC simulations.

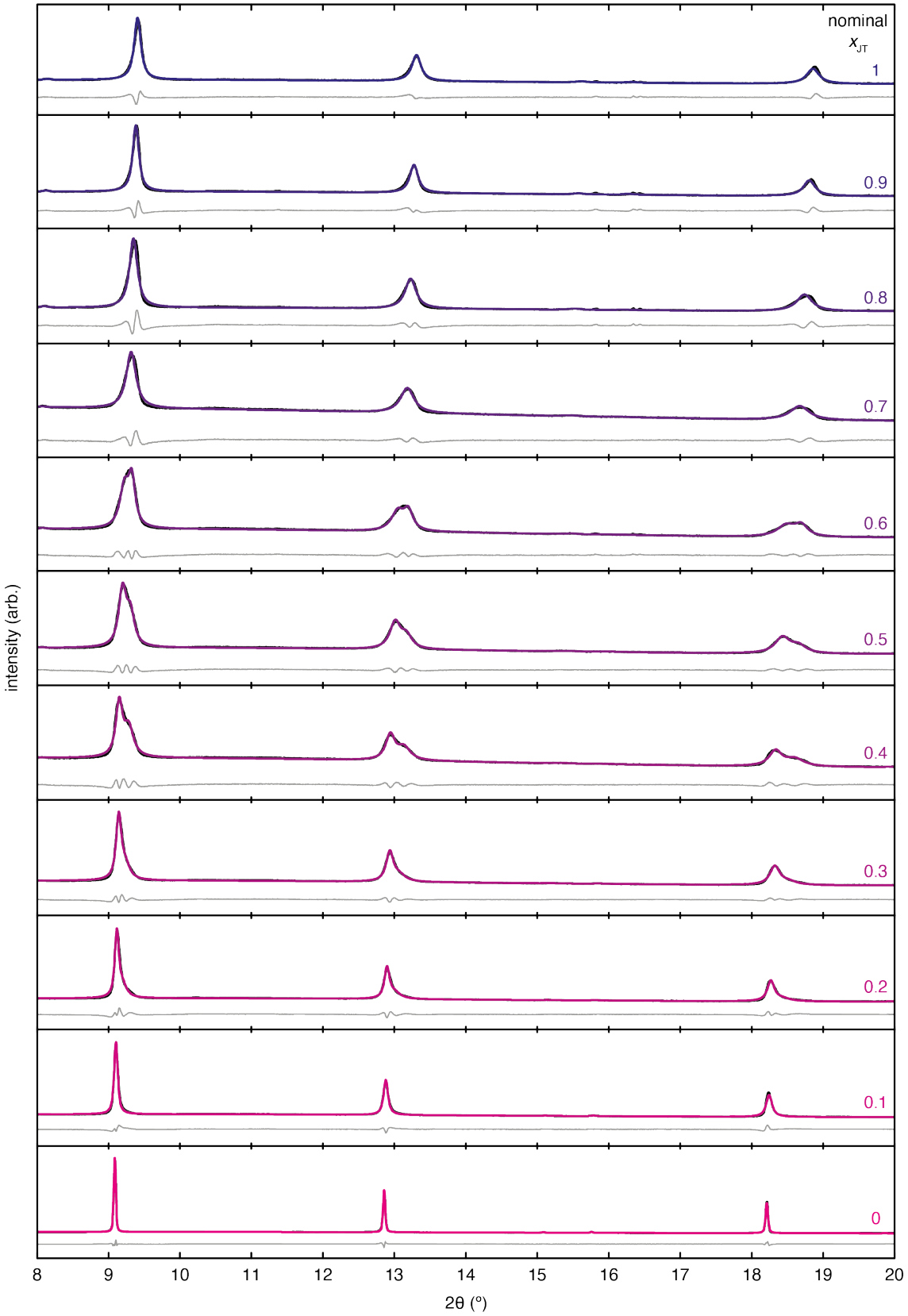


Figure B2.8: Synchrotron X-ray powder diffraction patterns ($\lambda = 0.825070$ Å) of $Cu_xMn_{1-x}[Co(CN)_6]_{2/3}$ (black lines) and corresponding Rietveld fits (coloured lines). The difference (data−fit) is shown as a grey curve shifted vertically.

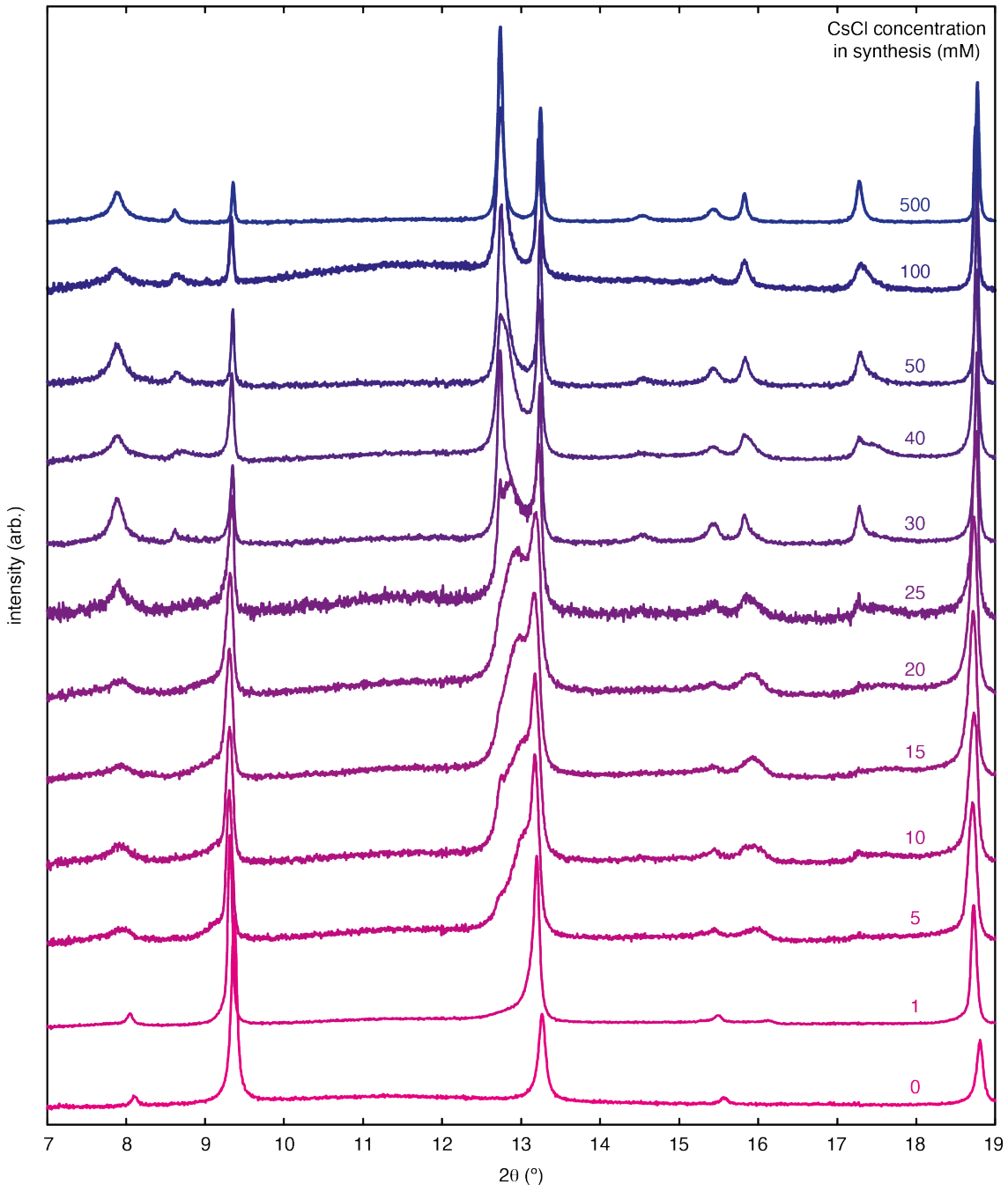


Figure B2.9: Synchrotron X-ray powder diffraction patterns ($\lambda = 0.826060\,\text{Å}$) of $Cs_xCu[Fe(CN)_6]_{(2+x)/3}$.

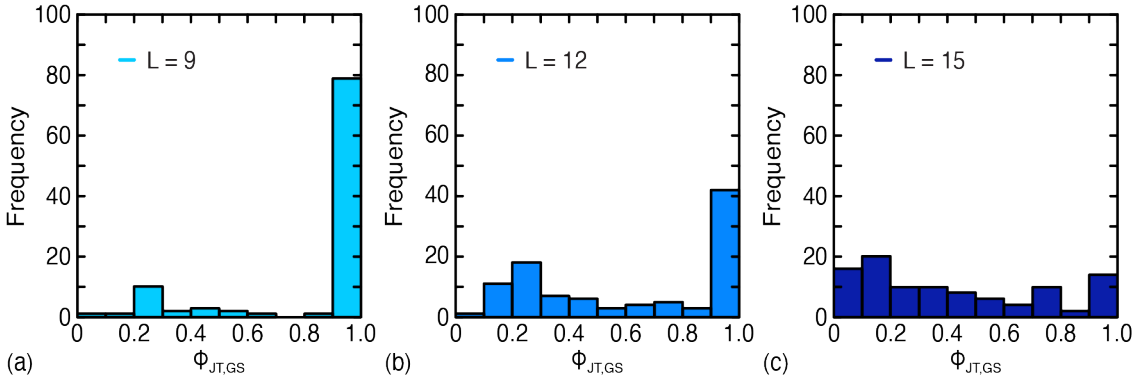


Figure B3.10: Distribution of the ground state order parameter, $\phi_{\mathrm{JT,GS}}$, for the composition $x_{\mathrm{vac}} = 1/3$, $x_{\mathrm{JT}} = 1$, for (a) $9 \times 9 \times 9$, (b) $12 \times 12 \times 12$, and (c) $15 \times 15 \times 15$ supercells. Strain-only model (no crystal-field term).

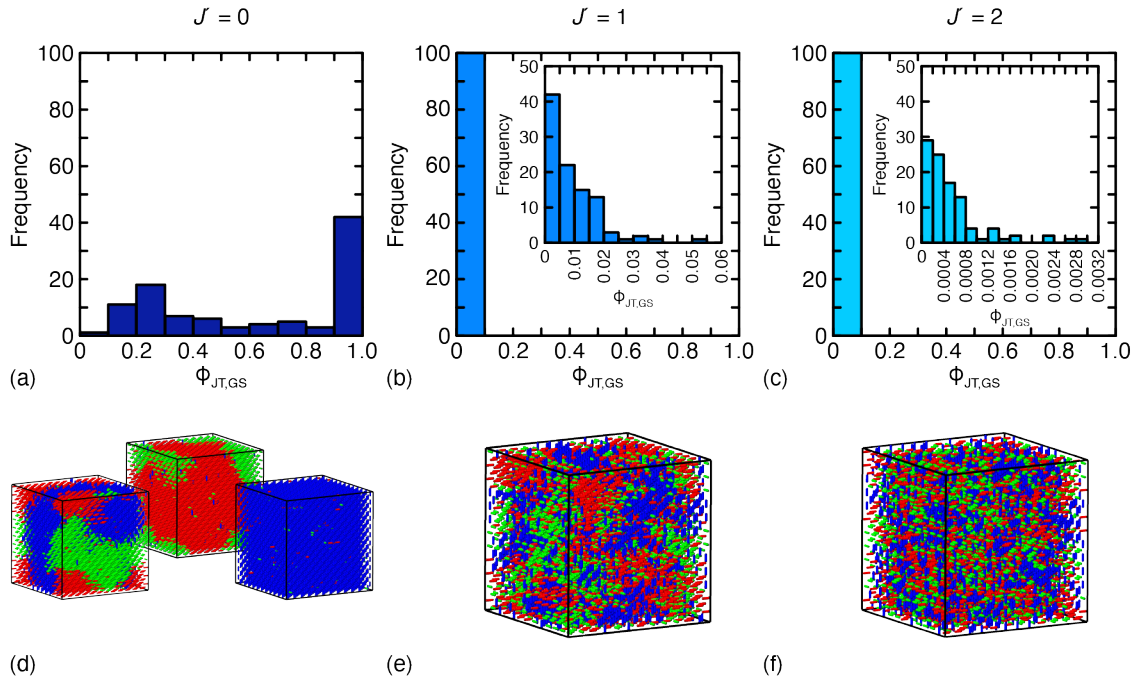


Figure B3.11: Distribution of the ground state order parameter, $\phi_{\mathrm{JT,GS}}$, for $12 \times 12 \times 12$ supercells with the composition $x_{\mathrm{vac}} = 1/3$, $x_{\mathrm{JT}} = 1$, for (a) $J' = 0$, (b) $J' = 1$, and (c) $J' = 2$. Examples of $12 \times 12 \times 12$ supercells for (d) $J' = 0$, (e) $J' = 1$, and (f) $J' = 2$.

B3 Monte Carlo simulations

Appendix C: The interplay between Jahn–Teller distortions and structural degrees of freedom in manganite perovskites

C1 $LaGa_{1-x}Mn_xO_3$: Monte Carlo simulations

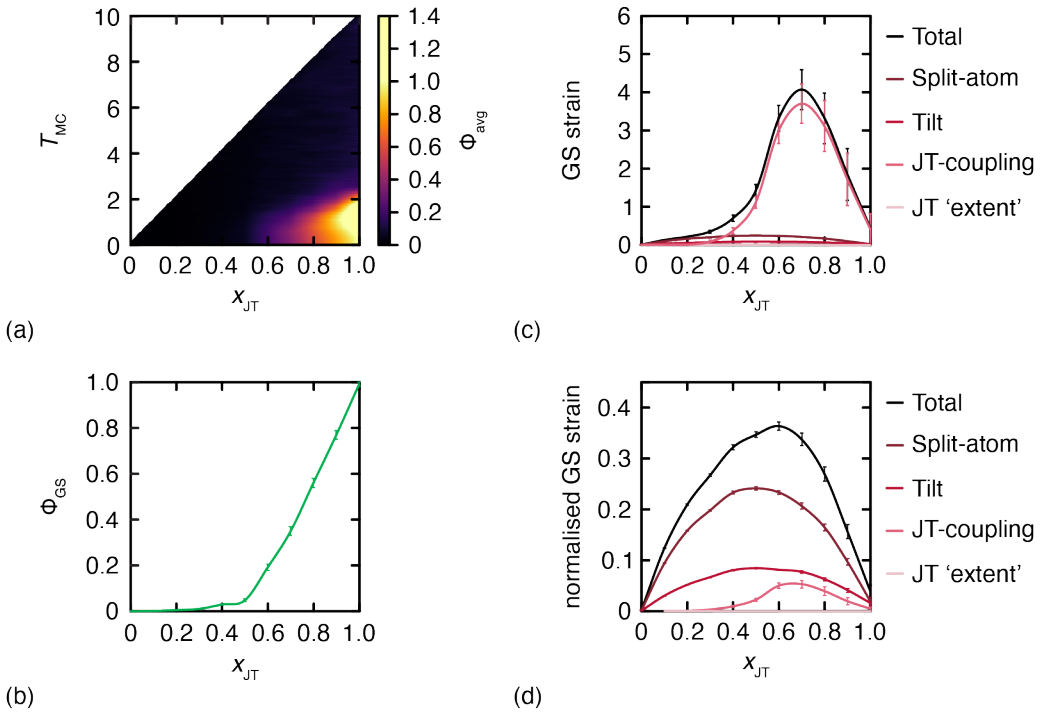


Figure C1.12: Fixed-box MC simulations (where the supercell is not allowed to shear) of 10×10 supercells of the $LaGa_{1-x}Mn_xO_3$ system as a function of JT concentration x_{JT}. (a) The evolution of the JT order parameter, ϕ_{avg}, during simulated annealing, averaged over 100 independent runs. (b) The ground state JT order parameter, ϕ_{GS} as function of JT concentration x_{JT}. (c) The contribution from the split-atom, tilt, JT-coupling, and JT 'extent' terms to the ground state strain and (d) normalised to x_{JT}.

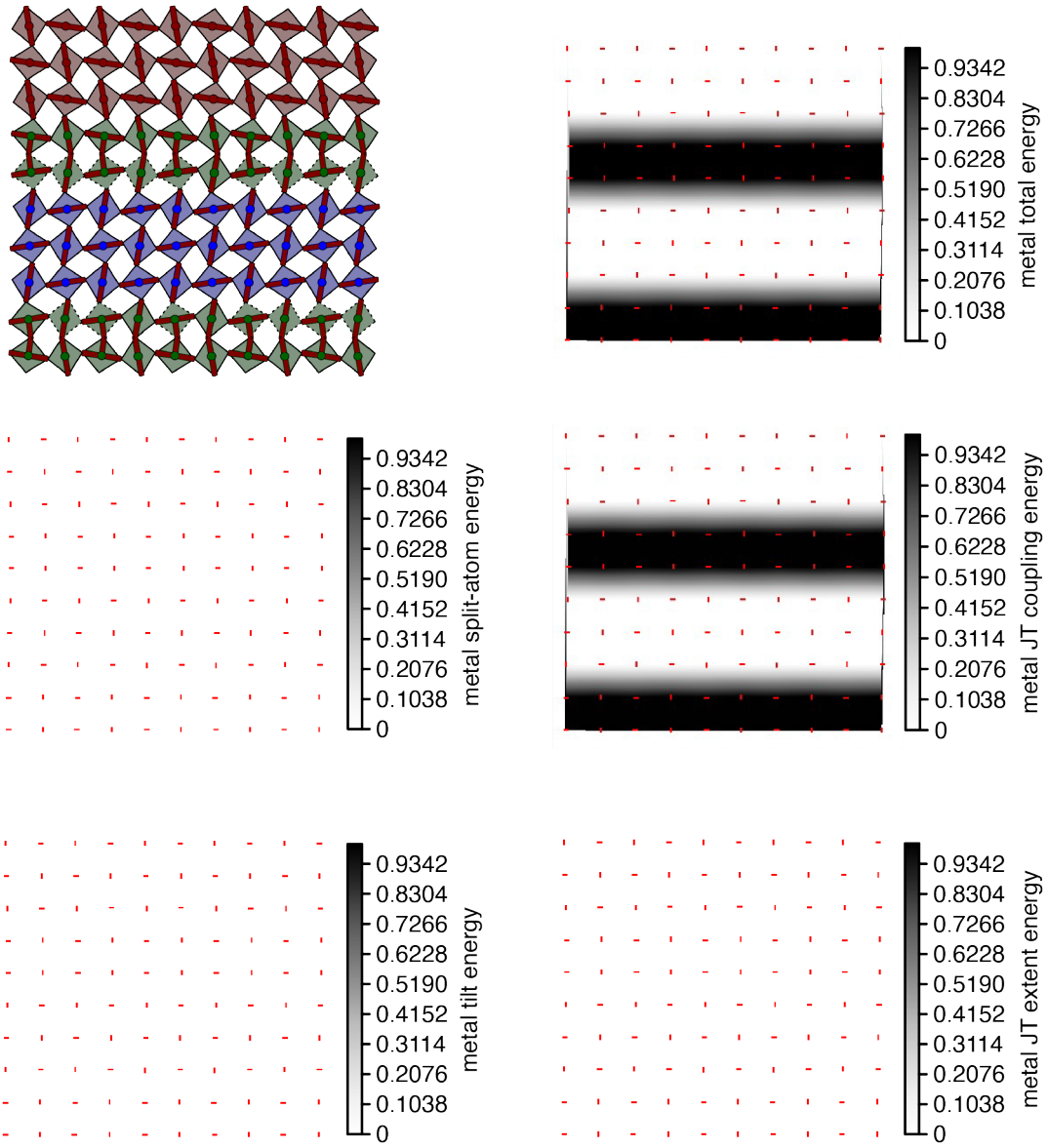


Figure C1.13: Representative $x = 1$ ($LaMnO_3$) ground state configuration with domains of opposite JT-order phase. Included are the contributions from each energy term to each metal site.

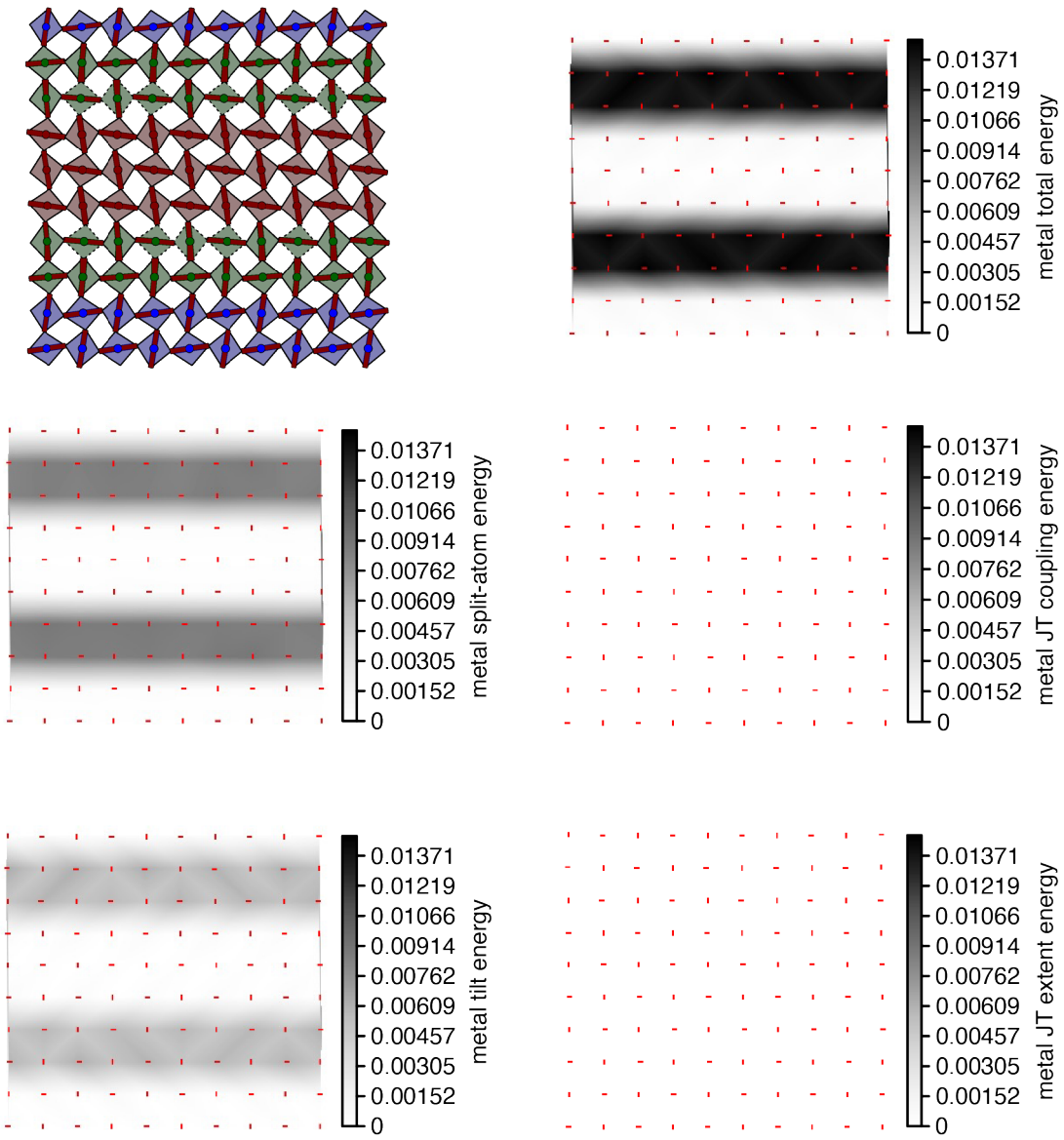


Figure C1.14: Representative $x = 1$ ($LaMnO_3$) ground state configuration with domain structures containing regions of opposite tilt phase. Included are the contributions from each energy term to each metal site.

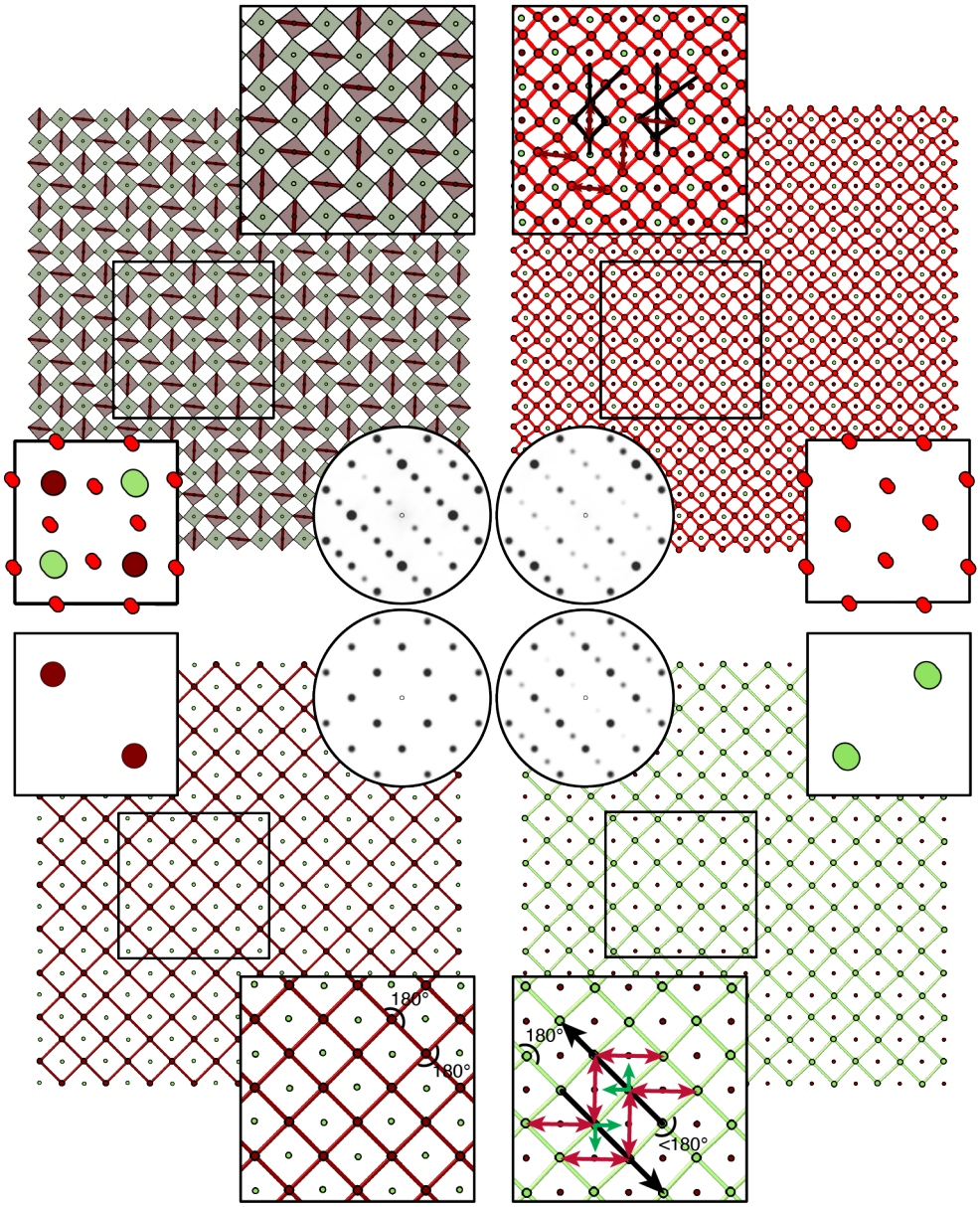


Figure C2.15: 20×20 supercell ($k_{\mathrm{SA}} = 100$) of the $La_{0.5}Ca_{0.5}MnO_3$ composition with the next-nearest Jahn–Teller coupling term included in the MC Hamiltonian to achieve the CE structure (with no domains). The Mn^{3+} (dark red), Mn^{4+} (green), and oxygen (red) sublattices and collapsed subcells are also shown alongside their corresponding simulated single-crystal diffuse scattering patterns (averaged over five configurations).

C2 $La_{0.5}Ca_{0.5}MnO_3$: Monte Carlo simulations

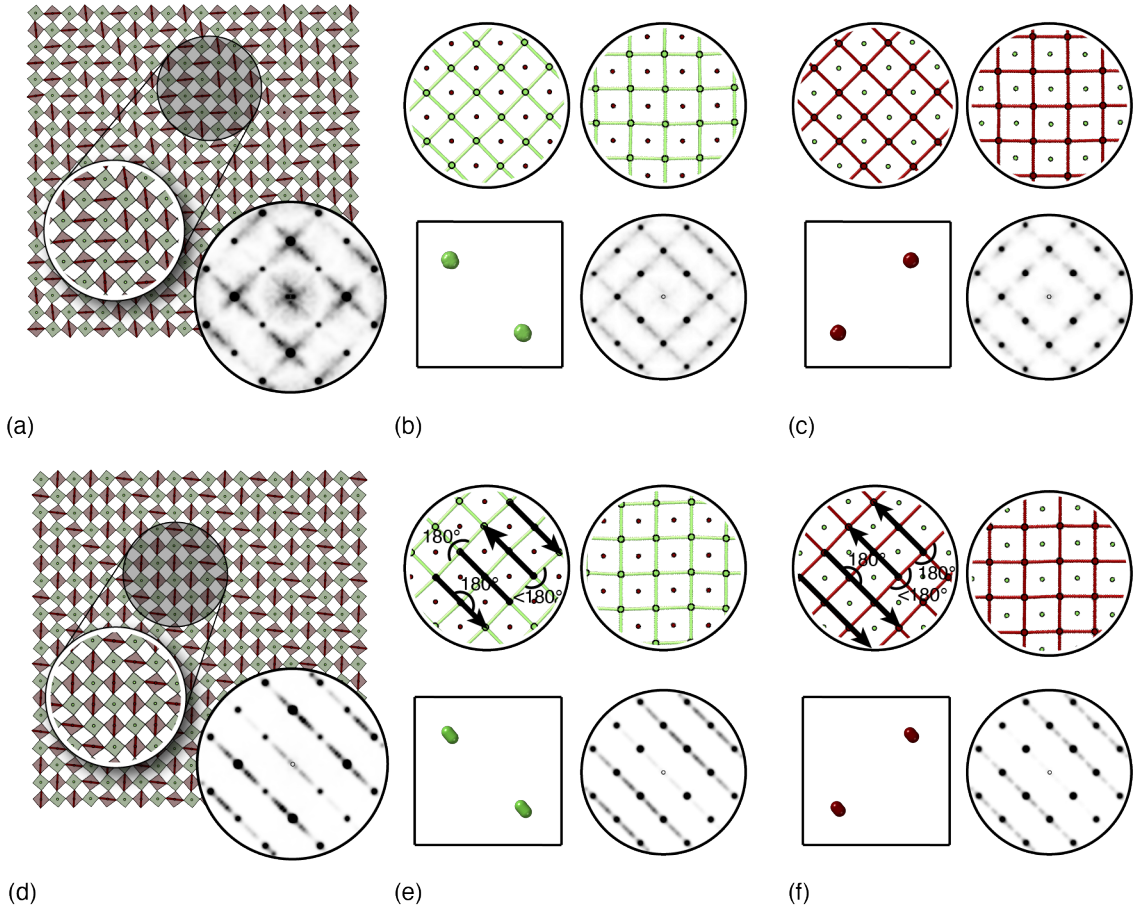


Figure C2.16: Simulated 20×20 supercells of $La_{0.5}Ca_{0.5}MnO_3$ where JT coupling, checkerboard charge order, and tilt terms have all been included in the MC Hamiltonian but no next-nearest JT coupling is included. (a)–(c) $k_{\mathrm{SA}} = 20$, (d)–(f) $k_{\mathrm{SA}} = 100$. (b), (c) Mn^{4+} (green) and (e), (f) Mn^{3+} (dark red) sub-lattices and their respective single-crystal diffuse scattering patterns, showing the impact of domain walls on their structure.

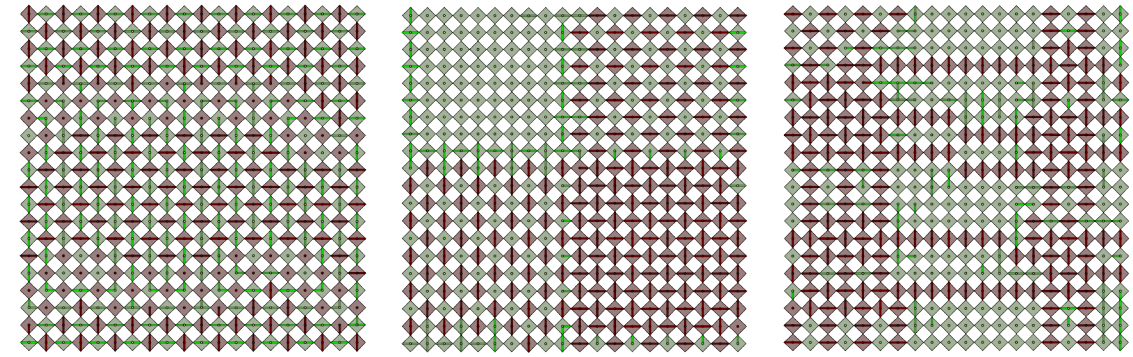


Figure C2.17: Effect of preventing rhombuses from tilting in the $La_{0.5}Ca_{0.5}MnO_3$ system. Split-atom and JT distortion magnitude terms in MC Hamiltonian in addition to (a) checkerboard charge ordering and nearest-neighbour JT coupling terms, (b) nearest-neighbour JT coupling term, and (c) neither checkerboard charge ordering nor nearest-neighbour JT coupling.

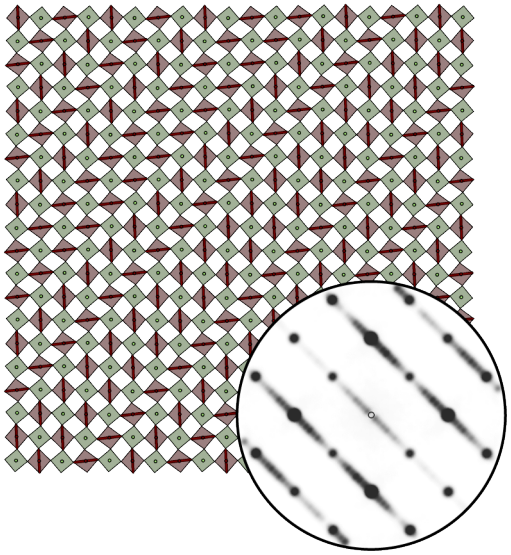


Figure C2.18: A 20×20 supercell ($k_{\mathrm{SA}} = 100$) of $La_{0.5}Ca_{0.5}MnO_3$ where the next-nearest JT coupling term was not included in the MC Hamiltonian. Even with $k_\gamma(\gamma - \gamma_{\mathrm{eq}})^2$ term in Hamiltonian with $\gamma_{\mathrm{eq}} = 89.688°$ (experimental value) and enforcing $a = b$, this is not enough to drive the CJT order to a single domain.

Appendix D: Measuring pair distribution functions with X-ray free-electron lasers: ultra-fast studies of disorder in Prussian blue analogues

D1 EuXFEL HED IC1: setup 1

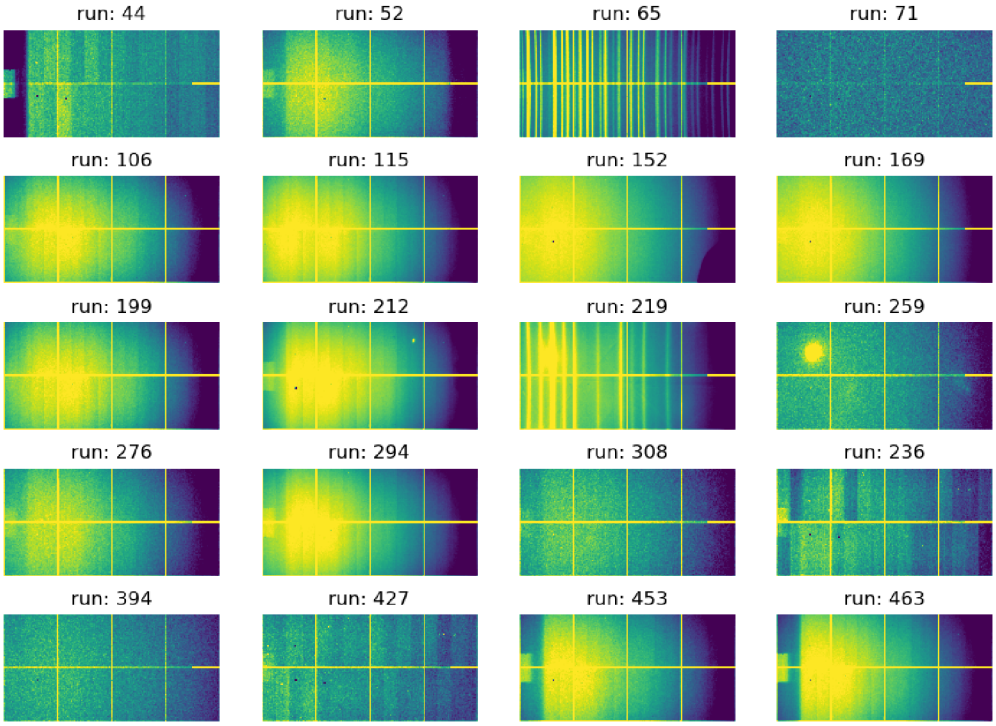


Figure D1.19: EuXFEL HED IC1 setup 1: low-Q shadowing

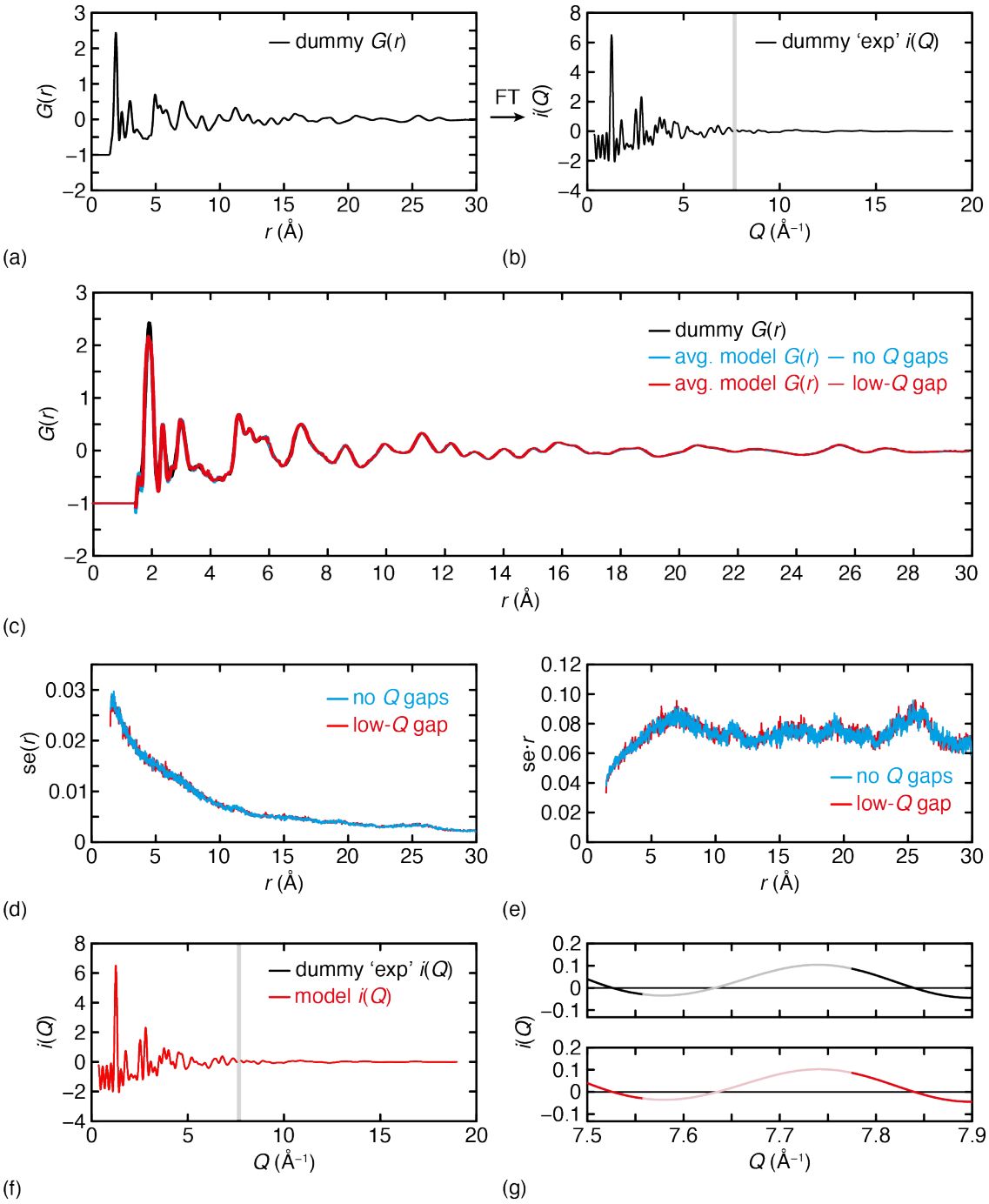


Figure D2.20: MCGR dummy data: impact of low-Q gap.

D2 Monte Carlo $G(r)$

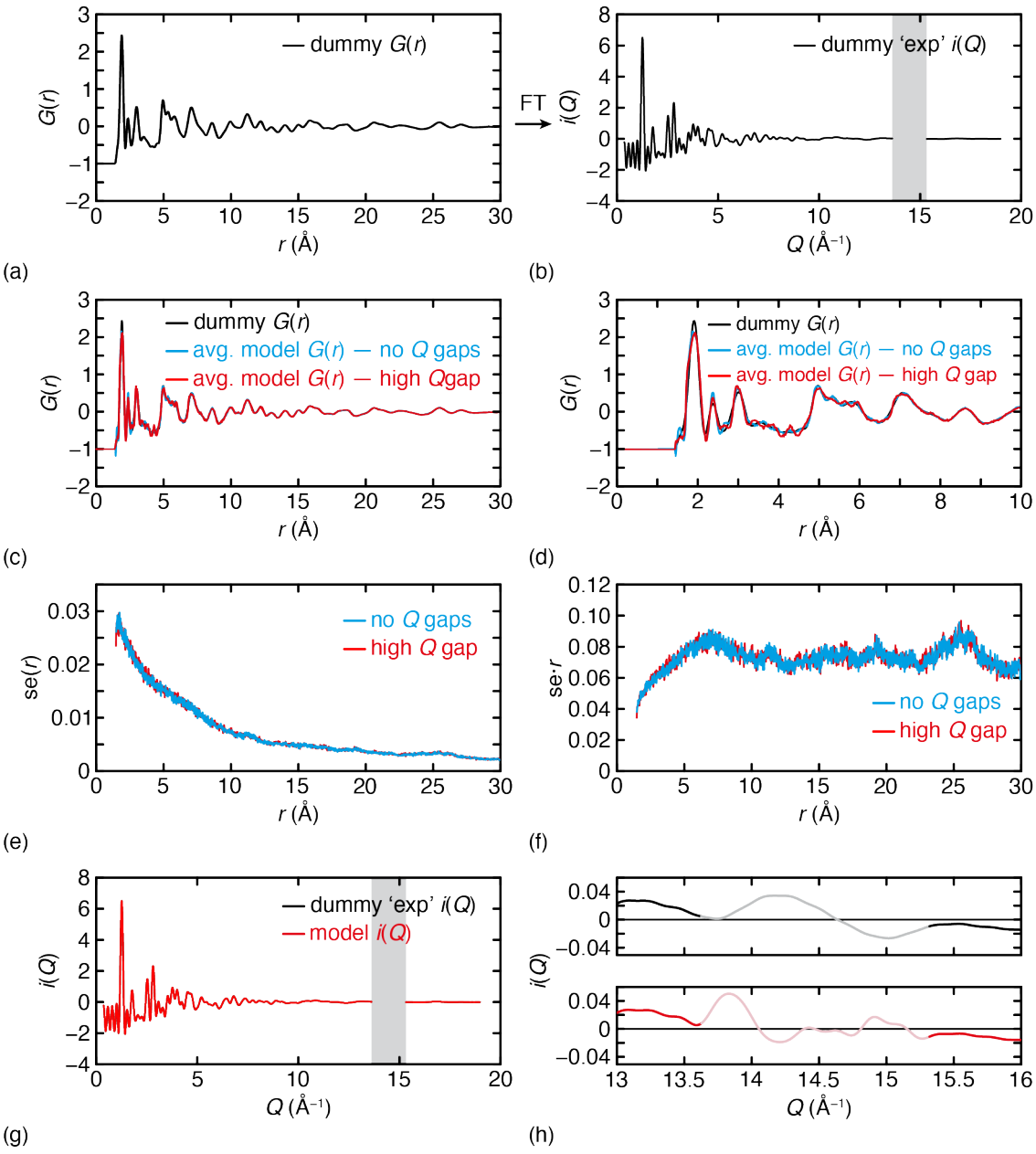


Figure D2.21: MCGR dummy data: impact of high-Q gap.